Western Michigan University
ScholarWorks at WMU

Dissertations | Graduate College

8-15-2016

Experimental Study of Simulated Geophysical Buoyancy-Driven Vortical Flow

Mohammad Hady Makhmalbaf
Western Michigan University, hmakhmalbaf@gmail.com

Follow this and additional works at: https://scholarworks.wmich.edu/dissertations

 Part of the Aerospace Engineering Commons

Recommended Citation

Makhmalbaf, Mohammad Hady, "Experimental Study of Simulated Geophysical Buoyancy-Driven Vortical Flow" (2016). *Dissertations*. 1954.
https://scholarworks.wmich.edu/dissertations/1954

This Dissertation-Open Access is brought to you for free and open access by the Graduate College at ScholarWorks at WMU. It has been accepted for inclusion in Dissertations by an authorized administrator of ScholarWorks at WMU. For more information, please contact wmu-scholarworks@wmich.edu.

EXPERIMENTAL STUDY OF SIMULATED GEOPHYSICAL BUOYANCY-DRIVEN VORTICAL FLOW

Mohammad Hady Makhmalbaf, Ph.D.

Western Michigan University, 2016

This paper describes an experimental study on the flow within a rotating cylinder with a counter-rotating disk located below to mimic certain aspects of the unique flow structures of the Great Red Spot (GRS) in Jupiter using a simple laboratory setup. The special design of this setup makes it capable of spinning the side wall of a vertical cylinder in both directions as well as rotating the bottom of the cylinder independently, where both can rotate in wide ranges of spin rates. Also, different thermal conditions can be applied on the bottom of the disk. All of these conditions provide the opportunity of generating two upward concentric vortices. Using the Particle Image Velocimetry (PIV) method in each set of experiments this study tries to track the particles of smoke in a pair of consecutive images in order to extract the velocity vectors for the entire domain in horizontal and vertical planes. Two dimensional velocity and vorticity fields are achievable by means of processing the consecutive images taken by the camera that mounted vertically on top of the cylindrical wall. The typical flow structures in the lower, transitional, and upper domains are described in detail, and in particular the intriguing features in the transitional domain are discussed. The three-dimensional flow structures of the torus vortices are qualitatively reconstructed. The thermal buoyancy effect induced by disk heating on the flow structures is investigated. Finally Co-rotating flow is introduced and different features of that flow is studied.

EXPERIMENTAL STUDY OF SIMULATED GEOPHYSICAL BUOYANCY-DRIVEN VORTICAL FLOW

by

Mohammad Hady Makhmalbaf

A dissertation Submitted to Graduate College
in partial fulfillment of the requirements
for the degree of Doctor of Philosophy
Mechanical Engineering
Western Michigan University
August 2016

Doctoral Committee:

Parviz Merati, Ph.D. Chair
Tianshu Liu, Ph.D.
Daniel Litynski, Ph.D.
Christopher Cho, Ph.D.

© 2016 Mohammad Hady Makhmalbaf

ACKNOWLEDGMENTS

First and above all, I praise Allah, the almighty for providing me this opportunity and granting me the capability to proceed successfully. This thesis appears in its current form due to the assistance and guidance of several people. I would therefore like to offer my sincere thanks to all of them.

I would like to start by thanking my mentor and dissertation committee member, Dr. Tianshu Liu for all of his guidance and patience in mentoring me to arrive at this point in my life. Also to Dr. Parviz Merati, I would like to express my sincerest gratitude for all his support, feedback and encouragement in making this work a success. Dr. Koorosh Naghshineh has also played an important role as the departmental graduate advisor in ensuring that my pursuit of this doctoral degree has been productive and trouble free, and for this I would like to recognize and thank him. I would like to state my gratitude and appreciation to other members of the committee Dr.Litynski and Dr.Cho.

I would like to thank Sai Kode and Patrick Wewengkang for their effort in the early stage of this research, Ali Merat and Andrew Verstraete for their remarkable help in preparing and conducting the experiments and data processing, and the important group from the Department of Industrial and Manufacturing Engineering at Western Michigan University that has contributed in designing and building the setup, Mr. Glenn Hall and Mr. Mike Konkel, I would like to thank them for all their hard work, unwavering commitment and excellent machining output that has been an important part in producing the high quality experimental results in this work.

Last but not least, I would like to recognize my family – my wife, mother, father, sister and brother for always being there for me and providing encouragement and support even when times were trying, I owe my success today to you, and I thank you for all that you have done.

Mohammad Hady Makhmalbaf

TABLE OF CONTENTS

Table of Contents—Continued

LIST OF TABLES

LIST OF FIGURES

List of Figures—Continued

List of Figures—Continued

List of Figures—Continued

List of Figures—Continued

List of Figures—Continued

List of Figures—Continued

List of Figures—Continued

List of Figures—Continued

List of Figures—Continued

1 Introduction

The family of rotating disk problems has been of interest for a long time. The simple case of a spinning disk in a semi-infinite, medium of viscous and incompressible fluid was first studied by Von-Karman study [1]. He derived the Navier-Stokes equations and simplified it to a system of ordinary differential equations. Cocharn[2] corrected Karman's study and reached more accurate results. There are many more theoretical numerical studies [3-5] that try to expand and develop Karman's solution. Subsequently, more complicated boundary conditions were proposed. Hanna [6] presented a solution for the forced flow against the rotating disk [7]. He changed the normal component of the velocity on a porous surface by solving the problem for a uniform suction and introduced a numerical solution for it. For laminar flow some theoretical solutions were suggested by Millsaps [8] and Wanger [9]. Cobb [10] presented one of the first results for turbulence flow conditions at least for a portion of disk. He tried to validate his experimental results with Wenger's when the flow is still laminar. Also, for the turbulent case he represented a correlation which was claimed to cover all the turbulent flow.

Riley [11] presented a theoretical solution based on his linear relationship between viscosity and temperature. According to his assumptions, the momentum equations can reduce to their incompressible form. Finally he came up with a heat transfer expression for both large and small Prandtl numbers. Dorfman [12] offered another solution for laminar flow and heat transfer near a rotating surface less than a year later. The key point of his study was an agreement between his own results for Nusselt number with respect to Reynolds number and some others such as Cobb's. The common boundary condition in all of the researches is the semi-infinite medium in Z direction (perpendicular to the plane). However, in some other studies (e.g. Owen’s [13]), the flow structure is between two disks, or the fluid itself, far from the disk, is rotating as a

solid body. Although these cases are not directly related to the subject, theoretically they can be somehow similar to the special case (Baseline Flows that are discussed later). Numerical solutions for Von Karman flow were developed in the earlier 80s especially by Lentini [14]. Further studies have been focused on the instability of the disk flow [15-19].

The family of Von Karman swirling flows has many interesting features and takes place frequently both in nature and industry. The flow structure around a disk shape part during the machinery process, Hard Discs, DVDs while spinning or an engine flywheel, are just a few examples of this big family in industry. Moreover, many geophysical vortices are being considered in the family of Von Karman swirling flows. In this study, the Jovian Great Red Spot, a persistent anti-cyclonic storm in Jupiter surface, and swirling flows in the earth atmosphere such as tornadoes and hurricanes, have been introduced, discussed, and experimentally modeled.

For the flow within a rotating cylinder with an infinite height, the exact solution of the Navier-Stokes equations gives a linear distribution of the azimuthal velocity of the steady laminar symmetrical flow [20]. In fact, this steady baseline flow is an asymptotic state of the unsteady solution of the viscous flow within a rotating cylinder [21]. The Taylor-Couette flow between two concentric rotating cylinders has been extensively studied, focusing on the flow instability and transition to turbulence [22-25].

In contrast to the extensive studies on the Taylor-Couette flow and the disk flow, the flow within a rotating cylinder with a counter-rotating disk located below has not been investigated. The baseline flow driven by the rotating cylinder wall has the linear azimuthal velocity distribution, but such a vortex flow structure will be broken down by the counter-rotating disk at the bottom. The complicated structures are expected to appear in the transitional domain between the upper and lower domains. In addition, the heating of the disk has the buoyancy-

induced effect on the flow. Although this project is defined as a fundamental research, the experimental setup has been designed to model unique features of the GRS with outer giant vortex and inner relatively low-velocity flow structures. Tornadoes with long height and relatively narrow width and hurricanes with wide shape and shallow geometry are all taken into consideration in design of this setup. Therefore, a comprehensive literature review of those phenomena and all classic studies is presented in this chapter.

1.1. Application, Motivation and Inspiring Phenomena: The Great Red Spot (GRS)

Ground-based and spacecraft observations have revealed that a system of zonal jets gas is dominant in both Jupiter and Saturn which causes the strips in different latitudes. There are respectively 8 and 4 eastward jets per hemisphere in Jupiter and Saturn respectively. A conspicuous characteristic of Jupiter for example is the existence of a broad-in-latitude eastward, equatorial jet with peak velocities of 150 m/s. Long-lived vortices in gas giants are located at latitudes with maximum local gradient of velocity along a constant longitude line. All vortices in gas giants have longitudinal drift; the cyclonic drifts eastward and the anticyclonic, the GRS for instance, drifts westward. The angular frequency of all of these vortices, including the GRS (~1 week) is much less than their planet rotation frequency (~10 hours for Jupiter). The flow structure in two hemispheres of both planets is more or less symmetric and as an example the GRS in 21^{o}S has a twin sister named Little Red Spot in 19^{o}N which is very similar to the GRS except for the size and life time (It is ~2.5 smaller and shows up and disappears in about every 5 years).

In order to study the Jovian atmosphere it seems important to have accurate understanding of the vertical structure of Jupiter. Visible clouds that form the GRS are located in

the upper few dozen of kilometers of Jovian atmosphere. This thickness is two or three orders of magnitude less than the GRS horizontal size. This thin layer sits on another 1000 km thick layer beneath it with much higher pressure. Based on calculations of Hank et.al.[26] by adiabatic law, 1000 kilometers below the visible surface the upper cloud pressure and temperature increase to 5600 *atm* and 2200K respectively. Liquid hydrogen is the main component. Further, 11000 kilometer beneath the upper clouds, hydrogen state changes to metal under the pressure of 3 million *atm* and at temperature of 11000K. The fact that the visible, cloudy upper layer rests on the invisible, thick liquid hydrogen layer seems to be a key factor in the formation of Jovian atmosphere and particularly in the GRS which will be discussed later.

The best known feature of Jupiter is the GRS, also known as 'The Eye of Jupiter' which was an inspiration to this project. The largest vortex in the solar system (twice the size of Earth) is located in 22^{o} south of the equator. It consists of a swirling mass of clouds that are higher and cooler than the surrounding ones and is known to have been in existence since at least 1831 and possibly since 1665 [27]. Its complex flow structure is completely different from terrestrial vortices like hurricanes and tornadoes as well as other Jovian structure i.e. the White Ovals. Not only the GRS, but also other large, long-lived vortices in gas giants are located at latitudes where the gradient of flow velocity along a zonal line is in a local maximum. Moreover, the sustenance of the GRS along the other features has been of interest for a long time. The GRS flow structure has a rotating vortex at the outer ring with maximum speed of about 400 km/hour (~250 mph). Here is some basic information about the GRS and Jupiter:

Longitudinal Diameter	24–40,000 km	Period of One revolution	~10Hr	Polarity	Anti-cyclone	Depth	Unknown
Latitudinal Diameter	12–14,000 km	Top speed of wind	120 m/s	Drift direction	westward	Life Time	>300yrs

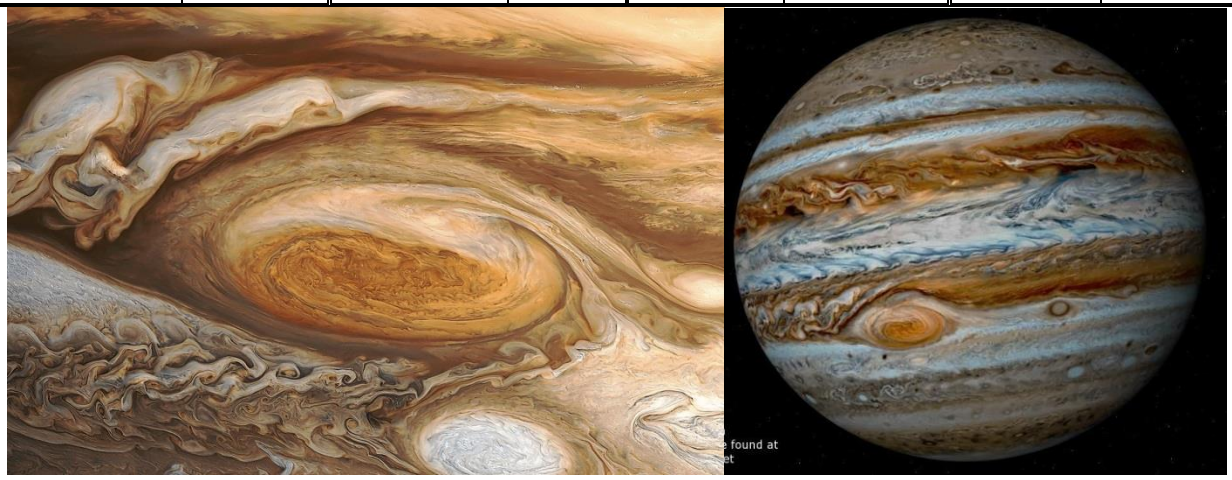

Figure 1.1 Great Red Spot (Left), Jupiter (Right)

The thick gaseous atmosphere of the planet has been modeled mathematically and experimentally. These models suggest GRS is stable and might be a permanent feature of Jupiter as it has been in the last centuries. Most of the theoretical and experimental approaches are based on one of these two models: Shallow layer model or Deep circulation model. Before introducing the setup and its specifications, a brief review of both models and enumerating their advantages and disadvantages seem necessary.

The Shallow Layer model extends only a few bars below the main upper cloud and has the solar radiation as the main energy source. In different latitudes the solar heat that the upper layer receives varies as well as the Coriolis force due to different distances from the axis of planet rotation around itself. As a result, the temperature difference drives the motion in a low friction and hydrostatic quasi-geostrophic balance. The equations of motion with the Shallow

layer assumptions were first formulated and solved by Williams [28-29].The high temperature gradient or the “shallow” meteorologically active layer in the giant planets seems to be dynamically similar to the Earth’s ocean “thermocline”, an upper oceanic layer of ~ 2 km depth [30]. A series of experiments on a parabolic vessel that is being used to generate Rossby vortices by counter-flows is example of experimental studies with Shallow layer approach by Nezlin et al. [31-33].

Shallow layer equations are derived from mass, momentum and energy conservation equations where the horizontal length scale is assumed much greater than vertical one. Therefore, mass conservation implies that the vertical component of velocity is comparatively small and thus negligible. Moreover, momentum equations show that vertical pressure gradient acts like the hydrostatic case. The horizontal pressure gradient, because of the displacement of the pressure surface, implies that the horizontal velocity field is constant over the depth of the fluid. Hence, the vertical component of velocity could be omitted by integrating in the vertical direction.

The spinning rate of a planet directly effects the Coriolis term [34-38]. Because Jupiter rotates relatively fast (each revolution takes 9 hours and 56 minutes), the Coriolis term plays the main role in momentum equations. The low temperature, high pressure and thick atmosphere of Jupiter amplify the visibility of those belts and horizontal stripes on its surface. Figure 1.2 shows a processed image of Jupiter surface and velocity profile with respect to latitude. This situation, always occurring on spinning planets, is called planetary wind.

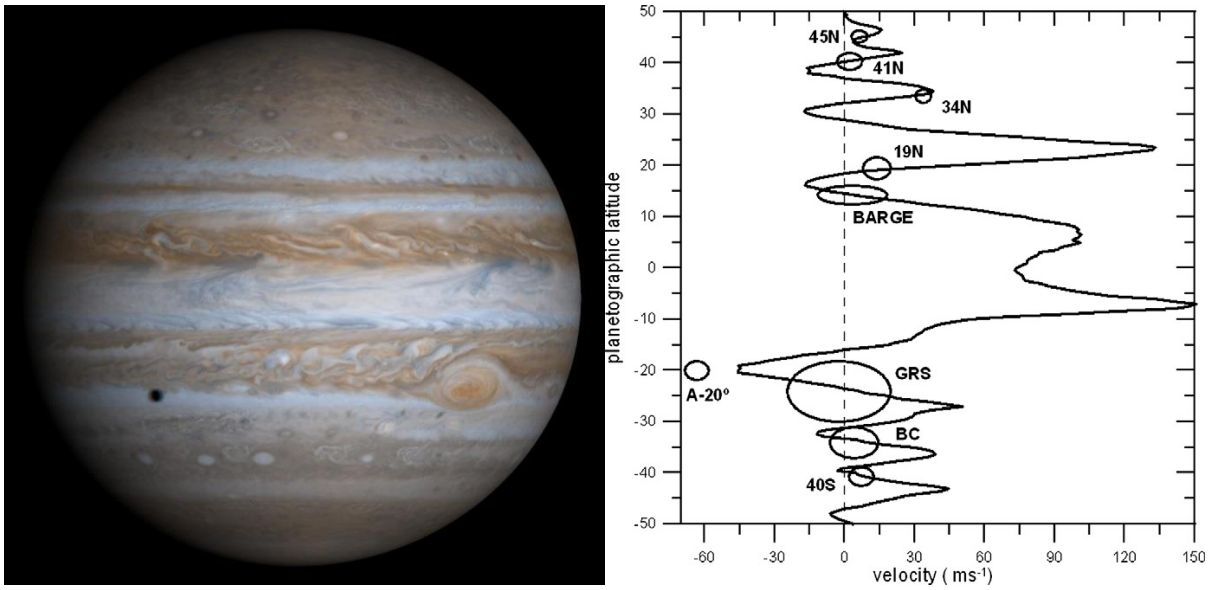

Figure 1.2 Jupiter's zonal wind profile. The vortices are scaled to their latitudinal size [39]

As such, the Coriolis force is simply balanced by the hydrostatic pressure gradient $p = \rho_0 g^* H$, where H is the effective depth of the planet's atmosphere, and g^* is the acceleration due to the resultant of the gravitational force and the centrifugal force from the global rotation.

Another feature of Jupiter and Saturn that prepares the situation for long lasting storms is the fact that these planets do not have solid surfaces or continents as do Earth and Mars. Jupiter's does not have the storm damping tendency due to mountains, valleys, and other heights that reduce the intensity and strength of flow structures. The rotation time scale of the planet around itself (in particular; Saturn: 0.44 Earth days, Jupiter: 0.41 Earth days) is much smaller than any vortices time scale (e.g. JGRS's time scale: ~ 6 Earth days). Besides, the ratios of planet radii to length scale of atmospheric structures on Jupiter and Saturn (about 10 or more) are much larger than that ratio in terrestrial atmospheric structures (few units). Therefore, these two facts make the gas giants' vortices more long-living compared to the terrestrial ones.

Many experimental setups that have been designed to model various types of vortices based on shallow layer model mostly try to generate a thin layer of rotating fluid which has a very small thickness compared to the whole model radius. This thickness cannot be too small or too large because being too small makes both the effect of boundary layer and vertical gradient of velocity significant while the large thickness is in contradiction with the main shallow layer assumption. The free surface of a rotating liquid in presence of gravity has a parabolic curvature. Based on this fact, the inner vessels in this type of setup have a parabolic curvature corresponding with certain spin rates. When the vessel reaches a particular angular speed, the free surface of liquid becomes parallel to their concave shapes. Figure 1.3 demonstrates the schematic and results of one of those setups as an example. The two images of vortices in this figure are captured when a particular set of boundary conditions from the bottom rings is applied to the shallow layer of liquid and several counter rotating vortices so called zonal counter-flow are generated (arrows in the schematic indicate rings spinning directions with respect to the vessel).

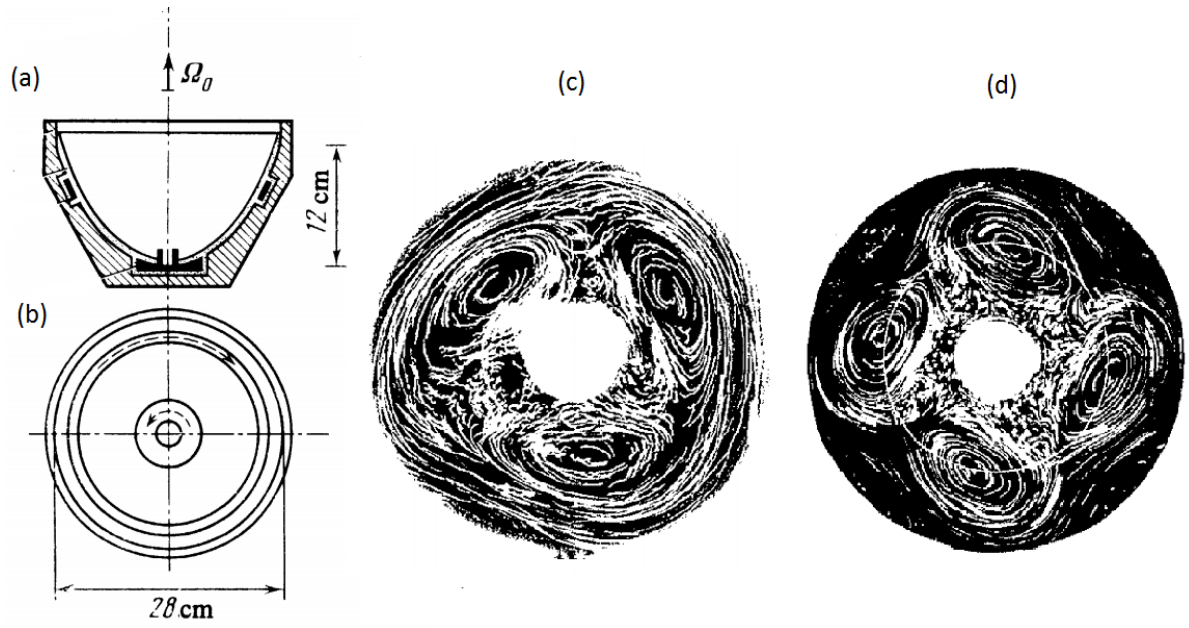

Figure 1.3 Shallow water experimental setup [40]. Top view (a), Side view (b)and Results (c and d)

This type of experimental setup has an important advantage. Because the position and spin rate of rings is adjustable, different boundary conditions are achievable. This advantage makes the system capable of not only modeling many vortices of Jupiter and Saturn, but also modeling the Galactic Spiral Structures [41]. However, building, casting and sealing the parabolic vessel as well as rotating the ring in different directions, radii and angular velocities are only a few of technical issues that make these setups complicated, expensive and difficult to build.

The deep circulation model was developed theoretically and experimentally, and first presented by Busse [42,43]. For an incompressible and inviscid fluid heated from below in a spherical layer that rotates rapidly, the fluid dynamic equations show that the convective motions are transporting the heat from the bottom to the top. According to Deep Circulation model Taylor-Proudman columns are causing the entire flow. As shown in figure 2.4, these columns are rotating cylinders parallel to the planet axis, and based on this equation the velocity component along the rotation axis of each column in zero. In other words, it implies that there would be some cylindrical vortices around the main rotating spherical core. The model suggests that these columns are shaped simply because they cannot keep up with the fast spinning liquid metal core. The cylindrical Counter-Rotating vortices are causing the surface patterns and strips on Jupiter and Saturn as they reach the exterior. Based on this hypothesis, the flow structure in deep layers is driven by the internal heat source and near the surface generates jet patterns hemispherically symmetric. These patterns remain steady in time due to large inertia and mass. Since the core of the planet acts as a rigid body for the fluids, this hypothesis indicates both poles of the planet are engaged with these vertical cylinders as demonstrated in Figure 1.4.

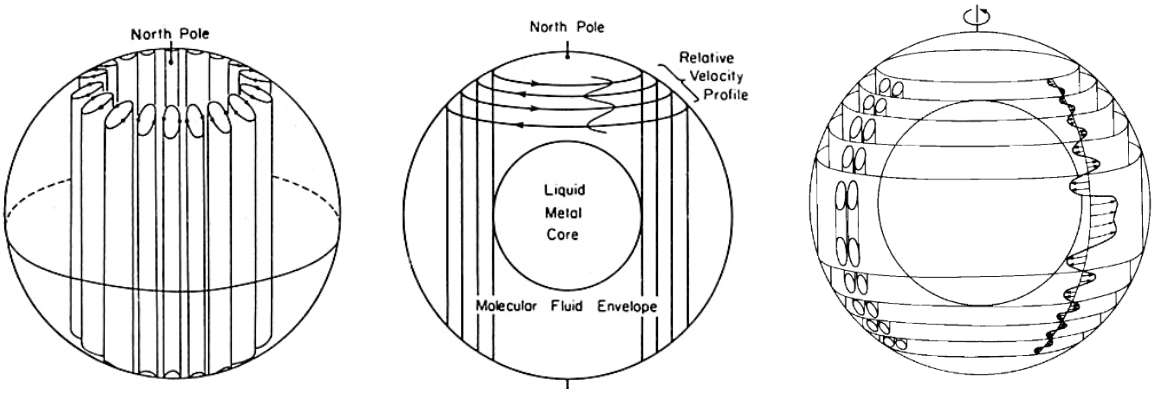

Figure 1.4 Deep circulation model (columnar convection & coaxial cylindrical circulation) for the giant planets [44]

The Taylor-Proudman theorem states that when a solid body is moved slowly within a fluid that is steadily rotated with a high angular spin rate, the fluid velocity will be uniform along any line parallel to the axis of rotation. This theorem is still valid because the dominant term is Coriolis force and non-linear terms are small relatively. The metal core of a planet can be assumed rigid and therefore $\partial \boldsymbol{V} / \partial \boldsymbol{x} = \mathbf{0}$ is used as boundary conditions in the spherical layer (in some studies, the core is considered as a thick liquid sphere and as a result the boundary conditions are slightly different [45]). Based on this approach, some studies [46 and 47], as the first attempts, demonstrated analytical solutions for the motion equations, while some others [48-50] numerically studied the GRS atmosphere. The key assumptions of Deep Circulation model are not completely realistic: Fluid has been considered incompressible which is contrary with the reality especially near both ends of the columns where jets are dealing with the fluids from deep levels with significant pressure, or the exterior levels with lower pressure. Also, knowledge about metal core radius, as a key factor in this method, is very limited and this raises serious question about this method's results.

Shallow Layer and Deep Circulation models can be compared from different points of view. Some phenomena in Gas Giants cannot be justified by one method, while the other one

explains that fact reasonably. Some facts cannot be justified by either, so other theories should be tried. Another problem about planetary phenomena is their mysterious characteristics and lack of information due to inaccessibility. Since all the existing information is based on observation, there is a world of unknowns, doubts and assumptions when it comes to a question about layers of planet atmosphere, pressure, materials, etc. Specifically in Jupiter, layers, depth, phase and materials are not completely known and the only fact that definitely can be relied on is the results from the images taken from its gaseous surface. In order to decide which method is more accurate, this question about the planet atmosphere needs to be answered; "How deep is it?"

Using the Shallow layer model or Deep one depends on that answer. If the former is applied, the convection term will not be taken into account directly. In the latter, although the convection term is being considered from the beginning, the depth of rigid body, which plays the main role, is utterly based on unreliable assumptions [51]. These assumptions can be in contradiction with observations that show the GRS is shallow compared to the size of planet and the big vortex is occurring only in upper layers of atmosphere. The criticisms soar when both of them are not able to justify asymmetry of flow structure in two hemispheres or different life time of some vortices. For instance, neither has an explanation for the fact that there is no consistent and giant vortex similar to the GRS in northern hemisphere. So far, there is no accepted theory to explain the nature of Gas Giants and these models are only on a rudimentary stage [52-53]. For validation of all these models, their results are being compared with the extracted velocity field and other relevant properties obtained by the multi-spatial images from Jovian atmosphere captured by spacecraft flying around the planet.

Tracking cloud elements along a given time interval allows us to measure atmospheric motions and consequently extract the velocity field at some levels (clouds and hazes are typically located between pressure levels 0.3 and 2 bar). Cloud speed is relative to the planet but since

Jupiter (and also Saturn) does not have a solid ground, spinning rate of the planet around itself is measured by the planet's magnetic field, which is assumed to be the spinning of the planet itself. This assumption is because the magnetic field is rooted to the deep interior rather than clouds in the surface of the planet [51].

Several methods of velocity extraction from the Jovian atmosphere have been presented by researchers. Manual tracking of Voyager images, taken on March 4, 1979, was done by Mitchell et.al. [54]. This study was one of the first accurate velocity tracking attempts. Further, a set of 2000 randomly scattered velocity vectors using manual tracking was presented by Dowling and Ingersoll [55] for the analysis of the potential vorticity and layer thickness variation. Based on these datasets many theoretical analyses were presented [56-59]. Several studies argued that an organized motion particularly a cyclonic (clockwise) vortex existed near the center. First, a manual tracking study presented by Sada et al. [60] obtained about 2500 velocity vectors in the inner region from the Voyager images. Further, the zonal velocity profile presented by Vasavada et al.[61] using both manual tracking and correlation method from the Galileo 1996 images offered clear cyclonic vortex at the center. Moreover, Simon-Miller et al.[62] demonstrated that the zonal velocity profile from Galileo 2000 images is in good agreement with the previous results. The fact that the rotation motion in the center was observed in results from Voyager 1979, Galileo 1996 and Galileo 2000 proves the consistency of this flow over the course of decades. Furthermore, processing those images showed higher resolution results obtained by Choi et.al. [63] and Asay-Davis et al. [64] which all confirm the existence of an elliptical ring of high velocity anti-cyclonic vortex and a relatively low velocity inner region and a cyclonic rotation near the center. Accuracy, resolution and number of vectors that a method can attain from a set of images is the key point in analyzing the flow field in this case in the inner region

and generally in all planetary studies. Among all methods that track the clouds in planetary images, the Optical Flow Method, a physics-based method developed by Liu and Shen [65], offers much higher resolution velocity vector fields (one vector per pixel) compared to correlation methods which are adaption of particle image velocimetry to images of continuous cloud patterns. The comprehensive comparison between these two methods and the mathematics behind each of them shows the optical flow's strength in processing images of continuous cloud patterns with smaller displacements [66]. Figure 1.5 compares different attempts of extracting the velocity field and obtaining the profile from the existing images of the GRS.

Using the optical flow method, Liu et al. [67] studied flow structure of the GRS from the two images (Both images are reconstructed mosaics of several shots with 4320 seconds interval between them) taken by Galileo on June26, 1996 [42] and presented high resolution velocity vector field for both outer and inner region as well as the zonal and meridional velocity profiles along the minor and major axes across the GRS. They compared those results with the previous ones and suggested that the role of a source node in the center and consequently the cyclonic system is necessary in the maintenance of the GRS. Based on their results, the vector field indicates that the outer ring has much higher velocities, the streamlines in the inner region show random and zigzag behavior and zonal velocity profile also exhibits that a counter rotating flow exists at the core. The center of this cyclonic flow is clearly highlighted as the associated Counter-Rotating source node. A simple topological constraint was given for the number of isolated singular points in the inner region of the GRS. Authors believe that according to this topological constraint, at least one node in the inner region is necessary for the presence of the GRS, and in this case the aforementioned node is considered as such a seed node [45].

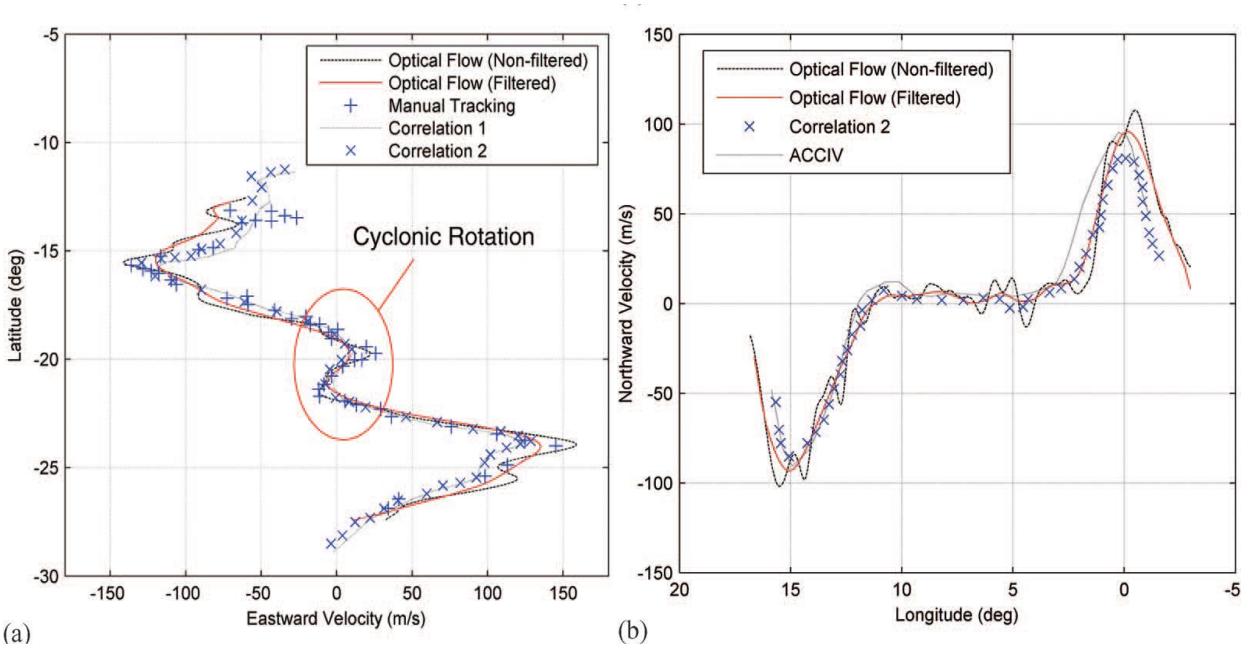

Figure 1.5 The profiles of (a) the zonal and (b) meridional velocities averaged along the minor and major axes across the GRS, respectively [67].

Although this proves the necessity of the Counter-Rotating flow at the center, the question remains unanswered; What is the main reason for this phenomenon? In other words, it is still unknown what physical factor in the Jovian atmosphere forces the core region the act to way it does. Considering that region as a control volume, it is surrounded by the outer collar and the bottom layers which our knowledge about it is very limited. Since there is no visual-based data and evidence of the lower layers, it is hard to say what are these layers are made of, at what pressure/depth the state changes, and what flow structure is dominant in those layers. Therefore, the experimental setup has to be designed long enough to model the depth, capable of modeling the thermal conditions and temperature difference, and independently capable of modeling any type of vortical flow caused by lower layers of the Jovian atmosphere as well as the outer collar. This was the initiative idea of designing and building the experimental setup.

The objective for this part of the current project is to simulate the similar conditions that take place on Jupiter surface for the GRS and generate a flow structure similar inside the

designed test zone. Thus, the experimental setup needs to simulate these two concentric, opposite-directions vortices. The extracted flow properties from the model and the GRS are being compared. This study can manifest the similarities between two cases and suggest the sources, causes and features of the GRS and give grounds for its sustenance and unique behaviors and life-time.

An intriguing question is whether this kind of the vortex flow can be simulated to some degree in a simple mechanical/thermal device in a laboratory. The objective of this work is to devise a simple rotating-cylinder-and-counter-rotating disk system to simulate the flow structure of the GRS and measure the flows in this system via PIV, focusing on an understanding of the effects of the disk spinning rate and the disk heating on the flow structures. The paper is organized as follows. First, the experimental setup and measurement techniques are described, including the rotating cylinder and the counter-rotating disk driven by the DC motors and PIV measurement system (the laser and camera). The relevant non-dimensional parameters are introduced. Next, the cylinder-baseline-flow and Disk-Baseline Flow are discussed, which provide the necessary references for comparison. The velocity fields in the counter-rotating-cylinder-disk-flows without disk heating are investigated particularly focusing on the flow structures in the transitional domain between the upper and lower domains. Finally, the effects of the thermal buoyancy induced by the heated disk on the flow structures in the counter-rotating-cylinder-disk-flows are presented.

1.2. Other Applications

Terrestrial vortices, tornadoes and hurricanes, are other phenomena that can be simulated by this setup. Studies on tornadoes began decades ago mostly about formation and prediction by examining the flow structure theoretically [e.g. 68-71] and also by making laboratory models

[e.g. 72-77] as well as the case studies that had taken place [78]. Since the real situation is too dangerous to do field studies, and access to higher levels of tornadoes flow structure for measurement purposes is very difficult, most of existing data in this area has come from laboratory setups and experiments. Numerical efforts are useful not only for the results they provide, but also those studies give more accurate and realistic ideas for designing closer experimental setups to the actual cases. This chapter reviews some of both numerical and experimental studies and compares them with this project and figures out the required data that needs to be extracted from the present setup.

First some primary information about tornadoes and a scientific definition needs to be provided. A tornado is basically a rapidly spinning column of air that contains a cumuliform cloud (predominantly vertical direction cloud). The longest lasting and most intense type of tornadoes which arises with a cumuliform cloud is known as Supercell thunderstorm which is characterized by the presence of a Mesocyclone: a deep, persistently rotating updraft. These storms are sometimes being referred to as rotating thunderstorms and they can last for hours and their highest speed reaches 180 mph. Figure 1.6 demonstrates wind field of the Saylor Park, Ohio, tornado of April 3, 1974 as an example of these tornadoes [78].

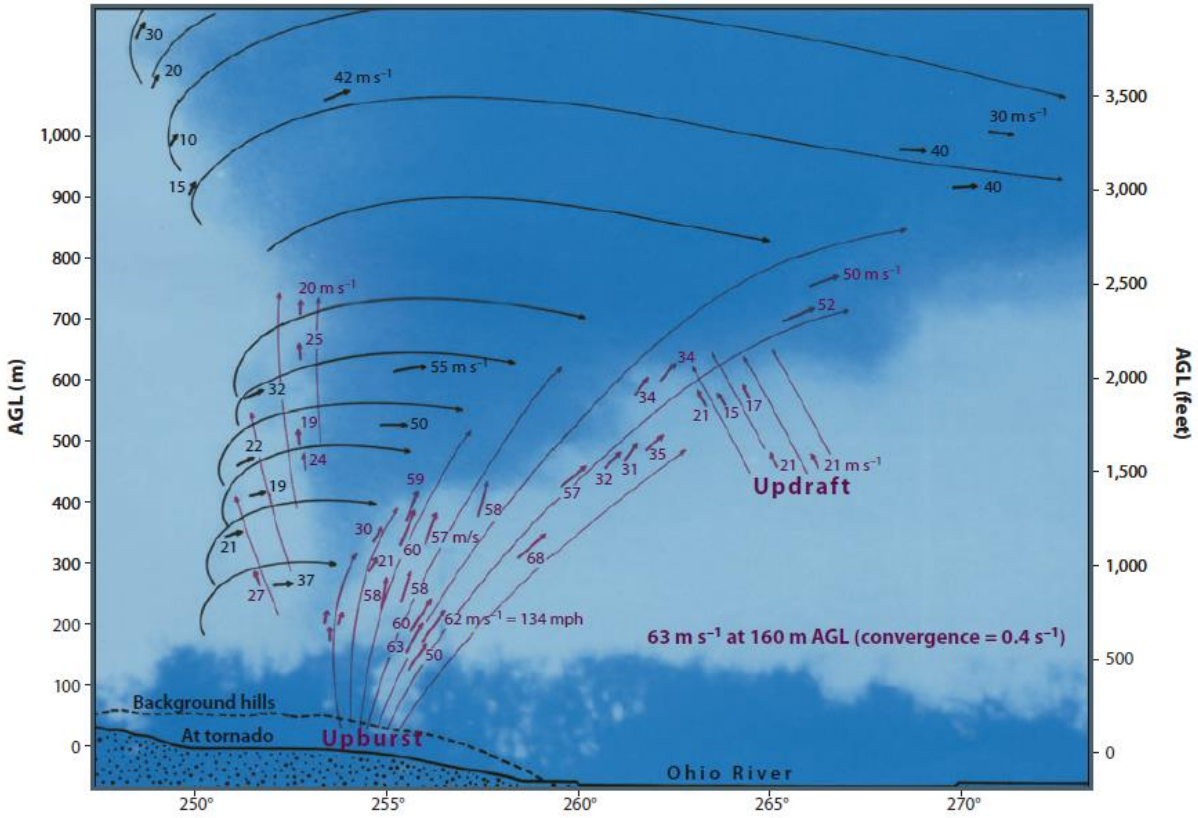

Figure 1.6 The black velocity vectors show the rotation of the column, and the red velocity vectors demonstrate the strong upward motion. Abbreviation: AGL, above ground level [79].

All of experimental setups have the main test section chamber in which a vortex takes place. This chamber is isolated from the outside and simulates and simplifies the essential feature of tornado formation: supercell thunderstorm. Figures 1.7 and 1.8 show two of the first and most important experimental setups that generate the updraft by Ward [72] and Church [73] respectively. In the first type of apparatus (figure a), which is called Ward-type, upward volumetric flow rate of $2\pi Q$, passes through the upper orifice of the device (outflow) with r_0 radius. Having the height of chamber, h, its radius r_s, exit radius r_0, air kinematic viscosity, ν , volumetric updraft flow rate Q and angular momentum $2\pi\Gamma_s$ ($\Gamma_s$representing circulation around the updraft center) six dimensional parameters are $r_s, r_0, h, \nu, Q, and\ \Gamma_s$. Therefore, according to Buckingham Π theorem, four non-dimensional parameters can be formed in this type of setups:

Swirl ratio$S = r_0\Gamma_s/(2Q)$, Reynolds number $Re = Q/(vh)$, aspect ratio $a = h/r_0$ and the ratio of updraft outlet radius to the chamber radius r_0/r_s.

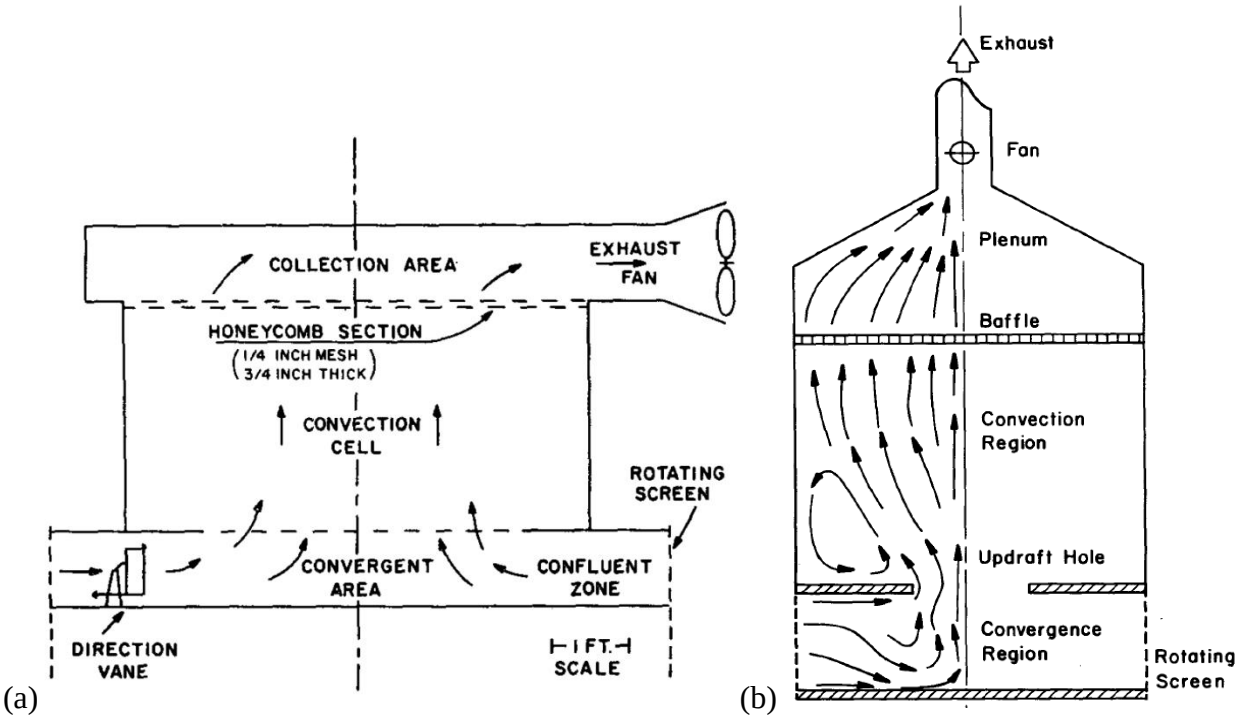

Figure 1.7 Two examples of Ward-Type setups. Left: Ward's [72] and Right: Church's [73]

Unlike the way this setup is designed, in most Ward-type cases the thermal interaction between earth and air and the temperature difference of atmosphere layers have not been taken into account. Simulating the thermal condition can be the new feature that the present setup offers by considering the effect of temperature difference in the formation of these updrafts . This can make the results more accurate and realistic.

Ward-type studies [e.g. 71, 73, 76] unanimously indicate that if the geometry parameters of setup stay constant, flow structure mainly depends on swirl ratio, S, and secondarily on Re. Besides, vortices in low S numbers have simple upward structure and as the swirl ratio grows a downward flow begins at the vertical axis. The stagnation point, caused by facing the two opposite vertical directions, descends when S increases until the updraft splits to two, and

eventually to multiple vortices as it has been shown in Figure 3.3. Several numerical studies are in good agreement with these experimental researches but the Re number has been considered much smaller in those numerical studies. Among these solutions, [68], [69] and [71] could be the best examples.

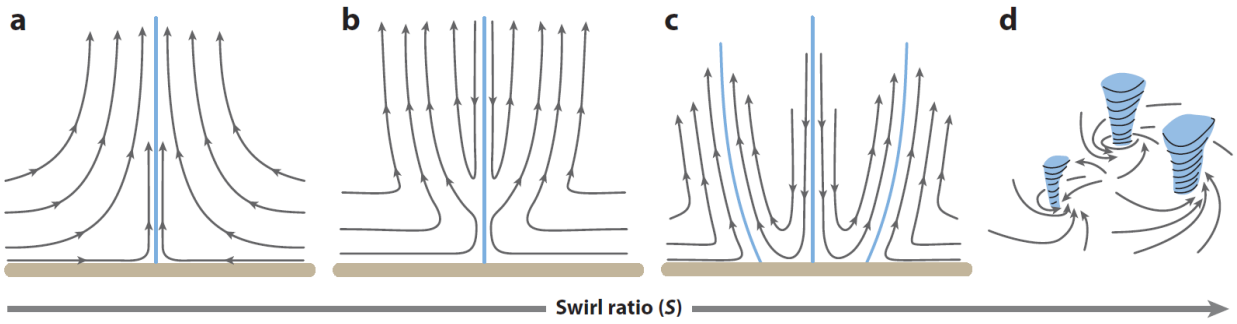

Figure 1.8 For increasing swirl ratio, the form of the vortex changes from (a) single-celled to (b) single-celled below and doubled-celled above to (c) doubled-celled to (d) multiple vortices. Figure adapted from [79]

Fiedler [75 and 79] also introduced another type of tornado simulator in which the entire body rotates to generate the spiral vortex. However, instead of a fan in Ward-type setups, buoyancy produces the upward flow. Schematics of both types are displayed in Figure 1.9.

Non-dimensional analysis shows that Fiedler model has eight external parameters (r_s, l_r, l_z; radial and vertical scales, z_m; the location of the maximum formation, h, ν, W; velocity scale and ω) where:

$$W = \sqrt{2\int_0^h b(o,z)dz} \qquad (3.1)$$

Where $b(r,z)$ is upward (buoyancy) force per unit mass.

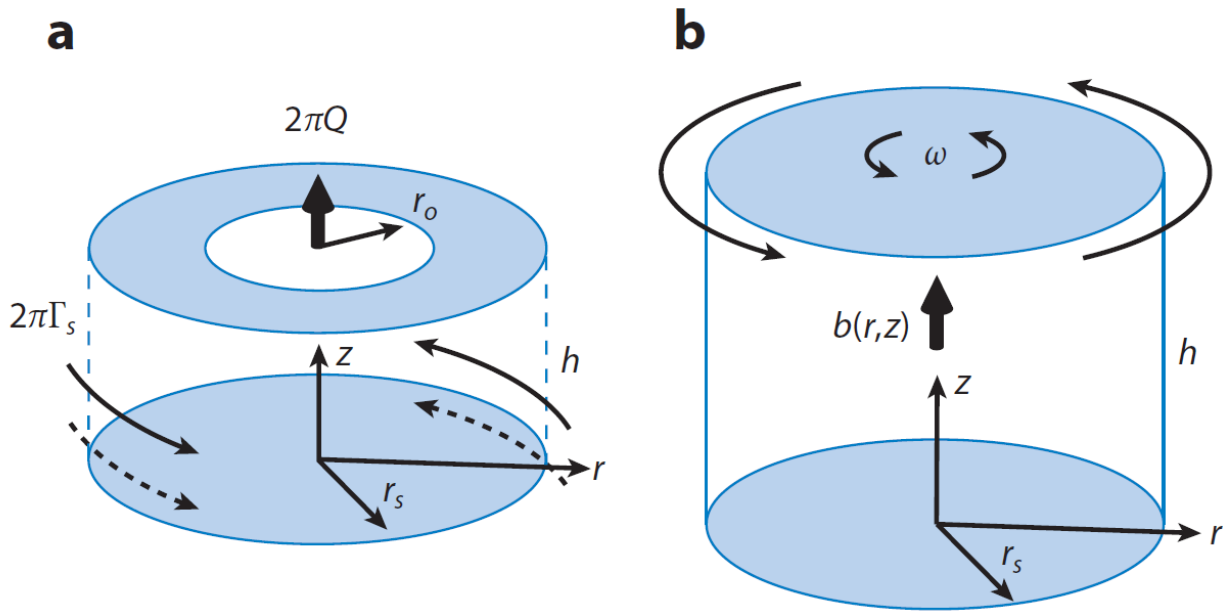

Figure 1.9 Two types of vortex chambers (a) Ward-type, (b) Fiedler-Type. Figure adapted from [80]

Therefore the first four parameters are fixed according to geometry and due to Buckingham Π theorem, two non-dimensional numbers; $\Omega = \omega h/W$ as the swirl ratio, and $Re = Wh/\nu$ as the Reynolds number can be achieved. Fiedler chamber studies cover a wide range of Ω and Re and these studies mostly are carried out in a virtual chamber. In other words, there are not so many actual laboratory investigations in this field other than those combined with Ward-type setup such as Yang [77]. In that particular work, a huge setup generates the main vortex with azimuthal blowing. The wind with guiding ducts directs the swirling flow and the upward flow in maintained by the main fan at the center of setup as it has been shown in Figures 1.10 and 1.11.

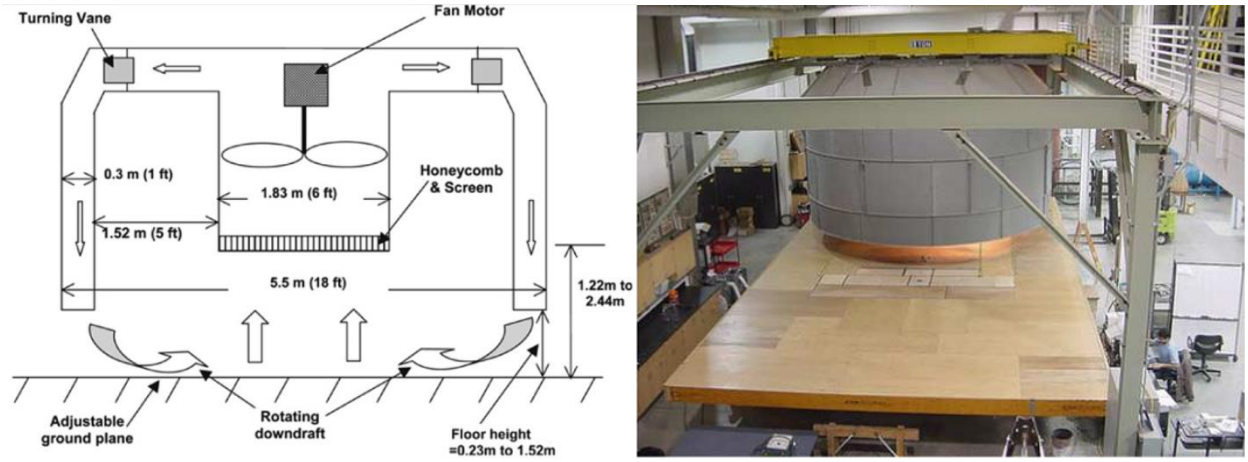

Figure 1.10 Yang's modern setup [77]

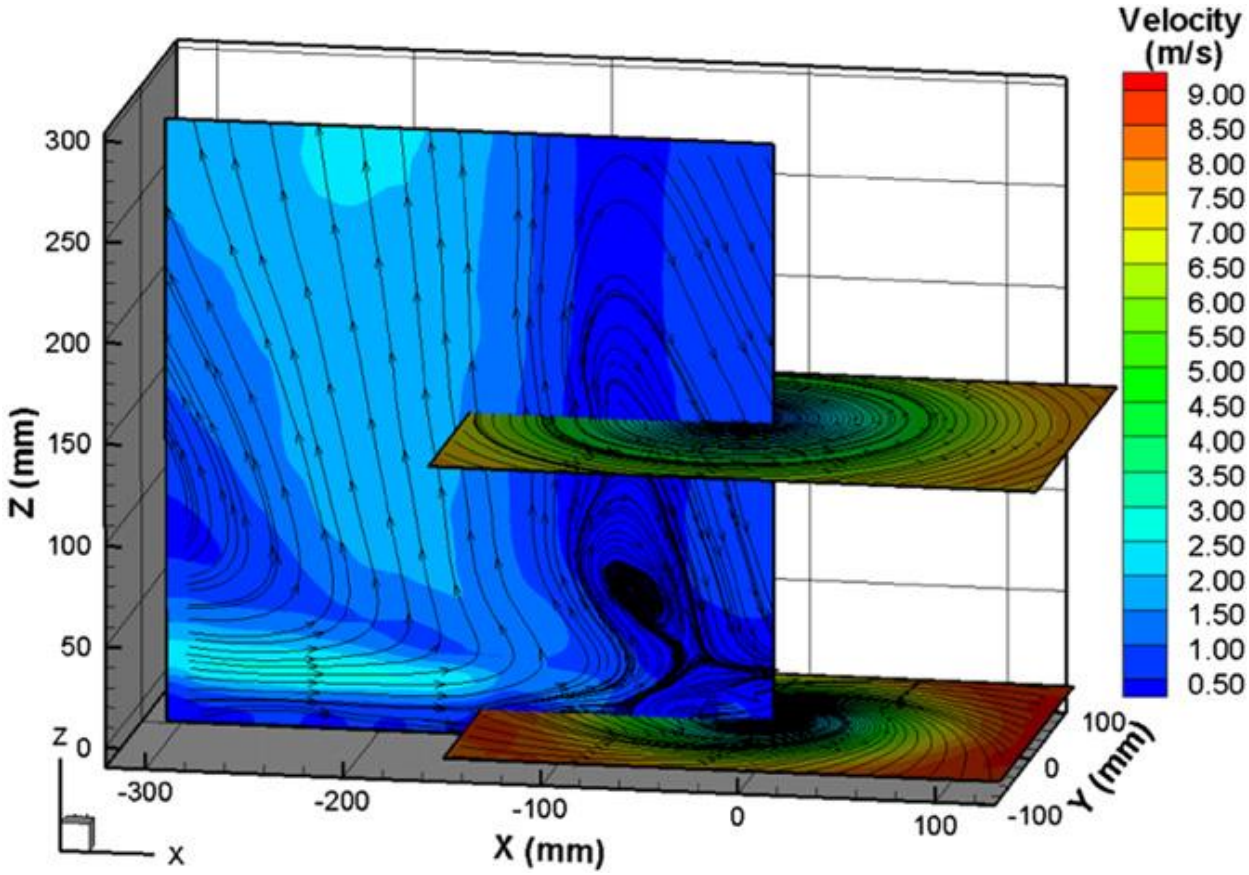

Figure 1.11 An example of Yang's experimental results [77]

The Yang's setup is also a combination of both ideas (Ward and Fiedler) and tries to extract the velocity fields in all three dimensions for the entire domain. The big advantage of Yang's setup can be its capability of applying the thermal condition from the bottom which

models the temperature gradient along the altitude and especially relatively higher temperature of soil that absorbs the solar energy.

A tropical cyclone is a rapidly-rotating storm system which is known by a low-pressure at the center (Eye), high speed flow structure, and a spiral arrangement of thunderstorms. Depending on its location and strength, a tropical cyclone is referred to by names such as hurricane (North Atlantic Ocean, or the NE Pacific Ocean east of the International Date Line, or the South Pacific Ocean east of $160^{o}\,E$, happens frequently in Caribbean Sea), typhoon (Northwest Pacific Ocean west of the International Date Line, happens frequently in South East Asia and China Sea), tropical storm, cyclonic storm, tropical depression, and simply cyclone. The direction of rotation is always clockwise in the southern hemisphere and counterclockwise in the northern hemisphere. All of these phenomena are caused by one basic reason; Coriolis effect of earth rotation. As opposed to tornadoes which are local and relatively small in diameter, these storms are much bigger and typically between 100 and 4,000 km (62 and 2,500 mi) in diameter.

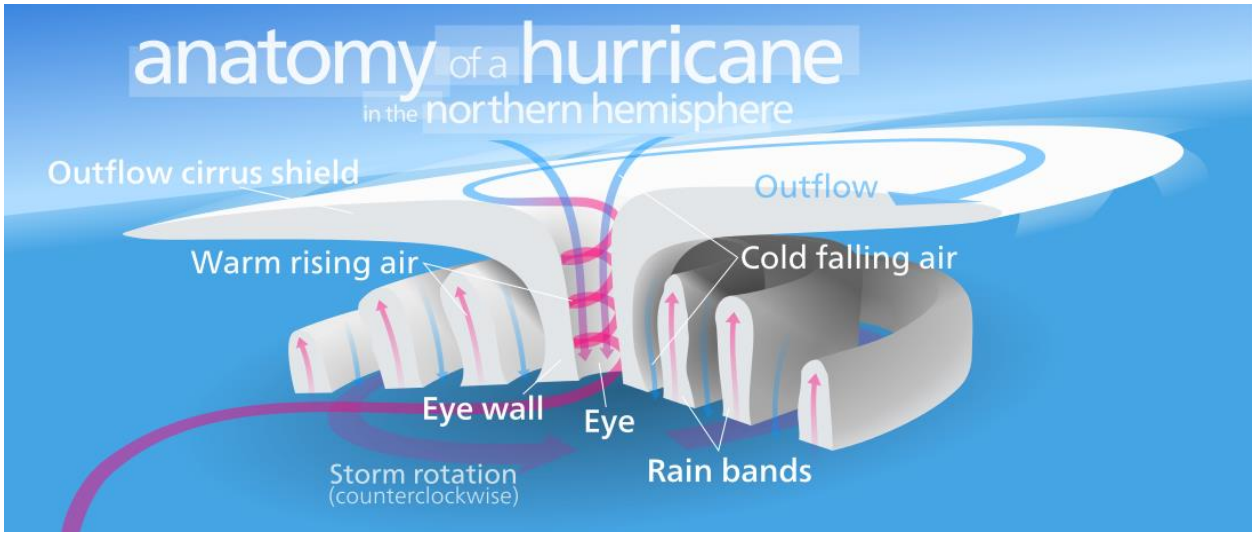

Figure 1.12 Schematic of a typical hurricane.

The flow structure near the ground for a tropical cyclone is characterized by rapidly-rotating flow around the center and also flowing radially toward it. At the outer edge of the storm, velocity is much lower, and it is near calm. As air flows radially toward the center, it begins to rotate cyclonically (counter-clockwise in the Northern Hemisphere, and clockwise in the Southern Hemisphere) and yet faster in order to maintain its angular momentum. As the flow approaches the center, it goes upward to the top of the troposphere. This radius, which is called the radius of maximum winds, is typically coincident with the inner radius of the Eye wall which has the strongest speed of wind on the ground [81].

Like the research about tornadoes, there are numerous numerical studies trying to simulate the hurricane's and typhoon's flow structure, and the ones mentioned below are just few examples of them: Willoughby [82] numerically modeled the velocity profile along altitude and radius of the vortex and reached promising but premature results. Shapiro [83] presented another solution for motion equation came up with maximum velocity radius, and tried to validate his results with some actual case study data. Bender [84] studied profiles of relative winds that rely on the environmental flow and their relation to asymmetries. Kwon and Frank [85] discussed energy flow of the numerically simulated vortices with and without environmental vertical shear and compared the structure of them on the upper layers.

Among a handful of existing experimental studies on tropical cyclones, a brief review of the Montgomery setup [86], which is shown in Figure 1.13, is presented here. The experimental apparatus is constructed to generate a mean boundary layer inflow similar to the flow an intense hurricane. Using PIV (Particle Image Velocimetry) method, they ended up with variety of vertical and azimuthal velocity profiles for a range of Re number. Spinning wall is a common feature between the present work and their setup. However, bottom rotating disk and adjustable

height are the remarkable features of the present work that distinguishes this setup from Montgomery's with its stationary lid.

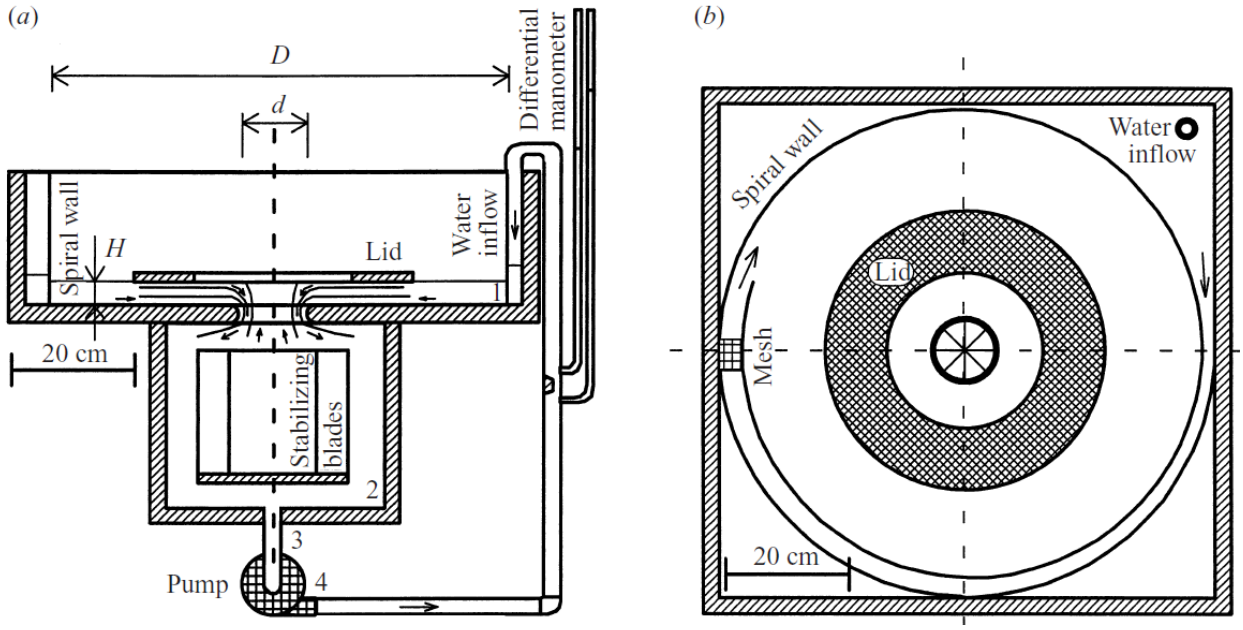

Figure 1.13 Montgomery's setup side (a) and top (b) view [86]

In order to simulate tornadoes and hurricanes with the present setup, the most similar boundary conditions to reality need to be found first. Then the preliminary results from that set of boundary conditions must be compared to the actual case study results. Based on this comparison boundary conditions are being revised and re-applied and experiments are being repeated. Once agreement between the experimental results and extracted results from actual cases is observed, similarities between these two can be studied. As it will be explained later, Baseline-Flow is the name that was chosen for a series of boundary conditions in this study. As will be discussed, some cases of the Baseline-Flow can be compared with Tornadoes and some others are more similar to Hurricanes. The same procedure is also need to be done to study the Jovian atmosphere and the GRS.

2 Experimental Setup

This setup is basically a cylindrical test zone with independent rotating side wall and bottom disk. The surface of bottom disk can be kept under different thermal condition (e.g. constant heat flux, constant temperature) by a set of heating elements from the bottom. As it has been demonstrated in Figure 2.1, this setup basically consists of three main sections; Frame, Side wall and Bottom part:

2.1. Bottom Part

The Bottom part is the piece that includes the disk, its rotating motor, the heating elements and the control devices of them. The 6” aluminum disk is 6 mm thick and is connected to a shaft that passes through the elements and connects the disk to a DC motor. This shaft was initially driven by an AC motor that could spin the shaft up to 10000 RPM and was controlled by a transformer that regulated the voltage. The maximum angular velocity of the motor was much higher than the required range. Therefore, in order to reach the desired spin rate, very low voltage needed to be applied to the motor. As a result, shaft torque decreased significantly and this could make the spinning rate unstable. Therefore, control over the disk was extremely difficult and this rate would significantly fluctuate during the tests. Hence, a new design for the bottom part was needed and the AC motor was replaced by a DC one with a narrower range of spin rate. Consequently, the design for the bottom part improved and proper insulation was used beneath and around the elements. This DC motor can be accurately controlled by voltage adjustment of a power supplier so the spin rate delicately ranges between 700 and 2500 RPM. The heating element set beneath the disk is capable of providing 400W. The applied power is also accurately adjustable with a transformer. Since the electric resistance of the elements is

known and transformer controls the voltage, the power can be simply calculated. The elements are located very close to the disk (~3mm). An insulation layer under the element set minimizes the heat loss to the ambient (from below) and mostly all of heat flux is directed to the disk. Another layer of ceramic, ring-shaped insulation around the disk separates it from the rest of plate and seals the flow from the bottom. Therefore, it can be assumed all the power generated by element set has to be absorbed by disk and consequently, transmitted to the test zone. In other words, in steady-state all of the electrical input power of the element set can be assumed equal to the heat power received by the test zone from the rotating disk. . If the constant temperature condition is required, power can be adjusted to maintain a desired temperature at steady state. In that case the temperature needs to be checked if any condition (e.g. disk/wall spin rate, ambient temperature, etc.) varies. The disk temperature is being measured by an optical thermometer with $\pm 0.3^{o}$C error.

Different ideas for spinning the flow from bottom and generating the vortex were tried. One of them was an impeller on top of a hot, stationary disk. The impeller was connected to a DC motor with a shaft passing from the middle of the hot disk. The intention was to generate rotating flow structure by spinning that impeller. Although different types of impellers with various sizes and number of blades were tried, the dominant phenomenon was disturbance and turbulence rather than a meaningful rotating flow structure. This attempt led to eliminating the impeller and connecting the shaft directly to the disk while the thermal condition was still being applied directly to the disk. The advantage of this design is that the smooth, flat, rotating surface of the disk generates a smoother rotating flow.

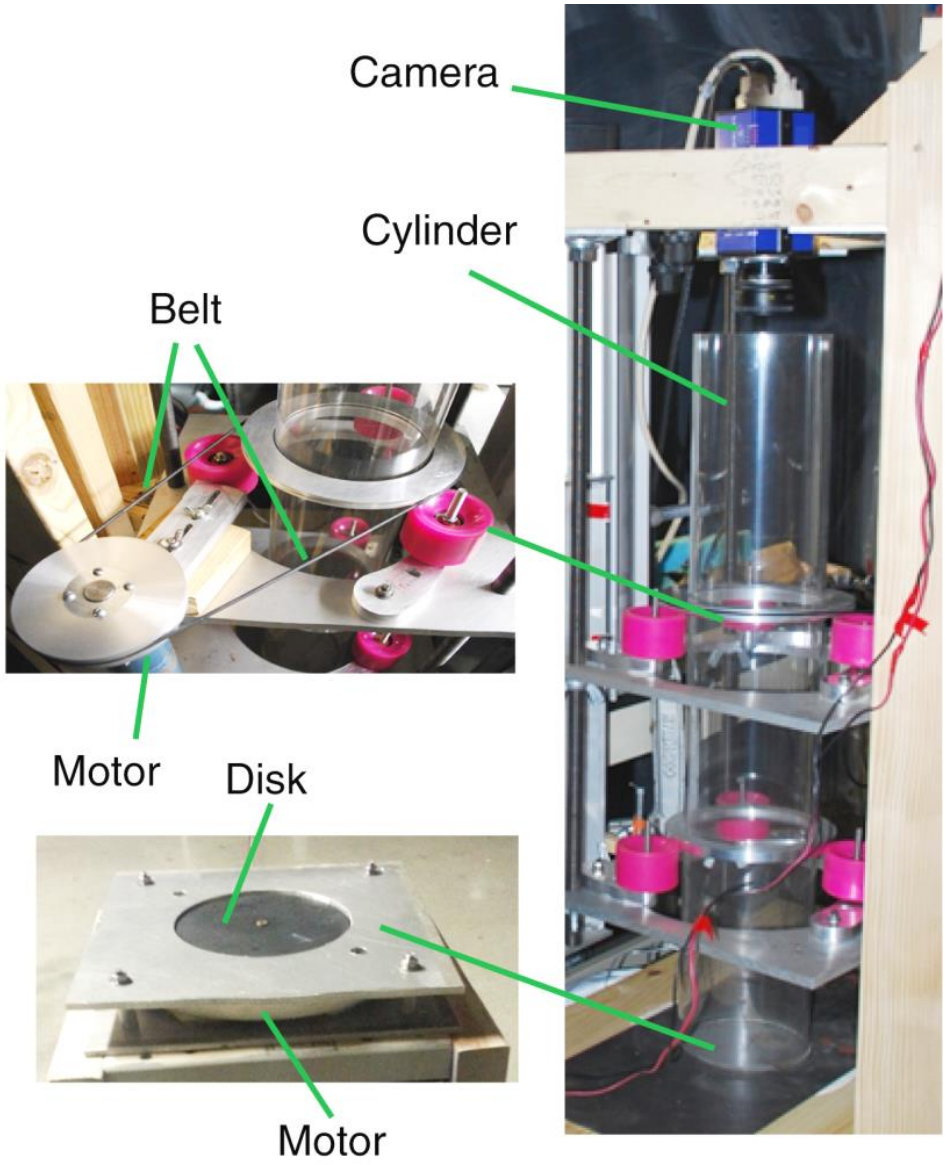

Figure 2.1 Setup details; side wall, its motor and bearing set (a), top view of the setup (b) and the bottom part (c)

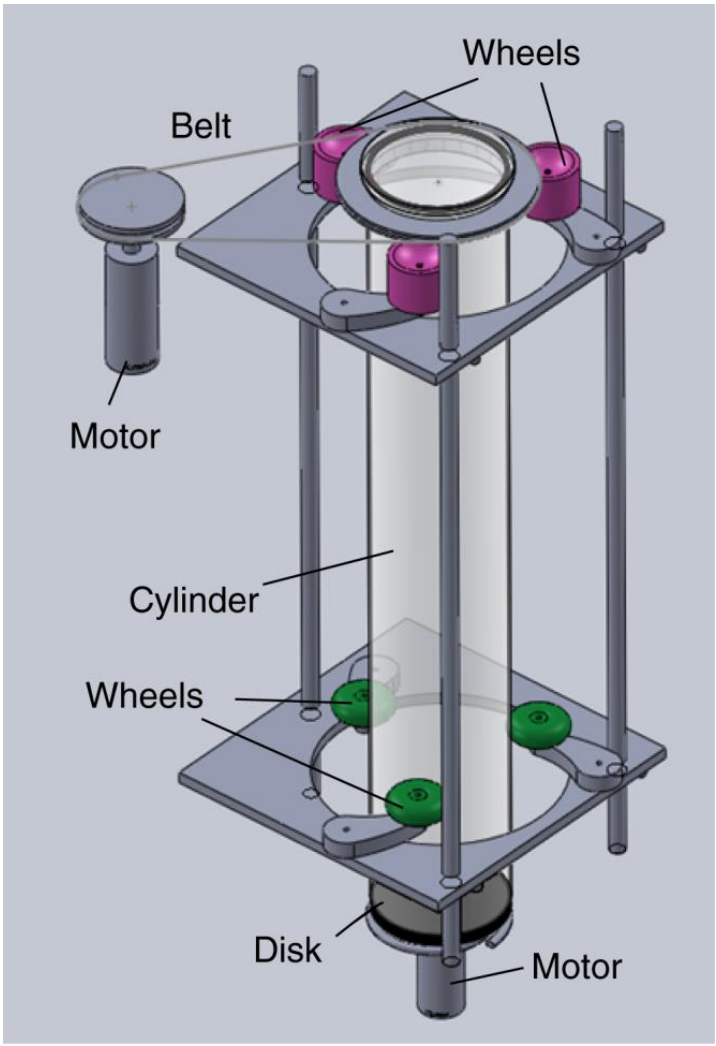

Figure 2.2 3D Model and conceptual design of a rotating cylinder with a counter-rotating disk installed beneath.

2.2. Side Wall

The Side wall is a cylindrical tube made out of polyethylene measuring three feet in length and six inches diameter with 0.25" thickness. Due to the pipe transparency, image-based techniques can be used in order to measure the flow speed in the entire test zone. Two aluminum rings around the pipe are connecting the pipe to the frame and constrain it axially and radially while allowing it to rotate around its vertical centerline smoothly. Each of these two rings sits on three hard rubber skate wheels working as "bearings" and enable the pipe not only to spin

without noise and vibration, but with very small required torque. The vertical position of both rings and pipe are independently adjustable so the rings can be moved up and down individually and also raise the entire pipe. This vertical degree of freedom not only makes it easier to do the imaging in different heights, but also allows the setup to lift the pipe in order to make a small distance between disk and cylinder that ae spinning separately and also make the room to inject the particles from the capsule. By setting a larger distant between the two sets of bearings smoother spinning and less noise and vibration is anticipated. Because of this, in most cases the upper set of bearing is located as high as possible on the top of the cylinder and the lower set is being fixed to the lowest possible (height of laser sheet and interested height for imaging is a key factor in setting the heights of bearing sets. The required torque for rotating the wall is provided by a DC motor connected to the upper ring with a delicate, 1/8" O-ring as the "belt" (two ends of the O-ring is gently glued together and become the customized belt). The motor is driven and controlled by a DC power supplier which regulates the spin rate of the cylinder that ranges from very low speed up to 400 RPM.

The upper disk of the cylinder can be designed completely closed, semi-open and fully open. The effect of opening radius in the flow is discussed in [80] and it was shown that changing the area of the upper disk of the cylinder can affect the flow structure drastically. In the present work also, this effect was observed in the preliminary experiments and larger diameter of upper disk caused more turbulence in the flow. When the top of the cylinder is fully open, results show so much turbulence and a single pair of images does not represent any meaningful flow structure. The only way to study the flow is averaging the results that are obtained from several image pairs and smooth out the effect of turbulence. Attaching a transparent disk on top of the cylinder as the lid means that the diameter of opening in the upper disk is set to zero and in this

case noises, random turbulences and disturbances are the least. All of the systematic tests are done while this upper lid was closed.

2.3. Frame

The Frame is mainly the structure that holds all of the setup pieces and components together. It consists of a strong vertical column with two horizontal arms on about 6’ height. The side wall and its auxiliary equipment are suspended from top by three threaded rods. These rods are bolted to two plates that the aforementioned skate wheels are seating on. The triangle position of the rods enables the operator to change the height of the rings independently and easily. This also makes the leveling and adjusting relatively easy and setting a new combination of bearing heights for the experiment does not take more than an hour. By using an inclinometer, the bearings and consequently, the side wall consequently can be precisely leveled and balanced. The heavy weight of frame itself and added several 10kg sand bags can damp the slight vibrations of the entire setup during the experiments.

After the setup was built, in order to inject the smoke into the test zone, many different approaches were tried. Providing the entire chamber with the required smoke for imaging is not easy. Since all walls of the chamber are moving, it is very difficult to design and build an opening to the test zone similar to an engine valve. The other idea that was tried in the first stages was opening the top lid and filling the cylinder from the top with smoke and waiting until the turbulence caused by the injection effect vanishes. After applying the wall boundary conditions, imaging begins. The main problem with this approach is the time that system requires between injection and beginning of imaging. If this time is too small, the turbulence and random flow caused by the injection are still the dominant structure in the test zone. On the other hand, if the delay time is too large, smoke becomes uniform and imaging so images do not show much

detail. Therefore, the best place to seed the flow seems to be the gap between the bottom disk and the wall. A capsule around this gap forces the seeding additive to the test zone. The height of this capsule (about 2cm) is lower than the lowest studied height (about 5cm) and it does not impact on imaging.

There are some main parameters that each experimental setup in this field needs to take into consideration. These parameters were introduced for Ward-type and Fiedler-type studies in the last sections. Based on the design of this setup, those parameters in this study are $\omega_w, \omega_d, A, H, h, R, r, T_d, \nu, \rho$ and . These respectively corresponds to angular velocities, exit area, cylinder height, height of interested point from bottom disk, inner radius of cylinder, horizontal distance of interested point from centerline, temperature, kinematic viscosity, density and expansion coefficient of fluid. Two indices of w and d refers to wall and disk respectively. The two angular speeds, ω_w and ω_d have operating ranges and many different combinatios are studied and shown in the next chapters. As it was mentioned before, by keeping the top lid closed during the experiments, A is set to zero. Geometry parameters of H and R are fixed by the setup design. Seven studied heights are associated with h and the studied radius, r, varies between 0 and R. Three disk temperatures, $T_d = 25^oC$, 50^oC and 75^oC are studied in this project. The studied fluid in the current project is air which defines ν, ρ and b.

3 Governing Equations, Dimensionless Analysis and Statistical Time-Averaging

The governing equations of similar cases were briefly discussed in the previous sections. In this part these equations are introduced for velocity and temperature in the cylindrical coordinate system according to the setup design. Each case has the corresponding assumptions and boundary conditions. For the present case, first the most generic form of equations is presented. Then assumptions and conditions that those assumptions remain valid are discussed. Finally, the simplified version of the equations and their dimensionless form are demonstrated.

3.1. Governing Equations

Below are the generic form of governing equation for in incompressible flow, The continuity equation (3.1), the Navier-Stokes equations $(3.2-4)$ and the energy balance equation(3.5) [87-88]:

$$\frac{1}{r}\frac{\partial(ru_r)}{\partial r}+\frac{1}{r}\frac{\partial u_\theta}{\partial \theta}+\frac{\partial u_z}{\partial z}=0 \tag{3.1}$$

$$\rho\left(\frac{\partial u_r}{\partial t}+u_r\frac{\partial u_r}{\partial r}+\frac{u_\theta}{r}\frac{\partial u_r}{\partial \theta}-\frac{{u_\theta}^2}{r}+u_z\frac{\partial u_r}{\partial z}\right) = \frac{\partial P}{\partial r}+\rho g_r+\mu\left(\frac{1}{r}\frac{\partial}{\partial r}(r\frac{\partial u_r}{\partial r})-\frac{u_r}{r^2}+\frac{1}{r^2}\frac{\partial^2 u_r}{\partial \theta^2}-\frac{2}{r^2}\frac{\partial u_\theta}{\partial \theta}+\frac{\partial^2 u_r}{\partial z^2}\right) \tag{3.2}$$

$$\rho\left(\frac{\partial u_\theta}{\partial t}+u_r\frac{\partial u_\theta}{\partial r}+\frac{u_\theta}{r}\frac{\partial u_\theta}{\partial \theta}-\frac{u_r u_\theta}{r}+u_z\frac{\partial u_\theta}{\partial z}\right) = \frac{1}{r}\frac{\partial P}{\partial \theta}+\rho g_\theta+\mu\left(\frac{1}{r}\frac{\partial}{\partial r}(r\frac{\partial u_\theta}{\partial r})-\frac{u_\theta}{r^2}+\frac{1}{r^2}\frac{\partial^2 u_\theta}{\partial \theta^2}+\frac{2}{r^2}\frac{\partial u_r}{\partial \theta}+\frac{\partial^2 u_\theta}{\partial z^2}\right), \tag{3.3}$$

$$\rho\left(\frac{\partial u_z}{\partial t}+u_r\frac{\partial u_z}{\partial r}+\frac{u_\theta}{r}\frac{\partial u_z}{\partial \theta}+u_z\frac{\partial u_z}{\partial z}\right)$$
$$=\frac{1}{r}\frac{\partial P}{\partial z}+\rho g_z+\mu\left(\frac{1}{r}\frac{\partial}{\partial r}(r\frac{\partial u_z}{\partial r})+\frac{1}{r^2}\frac{\partial^2 u_z}{\partial \theta^2}+\frac{\partial^2 u_z}{\partial z^2}\right) \quad (3.4)$$

$$\rho c_p\left(\frac{\partial T}{\partial t}+u_r\frac{\partial T}{\partial r}+\frac{u_\theta}{r}\frac{\partial T}{\partial \theta}+u_z\frac{\partial T}{\partial z}\right)$$
$$=k\left(\frac{1}{r}\frac{\partial}{\partial r}(r\frac{\partial T}{\partial r})+\frac{1}{r^2}\frac{\partial^2 T}{\partial \theta^2}+\frac{\partial^2 T}{\partial k^2}\right)+S\,, \quad (3.5)$$

where (u_r,u_θ,u_z) are the velocity components in the radial, azimuthal and vertical directions (r,θ,z), respectively, (g_r, g_θ, g_z) are the gravitational acceleration components in (r,θ,z), respectively, ρ is the density, μ is the dynamic viscosity, c_p is the specific heat capacity, k is the heat conductivity and S is the heat source term. In the case considered in this work, the static pressure can be considered to be homogenous in the entire domain such that $\partial P/\partial r=\partial P/\partial \theta=\partial P/\partial z=0$. The gravity force acts only in the vertical direction ($g_z\neq 0$). The gravity force acts only be affecting in the vertical direction and this gravity acceleration base on the Boussinesq approximation [89] is:

$$g_z=\frac{g(\rho_0-\rho)}{\rho_0}=g(1-\frac{T_0}{T}) \qquad (For\ ideal\ gas) \quad (3.6)$$

$$\beta={}^1\!/_T\approx\frac{2}{T_0+T_d} \qquad (For\ ideal\ gas) \quad (3.7)$$

where β is volumetric thermal expansion coefficient (for ideal gas and T is absolute temperature). Index 0 indicates the ambient condition and g is the acceleration due to Earth's gravity. Also, S, the heat generation term, is zero in this case.

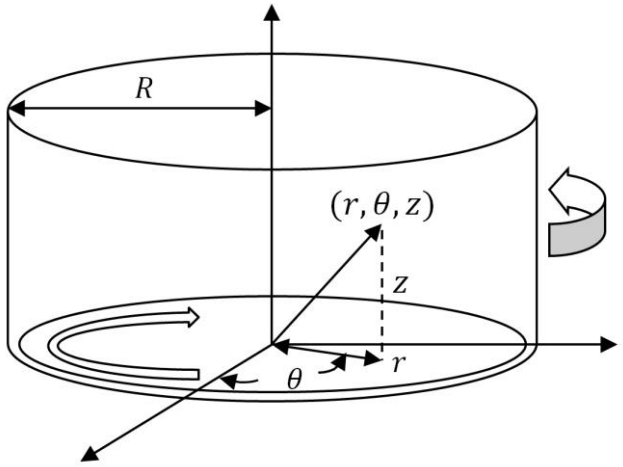

Figure 3.1 Schematic diagrams of coordination system and geometry

Therefore, the equation (3.4) is simplified to:

$$\frac{\rho}{\mu}\left(\frac{\partial u_z}{\partial t}+u_r\frac{\partial u_z}{\partial r}+\frac{u_\theta}{r}\frac{\partial u_z}{\partial \theta}+u_z\frac{\partial u_z}{\partial z}+g(1-\frac{T_0}{T})\right) = \frac{1}{r}\frac{\partial}{\partial r}(r\frac{\partial u_z}{\partial r})+\frac{1}{r^2}\frac{\partial^2 u_z}{\partial \theta^2}+\frac{\partial^2 u_z}{\partial z^2} \tag{3.8}$$

Since the disk and wall speed are measured in RPM, the wall and thermal boundary conditions for those equations are:

$$u_r = u_z = 0|_{z=0}, \quad u_r = u_z = 0|_{z=\infty} \ and \ u_r = u_z = 0|_{r=R} \tag{3.9}$$

$$u_\theta = u_{d,rpm}\frac{2\pi}{60}r|_{z=0} \qquad (rad/s) \tag{3.10}$$

$$u_\theta = u_{w,rpm}\frac{2\pi}{60}R|_{r=R,\ z=\infty} \qquad (rad/s) \tag{3.11}$$

$$\frac{\partial T}{\partial z} = \frac{1}{k}\dot{q}_D \qquad or \qquad T = T_s|_{z=0} \tag{3.12}$$

Equations (3.9) are governed by the geometry of test zone and walls. Equations (3.10) and (3.11) are expressing that flow at wall has the no-slip condition and follows the wall. The last one, equation (3.12), demonstrates two different possibilities that could practically be

applied in this case; constant surface heat flux and constant surface temperature where k is the fluid conductivity.

3.2. Dimensionless Analysis

In order to obtain the non-dimensional form of the equations $(3.1-5)$, the following coordinates are introduced:

$$x^* = x/R,\ \ y^* = y/R,\ \ z^* = z/R,\ \ r^* = r/R, \tag{3.13}$$

and the non-dimensional velocity components are

$$u_r^* = u_r/u_{ref},\ \ u_\theta^* = u_\theta/u_{ref},\ \ u_z^* = u_z/u_{ref}, \tag{3.14}$$

where the reference velocity is $u_{ref} = u_w$ (the inner wall velocity) for the rotating cylinder, and $u_{ref} = 0.1u_{d,edge}$ (10% of the disk edge velocity $u_{d,edge}$) for the rotating disk (only when the wall is stationary). The non-dimensional fluid temperature is $\Theta = (T - T_0)/(T_d - T_0)$, where the subscript "0" and "d" indicate the ambient and disk surface conditions, respectively.

With these non-dimensional variables, the governing equations are re-written as

$$\frac{u_r^*}{r^*} + \frac{\partial u_r^*}{\partial r^*} + \frac{\partial u_\theta^*}{\partial \theta} + \frac{\partial u_z^*}{\partial z^*} = 0 \tag{3.15}$$

$$\begin{aligned}&\frac{\partial u_r^*}{\partial t^*} + u_r^*\frac{\partial u_r^*}{\partial r^*} + \frac{u_\theta^*}{r^*}\frac{\partial u_r^*}{\partial \theta} - \frac{u_\theta^{*2}}{r^*} + u_z^*\frac{\partial u_r^*}{\partial z^*} \\ &\quad = \frac{1}{Re}\left(\frac{1}{r^*}\frac{\partial u_r^*}{\partial r^*} + \frac{\partial^2 u_r^*}{\partial r^{*2}} - \frac{u_r^*}{r^{*2}} + \frac{1}{r^{*2}}\frac{\partial^2 u_r^*}{\partial \theta^2} - \frac{2}{r^{*2}}\frac{\partial u_\theta^*}{\partial \theta} + \frac{\partial^2 u_r^*}{\partial z^{*2}}\right),\end{aligned} \tag{3.16}$$

$$\begin{aligned}&\frac{\partial u_\theta^*}{\partial t^*} + u_r^*\frac{\partial u_\theta^*}{\partial r^*} + \frac{u_\theta^*}{r^*}\frac{\partial u_\theta^*}{\partial \theta} + \frac{u_r^* u_\theta^*}{r^*} + u_z^*\frac{\partial u_\theta^*}{\partial z^*} \\ &\quad = \frac{1}{Re}\left(\frac{1}{r^*}\frac{\partial u_\theta^*}{\partial r^*} + \frac{\partial^2 u_\theta^*}{\partial r^{*2}} - \frac{u_\theta^*}{r^{*2}} + \frac{1}{r^{*2}}\frac{\partial^2 u_\theta^*}{\partial \theta^2} + \frac{2}{r^{*2}}\frac{\partial u_r^*}{\partial \theta} + \frac{\partial^2 u_\theta^*}{\partial z^{*2}}\right),\end{aligned} \tag{3.17}$$

$$\frac{\partial u_z^*}{\partial t^*} + u_r^* \frac{\partial u_z^*}{\partial r^*} + \frac{u_\theta^*}{r^*}\frac{\partial u_z^*}{\partial \theta} + u_z^* \frac{\partial u_z^*}{\partial z^*} - \frac{Gr}{Re^2}\Theta$$
$$= \frac{1}{Re}\left(\frac{1}{r^*}\frac{\partial u_z^*}{\partial r^*} + \frac{\partial^2 u_z^*}{\partial r^{*2}} + \frac{1}{r^{*2}}\frac{\partial^2 u_z^*}{\partial \theta^2} + \frac{\partial^2 u_z^*}{\partial z^{*2}}\right), \tag{3.18}$$

$$\frac{\partial \Theta}{\partial t^*} + u_r^* \frac{\partial \Theta}{\partial r^*} + \frac{u_\theta^*}{r^*}\frac{\partial \Theta}{\partial \theta^*} + u_z^* \frac{\partial \Theta}{\partial z^*}$$
$$= \frac{1}{Pr\,Re}\left(\frac{1}{r^*}\frac{\partial \Theta}{\partial r^*} + \frac{\partial^2 \Theta}{\partial r^{*2}} + \frac{1}{r^{*2}}\frac{\partial^2 \Theta}{\partial \theta^2} + \frac{\partial^2 \Theta}{\partial z^{*2}}\right), \tag{3.19}$$

The non-dimension form for boundary condition will also become:

$$u_r^* = u_z^* = 0|_{z^*=0}, \quad u_r^* = u_z^* = 0|_{z^*=\infty} \ and \quad u_r^* = u_z^* = 0|_{r^*=1} \tag{3.20}$$

$$u_\theta^* = \frac{u_{d,edge}}{u_{ref}} r^*|_{z=0} \tag{3.21}$$

$$\begin{cases} u_\theta^* = 1|_{r=R,\ z=\infty} & (rotating\ wall\ cases) \\ u_\theta^* = 0|_{r=R,\ z=\infty} & (disk-only\ cases) \end{cases} \tag{3.22}$$

$$\frac{\partial \Theta}{\partial z^*} = R\dot{q}_D^{\cdot} = \dot{Q}_D \qquad or \qquad \Theta = 1|_{z=0} \tag{3.23}$$

The Grashof (Gr), Reynolds (Re) and Prandtl (Pr) numbers are the relevant non-dimensional fluid-mechanic parameters. They are defined as $Gr = R^3\beta\rho^2 g(T_d - T_0)/\mu^2$, $Re = Ru_{ref}\rho/\mu$, and $Pr = c_p\mu/k$, where g is the gravitational constant, c_p is the overheat at a constant pressure, k the fluid conductivity and β is the volumetric thermal expansion coefficient of the fluid. The viscous effect is characterized by Re that depends on the selection of the reference velocity u_{ref}. The Prandtl number describes the fluid property and can be assumed constant based on air properties in the mean temperature. The buoyancy effect induced by disk heating is characterized by Gr in the momentum equation for the vertical velocity.

3.3. **Statistical Time-Averaging**

Below, statistical ensemble averaging of a time-dependent variable in fluid mechanics, a very common approach in turbulent flow studies, is represented. More information and detail derivation for many cases can be found in most of turbulence text books [e.g. 90-92]. In general, turbulent flow is time-dependent and three dimensional. For instance, measurement of the velocity component v_1 at a certain point, in a certain direction within a turbulent flow is expected to be similar to what is shown in Figure 3.2. In this figure, the velocity can be regarded as consisting of an average value $\overline{v_1}$ indicated by the dashed line, plus a random fluctuation v'_1:

$$u_r(t)=\overline{u_r}\,(t)+u'_r(t) \qquad (at\ a\ certain\ point) \qquad (3.24)$$

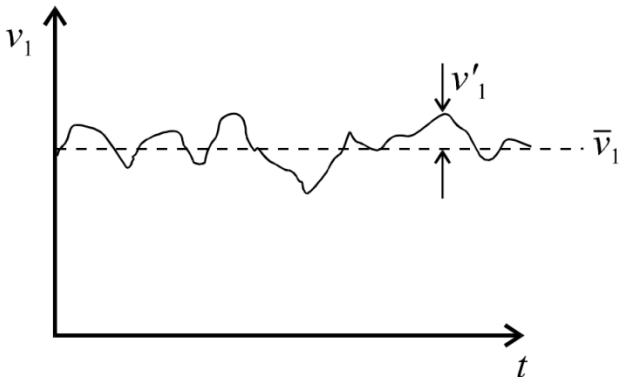

Figure 3.2 Velocity, fluctuations and mean velocity

Similarly, other components of velocity and temperature may also fluctuate. So at a certain point:

$$u_\theta(t)=\overline{u_\theta}\,(t)+u'_\theta(t) \qquad (3.25)$$

$$u_z(t)=\overline{u_z}\,(t)+u'_z(t) \qquad (3.26)$$

$$T(t)=\bar{T}\,(t)+T'(t) \qquad (3.27)$$

It seems beneficial to review some of the fundamental rules and properties of ensemble averaging. First, time-averaged quantity $\bar{a}\,(t)$ as the average of the instantaneous quantity $a(t)=\bar{a}\,(t)+a'(t)$ over a time period T is being defined as:

$$\bar{a}\,(t) = \frac{1}{T}\int_{t-0.5T}^{t+0.5T} a(\tau)d\tau \tag{3.28}$$

Obviously, if time period T is long enough, the effect of fluctuation term is zero:

$$\overline{a'}\,(t) = \frac{1}{T}\int_{t-0.5t}^{t+0.5t} a'(\tau)d\tau = 0 \tag{3.29}$$

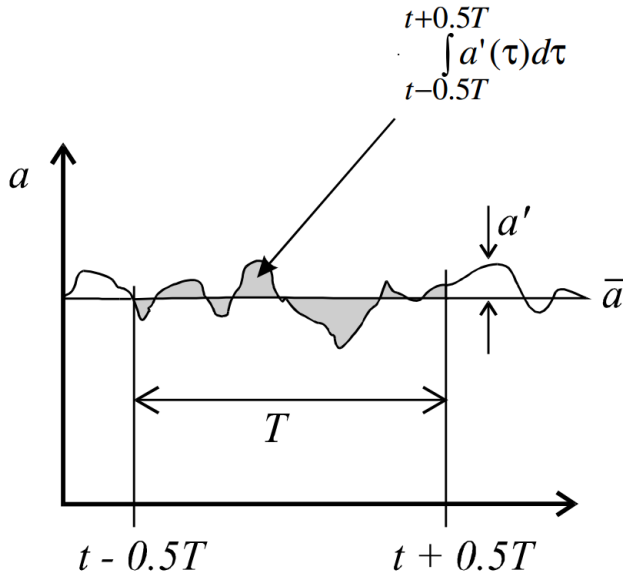

Figure 3.3 Statistical Averaging of ā (t)

Using equations (3.28) and(3.29), it is straightforward to show:

$$\overline{a+b}=\overline{\bar{a}+a'+\bar{b}+b'} = \bar{a}+\bar{b} \tag{3.30}$$

$$\overline{ca}=\overline{c(\bar{a}+a')} = c\bar{a} \qquad \text{(c is a constant)} \tag{3.31}$$

$$\overline{ab}=\overline{(\bar{a}+a')(\bar{b}+b')} = \overline{\bar{a}\bar{b}+a'\bar{b}+\bar{a}b'+\overline{a'b'}}=\overline{\bar{a}\bar{b}}+\overline{a'\bar{b}}+\overline{\bar{a}b'}+\overline{\overline{a'b'}} = \overline{ab}+\overline{a'b'} \tag{3.32}$$

Note that the ensemble average of the product of the two fluctuations a′ and b′ cannot be set to zero; for instance, if a = b, the product of the two fluctuations would be a′a′ = a′^{2}. Clearly, a squared term like a′^{2} will always is positive, and so its time-average will not be zero.

Also, the order of differentiation with respect to a coordinate, x_i, and integration over τ can commute:

$$\overline{\frac{\partial a(t)}{\partial x_\iota}} = \frac{1}{T}\int_{t-0.5t}^{t+0.5t} \frac{\partial a(t)}{\partial x_i} d\tau = \frac{\partial}{\partial x_i}\frac{1}{T}\int_{t-0.5t}^{t+0.5t} a(\tau) d\tau \quad or \quad \overline{\frac{\partial a(t)}{\partial x_\iota}} = \frac{\partial \overline{a(t)}}{\partial x_i} \tag{3.33}$$

Similarly, it can be easily proven that:

$$\overline{\frac{\partial a(t)}{\partial t}} = \frac{\partial \overline{a(t)}}{\partial t} \tag{3.34}$$

$$\overline{\nabla a(t)} = \nabla \overline{a(t)} \tag{3.35}$$

In the present work, $\langle\ \rangle$ also denotes the ensemble average. As will be explained in the next chapters thoroughly, the normalized velocity magnitudes for the horizontal and vertical planes are respectively defined as:

$$\left|u^*\right| = \left(\left\langle u_\theta^2 \right\rangle + \left\langle u_r^2 \right\rangle\right)^{1/2} \Big/ u_{ref}\ , \tag{3.36}$$

$$\left|u_V^*\right| = \left(\left\langle u_z^2 \right\rangle + \left\langle u_r^2 \right\rangle\right)^{1/2} \Big/ u_{ref}\ , \tag{3.37}$$

4 Measurements Techniques and Data Processing

As briefly mentioned before, image-based methods and particularly PIV (Particle Image Velocimetry) was used in this project to study the flow field. The pipe transparency allows the PIV method or similar techniques to be used. The rotating cylinder is made of polyethylene, with the 914.4 mm height, 146.5 mm inner diameter and 3.5 mm thickness. The laser sheet can pass through the transparent side wall of the pipe to illuminate the flow, and a PIV camera is mounted to captures images from the top of the cylinder in most of the cases as shown in figure 4.1. With this configuration of setup azimuthal and radial components of velocity are achievable. In some other experiments, in order to measure the vertical component of the velocity, the lens is rotated 90 degrees. Therefore, the laser sheet becomes vertical and camera is mounted perpendicular to the laser sheet in front of the side wall. In those cases radial and vertical components of velocity are studied and azimuthal component is normal to the laser plane.

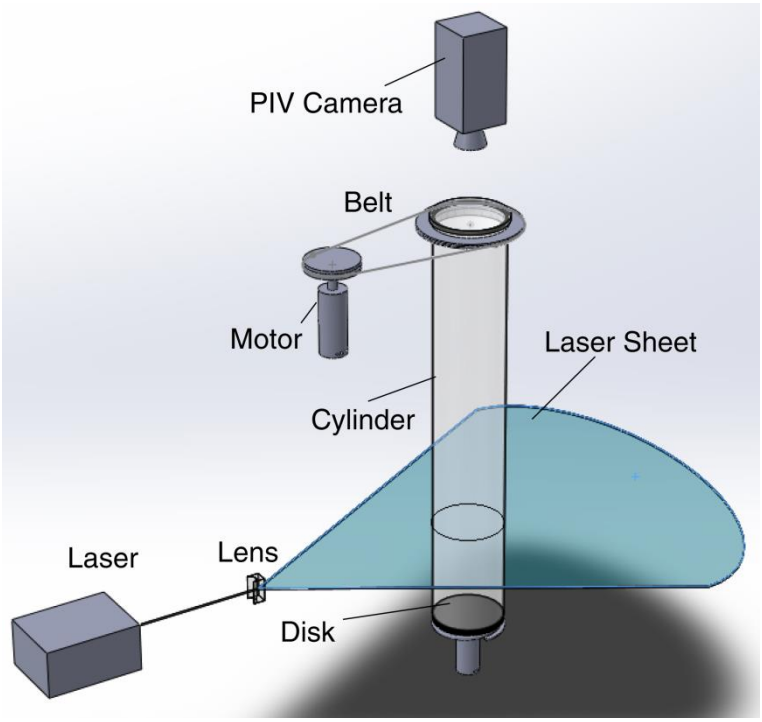

Figure 4.1 Illustration of PIV velocity measurements.

Sidewall's curvature however, makes some images, especially the ones taken from side view, far from the vertical centerline and close to the wall, blurry and unclear. Because of this reason and also because of low particle concentration near the wall, which will be discussed later, obtained results from locations very close to the wall are not very reliable. Therefore, those results are masked and not presented in this work in both vertical and horizontal plane measurement. Before explaining the curvature problem and its solutions, it seems necessary to discuss about different velocimetry methods that are used in this project in order to extract the velocity field for the entire domain by comparing and processing two consecutive images of the field. In all of these image-based methods the fluid inside the test zone needs to be traced. Therefore, some visible additive is injected to the test zone to make the flow structure traceable. This procedure, which is called seeding, can be done by injecting small floating particles, different types of smoke or oil tiny drops. Each seeding technique requires proper injector (or smoke generator) which controls the concentration of added materials. For different cases and purposes, as it is discussed thoroughly in appendix A, olive oil smoke generator, cigarette smoke generator and particle injector have been designed, built and used in early stages of this project.

A PIV commercial package (CCD camera, laser, trigger, control hard ware and processing software) manufactured by LaVision (version 7.1, BigSky pulsed laser and CCD Image ProX 2m) is being used to shoot a consecutive pair of laser pulses with a precise time difference. Energy intensities of these two beams of laser are adjustable individually. The calibration and alignment of the two beams are tested by putting a light sensitive paper in front of laser and far enough from the source. Then shooting the laser leaves burn marks on the paper. The burn mark caused by only one laser source is compared with the burn mark from the other one. This way it is made sure that both beams are hitting the same point on target. A set of

optical lenses between the source and the test zone converts the laser beam to a horizontal or vertical laser plane. The thickness of laser sheet (~2 mm) is shown in figure 4.2.

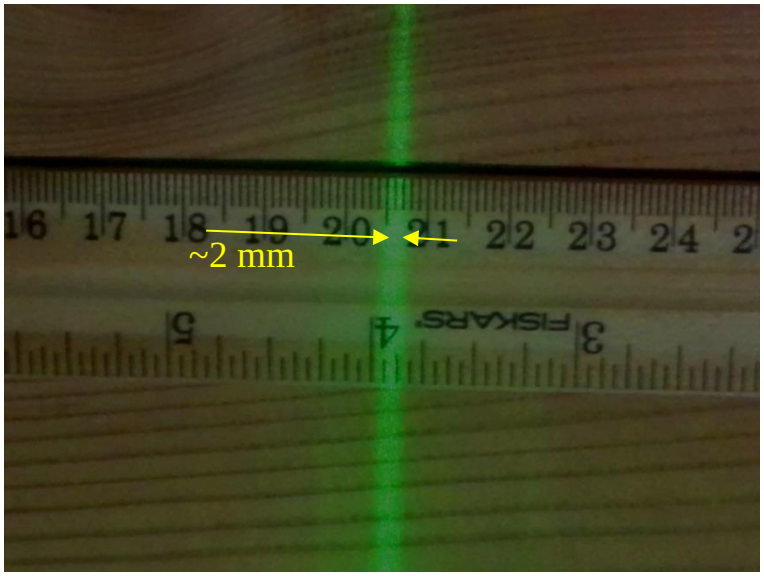

Figure 4.2 Thickness of the laser sheet

When this laser plane intersects with the side wall, it illuminates a thin layer of fluid while the CCD camera is recording this plane from a normal view. In cross section data acquisition there is a horizontal laser plane and recording camera from the top, located along the center line of the cylinder. Since the trigger system ignites the laser and captures the images precisely at the same time, after a proper calibration of trigger timing, laser intensity and camera aperture and focus, pairs of images with fairly same light intensity and known time difference and height are expected. Patterns and particles in one pair of images are being used to extract velocity vectors in the domain by variety of different methods. Among several methods of processing, Optical Flow, Davis (LaVision 7.1) and PIVlab 1.41 (an open source, famous code [93]) have been frequently used in this project.

In this project in order to cover the test zone entirely, images need to be taken either from the side and close to the center line or from the top so the camera does not interfere with the

curved wall at all. Imaging from the top needs a horizontal laser plane in front of the camera. The platform that laser device is mounted on, is designed to be vertically adjustable so the height of laser plane can change from the bottom to the top of test zone. This height defines the area of interest that the images are taken of. Accordingly, camera focus has to be adjusted as the laser height changes. There are other optical issues caused by surface scratches, non-uniform wall thickness and/or dirt, grease or contamination on inner or outer cylinder wall. All of these issues locally change the optical behavior of wall and as a result, lines of beam light could be seen in the laser sheet as it is shown in figures 4.4-a if the inner surface is not clean enough. As is can be seen, these lines are not parallel because they are all coming from a source point and acting unpredictably. The presence of these lines makes the image processing even harder especially when the wall rotates. When a pair of images is being processed compared with each other, all commercial codes as well as optical flow method recognizes the line movements as the primary motion instead of the particles movements. In order to obtain better results, a delicate way of seeding is required in which concentration of particles is not too high and background noise is the least.

In vertical velocity measurements laser sheet is vertical, passing the cylinder centerline and the camera is normal to the laser sheet and aside the cylinder. The imaging close to the inner wall is difficult due to the curvature of the wall. Figure 4.3 shows two the image of identical rulers next to each other, one inside and the other one outside of the cylinder. As shown in this figure, except for the small region very close to the wall (about 5 mm from the inner wall), both rulers are aligned and deflection of the light can be neglected.

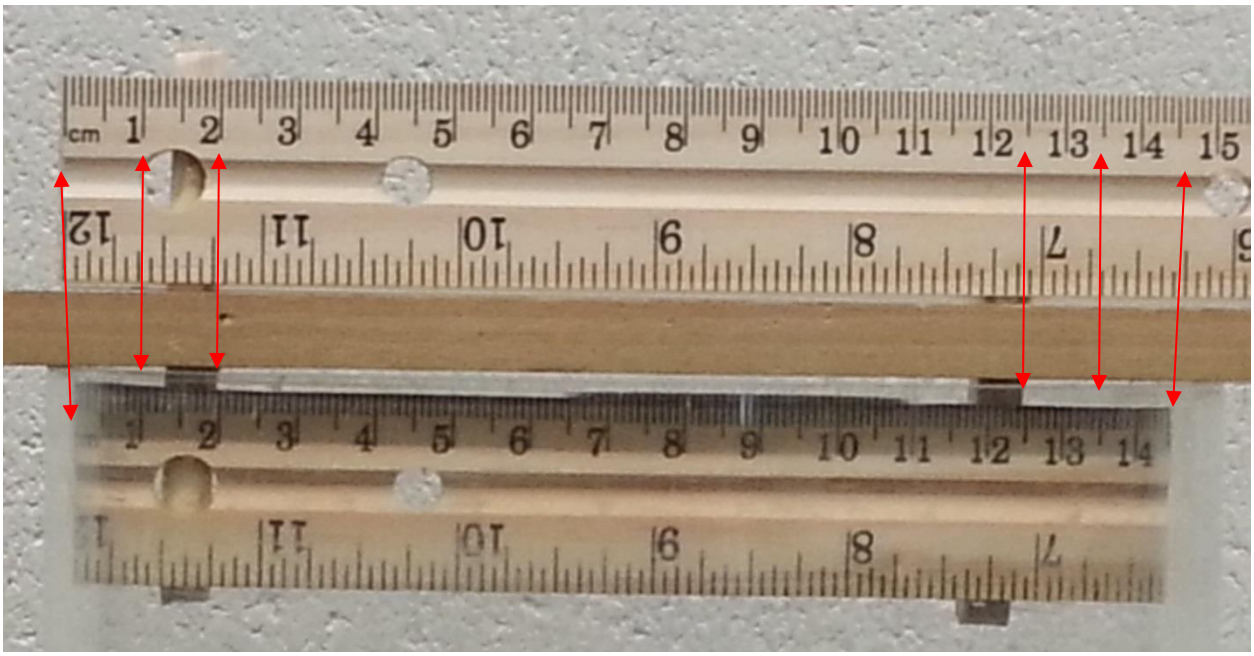

Figure 4.3 Effect of wall curvature in images (side view)

Also, the inner surface of the test zone needs to be wiped and cleaned frequently (usually every 20 minutes of experimenting). When seeding method is injecting the particles and the concentration of particles is not very high in the chamber, those lines that caused by wall effect would not be recognizable in the images and the results are not being affected. As a result, by comparing each pair the PIV codes and the Optical Flow method recognize the particles movements as the dominant phenomenon. Polyamid Seeding Particles, PSP with average diameter of 5 μm, is sprayed with air through a capsule around the bottom part of cylinder and uniformly injected to the test zone through the gap between the cylinder and disk. As an example of results, figure 4.4-b demonstrates a closed up view of an image taken utilizing this technique. The development procedure of this technique and seeding setup detail and improvement steps are explained in appendix A.

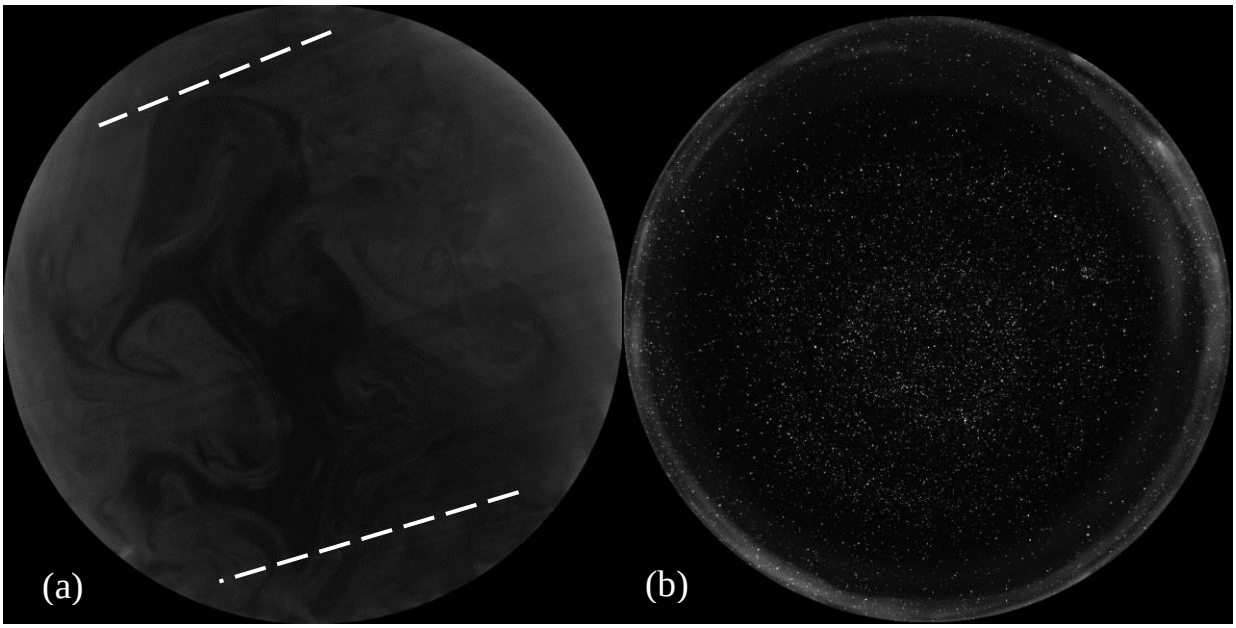

Figure 4.4 Lines in image using smoke for seeding (a), An example of high quality images without noise using PSP 5 μm (b).

There are two types of error sources in this project; the first type is caused by uncertainties in measurement and data acquisition and the second type is resulted by uncertainty in data analysis, after measurement are done. The second type is thoroughly discussed in the next chapter but the first type is of interest in this section. During each experiment several parameters are measured and each could be an error source. The time difference, dt, between two snapshots in PIV for one thing is being control by software. This value ranges from $0.15\ ms$ to $1.5\ ms$ and this range is much larger than the range of uncertainty. The proof is when any snapshot is manually shifted either forward or backward in time with respect to laser trigger, the laser shot and image capturing will not occur simultaneously anymore. The largest shift that does not cause that problem cannot exceed $3\ \mu s$ which is very small compared to dt.

Disk surface temperature is another parameter, controlled by a transformer. By adjusting the voltage on elements, electrical power that is received by heating elements can be regulated. If constant heat flux as the boundary condition is needed, it can be assumed that, except for a small

portion (due to proper insolation) of inlet power, which is assumed to be heat loss to the ambient from beneath, the rest is conducted thorough the disk. On the other hand, if constant surface temperature is set as the case boundary condition, an optical thermometer is used to adjust the transformer voltage that supplies the element set. Since the convective coefficient between the disk and the test zone changes when the disk spin rate varies, the temperature measurement needs to be done either while the disk is spinning or in a very short break right after spinning stops. The former generates noises in the optical thermometer and the latter could be unreal if it does not get done quickly enough. The fluctuation in temperature measurement is about $\sim 0.5\ ^{o}C$ and thermometer manufacturer claims the error, after calibration with one point, is less than $\pm 1\ ^{o}C$. Hence, the total error in disk surface temperature could be assumed within $\pm 1.5\ ^{o}C$. By measuring the temperature several times and averaging, it is made sure that error in temperature does not exceed that range.

The spinning rate of the disk and the wall are two other parameters that need to be measured accurately. They both are boundary conditions that are manually adjustable using two similar DC power suppliers. These power suppliers each use two controls: one for large adjustment, and one for fine ones. This makes it easier and more accurate for the operator to control the applied voltage on each motor. The current (amperage) and shaft torque of motors are directly related in DC motors. Therefore, when the friction and losses are kept constant by performing lubrication, very small variations of current is expected in the motor operating rpm range. In other word, as long as the current is kept same rpm and voltage are directly related by a linear correlation. As measured, the disk motor current does not exceed $0.13\ A$ and the wall's always stays between $0.33\ A$ and $0.36\ A$ provided that proper lubrication is always applied on contact surface between the top ring that holds the side wall and the bearings (skate wheels). The

higher current of a DC motor with same voltage represents that shaft torque has increased and spin rate has decreased. When this happens, the lubrication in the system has to be redone about every fifteen minutes to minimize the friction and keep the spinning rate steady. Also, the lubrication reduces the noise and vibration of the whole system significantly and makes it very smooth and almost silent. Without applying it or doing it improperly, the contact surface gets dry, friction increases and not only the current increases, but the spin rate changes and does not follow the same manner. In other word, as long as the current is not changing significantly, the spinning rate of both cases can be calibrated with the inlet voltage.

A series of PIV tests has been run without presence of particles in the test zone, while two white and black marks were placed on the dark disk and the lid of cylinder, respectively. These two indicate the relative angular positions of both spinning objects. A certain time difference between the snapshots ($dt = 10\,ms$ for the cylinder and $dt = 3\,ms$ for the disk) is given to the system and angle displacement is measured for each case. Having this angle displacement and the corresponding time difference, rotating speeds could be simply calculated. This procedure has been repeated many times with various supplied voltages and pairs of data points (rpm vs voltage) were acquired for both disk and wall. Since both express approximately linear relationship between rpm and voltage in their operating range, two below linear correlations were fitted by a simple MATLAB code. Therefore, based on these two correlations, less than $\sim 5\%$ error in the calculated rpm for any input voltage in the operating range is expected. Both of the curves and their data points as well as linear correlation between input and output are also shown in figure 4.5 and equations (4.1) and (7.2).

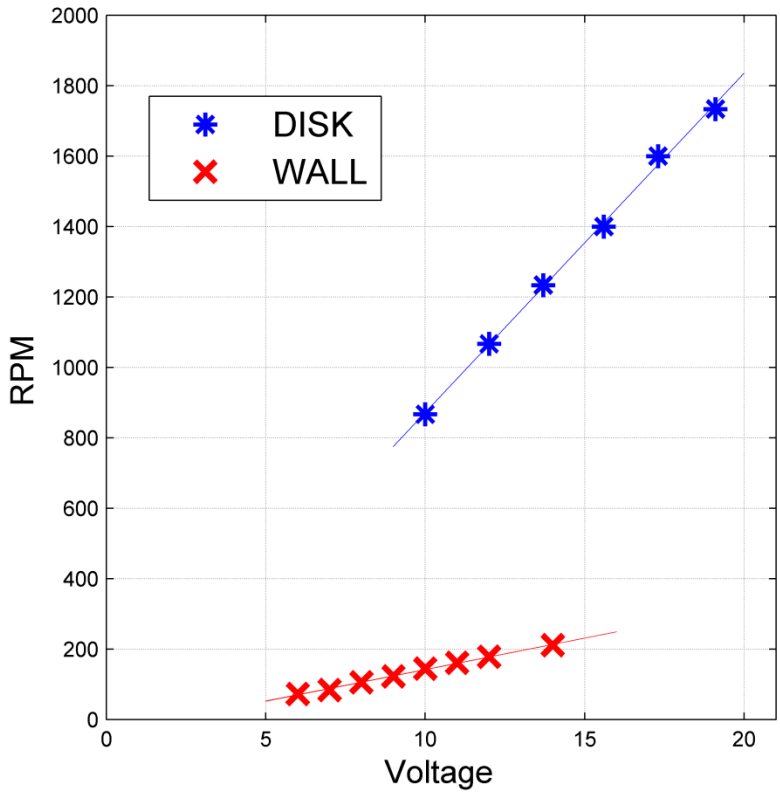

Figure 4.5 Graph of disk and wall spinning rate calibration

$$\omega_D(rpm) = 96.359V - 91.784 \qquad 8 < V < 26 \tag{4.1}$$

$$\omega_W(rpm) = 17.906V - 37.621 \qquad 12 < V < 25 \tag{4.2}$$

Since hundreds of experiments and data are required for this project and different cases can mix up easily, acquired data need to be organized and saved carefully. A naming code was established in order to cover all of the cases and make it comfortable to save and find them. This naming code includes date and starting time of each experiment as well as the disk type (whether it is plain or with openings), wall and disk angular speed, temperature difference between disk and ambient, the time difference between each pair of snapshots and the height of the laser plane. In vertical measurements the four digits at right, Height, indicate the height of the lowest and

highest points of the image frame. Table 4.1 expresses an example of the name for a set of acquired data and meaning of each part:

Table 4.1 Naming code and its meaning in an example

Example: Cam_Date=140131_Time=103530-D1-1000CC-150CC-00-0300-0200							
Cam_Date=150131	Time=103530	D1	1000CC	150CC	00	0300	0200
Recorded on Jan 31, 2015	Starts at 10:35 & 30 sec	Disk Type 1	Disk RPM + Direction	Wall RPM + Direction	ΔT	Time(μs)	Height (inches)

Since variety of boundary conditions (side wall and disk spin rate and temperature difference between disk and ambient) in different heights are required for this work, four main types of experiments have been designed and performed which will be presented in separate chapters: Cylinder and Disk Baseline-Flow, Counter-Rotating Flow and Co-Rotating Flow. The Baseline-Flow implies the case that either of side wall or disk is stationary and the other one is spinning. This case shows the effect of a solo rotating surface in different rates and temperature difference and also studies the flow structure under those conditions. The Co-Rotating flow and the Counter-Rotating flow cover different combinations of boundary condition when rotating surfaces are acting in same direction and opposite directions respectively.

Three spinning rates for the wall (100, 150 and 200 rpm) and 6 rates for the disk (1000, 1200, 1400, 1600, 1800 and 2000 rpm) are considered in this study and spin rates in all cases are combination of them. For the sake of normalizing the values and easiness in referring each case, the smallest angular of both wall and disk spin rate is named wall/disk reference speed:

$$\Omega_{ref,w} = 100\ rpm = 10.47\frac{rad}{s} \Rightarrow \Omega_w^* = \frac{\Omega_w}{\Omega_{ref,w}} \qquad (4.3-a)$$

$$\Omega_{ref,d} = 1000\ rpm = 104.72\frac{rad}{s} \quad \Rightarrow \quad \Omega_d^* = \frac{\Omega_d}{\Omega_{ref,d}} \qquad (4.3-b)$$

The selection of the rotating rates for the cylinder and the disk was a delicate decision based on the observations in different cases. The rotating cylinder wall has a stronger influence on the whole flow field since its wall area is much larger (one order larger) than the disk area. In contrast, the rotating disk influences the neighboring flow field near the disk by diffusion. Therefore, the rotating rate of the disk should be much higher than that of the cylinder to achieve the comparable effect on the flow. In other words, due to large engaged area of wall in the test zone, the most dominant boundary condition is the wall spinning rate. Thus, velocity of wall is the reference velocity for all cases that disk spins. In absence of this boundary condition and in cases that only the disk spins with a particular rate it was noticed that the flow behavior is similar to the cases that wall solely spins in the same direction but with tenth of that particular rate. For instance, in two cases, when only the wall spins 1500 rpm and only the disk spins 150 rpm in the same direction, the flows are very similar and velocity scale seems very close. Therefore, reference velocity for all cases is defined as:

$$\begin{cases} if\ u_w = 0 \Longrightarrow & u_{ref} = 0.1\ u_{D.E.} \\ if\ u_w \neq 0 \Longrightarrow & u_{ref} = u_w \end{cases} \tag{4.4}$$

where $u_{D.E.}$ is the disk edge speed and u_w is the wall speed (inner surface).

By observing numerous cases and iterating the experiments for a wide range and combinations of rates, the following spin rates and heights have been found ae the most interesting ones. Data are collected from 7 heights above the bottom disk (2”/51 mm, 3”/76 mm, 4.5”/114 mm, 6.5”/165mm, 8.5”/216mm, 11.5”/292mm and finally 15”/381mm. Respectively $H^* = 0.67, 1, 1.5, 2.17, 2.83, 3.83$ and 5). As explained earlier in the governing equation section, these heights are also normalized by the test zone radius as shown in previous chapter. Since PIV naturally needs larger displacement between two frames compared to Optical Flow method correlation methods [65], this time difference should be chosen accordingly. Moreover, mean

velocity magnitude in each case is very important to choose the right time difference. All things considered, this time difference has been considered 0.001 second (1000 μS) for most experiments in horizontal plane and 0.002 second (2000 μS) for most experiments in vertical plane and for the ones with higher mean velocity lower time differences have been selected.

Unlike the Counter-Rotating flow, the Baseline-Flow has a smoother nature. Therefore, each batch of data in every experiment consists of about 100 hundred pairs of images for the Baseline-Flow and about 1000 pairs for the Counter-Rotating flow. In vertical measurements each batch always has about 1000 pairs of images. In longer experiments concentration of particles decreases over the time and more particles need to be injected into the test zone (while it is being recorded). This injection might slightly disturb the main flow. As a result, for more accurate results small portion images have been manually found and deleted from the batch (not more than 5% of pairs in each batch) due to either low concentration or being captured at the same time with the injection.

Images from all digital cameras are always saved in a rectangular camera head and exported to a matrix pixel by pixel. Each array of that matrix represents the light intensity (and/or color in the colorful images) of the corresponding pixel. Since they are all arranged in a rectangular order with rows and columns, the default and preference setting of all image processing softwares and code is performing the analysis in the Cartesian coordinate system. Previously, the necessity of using a cylindrical coordinate and its advantages for this study were discussed. Hence, in order to switch to the cylindrical coordination, a simple mathematical transformation on the velocity vector field for the entire domain needs to be done (only for horizontal plane measurements) as the first step of processing. Figure 4.6 schematically displays a typical raw image captured from the top. Intensity of light for each pixel of image is saved in an array of a matrix. The area of

interest, as it is shown in this figure, is not necessarily at the center of image. Therefore, each batch of images needs to be manually masked. This means that a simple code crops the arrays of a matrix in the square frame ($M \approx N$) and saves them into new files. Another part of the masking code sets all arrays outside the inner circle zero (dark points). Note that in order to avoid the noise and large light intensity gradient caused by intersection of laser plane and wall, the area of interest is just few pixels (1-2 mm) inside the cylinder as it is demonstrated in the figure. Center of this frame in these new files is now at the centerline of cylinder and it is considered as the origin of new cylindrical coordinate. To convert the velocity component from Cartesian to Cylindrical coordinate, the procedure below can be followed:

$$r = \sqrt{(i - x_c)^2 + (j - y_c)^2} \quad , \qquad \theta = \tan^{-1}\frac{(j - y_c)}{(i - x_c)} \qquad (4.5, \text{a and b})$$

For each pixel it can be said that:

$$u_r = u_x \cos\theta + u_y \sin\theta \, , \qquad u_\theta = u_y \cos\theta - u_x \sin\theta \qquad (4.6, \text{a and b})$$

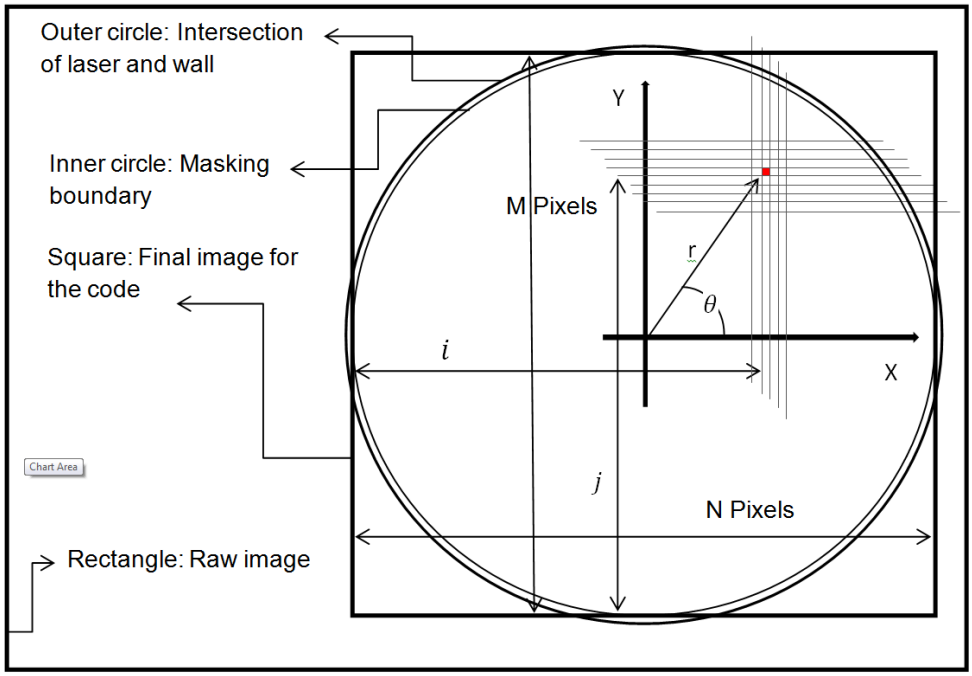

Figure 4.6 Schematic of an image and masking frame taken from the top view

Near the wall control over the concentration of particles is very limited. In some cases concentration is not very high and it changes drastically in different angles. Compared to the results from Optical Flow, the quality of velocity vector fields obtained by Davis/LaVision near the walls was higher even though the resolution of vector field from this method is less than the results from the Optical Flow method (e.g. for a particular case vector field from an image is a 124x124 matrix whereas the similar Matrix from the Optical flow method is as large as the original size of image 992x992).

Each batch of data is processed by LaVision software in about an hour (depends on size of image) on a regular PC (CPU: 3.0GHz and RAM: 4GB). Exporting and masking of each batch which was the previous step also takes about 20-30 minutes. The LaVision software provides two matrices of vertical and horizontal velocity components corresponding to each point. Having these two matrices, the direction and magnitude of velocity for each point in the plate is simply achievable. The run time for ensemble averaging of those two series of matrices for a batch of 1000 pairs of images takes between 10 to 20 minutes. For one set of boundary condition (wall and disk spin rate and the thermal condition) 7 batches of horizontal data and 2 batches of vertical data is required (9 batched that each has ~1000 pairs of image). Overall time is about 24 hours and since this procedure is being done on different computers the transporting time also doubles that time. The plotting code is a comprehensive MATLAB code that calculates and plots the velocity magnitude, velocity vectors, turbulent kinetic energy, vorticity and circulation for each data batch. The run time for this code is between 40 to 60 minutes for a batch of 1000 pairs of images on the same computer. Although it has never been exactly calculated, the total CPU run time of all cases (different combinations of disk, wall and thermal conditions) in this work is several months!

The calibration of attained matrices from LaVision has two steps. The first step is translating the results from the code into a meaningful unit and the second one is making sure that the matrices and the actual geometry are compatible in all final plots and figures. When each pair of images is processed with LaVision, no calibration is being applied on the results. In other words, the velocity vectors of each segment are presented in pixel/time difference. In the horizontal plane measurements the laser sheet does not move vertically. Therefore, in each height size of the domain boundary does not change very much and number of pixels in an image from one side to another side indicates the length of domain. Those very small variations (few pixels of difference in measuring the diameter of cylinder) in each height during one experiment and also for the same height in different data batches are because of either not-perfect circular cylinder or error of finding the brightest point of boundaries in the images during the masking procedure. This error has been minimized by measuring the diameter of cylinder in pixels for several cases and averaging the results. The time difference for each pair of images is also known. Knowing the time difference for each case and the actual inner cylinder diameter which is always 146.5 mm regardless of the height, a constant coefficient for every height is achievable. This coefficient has to be multiplied to the corresponding velocity vector matrices to change their unit from pixel/time difference to a physical/normalized unit such as m/s (finally it will be normalized). For the second step, number of columns and rows in each matrix are being translated to actual size of the domain in a physical/normalized length unit (e.g. mm).

For an actual example that covers both two aforementioned steps, a masked 818x818 pixels image pair, taken from top, was processed by the LaVision code. This pair was captured at the height of 2” from the bottom. By choosing 64x64 windows for the first pass of process and 32x32 for the second pass of process, best results were obtained (Reference [94] provides more

information about choosing the windows and passes of PIV as well as maximum pixel shift in a pair). The output are two103 by 103 velocity vectors matrices, one shows the velocity component in X and the other one in Y directions. In the raw images average of cylinder diameter in pixels for several cases are 835 pixels. This is slightly higher than the size of masked image firstly because the thickness of the plexi-glass is few millimeters and the masked images do not include that and secondly because the masked images circularly exclude few pixels from outside to attain more uniform intensity images. Actual outer diameter of cylinder is 152 mm and time difference in each pair is so 300 μS so a coefficient that needs to be multiplied to all 2" matrices from the code can be calculated as:

$$Coef = \frac{0.103\ m}{835 pixel \times 0.0003\ Sec} \rightarrow \text{Changes the unit of matrices to } m/s \qquad (4.7)$$

Then these matrices or their products such as U_θ, Re stress, etc are being plotted for the domain so a square of 103 by 103 (from velocity vector matrix) is plotted over a square of 146 by 146 mm (the actual size of square that surrounding the circle of masked image). In other words, number of rows and columns of each array multiplied by $146 \div 103 = 1.42$ is the position of that point in mm from the left lower corner of the frame. Obviously, a shift of 73 mm, half of the frame size in mm, should be applied to the entire domain to align the center of coordinate with the cylinder's centerline.

In order to calculate the non-dimensional form of velocity and geometrical characteristics, air properties in the condition that experiments were done are needed. Based on needed air properties in equations $3.1 - 5$, density, kinematic viscosity, expansion coefficient and Prundtl in the temperature range of experiments are represented [95]:

Table 4.2 Air properties (*20 °C* to *100 °*C)

Temperature $-T-\ ^{o}C$	**Density** $-\rho-kg/m^3$	**Kinematic Viscosity** $-\nu-\times 10^{-6}\ m^2/s$	**Expansion Coefficient** $-b-\times 10^{-3}\ 1/K$	**Prandtl's Number** $-Pr-$
20	1.205	15.11	3.43	0.713
40	1.127	16.97	3.20	0.711
60	1.067	18.90	3.00	0.709
80	1.000	20.94	2.83	0.708
100	0.946	23.06	2.68	0.703

5 Results and Discussion: Baseline-flows

As the first step, the Baseline-Flow with the simplest boundary conditions are studied. In these cases just one of the test zone inner surfaces (either the side wall or the bottom disk) is spinning and the other one stays stationary. The cylinder-baseline-flow is the flow driven by the rotating cylinder wall while the disk remains stationary. The disk-baseline-flow is the flow driven by the rotating disk without heating while the cylinder remains stationary. To understand these baseline flows, PIV measurements were conducted separately at 3 rotating rates of the cylinder (100, 150 and 200 rpm) and 6 rotating rates of the disk (1000, 1200, 1400, 1600, 1800 and 2000 rpm). For normalization, the non-dimensional spinning rates for the cylinder wall and the disk were previously introduced in $(4.3 - a)$. The Baseline-Flow data are being used as references to study the impact of only one rotating wall and to compare it with more complicated cases. In the next section, in Counter-Rotating flow spin rates are similar to Co-Rotating flow but the disk and the wall spin in opposite directions. Beside the no-heating case, two other thermal conditions, where the temperature differences between disk and ambient temperature are set to $\mathrm{T}_d - \mathrm{T}_{amb} = 25^o C$ and $50^o C$, are applied to Counter-Rotating flow for the last step. Furthermore, wall spinning rates remain constant at $\Omega_{\mathrm{w}}^* = 1.5$ and the disk spins in the same direction with the 6 different rates. This flow is named Co-Rotating flow. Results for Baseline flow cases are discussed in this section and Counter-rotating flow and Co-rotating flow are discussed in the next sections.

Figures 5-1, 5-2, and 5-3 represent the Baseline-Flow results for the case that the wall spins while the disk does not. For convenience, the cylinder-baseline-flow case is named Baseline-Flow I, whereas Baseline-Flow II is the disk-baseline-flow. Since the pattern of velocity field for different heights in the entire domain at all three measured wall speeds ($\Omega_w^* = 1, \Omega_w^* = 1.5$ and

$\Omega_w^* = 2$) do not change significantly, the ensemble averaged velocity magnitude/vector field in figure 5-1 is only shown for one case: $\Omega_w^* = 1.5$ and $H^* = 2.17$, which is at mid-level and mid-spin-rate among the conditions that are performed in this study. The only difference between velocity vector/magnitude fields for this height and the other heights is that in the higher ones maximum velocity is very slightly less than the lower ones. . The Reynolds number in this case of $\Omega_w^* = 1.5$ is $Re = u_w R/\nu = 580$. The normalized velocity magnitude is previously defined as $|u^*|$ and $|u_V^*|$ in (3.36) and (3.37) for cross section and vertical planes. The $|u_V^*|$-field does not show the coherent motion in unheated cases (figures b and c) and $|u^*|$ is much larger than $|u_V^*|$, indicating that this flow is basically axisymmetric in the averaging sense. However, in heated cases and particularly when $\Delta T = 50^o C$ (figures d and e) there is a weak upward flow near the inner wall and a downward flow close to the centerline.

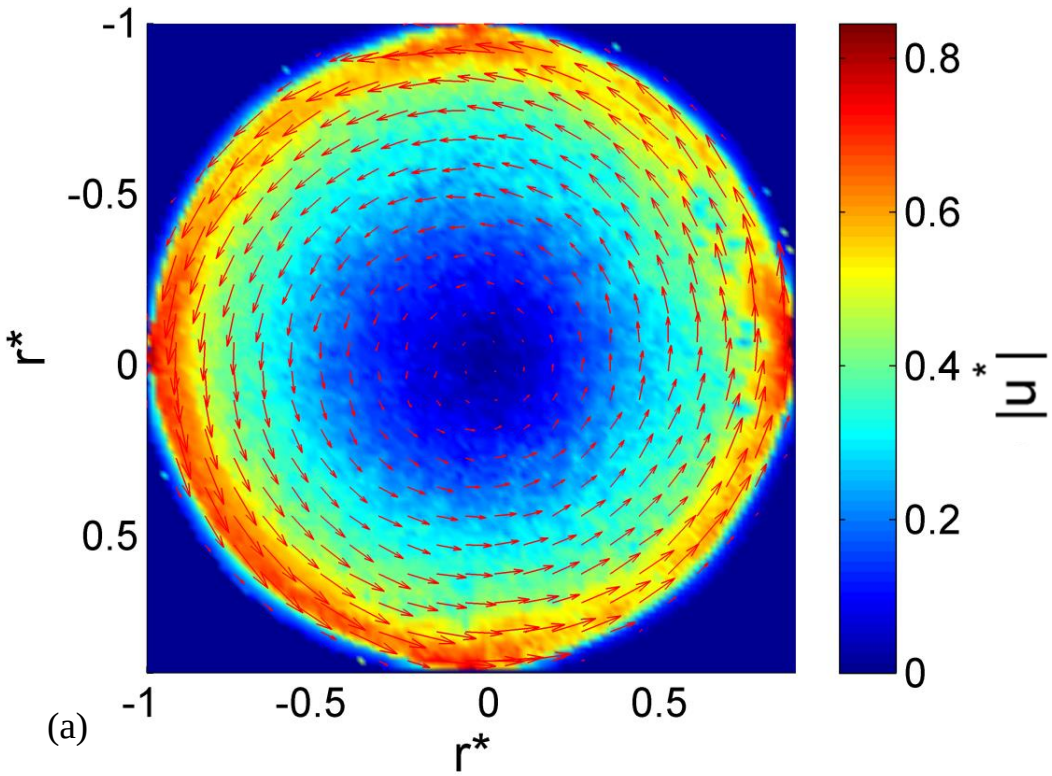

(a)

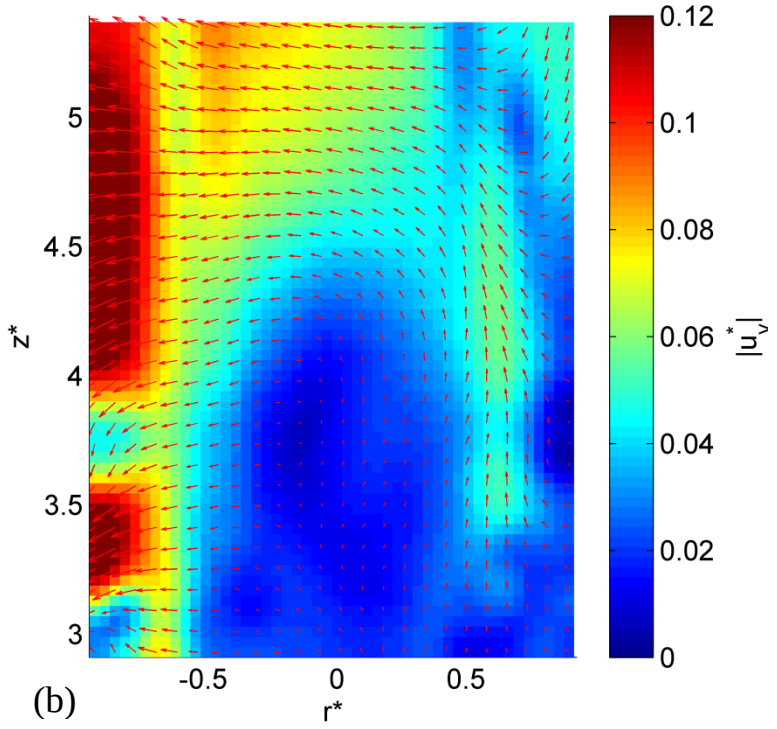
0.12
0.1
0.08
0.06
0.04
0.02
0
$|u_v^*|$
5
4.5
4
3.5
3
z*
-0.5
0
0.5
r*

(b)

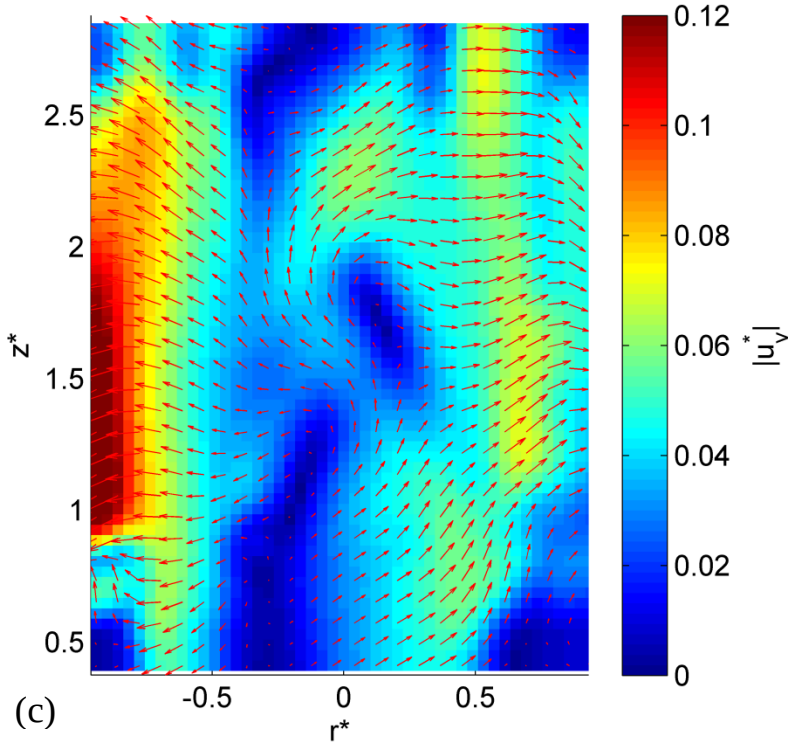
0.12
0.1
0.08
0.06
0.04
0.02
0
$|u_v^*|$
2.5
2
1.5
1
0.5
z*
-0.5
0
0.5
r*

(c)

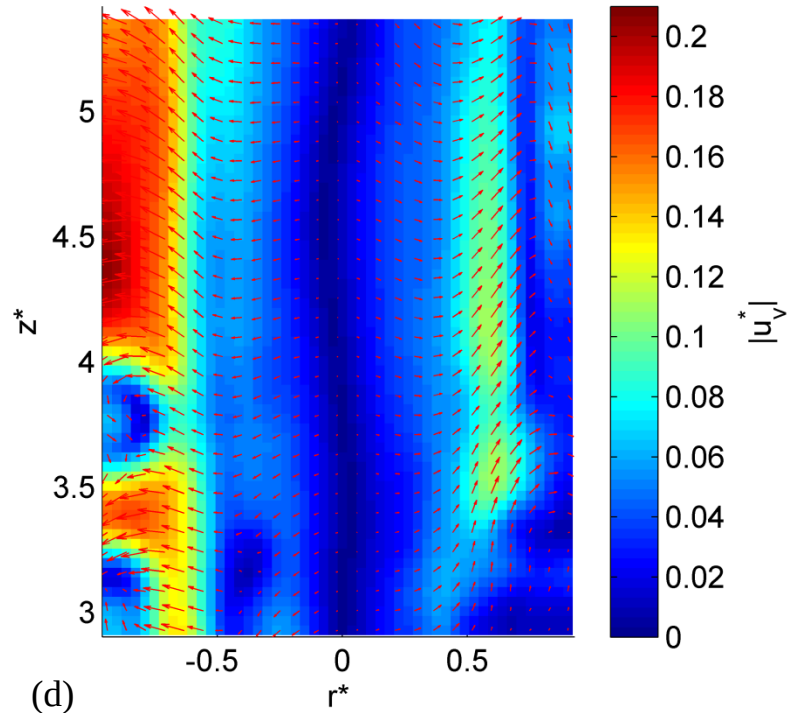

(d)

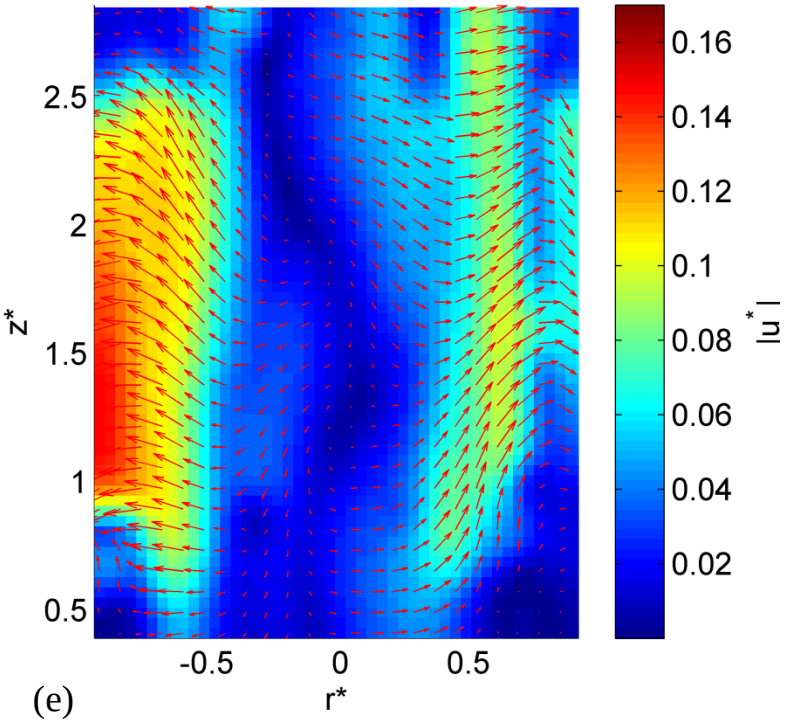

(e)

Figure 5.1 The velocity vector superposed on the magnitude field for the Baseline-Flow I: $\Omega_w^* = 1.5$ (a) cross-section at $z^* = 1.5$ (b) vertical plane for unheated case $2.92 < z^* < 5.25$ (c) vertical plane for unheated case $0.42 < z^* < 2.92$(d) vertical plane for heated case $\Delta T = 50^o C$ $2.92 < z^* < 5.25$ (e) vertical plane for heated case $\Delta T = 50^o C$ $0.42 < z^* < 2.92$

Since the whole flow is driven by the rotating wall, the highest velocity region is expected to occur close to the side wall. On the contrary, in a very narrow ring near the wall velocity suddenly decreases. In this region PIV measurements are not accurate due to the lower particle concentration induced by boundary layer effect on attracting/ repelling particle. As such results very close to the wall are not reliable. Thus, in figure 5-2 and other velocity profiles in this work, velocity profiles curves close to the wall are cut and not demonstrated. To examine the axisymmetric property of the flow, as an example, figure 5-2 shows the $\langle u_\theta^* \rangle$-profiles at four different cuts ($\theta = \pi/4, -\pi/4, 0, \pi/2$) along with the sector-averaged $\langle u_\theta^* \rangle$-profile over the right and left sectors of a circle ($\theta = 0$ *to* π and $\theta = \pi$ *to* 2π). ($z^* = 1.5$). In other words, the thick curve exhibits the average of velocity profiles along 90 different sections where each section and its neighbor are 2^oapart. This curve in $-1 < r^* < 0$ shows the average of 90 radial sections in the upper half of domain in figure8-1-a ($0 < \theta < \pi$) and $0 < r^* < 1$ demonstrates the average of the lower half of the domain ($\pi < \theta < \pi/2$) and the matrices of velocity profiles along 90 different radial sections are collected, averaged and presented in the red curve ($\langle u_\theta^* \rangle$-profile). The cylinder inner-wall velocity $u_w^* = 1$ is marked by stars in this figure for reference. The velocity of the small ring close to the wall can be simply interpolated from the velocity of its inner neighbors and rotating condition. It can be seen that there is good agreement between each section results and the average due to the axisymmetric behavior of the flow structure. The normalized wall speed is also indicated in figure 5-1.

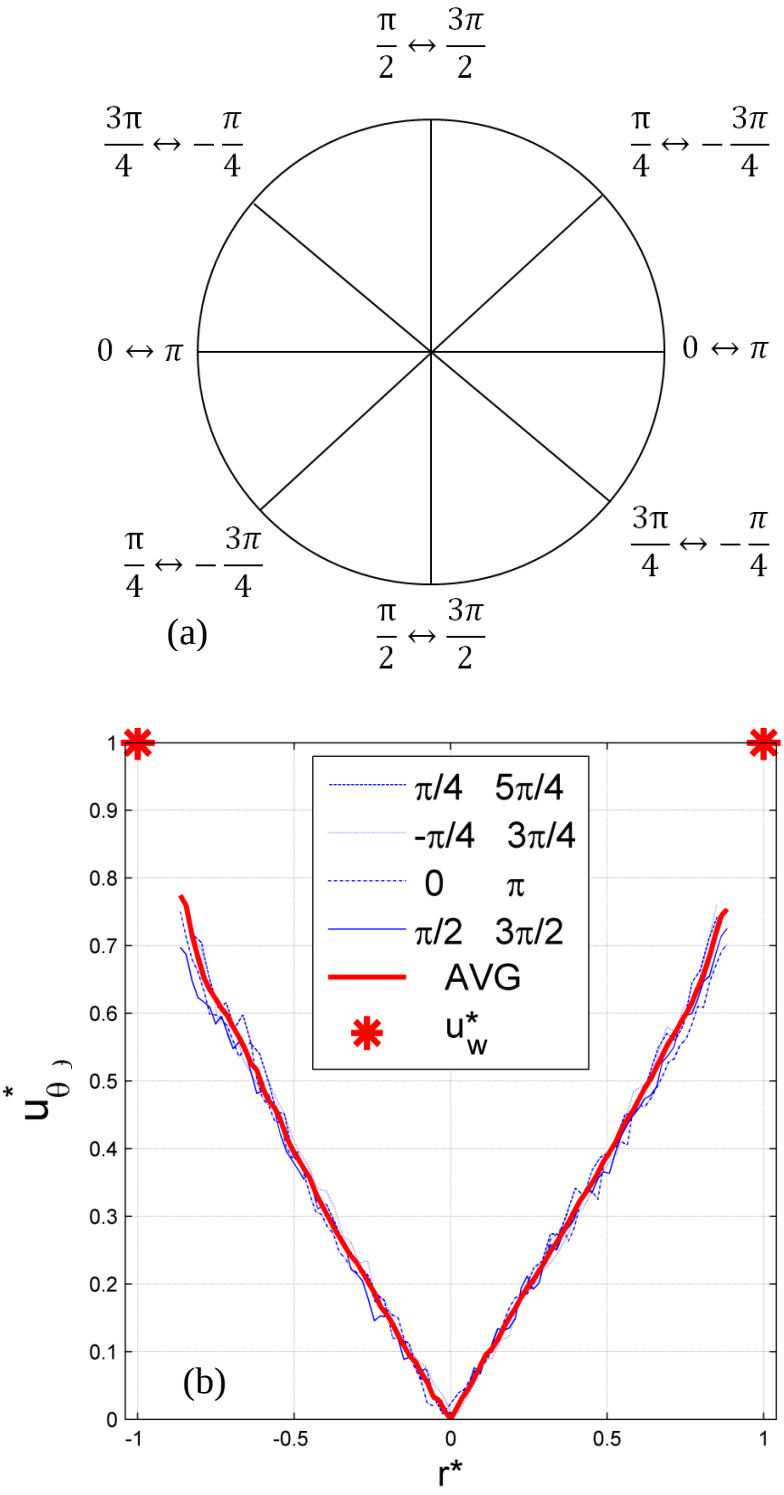

Figure 5.2 (a) Schematic diagram of the four radial sections (b) Normalized azimuthal velocity profile averaged over the half-circle-sectors and selected profiles across four radial sections for the Baseline-Flow I: $\Omega_w^* = 1$

The velocity data were obtained only in $-0.8 \le r^* \le 0.8$ in the cross-section and $-0.9 \le r^* \le 0.9$ in the vertical plane since few particles existed near the rotating cylinder wall and light refraction was large through the curved cylinder wall there. The flow approaches to a solid-body-like rotation in the core region of the cylinder-baseline-flow, which can be reduced from the base-flow solution of the Taylor-Couette flow [96], which will be used as a reference to compare with other cases.

In Figures 5-2 and 5-3 the velocity data were obtained only in $-0.8 \le r^* \le 0.8$ in the cross-section and $-0.9 \le r^* \le 0.9$ in the vertical plane since few particles existed near the rotating cylinder wall and light refraction was large through the curved cylinder wall there. In Figure 5-3-a, b and c, three different sets of normalized velocity profiles associated with three wall spin rates are represented and marked distinctly. In each spin rate all studied heights are displayed with different marks. Figure 5-3-d also combine all data from the previous three figures together and shows that regardless of the disk speed, all data are to great extent homogenous in the vertical direction and they collapse together and show near-linear distribution in $-0.8 \le r^* \le 0.8$, although the behavior near the rotating wall is not known.

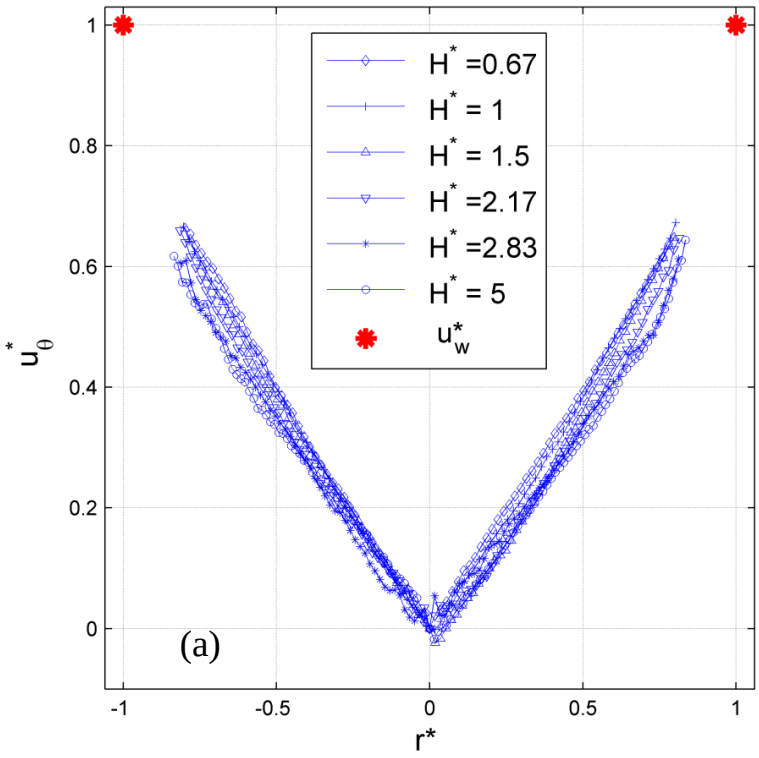
H* =0.67
H* = 1
H* = 1.5
H* =2.17
H* =2.83
H* = 5
u*w
u*θ
r*
(a)

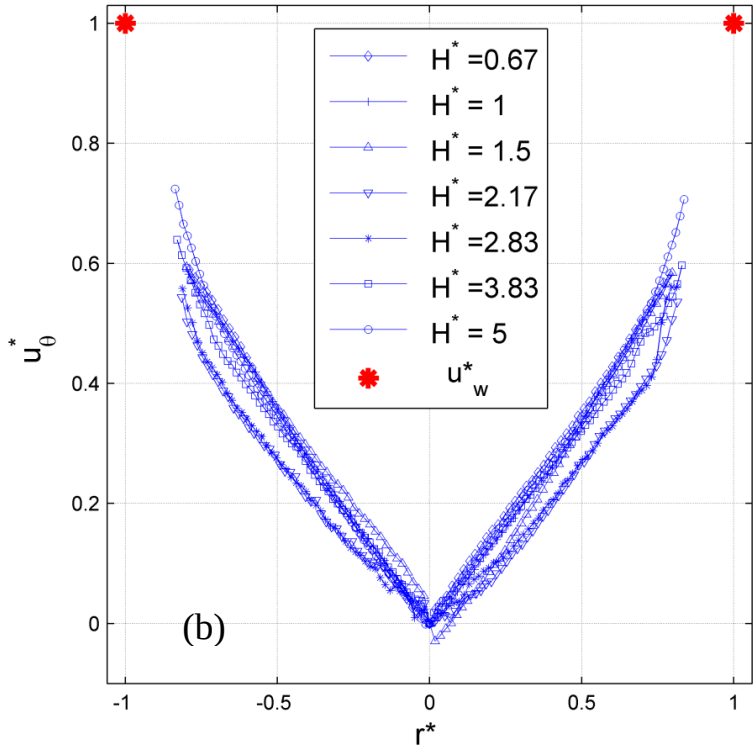
H* =0.67
H* = 1
H* = 1.5
H* =2.17
H* =2.83
H* =3.83
H* = 5
u*w
u*θ
r*
(b)

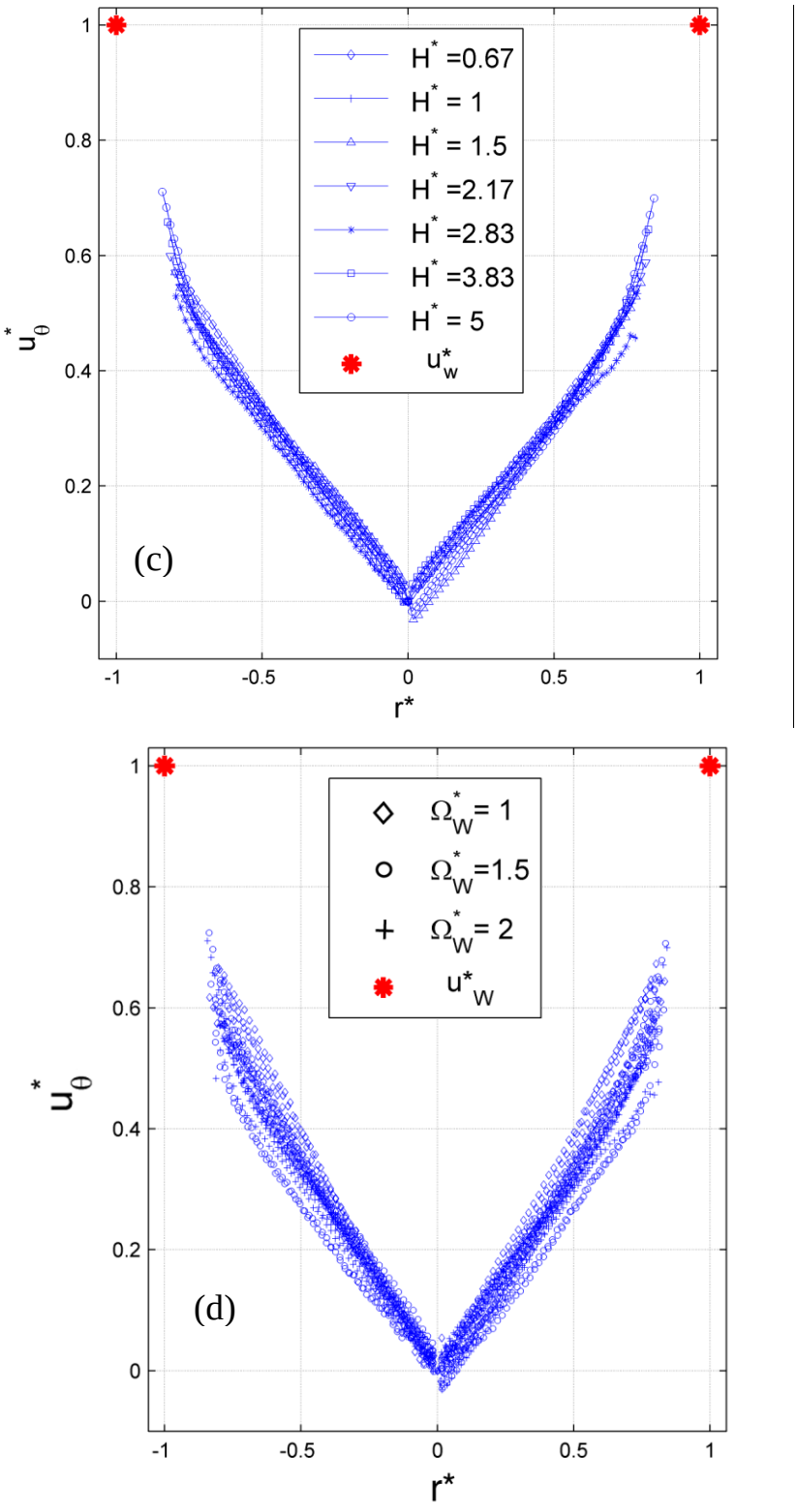

Figure 5.3 $\left\langle u_{\theta}^{*} \right\rangle$-profiles in all measured heights for three Baseline-Flow I: (a): $\Omega_{w}^{*} = 1$, (b): $\Omega_{w}^{*} = 1.5$, (c): $\Omega_{w}^{*} = 2$ and (d):all spin rates together

The turbulence kinetic energy is calculated for each case at each any position and compares different cases within the test zone. The normalized turbulent kinetic energy is defined as:

$$k = \langle {u'_r}^2 + {u'_\theta}^2 \rangle \Rightarrow k^* = k/{u^*_{ref}}^2 \qquad (5-1-a)$$

$$k_V^* = \left(\left\langle {u'}_z^2 \right\rangle + \left\langle {u'}_r^2 \right\rangle \right) / u_{ref}^2 \qquad (5-1-b)$$

where the operator $\langle \quad \rangle$ denotes the ensemble average of a data batch, u'_r and u'_θ are fluctuation terms of velocity ($u'_{r,\theta} = u_{r,\theta} - \langle u_{r,\theta} \rangle$). Also, k_V^* is the normalized turbulent kinetic energy based on the two velocity components in the $\left(z^*, r^* \right)$ vertical plane.

Table 5.1 Volumetric average of $\boldsymbol{k^*}$, for all studied boundary conditioned

DISK→ / WALL↓	$\Omega_D^* = 0$ (Only-Wall)	$\Omega_D^* = -1$	$\Omega_D^* = -1.2$	$\Omega_D^* = -1.4$	$\Omega_D^* = -1.6$	$\Omega_D^* = -1.8$	$\Omega_D^* = -2$
0 (Only-Disk)	NA	0.0332	0.0234	0.0256	0.0238	0.016	0.0165
$\boldsymbol{\Omega_w^* = 1}$	0.0363	NA	NA	NA	NA	NA	NA
$\boldsymbol{\Omega_w^* = 1.5}$	0.0216	0.0395	0.0337	0.0275	0.0275	0.0291	0.0257
$\boldsymbol{\Omega_w^* = 2}$	0.0085	NA	NA	NA	NA	NA	NA
Co-Rotating	0	$\Omega_D^* = 1$	$\Omega_D^* = 1.2$	$\Omega_D^* = 1.4$	$\Omega_D^* = 1.6$	$\Omega_D^* = 1.8$	$\Omega_D^* = 2$
$\boldsymbol{\Omega_w^* = 1.5}$	NA	0.012	0.0104	0.0096	0.022	0.0114	0.0245

Table 5.1 shows the volume averaged turbulent kinetic energy for each set of boundary conditions. This means that each number is the average of all data points for the entire measurement domain in all heights. k^* along various radial sections for different heights, similar to the azimuthal velocity profile in figure 5.3, k^*-profiles are presented in figures 5.4-a, b and c for $\Omega_w^* = 1$, $\Omega_w^* = 1.5$ and $\Omega_w^* = 2$ respectively. Unlike the $\left\langle u_\theta^* \right\rangle$-profiles that were collapsed approximately at different heights, the k^*-profiles are considerably different in the vertical direction. As figure 5.4-a shows, in mid and higher heights ($H^* = 1.5$, 2.17 and 2.83) k^* is significantly higher. The maximum occurs at $z^* = 2.83$ and it is multiple times larger than the intensity at lower heights ($z^* = 0.67$ and $z^* = 1$). In $z^* = 3.83 - 5$ intensity decreases and

becomes similar to lower heights. In general, k^*-profiles can be presented to three domains ($z^* = 0.67,–1.5\,, z^* = 2.17 – 2.83\,, z^* = 3.83 – 5.0$) as shown in figure 5.4-d. Similar behavior in curve associated with $z^* = 5$ can be seen in Counter Rotating flow too and even in those cases turbulence is lower than other heights. This phenomenon is also observed at the two other values of Ω_w^* in figure 5-4-b and 5-4-c. Nonetheless, in figure 5-4-c k^* at $z^* = 0.67$ is much higher than its vicinity (e.g. at $z^* = 1$).

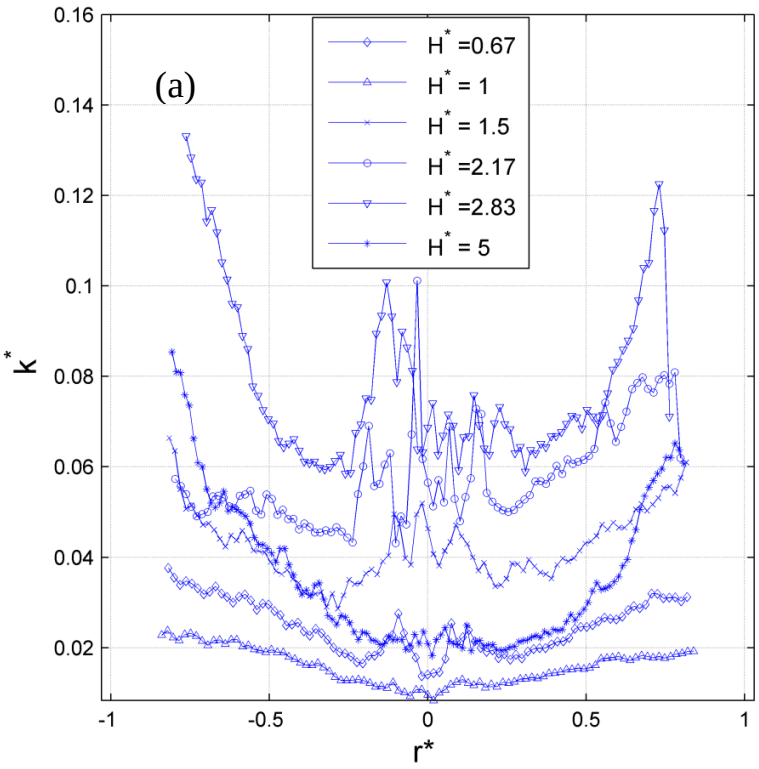

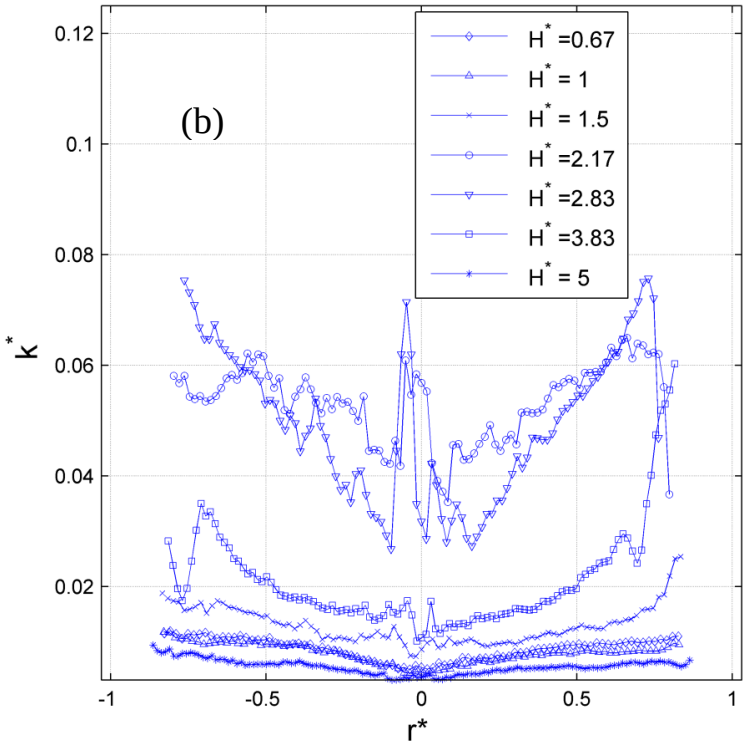
(b)
H* =0.67
H* = 1
H* = 1.5
H* =2.17
H* =2.83
H* =3.83
H* = 5
k*
r*
0.12
0.1
0.08
0.06
0.04
0.02
-1
-0.5
0
0.5
1

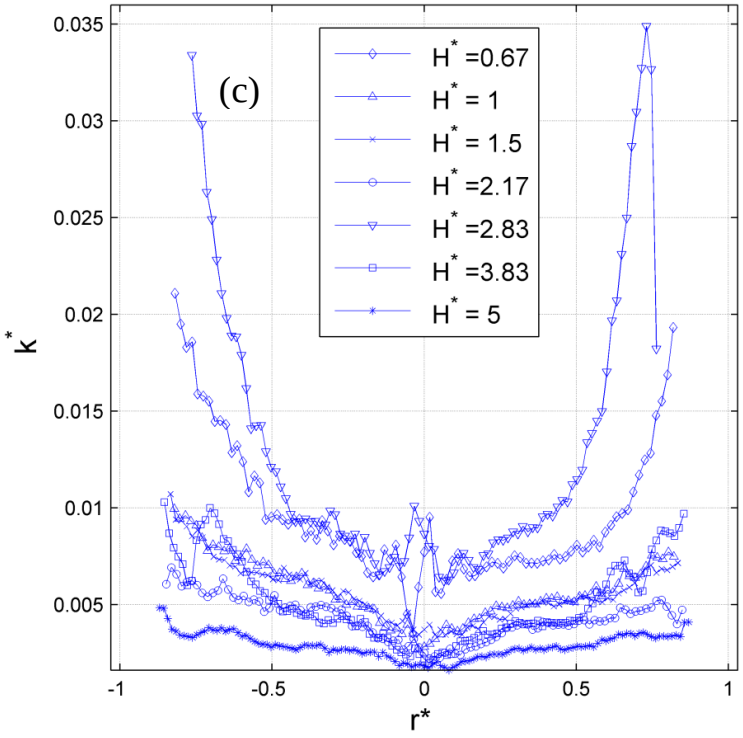
(c)
H* =0.67
H* = 1
H* = 1.5
H* =2.17
H* =2.83
H* =3.83
H* = 5
k*
r*
0.035
0.03
0.025
0.02
0.015
0.01
0.005
-1
-0.5
0
0.5
1

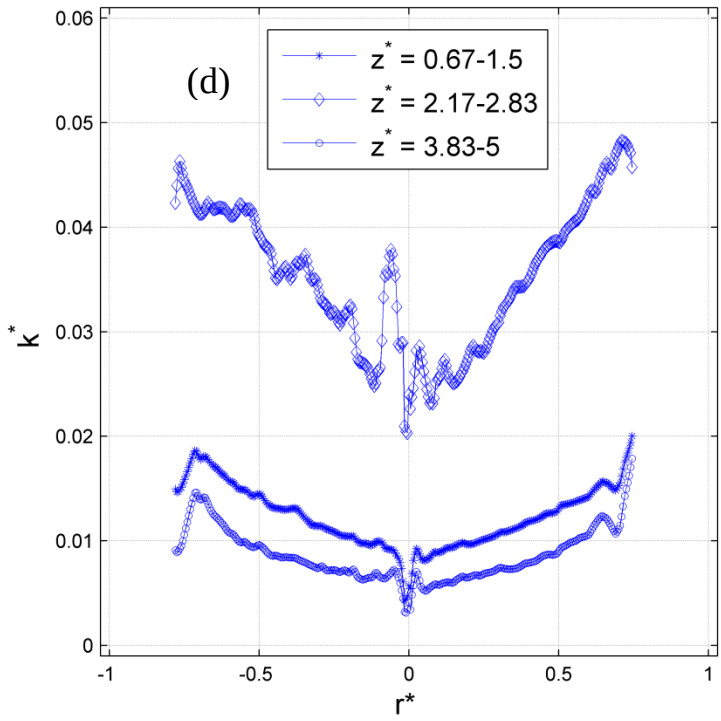

Figure 5.4 Normalized turbulent kinetic, k^*-profiles, in all measured heights for Baseline-Flow I (a) $\Omega_w^* = 1$, (b) $\Omega_w^* = 1.5$, (c) $\Omega_w^* = 2$ and (d)averaged in three domains at $\Omega_w^* = 1.5$

Another interesting fact is that the maximum k^* at these three spin rates, $\Omega_w^* = 1$, $\Omega_w^* = 1.5$ and $\Omega_w^* = 2$, are $k_{Max}^* = 0.13$, $k_{Max}^* = 0.075$ and $k_{Max}^* = 0.035$ which shows the normalized intensity decreases as the spin rate grows. This seems to be caused by the normalization procedure. As the wall spins faster, the ${u_{ref}^*}^2$ in denominator of equation 5-1 becomes larger and consequently k^* decreases. Although all curves show random pattern in some points and do not exactly follow smooth paths, in lower heights they are closer to linear shapes than the mid and higher heights that seem parabolic (except for the case: $\Omega_w^* = 2$ and $z^* = 0.67$ which behave similar to higher domain). This random behavior and zigzag pattern is stronger near the center in middle domain. The entire flow is caused by the wall and velocity in outer radii is larger, so are the perturbations and, consequently, k^*. Thus, in all curves the intensity in higherr^* is larger.

Figures 5.5, 5.6 and 5.7 exhibit the Baseline-Flow II (disk-baseline-flow: the disk spins while wall remain stationary). The entire flow, in all heights, is clock-wise in the same direction with the disk, unlike the previous cases in which wall was rotating counter-clock-wise. Compared to the wall spin rate in the previous case, the disk spins much faster. Thus, higher velocities and more turbulent flows are expected in lowest measured height (lower than $z^* = 0.67$). It is found that the rotating disk induces the significant downward flow in the central region and the upward secondary flow near the cylinder wall. For $z^* < 0.7$ near the center, there is a low-speed flow region. Near the lower corners, the vortices are formed (figures b and c). This flow becomes stronger in heated cases and particularly when $\Delta T = 50^o C$ (figures d and e).

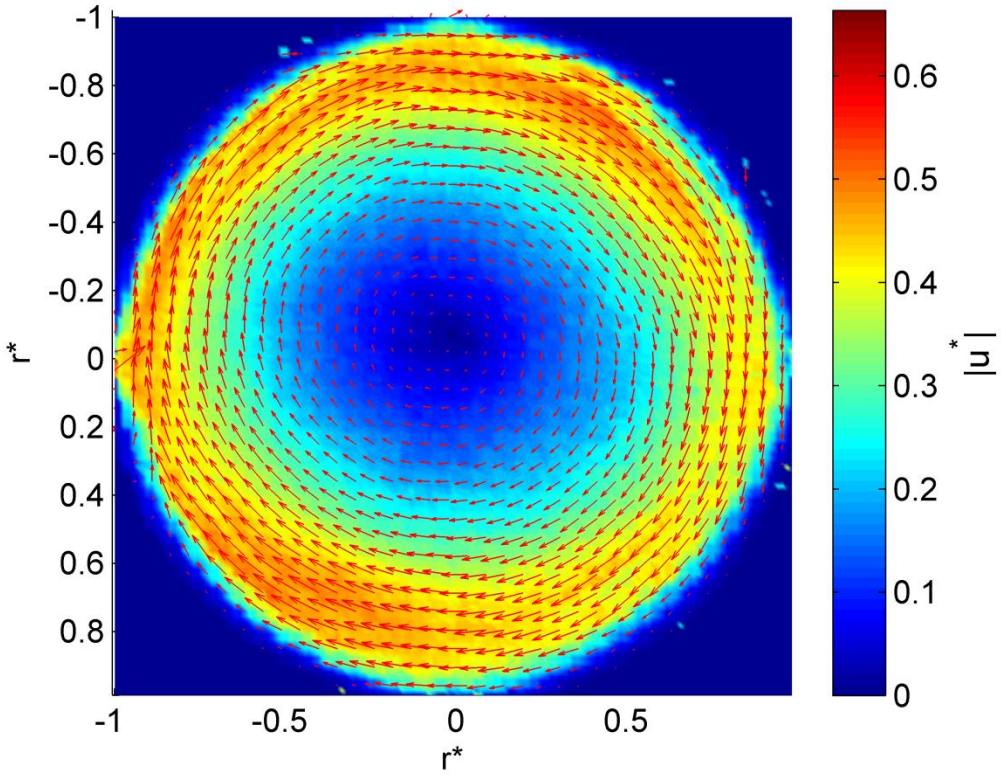

(a)

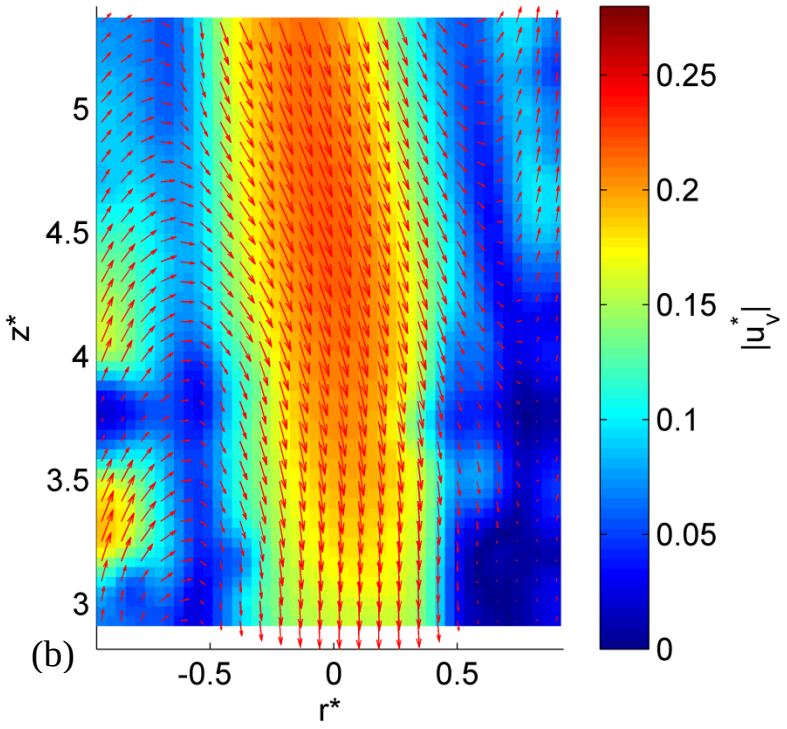
5
4.5
4
3.5
3
z*
-0.5
0
0.5
r*
0.25
0.2
0.15
0.1
0.05
0
|u_v|*

(b)

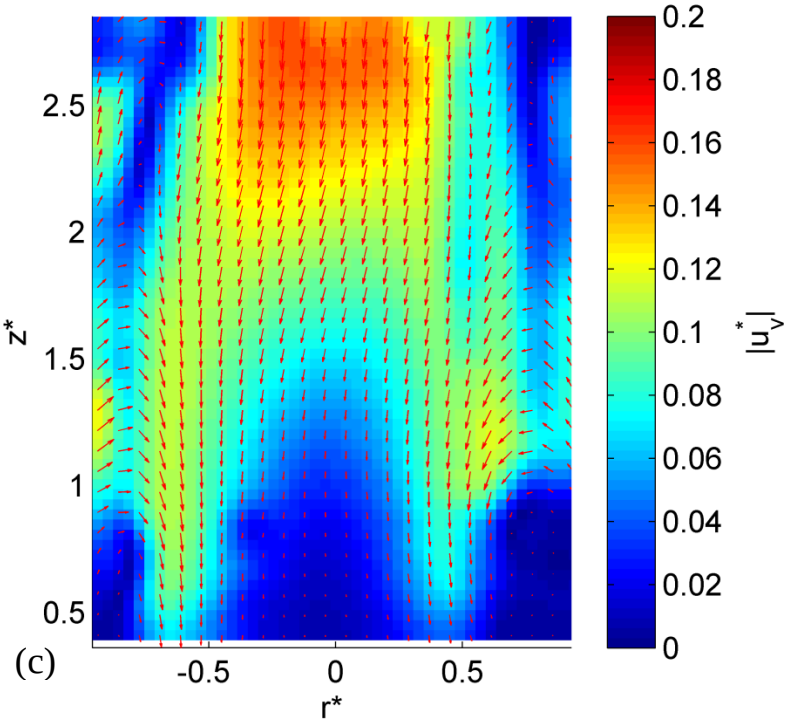
2.5
2
1.5
1
0.5
z*
-0.5
0
0.5
r*
0.2
0.18
0.16
0.14
0.12
0.1
0.08
0.06
0.04
0.02
0
|u_v|*

(c)

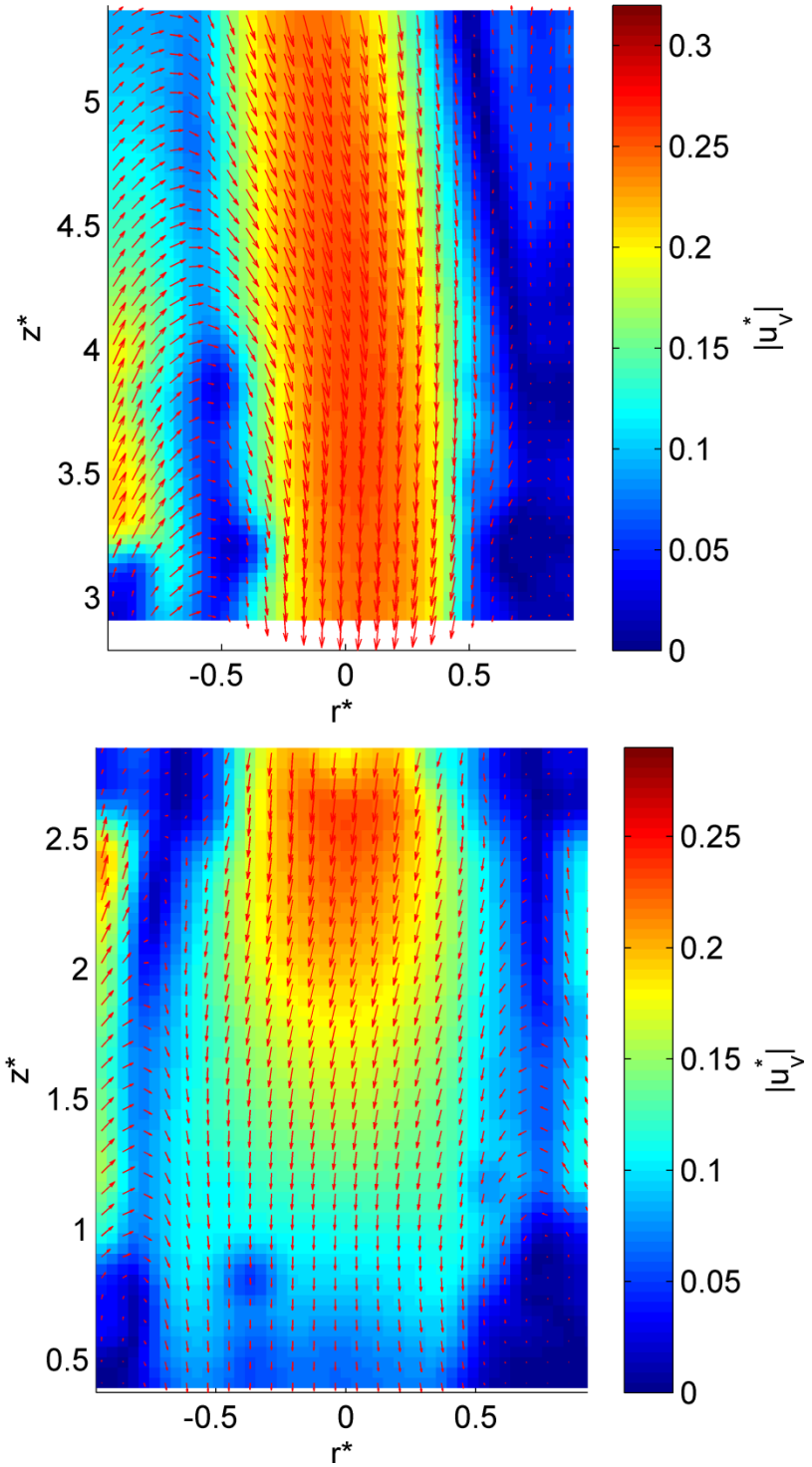

Figure 5.5 The velocity vector superposed on the magnitude field for the Baseline-Flow II: $\Omega_d^* = -1.4$ (a) cross-section at $z^* = 2.83$ and vertical plane at (b) vertical plane for unheated case $2.92 < z^* < 5.25$ (c) vertical plane for unheated case $0.42 < z^* < 2.92$(d) vertical plane for heated case $\Delta T = 50^o C$ $2.92 < z^* < 5.25$ (e) vertical plane for heated case $\Delta T = 50^o C$ $0.42 < z^* < 2.92$

As shown in Figure 5.6, Normalized velocity profiles, unlike the BF II which had linear distribution from the centerline to the wall in all heights, the velocity profile varies drastically from $z^* = 0.6$ to $z^* = 5$. As a result, the velocity profile cannot all be shown in the same figure as they were previously. Hence, three spin rates of $\Omega^* = 1, 1.4$ and 2 were selected to show the beginning, middle and end of the studied range. At the lower z^*-locations $(z^* = 0.67 - 1.5)$, the azimuthal velocity $\langle u_\theta^* \rangle$ rapidly increases in $r^* > 0.6$ near the stationary cylinder wall, while $\langle u_\theta^* \rangle$ remains small in the inner region ($-0.5 < r^* < 0.5$). As z^* increases, the $\langle u_\theta^* \rangle$-profiles become fuller in $-0.5 < r^* < 0.5$ due to the viscous diffusion to the disk edge to the center. The distribution of $\langle u_\theta^* \rangle$ is more complicated than the similarity solution of the laminar boundary layer on a rotating disk with an infinite radius where the azimuthal velocity has a linear distribution at the different vertical locations [96].

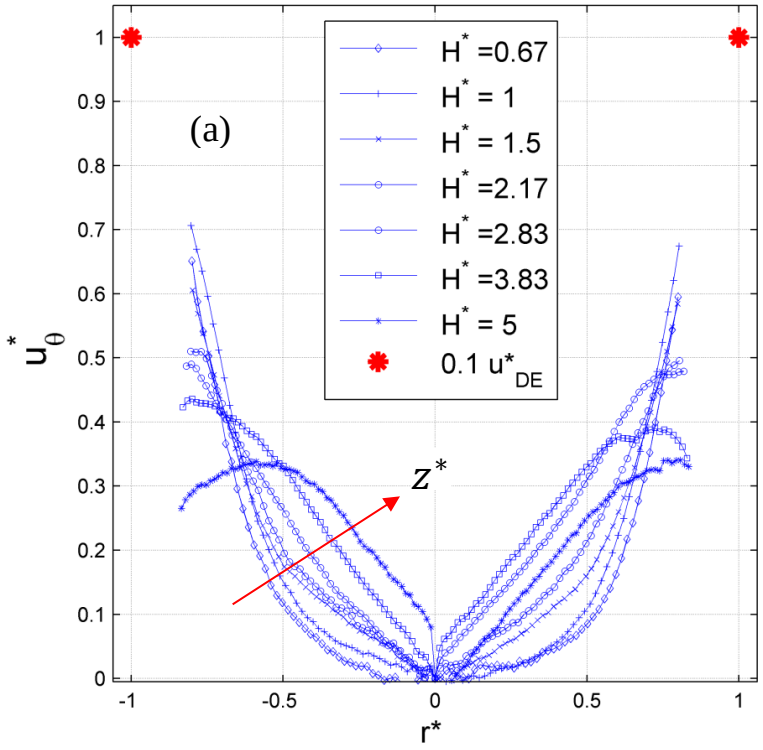
(a)
H* =0.67
H* = 1
H* = 1.5
H* =2.17
H* =2.83
H* =3.83
H* = 5
0.1 u*DE
z*
u*θ
r*
1
0.9
0.8
0.7
0.6
0.5
0.4
0.3
0.2
0.1
0
-1
-0.5
0
0.5
1

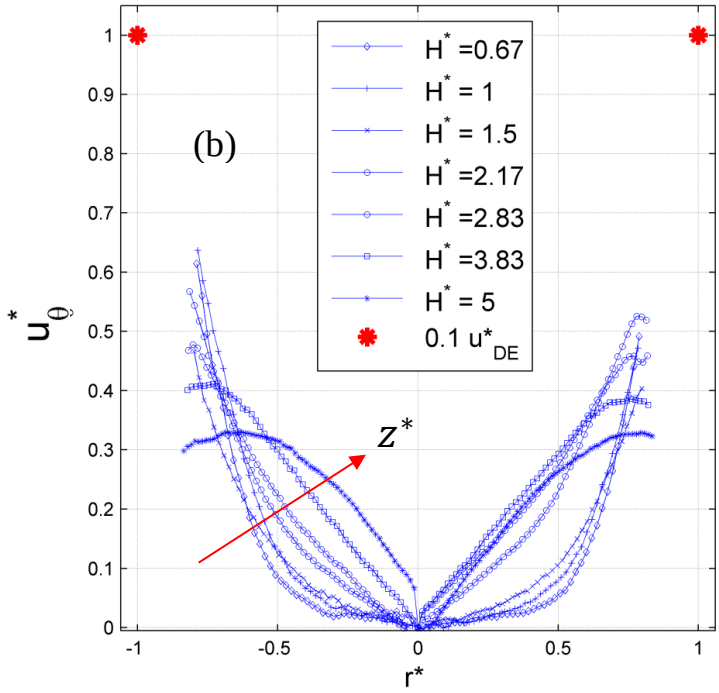
(b)
H* =0.67
H* = 1
H* = 1.5
H* =2.17
H* =2.83
H* =3.83
H* = 5
0.1 u*DE
z*
u*θ
r*
1
0.9
0.8
0.7
0.6
0.5
0.4
0.3
0.2
0.1
0
-1
-0.5
0
0.5
1

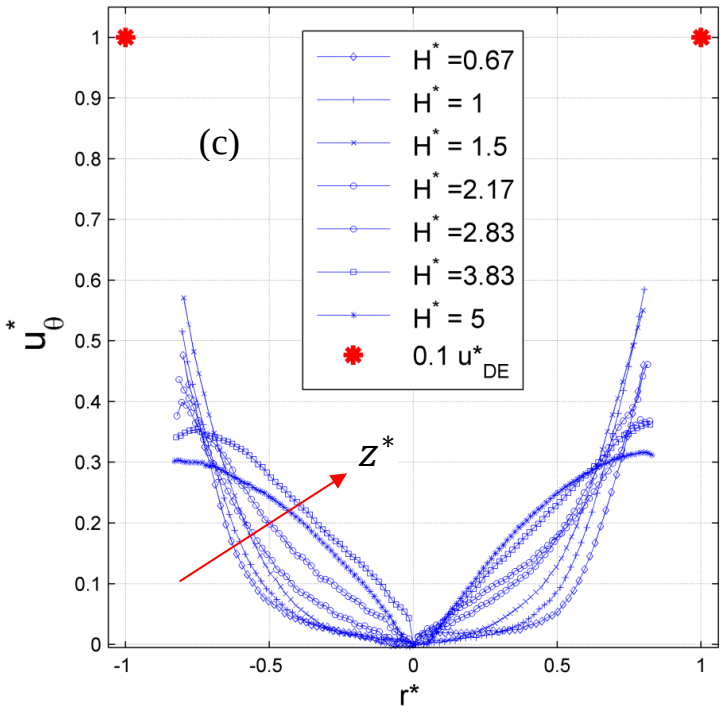

Figure 5.6 $\left\langle u_\theta^* \right\rangle$-profiles in all measured heights for one Base Flow II (a) $\Omega_d^* = -1$, (b) $\Omega_d^* = -1.4$ and (c) $\Omega_d^* = -2$

In figure 5-6, the reason of the formation of the high velocity ring in the lower height might be the centrifugal force at the bottom caused by high speed spin rate. Another interesting fact in this figure is as the height increases, both mean velocity and maximum velocity significantly decrease slightly. In figure 5.5-a at $z^* = 0.67$ maximum normalized velocity is $u_{max}^* \approx 0.7$. As the height increases, this value drops to $u_{max}^* \approx 0.6$ at $z^* = 1$, $u_{max}^* \approx 0.6$ at $z^* = 1.5$, $u_{max}^* = \sim 0.6$ at $z^* = 3.83$, $u_{max}^* = \sim 0.4$ and finally $u_{max}^* = \sim 0.32$ at $z^* = 5$. In much higher heights, the maximum velocity is expected to drop to very low velocity and close to zero. This is because the entire vortex is caused by viscous diffusion effect from the disk rotation and this effect vanishes gradually as the height increases. Velocity profiles in Baseline-Flow II show that the

center of the vortex and the centerline of the cylinder in some heights are very close (although they are not completely aligned).

In figure 5.6-b and c the overall form of all curves is similar to figure 5.5-a. However, as the disk spin rate increases, so does flow velocity but not with the same rate and the flow cannot catch up with that increase. Consequently, the normalized curves are slightly lower for $\Omega_{\mathrm{D}}^{*} = 1.4$ and $\Omega_{\mathrm{D}}^{*} = 2$. In all heights curves do not have an exact axisymmetric shape and peaks in one side are higher than the one on the other side even though, an overall and approximate asymmetry is observed in the whole curve. However, as an exception, at $z^{*} = 5$ curves are less axisymmetric and especially near the center at the left side velocity is higher.

Figures 5-7-a, b, c and d show k^{*} for Baseline-Flow II. Since flow is only driven by disk, turbulence, as expected, is larger in the lower heights compared to figures 5.3-a, b and c. This can be seen at $z^{*} = 0.67$ and $z^{*} = 1$ in all three disk spin rates. In higher heights and particularly at $z^{*} = 2.83$ and $z^{*} = 3.83$ all three figures show much lower k^{*}compared to figures 5-4-a, b and c because those heights are far from the source of rotating flow (as opposed to BF I). In lower heights, k^{*} in larger radii is significantly larger than the central region. When disk spin rate is $\Omega_{D}^{*} = -1$, the value of k^{*} in higher heights for most part of domain is about 0.02 and for lower heights it is about 0.05. These two values drop to half in higher spin rates*:* $\Omega_{D}^{*} = -1.4$ and $\Omega_{D}^{*} = -2$. In both Baseline-Flow cases k^{*} decreases in higher spin rates. As mentioned before, since the value of k^{*} is being normalized by ${u_{ref}^{*}}^{2}$, the denominator becomes larger and the value of k^{*} decreases in higher disk spin rates. Figure 5-7-d shows the k^{*}-profiles in the lower and upper domains ($z^{*} = 0.67 - 1.5$ and $z^{*} = 2.17, -5.0$) at $\Omega_{d}^{*} = -1.4$. In the lower domain ($z^{*} = 0.67 - 1.5$), k^{*} is rapidly increased near the disk edge, which corresponds to the strong

shear layers in the $\left\langle u_\theta^* \right\rangle$ -profiles in Figure 5.4-d. In contrast, in the upper domain ($z^* = 2.17, –5.0$), k^* becomes much smaller and its distribution is much flatter.

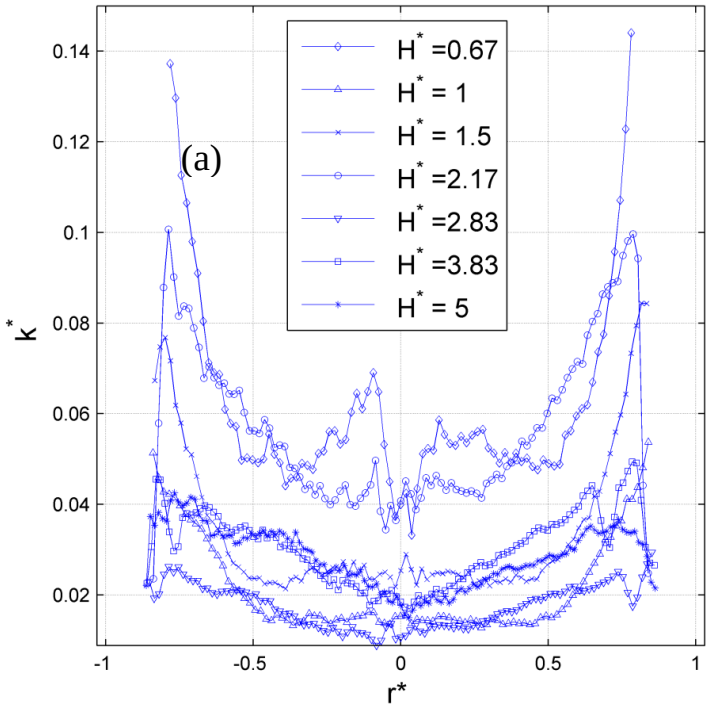

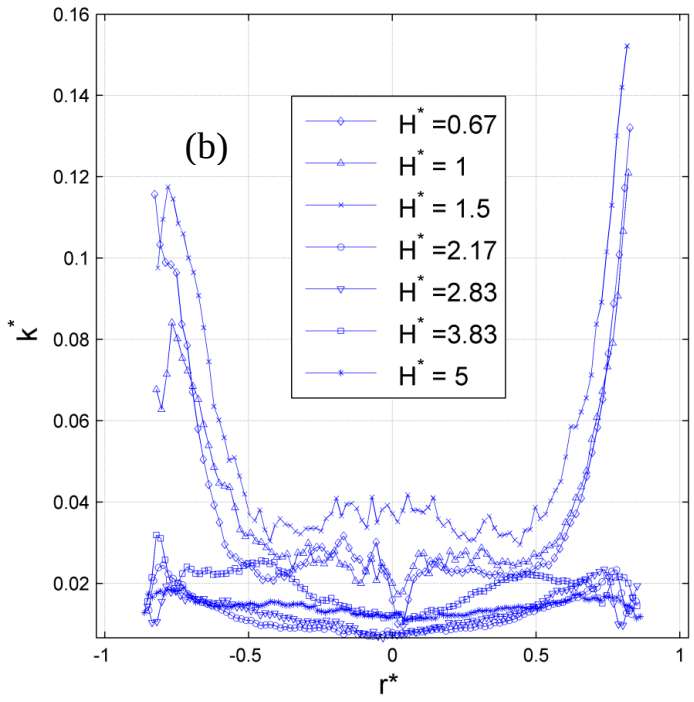

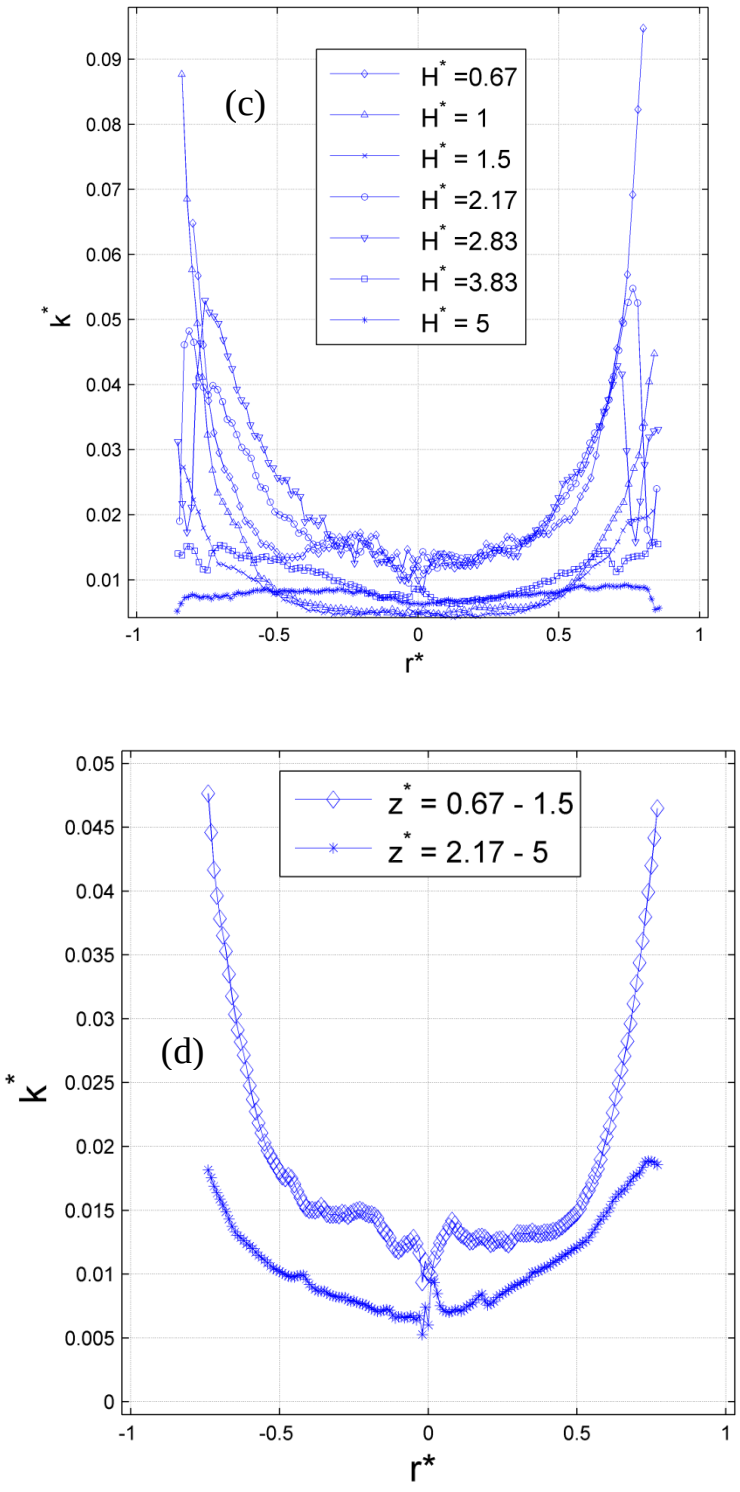

Figure 5.7 k^*-profiles in all measured heights for one Base Flow II (a) $\Omega_D^* = -1$, (b) $\Omega_D^* = -1.4$, (c) $\Omega_D^* = -2$ and (d) averaged in two domains at $\Omega_d^* = -1.4$

Figures 5.8-a and 5.8-b demonstrate the velocity vector field in all 7 studied heights for two Baseline-Flows cases: BF I: $\Omega_{w}^{*} = 1.5$ and BF II: $\Omega_{D}^{*} = -1.4$.

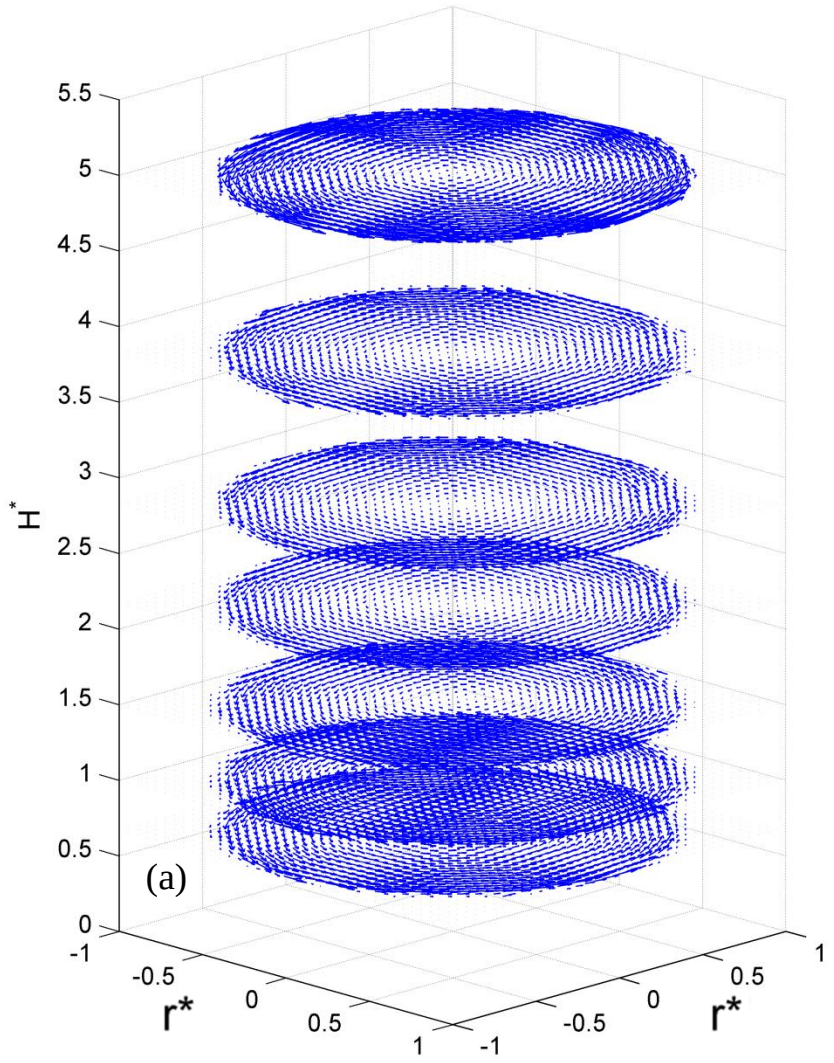

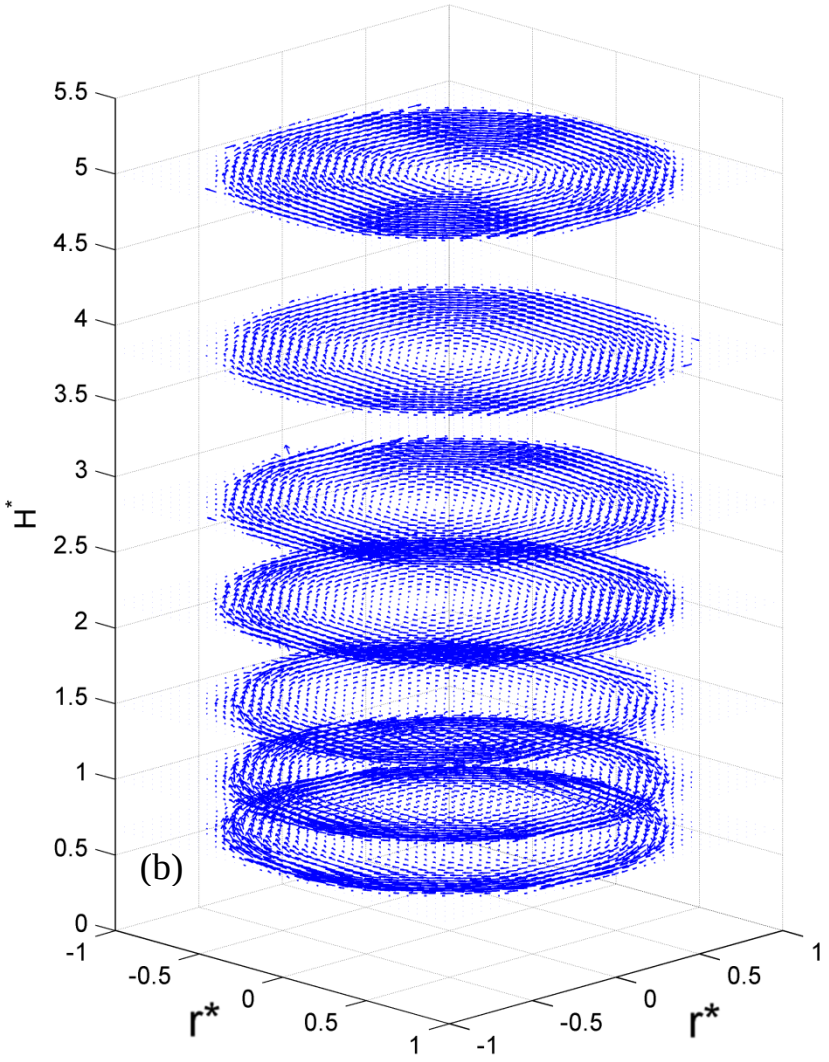

Figure 5.8 Velocity vector field for all studied layers for two (a): Base Flow I and $\Omega_w^* = 1.5$ and (b): Base Flow II and $\Omega_d^* = -1.4$

6 Results and Discussion: Counter-rotating-cylinder-disk-flow without disk heating

The flows in the rotating cylinder with the unheated counter-rotating disk were measured at $\Omega_d^* = -1.0$, -1.2, -1.4, -1.6, -1.8 and -2.0, while the cylinder spinning rate was fixed at $\Omega_w^* = 1.5$. This flow is simply called the Counter-Rotating flow without disk heating. $\langle u_\theta^* \rangle$-profiles for all disk is spinning rates are extracted and shown in figures 6-1-a, b, c, d, e and f. For convenience of analysis, the measurement domain in this case is approximately divided into the upper domain, transitional domain and lower domain, depending on the relative influences of the rotating cylinder and the counter-rotating disk on the flow. The transitional domain is characterized by the presence of distinct zero-crossing points in the $\langle u_\theta^* \rangle$-profiles, where the clockwise and counter-clockwise fluid rotations are mixed.

In figure 6-1-a, for $\Omega_D^* = -1$, all curves are in the upper domain and flow in the same direction as the wall at all heights. Comparing the velocity profiles in this figure and figure 5-3 clearly shows the impact of the disk in this case. Linear behavior of velocity profile curves in figure 5-3 has completely changed in figure 6-1 and velocity is very low in the inner region and rapidly rises in outer region, while the entire flow follows the wall-rotating direction. In this disk spin rate both lower domain and transitional domains are below $z^* = 1$. in higher heights although disk effect is not strong enough to reverse the flow direction even in the lowest studied height, it can change the velocity profile curvature.

As the disk spin rate increases, in figure 6-1-b where $\Omega_D^* = -1.2$, the flow direction at the lowest height ($H^* = 0.67$) is reversed, following the disk-rotating direction. Also, at $z^* = 1$ $\langle u_\theta^* \rangle$-profiles is close to zero in the entire inner region and the outer ring that follows the wall-

rotating direction has become much narrower. This is where the $\langle u_\theta^* \rangle$-profiles have distinct zero-crossing points, indicating that the significant clockwise and counter-clockwise flow motions co-exist in the domains. It is found that both lower and transitional domains have ascended. The two lowest measured height, $z^* = 0.67$ and $z^* = 1$, are in the lower domain and the third one, $z^* = 1.5$, in the transitional domain.

At $\Omega_D^* = -1.4$ and $\Omega_D^* = -1.6$ the flow in the lower and transitional domains have risen and upper domain is affected more by the disk. In $\Omega_D^* = -1.6, -1.8$ and -2 there are three curves ($z^* = 0.67$, $z^* = 1$ and $z^* = 1.5$) in the lower domain which means that flow in the three lowest heights follows the disk-rotating direction. The flow direction is always positive (counter-clock-wise) in three highest heights ($z^* = 2.83 - 5.0$) for the two fastest disk spin rates ($\Omega_D^* = 1.8$ and $\Omega_D^* = 2$). It is found that these heights are always in the upper domain.

The interesting flow phenomena occur in the transitional domain between the lower and upper domains. Surprisingly, curves in these heights in all spin rates are not symmetric and have a very unique shape. The shapes of two sides in that particular curve for these cases are completely different. For instance in figure b the curve corresponding with $z^* = 0.67$ has two different shapes in $-0.85 < r^* < 0$ and $0 < r^* < 0.85$. Nonetheless, this unique shape of curve at those particular heights follows the same pattern in all cases (even the heated cases as shown in the next section). In these curves a big jump right at $r^* = 0$ exists as the sign of u_θ^* changes suddenly. When center of rotation is not at $r^* = 0$, this jump and unique shape is more likely to be seen. In this situation a smooth flow perpendicular to section and close to the center has same magnitude but two opposite sign when $r^* \to 0^+$and $r^* \to 0^-$. This flow is influenced equally by the rotating cylinder and the counter-rotating disk. The complicated mixing layer in

the transitional domain is worthwhile to be examined more closely. Therefore, more details and figures are presented for this region.

In transitional domain the shape of $\langle u_\theta^* \rangle$-profiles are significantly different and flow is not axisymmetric. At figure 6.1-a this unique shape of the curves with the large jump at the center is not completely formed yet (Although it is about to take place at $r^* = -0.2$ for $z^* = 0.67$). When disk spins faster in figure 6-1-b, the lowest curve at $z^* = 0.67$ has that off center behavior which is also shown clearly in figure 6.6. In figure 6.1-c this transitional domain has moved one step higher at $z^* = 0.67$ and in figure 6.1-d three lower cures are in the transitional domain. In the two fastest studied disk spin rates in figures 6.1-e and 10.1-f this off-center shape is only seen at $H^* = 1.5$ and this height divides the entire domain to three distinct clock-wise and counter-clockwise and transitional domains. More details of flow for all disk speed in each height are presented in layer by layer velocity vector fields as well as velocity vector/magnitude fields later. Since this interesting flow phenomena takes place in the transitional domain, the focus is to show more detail in this region.

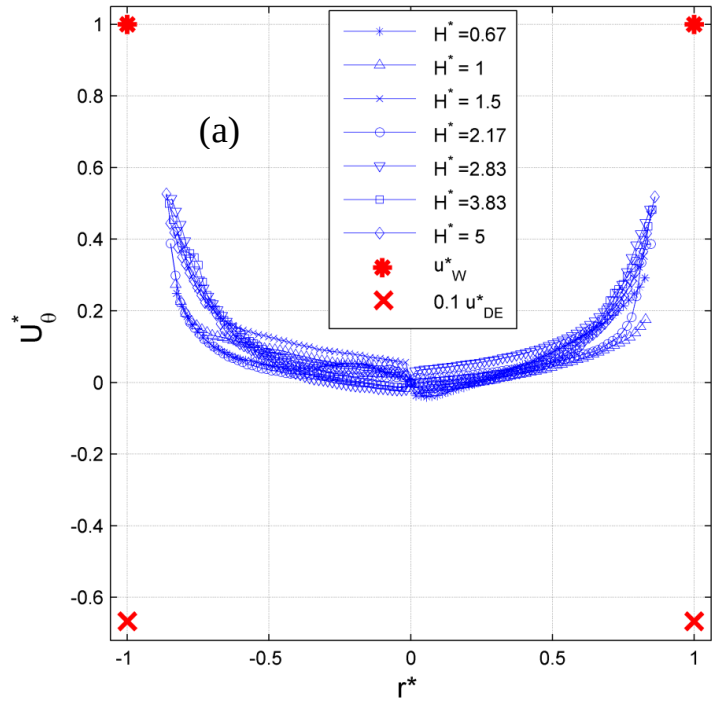
(a)
H* =0.67
H* = 1
H* = 1.5
H* =2.17
H* =2.83
H* =3.83
H* = 5
u*W
0.1 u*DE
U*θ
r*
1
0.8
0.6
0.4
0.2
0
-0.2
-0.4
-0.6
-1
-0.5
0
0.5
1

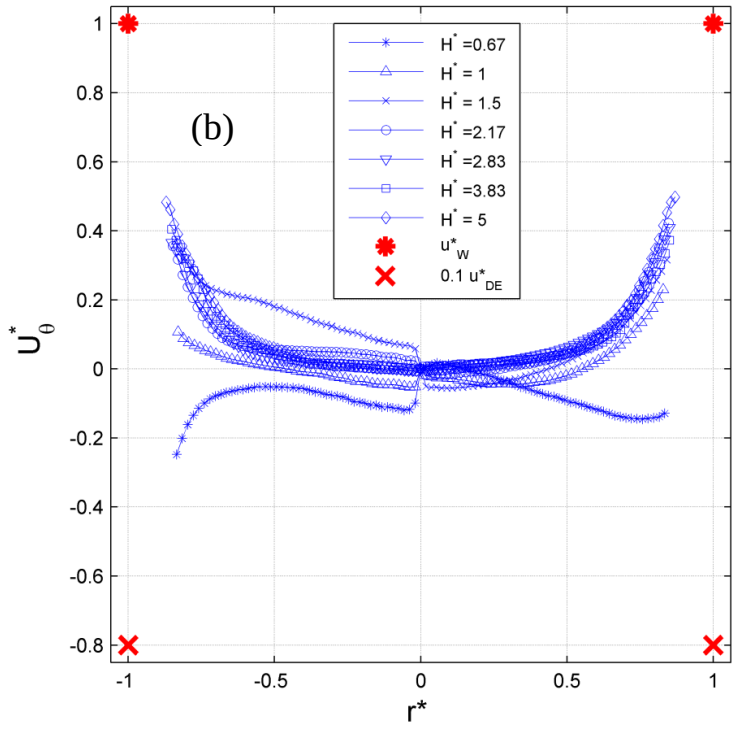
(b)
H* =0.67
H* = 1
H* = 1.5
H* =2.17
H* =2.83
H* =3.83
H* = 5
u*W
0.1 u*DE
U*θ
r*
1
0.8
0.6
0.4
0.2
0
-0.2
-0.4
-0.6
-0.8
-1
-0.5
0
0.5
1

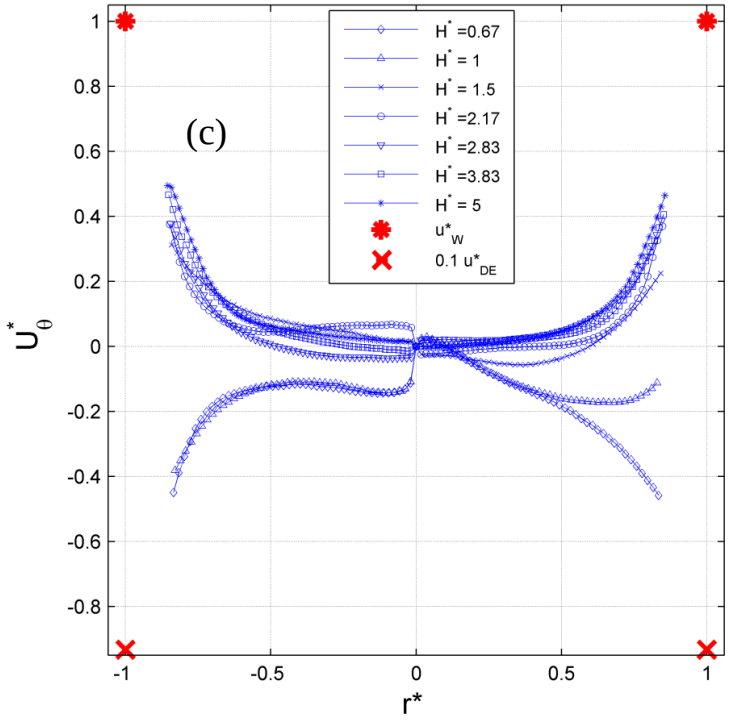
(c)
H* =0.67
H* = 1
H* = 1.5
H* =2.17
H* =2.83
H* =3.83
H* = 5
u*W
0.1 u*DE
U*θ
r*
1
0.8
0.6
0.4
0.2
0
-0.2
-0.4
-0.6
-0.8
-1
-0.5
0
0.5

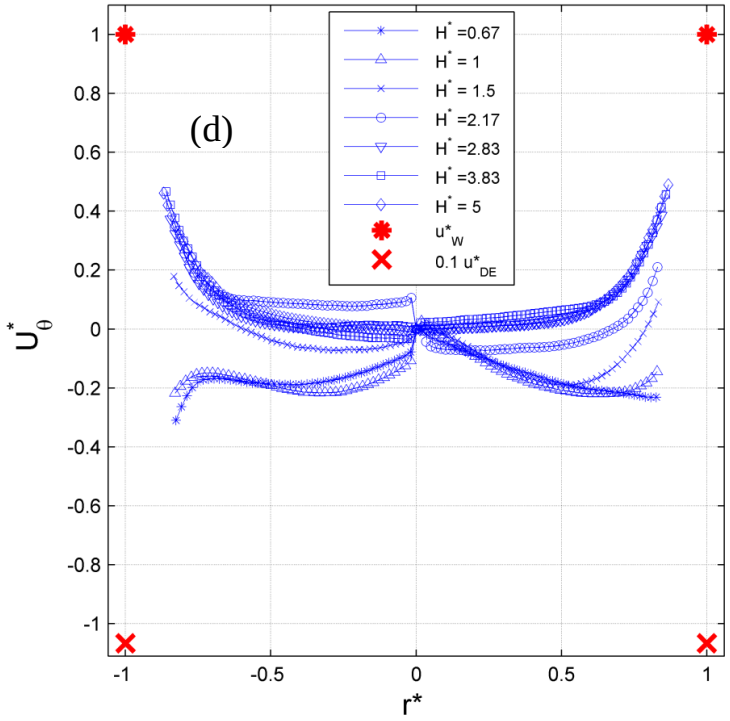
(d)
H* =0.67
H* = 1
H* = 1.5
H* =2.17
H* =2.83
H* =3.83
H* = 5
u*W
0.1 u*DE
U*θ
r*
1
0.8
0.6
0.4
0.2
0
-0.2
-0.4
-0.6
-0.8
-1
-0.5
0
0.5

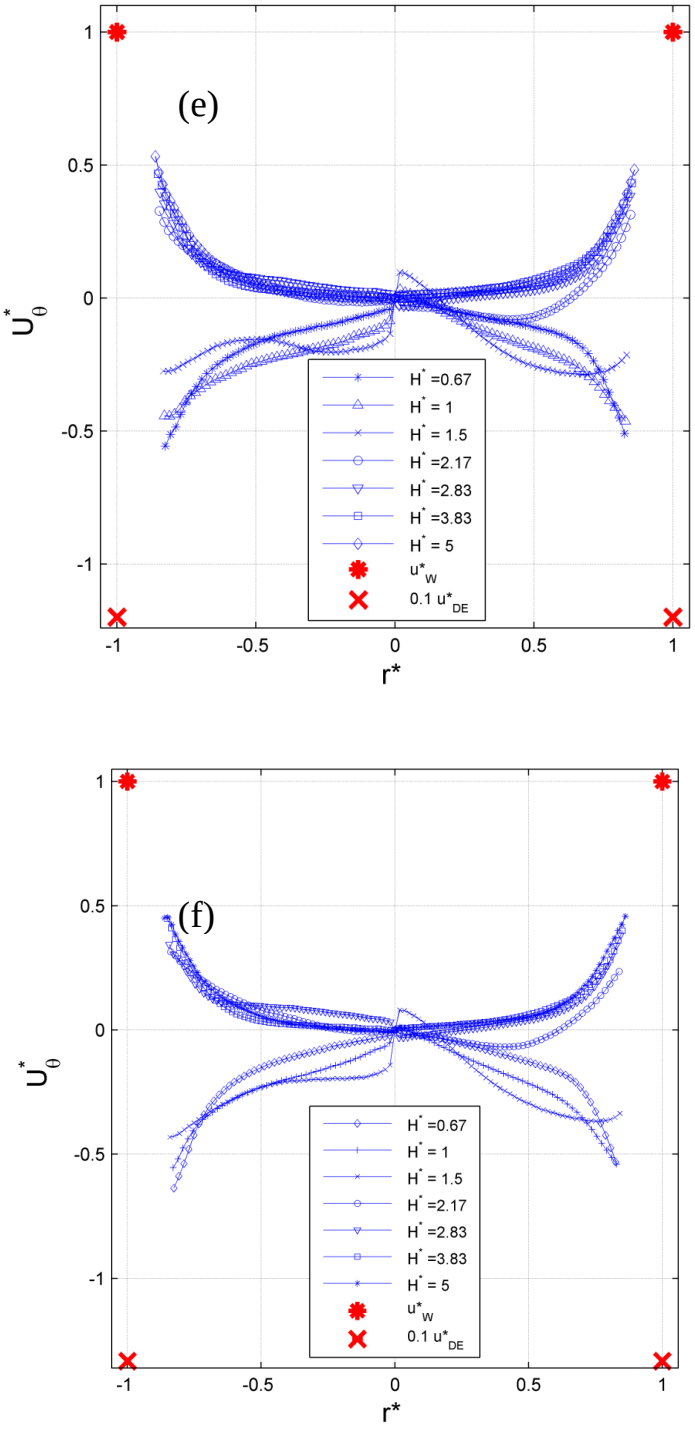

Figure 6.1 $\left\langle u_\theta^* \right\rangle$-profiles in all measured heights for one Co-Rotating Flow case when the wall spinning rate is $\Omega_W^* = 1.5$ and the disk is spinning at rate of (a)$\Omega_D^* = -1$, (b)$\Omega_D^* = -1.2$, (c)$\Omega_D^* = -1.4$, (d)$\Omega_D^* = -1.6$, (e)$\Omega_D^* = -1.8$ and (f)$\Omega_D^* = -2$

In order to take a closer look at the flow and have a better understanding of the three lower, upper and transitional domains, one of these disk spin rate, $\Omega_D^* = -1.6$, is selected and presented in Figure 6.2. In the upper domain ($z^* = 2.83 - 5.0$), as shown in this figure, the velocity vectors are overall in the counter-clockwise direction, indicating that the flows are mainly driven by the counter-clockwise rotating cylinder wall and thus the $\langle u_\theta^* \rangle$-profiles are basically positive in the cross-sections. However, compared to the nearly linear velocity profiles in the cylinder-baseline-flow shown in Figures 5-3 and 5-6, the $\langle u_\theta^* \rangle$-profiles are flat and the $\langle u_\theta^* \rangle$-magnitudes are small in the inner region ($-0.5 < r^* < 0.5$), which mimic the so-called "hollow vortex" structure of the GRS [97-98 and 52]. The extended inner region with the low velocity in the upper domain can be clearly seen in Figure 6.2. This means that the effect of the counter-rotating disk is still appreciable there. Interestingly, subtle zero-crossing points in $\langle u_\theta^* \rangle$ appear near the center at $z^* = 2.83$ and $z^* = 3.83$, indicating the tendency of the clockwise rotation there. This resembles the cyclonic (clockwise) rotation motion near the center of the GRS [67]. In contrast to the upper domain, in the lower domain ($z^* = 0.67 - 1.0$), the velocity vectors are in the clockwise direction, indicating the dominant influence by the counter-rotating (clockwise) disk .

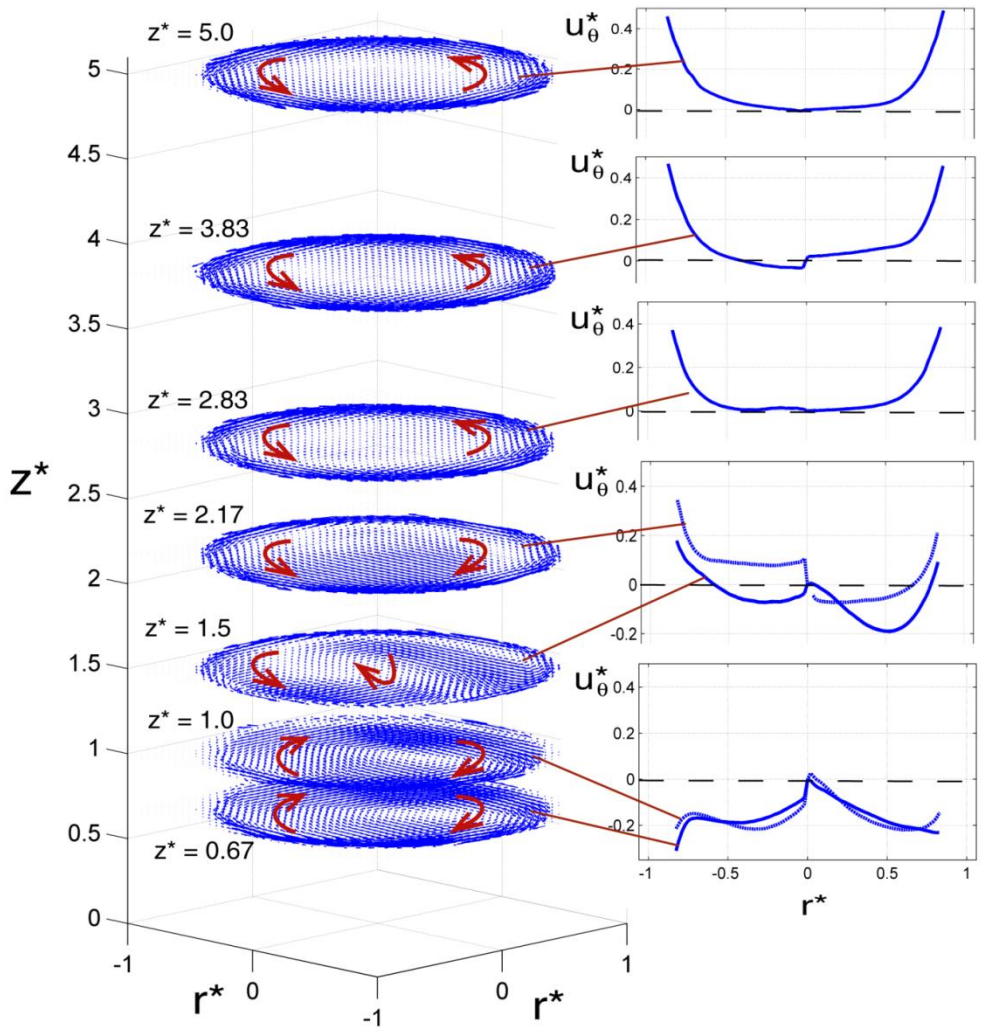

Figure 6.2 Velocity vector fields and normalized azimuthal velocity profiles at $\Omega_w^* = 1.5$ and $\Omega_d^* = -1.6$ in the counter-rotating-cylinder-disk-flow without disk heating.

Similar to previous averaged turbulent kinetic, k^*-profiles, these curves are demonstrated for the Counter-Rotating flow in figure 6.3. Typically, at lower heights k^* is higher and vice versa. However, there are cases that do not follow this order. These exceptional cases happen in transition domain. For example, in figures 6.2-c two curves of $z^* = 1$ and $z^* = 1.5$ do not follow the order that other ones do. These two heights are the ones that have asymmetric, odd shape in figure 6-1-c. This fact can also be observed in other sections of this figure. To provide more evidence for tis fact, Figure 6.3-g is shown in which the profiles of the normalized turbulent

kinetic energy (k^*) in the upper, transitional and lower domains at $\Omega_w^* = 1.5$ and $\Omega_d^* = -1.6$ are demonstrated. In the transitional domain, the k^*-profile is relatively flat, and the averaged magnitude of $k^* \approx 0.07$ is much higher than those in the upper and lower domains, which is generated by the stronger 3D mixing layer there. The k^*-profile in the upper domain has a flatter distribution with a smaller magnitude, which is similar to those in the BF I and BF II. In contrast, the k^*-profile in the lower domain has the higher values near the disk edges, which is similar to that in the BF II in Figure 5.4-d. It is noted that k^* was evaluated based on the two velocity components in a cross-section since the component of velocity normal to the cross-section was not measured. The value of k_V^* in the vertical plane is smaller than the value of k^* in the cross-section. Also, unlike the k^*-profiles, the curves for the three domains k_V^* are not very different.

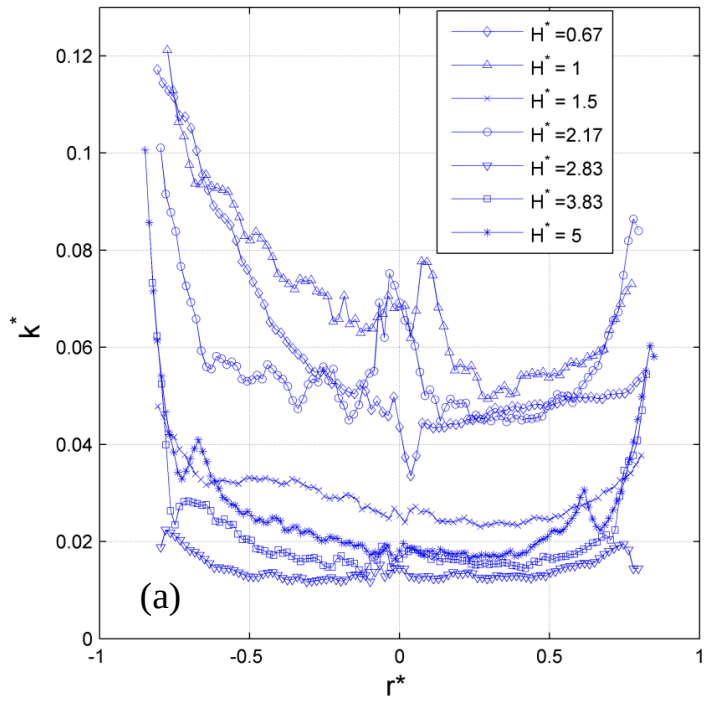
H* =0.67
H* = 1
H* = 1.5
H* =2.17
H* =2.83
H* =3.83
H* = 5
(a)
k*
r*
0.12
0.1
0.08
0.06
0.04
0.02
0
-1
-0.5
0
0.5
1

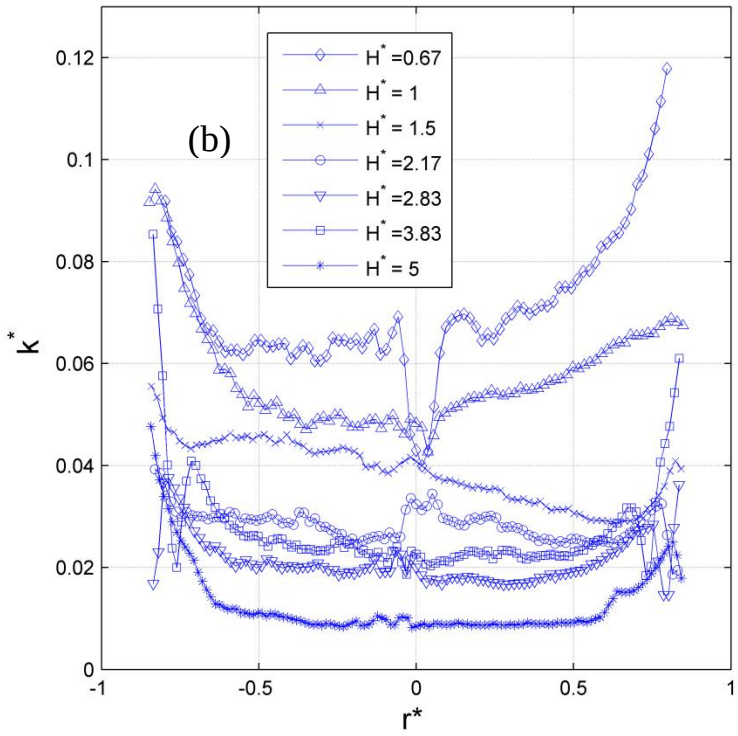
H* =0.67
H* = 1
H* = 1.5
H* =2.17
H* =2.83
H* =3.83
H* = 5
(b)
k*
r*
0.12
0.1
0.08
0.06
0.04
0.02
0
-1
-0.5
0
0.5
1

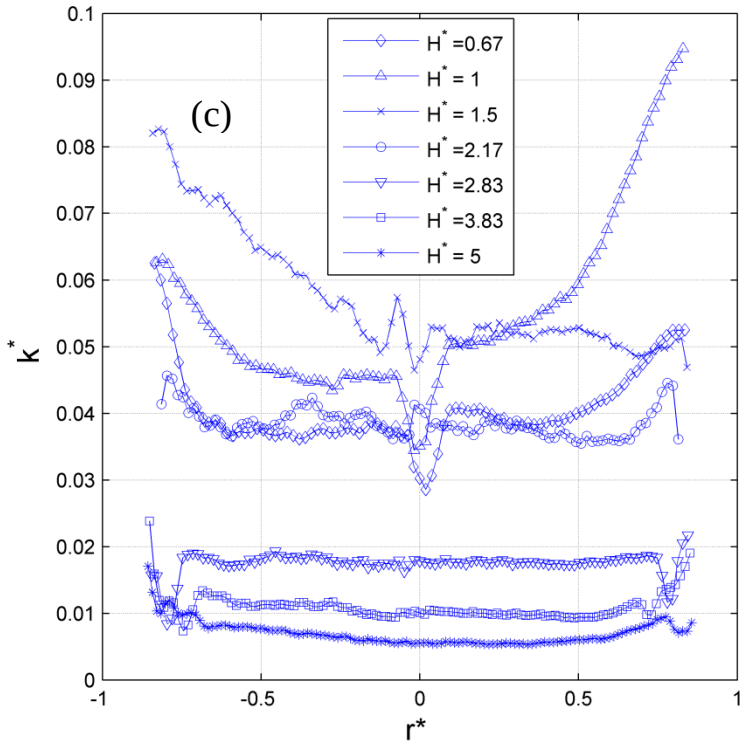
(c)
H* =0.67
H* = 1
H* = 1.5
H* =2.17
H* =2.83
H* =3.83
H* = 5
k*
r*
0.1
0.09
0.08
0.07
0.06
0.05
0.04
0.03
0.02
0.01
0
-1
-0.5
0
0.5
1

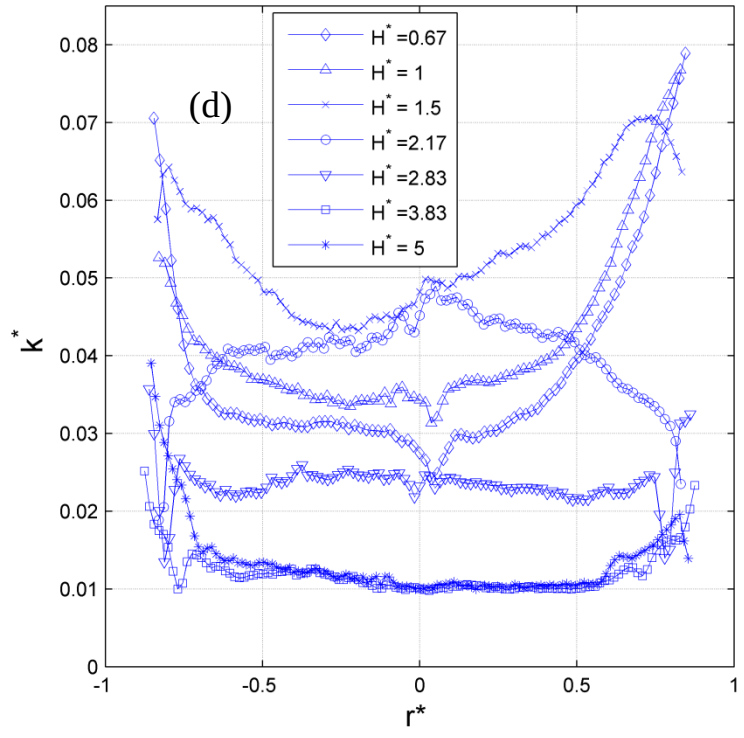
(d)
H* =0.67
H* = 1
H* = 1.5
H* =2.17
H* =2.83
H* =3.83
H* = 5
k*
r*
0.08
0.07
0.06
0.05
0.04
0.03
0.02
0.01
0
-1
-0.5
0
0.5
1

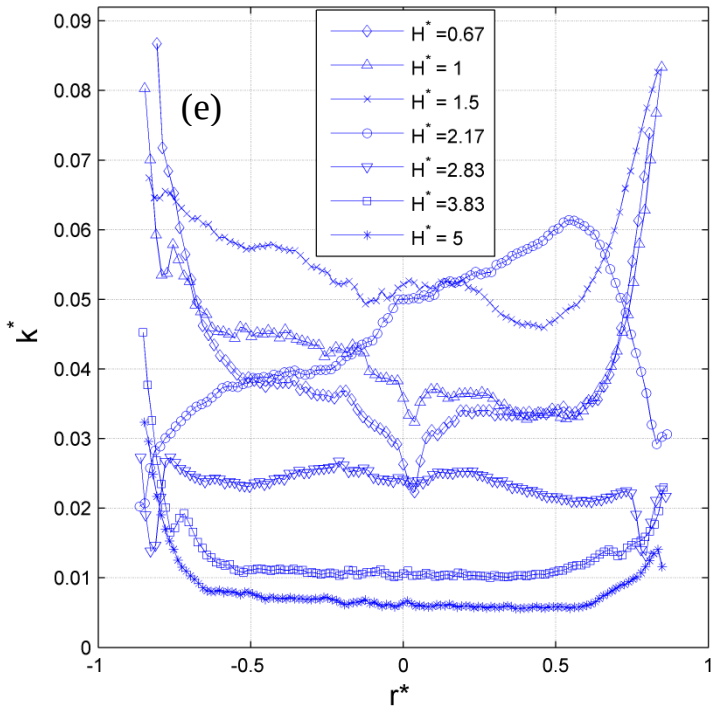
(e)
H* =0.67
H* = 1
H* = 1.5
H* =2.17
H* =2.83
H* =3.83
H* = 5
k*
r*
0.09
0.08
0.07
0.06
0.05
0.04
0.03
0.02
0.01
0
-1
-0.5
0
0.5
1

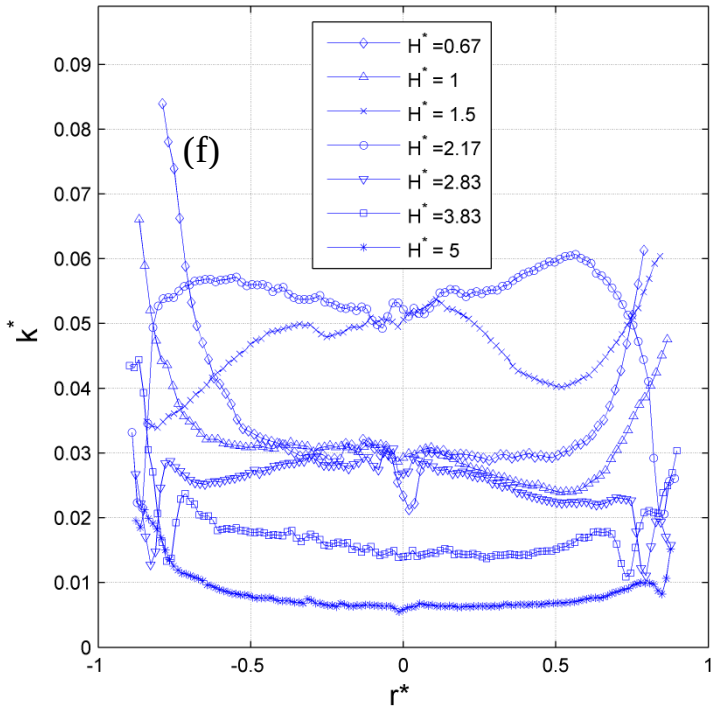
(f)
H* =0.67
H* = 1
H* = 1.5
H* =2.17
H* =2.83
H* =3.83
H* = 5
k*
r*
0.09
0.08
0.07
0.06
0.05
0.04
0.03
0.02
0.01
0
-1
-0.5
0
0.5
1

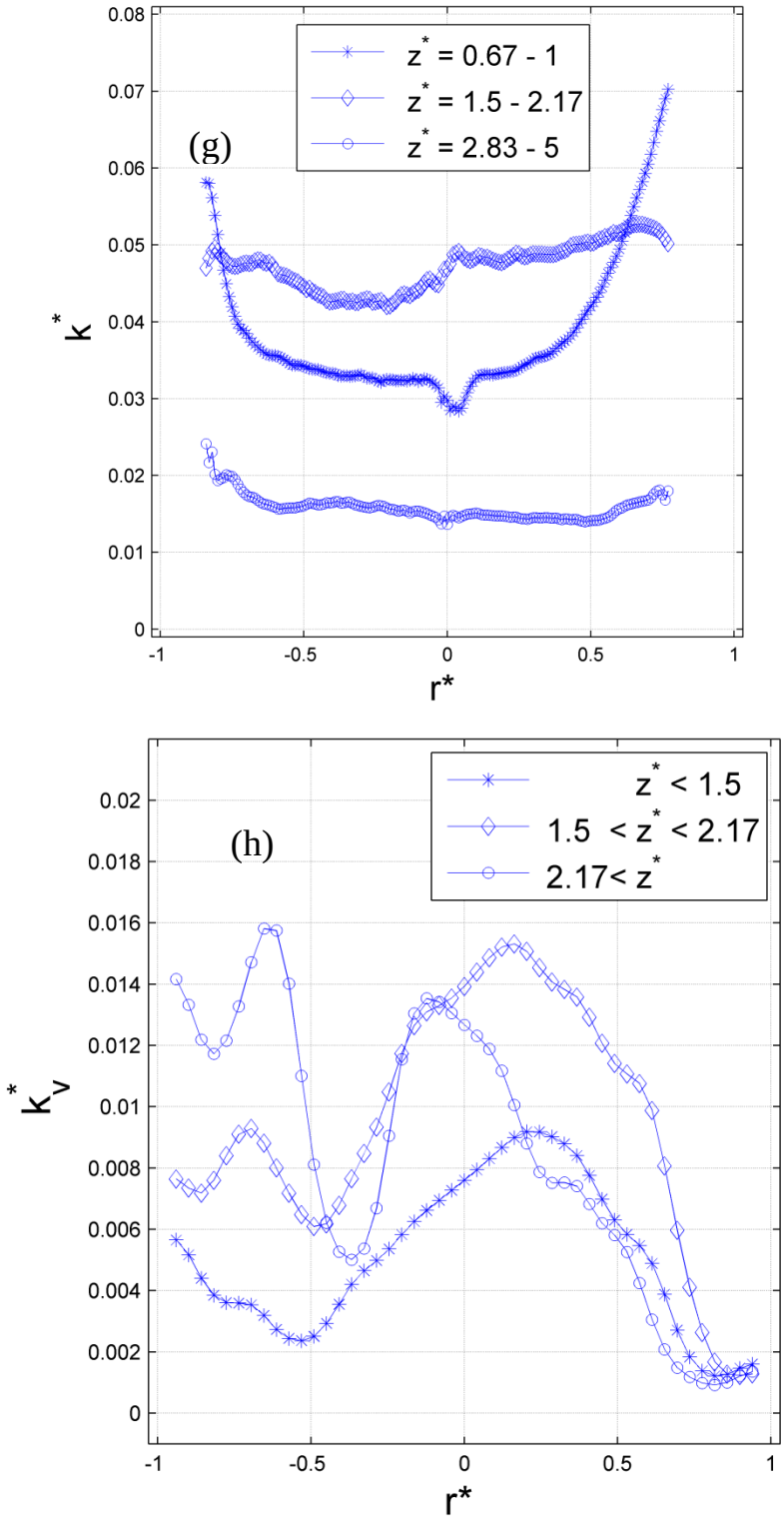

Figure 6.3 Normalized turbulent kinetic energy in all measured heights for Counter-Rotating Flow case when $\Omega_w^* = 1.5$ (a) $\Omega_D^* = -1$, (b) $\Omega_D^* = -1.2$, (c) $\Omega_D^* = -1.4$, (d) $\Omega_D^* = -1.6$, (e) $\Omega_D^* = -1.8$, (f) $\Omega_D^* = -2$ and (g) the volumetric average of k^* in three domains for $\Omega_D^* = -1.6$ and (h) k_V^* in vertical plane

As it is shown in the next section, k^* in un-heated cases is significantly lower than the heated ones. Therefore, the impact of noise and measurement errors in the results is more obvious in the un-heated cases and the curves are remarkably smoother.

Figure 6.4 shows the averaged velocity vector field and magnitude field for the Counter-Rotating cases in different heights when the wall spin rate is $\Omega_w^* = 1.5$ and disk spin rate is $\Omega_D^* = -1$. Closer look at the vector field shows that at $z^* = 0.67$ flow is not axisymmetric anymore and the sign of vorticity varies in the domain. As explained before, this is the transitional domain that the disk and the wall have similar impact on the flow and there is not an exact direction for the rotation of flow. The velocity magnitude/vector field is separately shown in figure 6-5. Although the outer ring follows the spin direction of wall, the inner is not completely following that direction which is the reason that the corresponding curve in figure 6.1-a ($z^* = 0.67$) looks differently and has the asymmetric shape (for this curve gradient of u_θ^* at $r^* = 0$ is larger than anywhere else) that was described previously. Another feature of this height that distinguishes it from other heights is the larger magnitude of velocity in the inner region. The area in which velocity magnitude is approximately $0.15 < |u^*| < 0.3$ is much larger than the same area in other heights. Unlike inner region, velocity magnitude of the outer ring is relatively smaller in this height. In other words, comparing the outer ring that has the maximum velocity in both figures 6-5-a and b shows that this value is significantly smaller at $z^* = 0.67$ due to being closer to the counter rotating effect source.

An easy, visual way to address the location of the vortex center is using the 12 clock numbers from the top view. For example, in figure 6-4 this center is located at 7 O'clock. This is how the position of center will be addressed from this point on. The fact that this center is not at the geometric center clearly proves that flow has a strong axisymmetric behavior in this height.

At $z^* = 2.83$ finding the center of vortex that locates at 11 O'clock is not as easy as it is at $H^* = 0.67$ since the velocity magnitude has smaller values in the inner region.

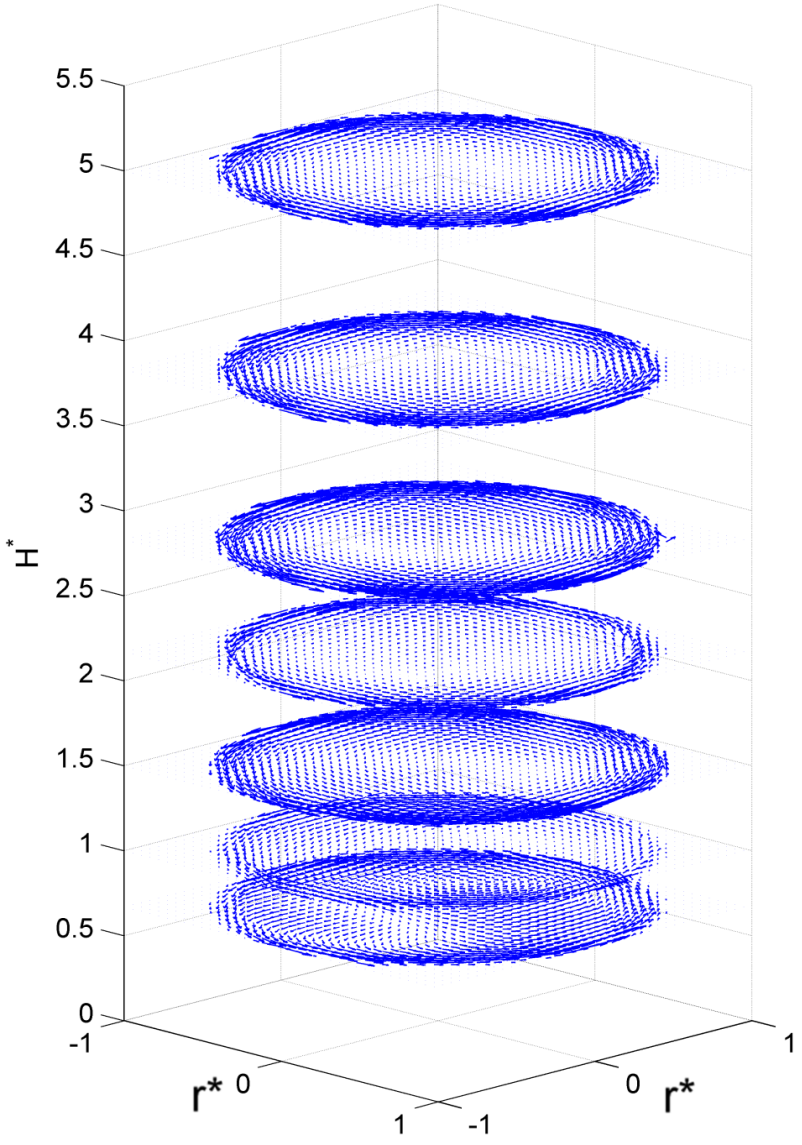

Figure 6.4 Velocity vector field for all studied heights for one Counter-Rotating flow case: With wall spin rate $\Omega_w^* = 1.5$ and disk spin rate $\Omega_d^* = -1$

An easy, visual way to address the location of the vortex center is using the 12 clock numbers from the top view. For example, in figure 6.5 this center is located at 7 O'clock. This is how the position of center will be addressed from this point on. The fact that this center is not at

the geometric center clearly proves that flow has a strong axisymmetric behavior in this height. At $z^* = 2.83$ finding the center of vortex that locates at 11 O'clock is not as easy as it is at $z^* = 0.67$ since the velocity magnitude has smaller values in the inner region.

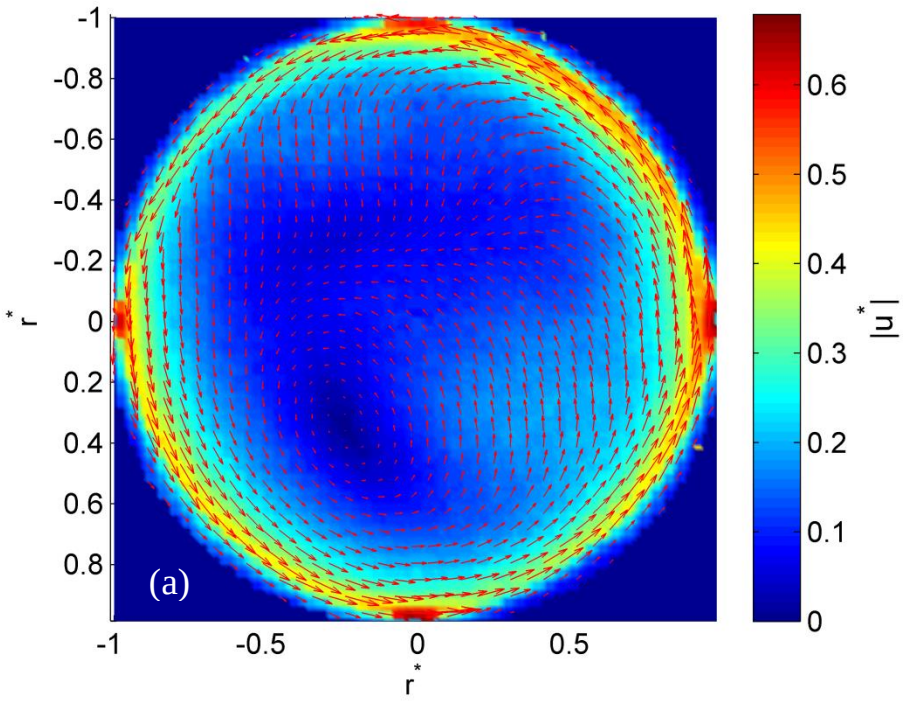

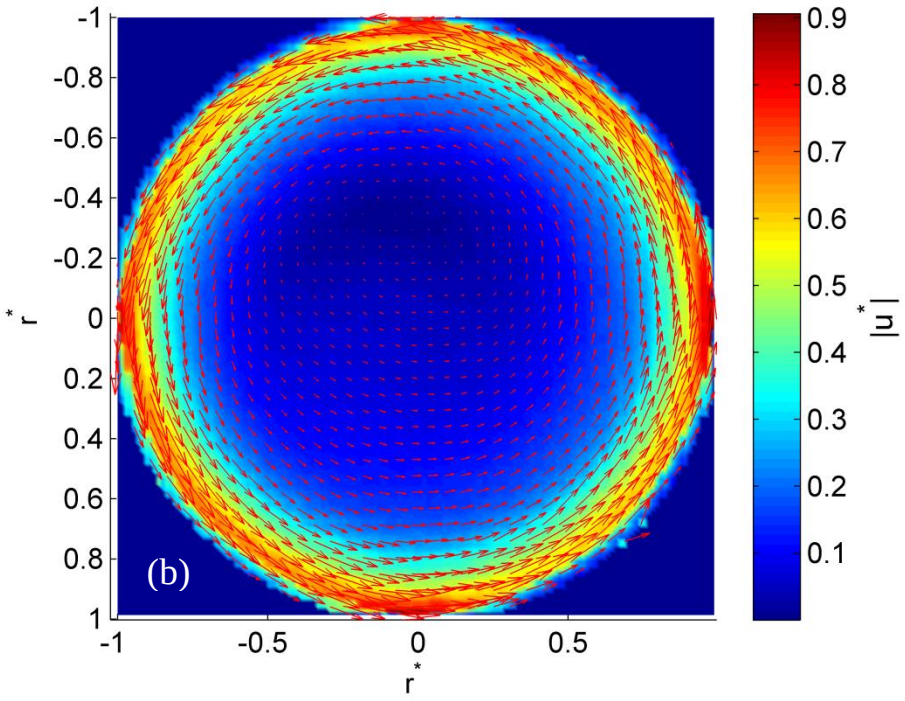

Figure 6.5 The velocity vector and magnitude field for the Counter-Rotating Flow: $\Omega_w^* = 1.5$, $\Omega_D^* = -1$ when (a): $z^* = 0.67$ and (b): $z^* = 2.83$

The difference between the flow structures in various heights can be illustrated more clearly in the figure 6.6-a and b that shows the azimuthal velocity component along 4 sections as well as the $\langle u_\theta^* \rangle$-profile similar to figure 6-2. This figure only intends to demonstrate the inner region and covers lower values of u_θ^*. Therefore, the red asterisk that was presenting the wall velocity is not shown in this figure. Generally, this velocity component is the dominant one. However, in the heights that flow is not completely following either of disk and wall, azimuthal velocity component is not necessarily much larger than the radial one. Clearly, the difference between the four sections and the average curve in figure 6.6-a is larger than that in figure b.

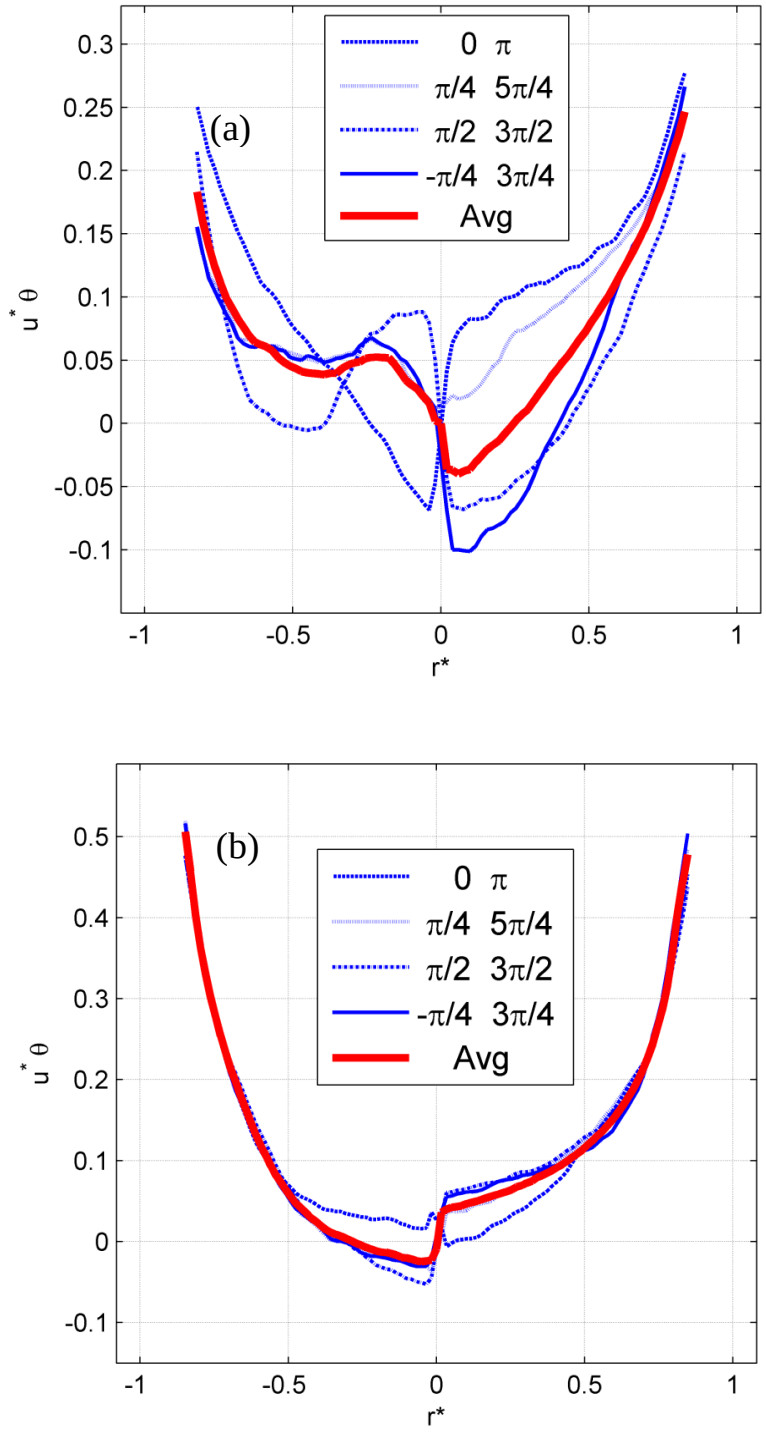

Figure 6.6 Normalized azimuthal velocity profile averaged over the half-circle-sectors and selected profiles across four radial sections for the Counter-Rotating flow when: $\Omega_w^* = 1.5$, $\Omega_D^* = -1$ when (a): $z^* = 0.67$ and (b): $z^* = 2.83$

For the next disk spin rate, $\Omega_d^* = -1.2$, all heights are shown in figure 6.7-a similar to $\Omega_d^* = -1$. In addition, in order to show more detail, three lower heights are also separately presented in figure b. As mentioned in previous figure at $z^* = 0.67$ flow is rotating clock-wise and following the disk rotation (lower domain). At $z^* = 1$, however , flow does not have a clear spinning direction (transitional domain). Interestingly, there are two weak counter rotating vortices right next to each other. At $z^* = 1.5$ and above, flow is following the wall (upper domain). The figure shows that in higher heights flow behavior is similar to the previous disk spin rate. Nonetheless, this behavior changes significantly in lower heights as the disk spin rate increases and transitional domain ascends.

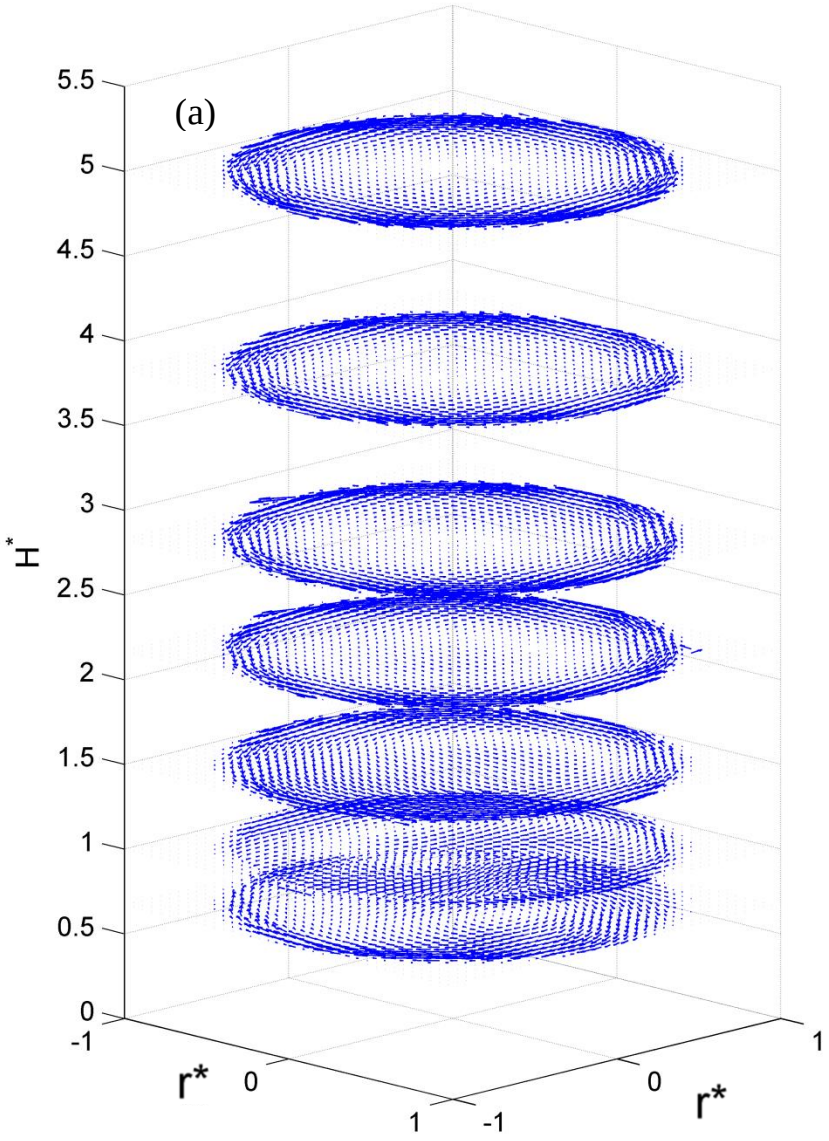
(a)
5.5
5
4.5
4
3.5
3
2.5
2
1.5
1
0.5
0
H*
-1
0
1
r*
-1
0
1
r*

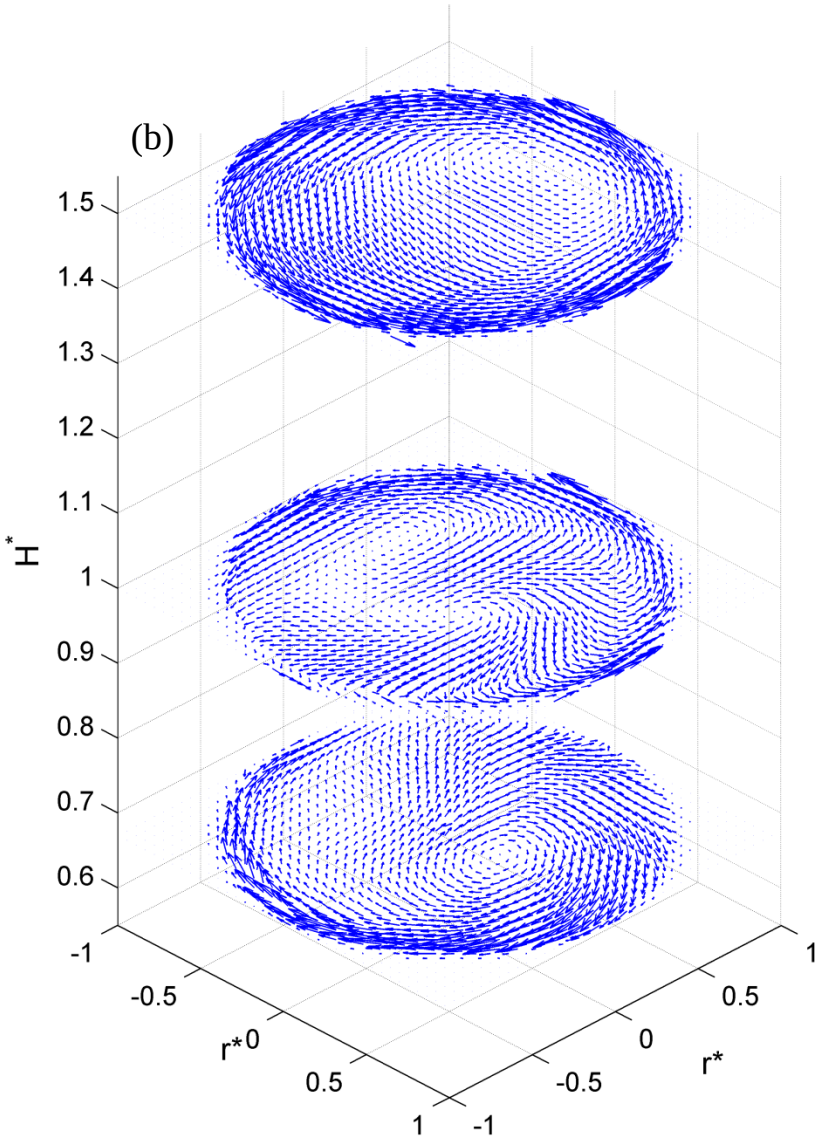

Figure 6.7 Velocity vector field for (a) all studied heights and (b) three lowest measured heights for one Counter-Rotating flow case: with the wall spin rate $\Omega_w^* = 1.5$ and the disk spin rate $\Omega_d^* = -1.2$

The particular height of $z^* = 1$ seems interesting enough to be presented separately in figure 6.8 due to presence of transitional domain. In this figure the velocity vector/magnitude field illustrates the two vortices in the inner region. Unlike the higher heights, the outer ring has a much lower velocity magnitude and does not follow any direction completely. Also, in the inner region the area with mid-velocity magnitude is remarkably larger than other heights.

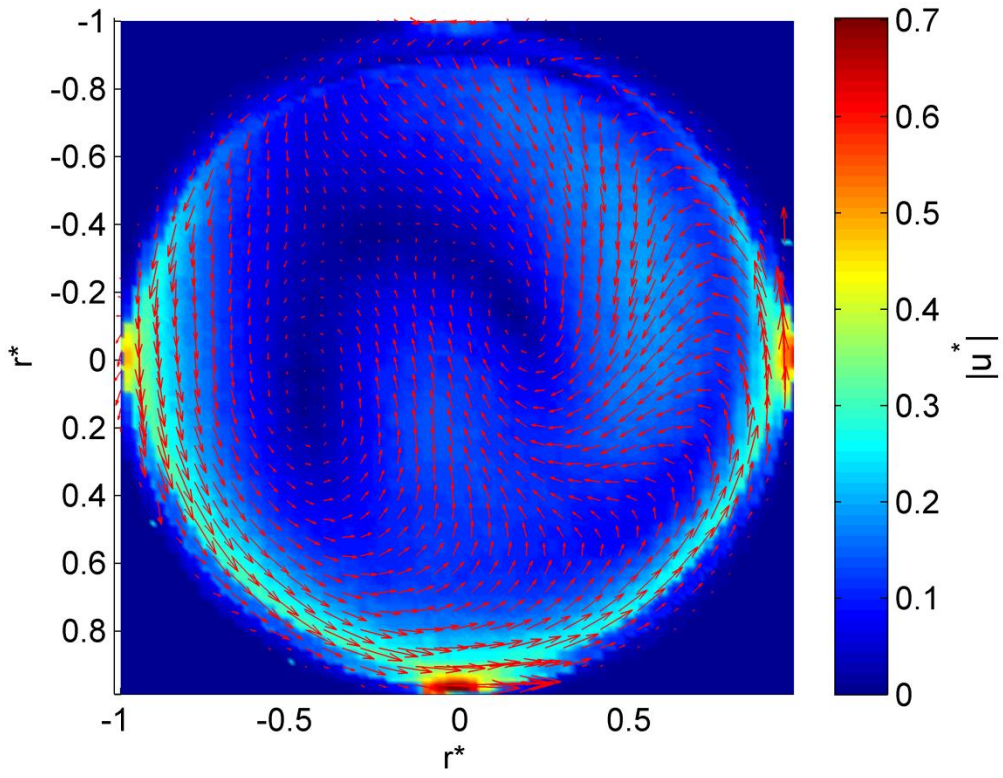

Figure 6.8 The velocity vector and magnitude field for the Counter-Rotating flow: $\Omega_w^* = 1.5$, $\Omega_d^* = -1.2$ when:

$$z^* = 1$$

Azimuthal component of the velocity profiles for these two heights are presented for several section in figure 6.9-a and b. Clearly, at $z^* = 1$ flow demonstrates much more symmetric behavior and curves corresponding to different sections look more similar. On the contrary, at $z^* = 0.67$ curves in each section have a different shape due to axisymmetric pattern of the flow. The two thicker curves are averages of 90 sections that previously were also presented in figure 6.1-b.

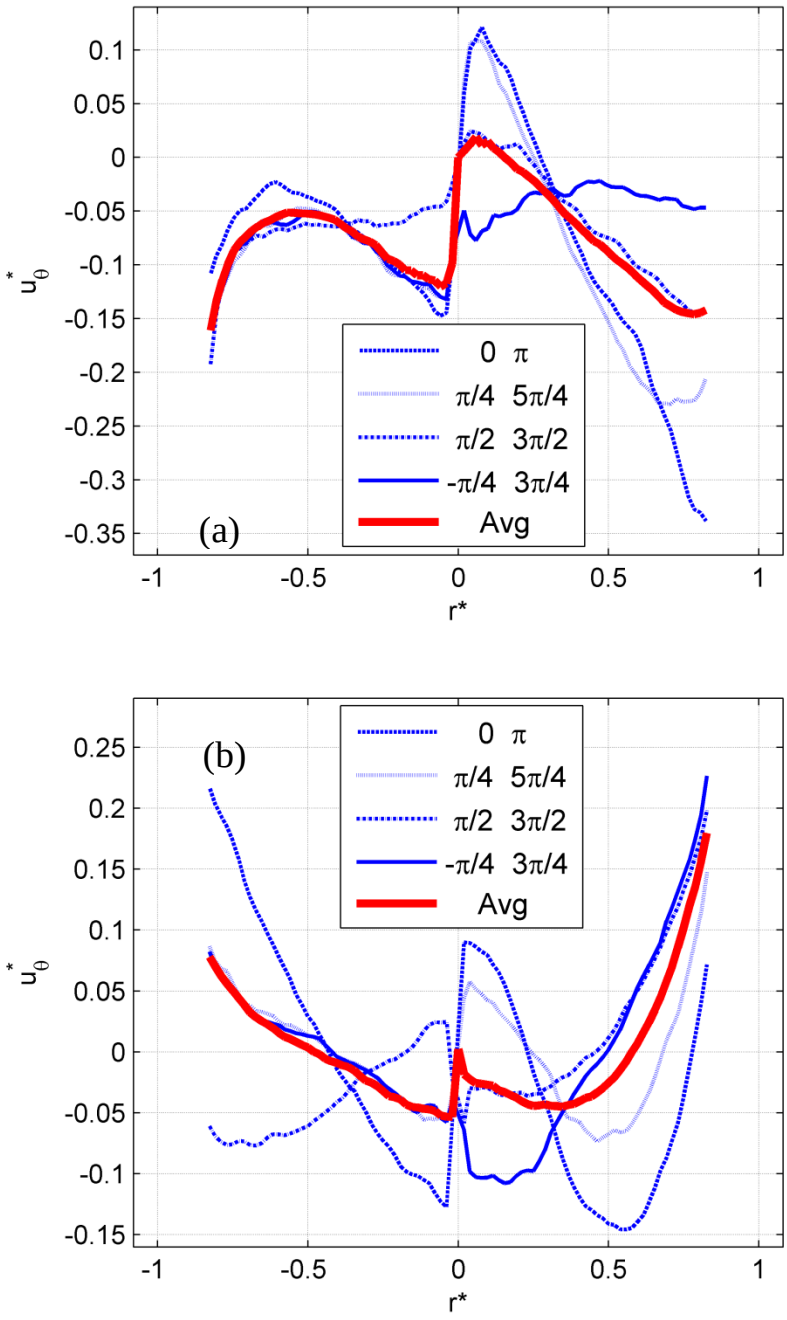

Figure 6.9 Normalized azimuthal velocity profile averaged over the half-circle-sectors and selected profiles across four radial sections for the Counter-Rotating flow when: $\Omega_w^* = 1.5$, $\Omega_d^* = -1.2$ when (a): $z^* = 0.67$ and (b): $z^* = 1$

The next disk spin rate is $\Omega_d^* = -1.4$ and similar to other two ones, velocity vector fields are presented in figure 6.10. Since disk spin rate has increased, as expected, transitional domain has moved upward. For instance, at $z^* = 0.67$ the clock-wise rotating is much stronger than the

case that the disk spin rate is $\Omega_d^* = -1.2$ and this height is now completely in the lower domain. In this height a strong vortex is following the disk rotation and even at one higher height at $z^* = 1$ this vortex still exists. At the third height, $z^* = 1.5$ though, that clock-wise vortex vanishes and direction of flow rotation changes and becomes counter-clock-wise and follows the wall and the upper domain begins. It seems that this transition has happened somewhere between $z^* = 1$ and $z^* = 1.5$. Therefore, it is expected that the transition height ascends in the next disk spin rate, $\Omega_d^* = -1.6$, coming closer to $H^* = 1.5$.

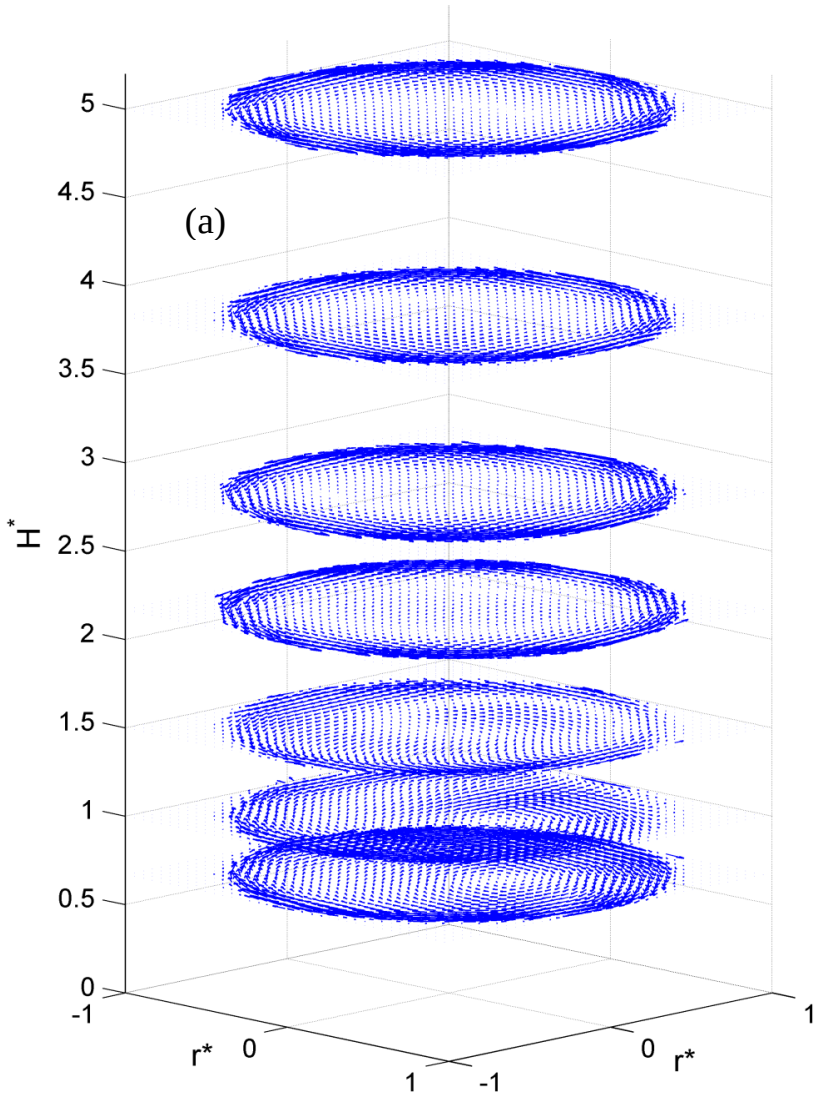

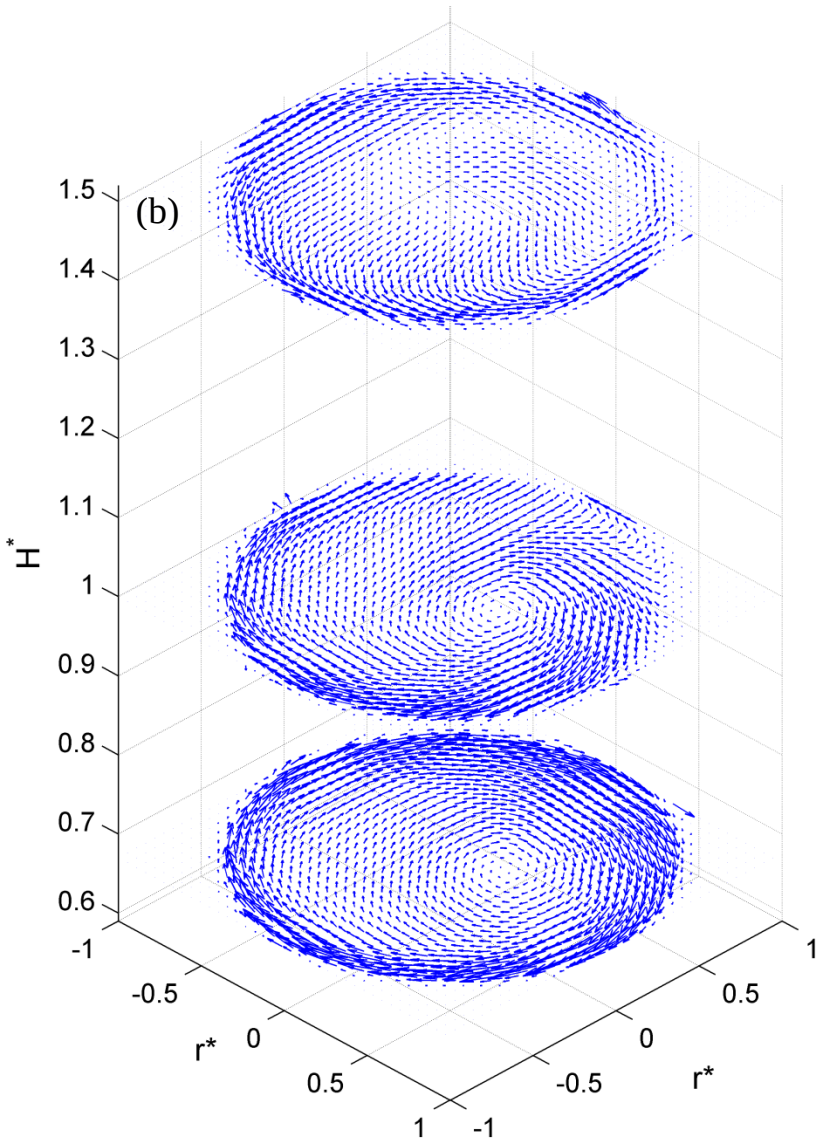

Figure 6.10 Velocity vector field for (a) all studied heights and (b) three lowest measured heights for one Counter-Rotating flow case: with the wall spin rate $\Omega_w^* = 1.5$ and the disk spin rate $\Omega_d^* = -1.4$

In order to show more detail of the flow, velocity vector/magnitude fields for the two heights that the transition occurs in between are shown in figure 6.11-a and b. Higher heights are not presented since the results are quite similar to figure 6.5-b.

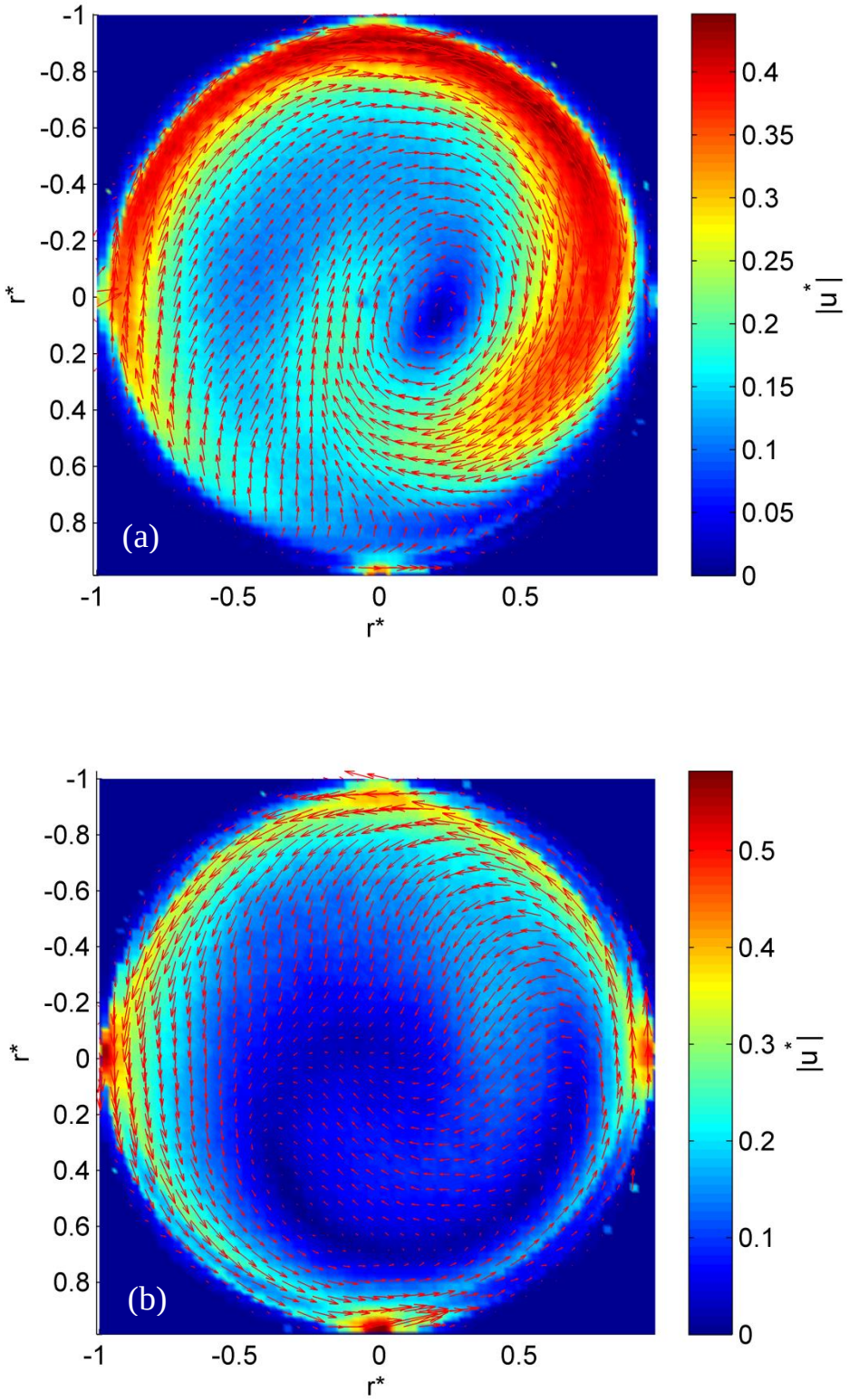

Figure 6.11 The velocity vector and magnitude field for the Counter-Rotating Flow: $\Omega_w^* = 1.5$, $\Omega_d^* = -1.4$ when (a): $z^* = 1$ and (b): $z^* = 1.5$

For the major part of the section in the figure 6.11-a, where $z^* = 1$, flow is clock-wise (lower domain) and there is a strong vortex center in the inner region. In figure b, however, the counter-clock-wise flow in the outer ring follows the wall-rotating direction (upper domain) and the inner region has smaller magnitude compared to figure a. The "horse show" shape of minimum magnitude in the latter is similar to previous disk spin rate in figure 6-8 but it is located in a different angle.

Figure 6.12-a and b demonstrate the azimuthal component of the velocity profiles for the two aforementioned heights. The negative value of the average curve shows the clock-wise rotation in figure a. Nonetheless, at some point positive values show that flow is not completely following the disk-rotating direction (beginning of the transitional domain). Also, the axisymmetric behavior of flow can be seen by the difference of the section curves and the average one. In figure b however, the values are mainly positive except for a small region that flow spins clock-wise. At $z^* = 1.5$, flow behaves more axi-symmetrically and section and average curves have less difference compared to figure a ($z^* = 1$,)

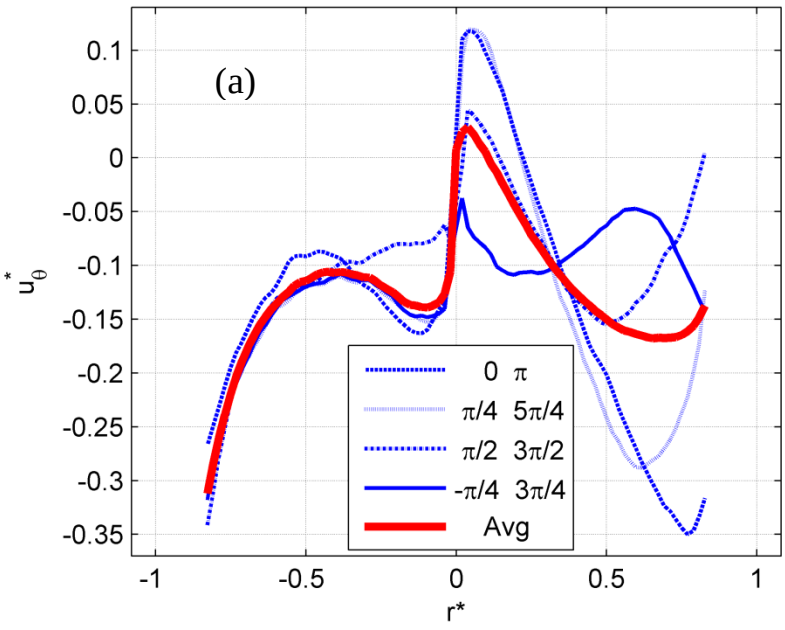

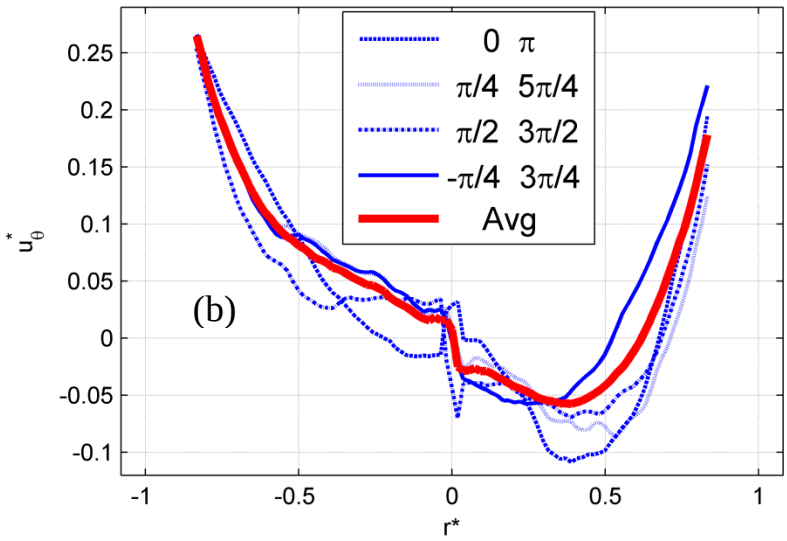

Figure 6.12 Normalized azimuthal velocity profile averaged over the half-circle-sectors and selected profiles across four radial sections for the Counter-Rotating flow when: $\Omega_w^* = 1.5$, $\Omega_d^* = -1.4$ when (a): $z^* = 1$ and (b): $z^* = 1.5$

The next disk spin rate is $\Omega_d^* = -1.6$ and velocity vector fields are presented in figure 6.13. As expected, in lower heights the clock-wise rotating effect is stronger in each height and in transitional domain this effect changes the flow behavior compared to $\Omega_d^* = -1$, $\Omega_d^* = -1.2$ and $\Omega_d^* = -1.4$. Two lower heights have stronger clock-wise vortices and at the third height from the bottom there are two interesting concentric opposite direction vortices: the inner one follows the disk and the outer one, even though not thoroughly, rotates counter-clock-wise. The velocity magnitude/vector field of this particular height is also separately shown in figure 6.13. There is also another relatively small vortex at 5 O'clock. At 12 O'clock the outer ring in a very small region does not follow the wall-rotating direction. The mid velocity region in the inner region is larger than other cases. Two horse shoe shapes of the low velocity region and the high velocity region are beautifully merged and formed an artistic velocity magnitude field.

For this particular disk spin rate measurements have been done for heated and unheated cases. Similar to the results for the BF I and BF II, vector field is presented in two figures: 6.14c

and d which show velocity vectors in $\left(z^*, r^*\right)$ superposed on the $\left|u_V^*\right|$-fields at $\Omega_w^* = 1.5$ and $\Omega_d^* = -1.6$ in the counter-rotating-cylinder-disk-flow without disk heating. The flow field in these two figures could be divided into the lower, transitional and upper domains. In the lower domain ($z^* = 0.67 - 1.0$), as shown in Figure c, the flow moves downward in the central region and the velocity is small near the lower corner of the cylinder. In contrast, in the upper domain ($z^* > 2.17$) in Figure d, the flow generally moves upward in the central region while the flow near the cylinder wall moves downward. Across the transitional domain ($z^* = 1.5 - 2.17$), the flow switches from the downward motion to upward motion in the central region.

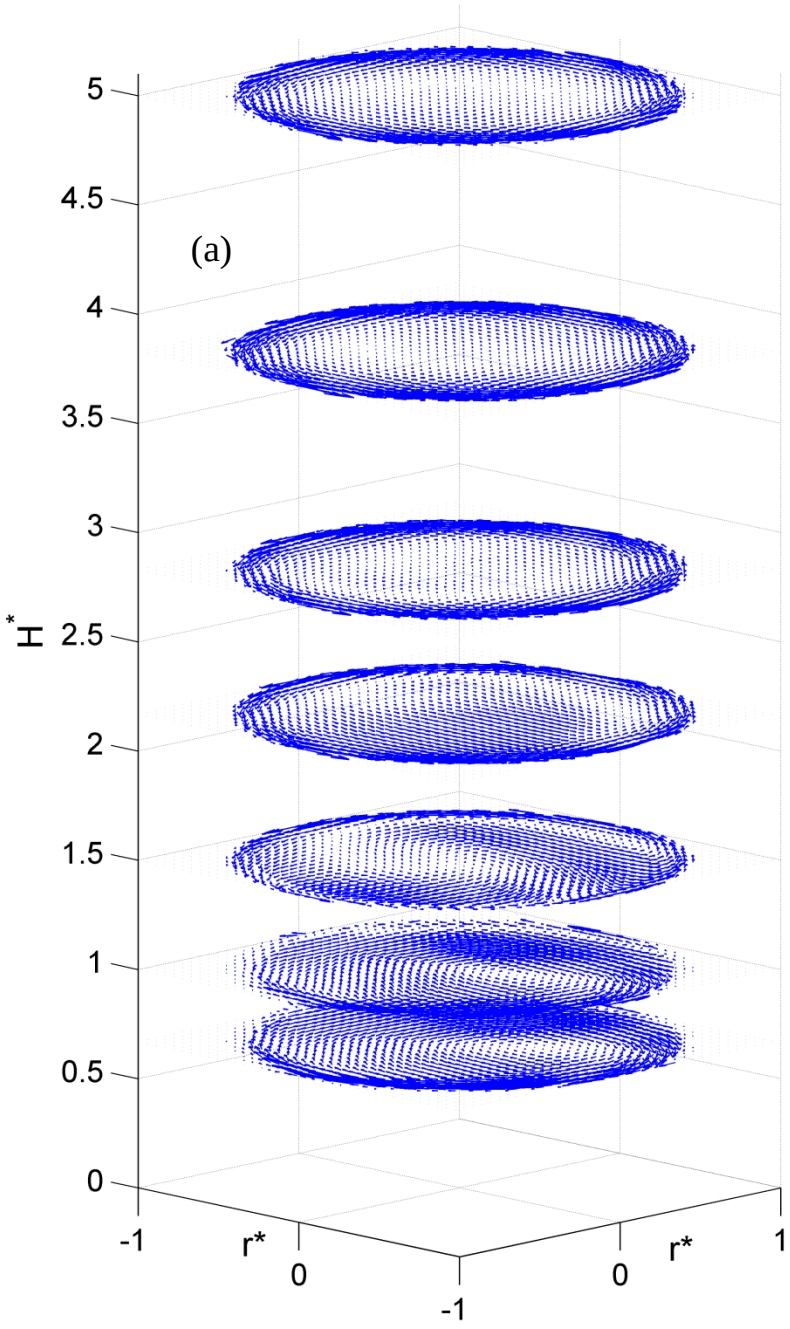
(a)
5
4.5
4
3.5
3
2.5
2
1.5
1
0.5
0
H*
-1
r*
0
-1
0
r*
1

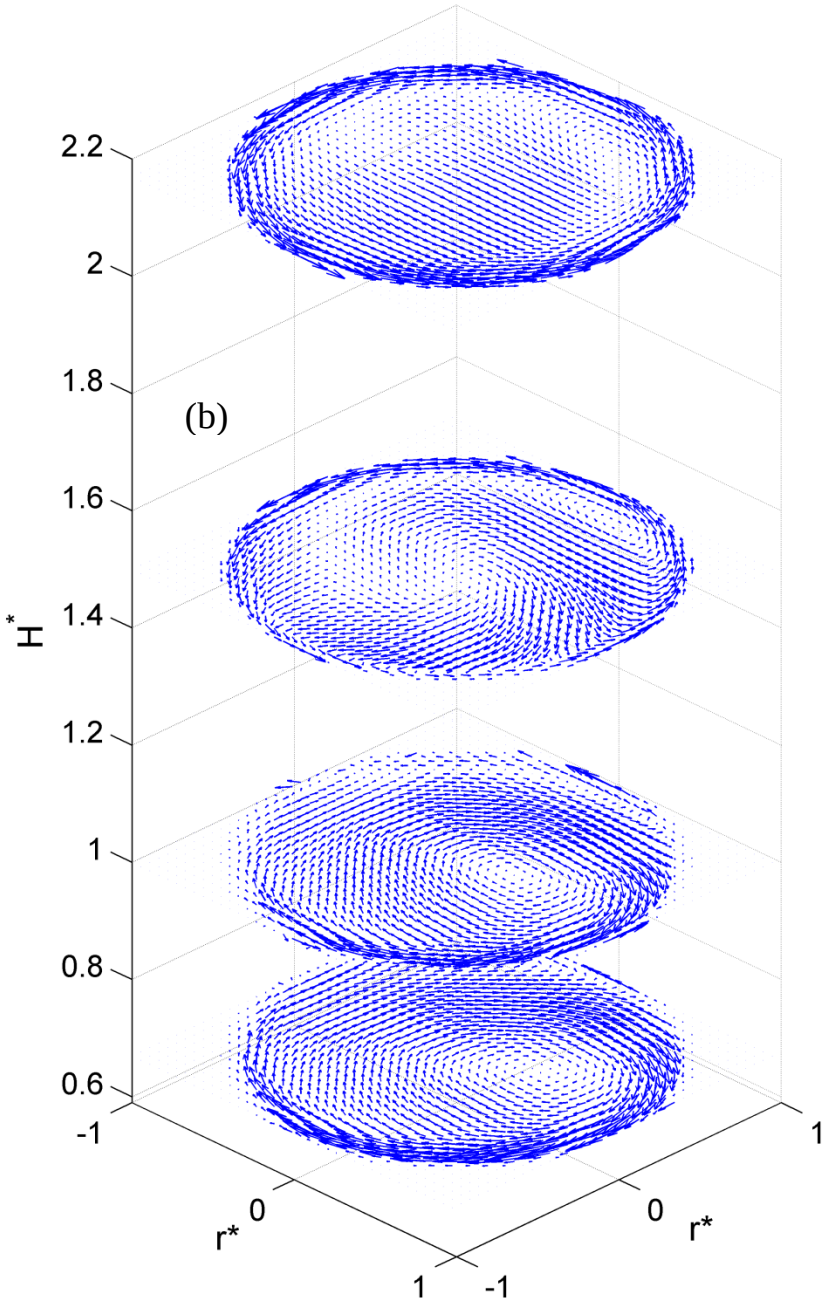

Figure 6.13 Velocity vector field for (a) all studied heights and (b) four lowest measured heights for one Counter-Rotating flow case: with the wall spin rate $\Omega_w^* = 1.5$ and the disk spin rate $\Omega_D^* = -1.6$

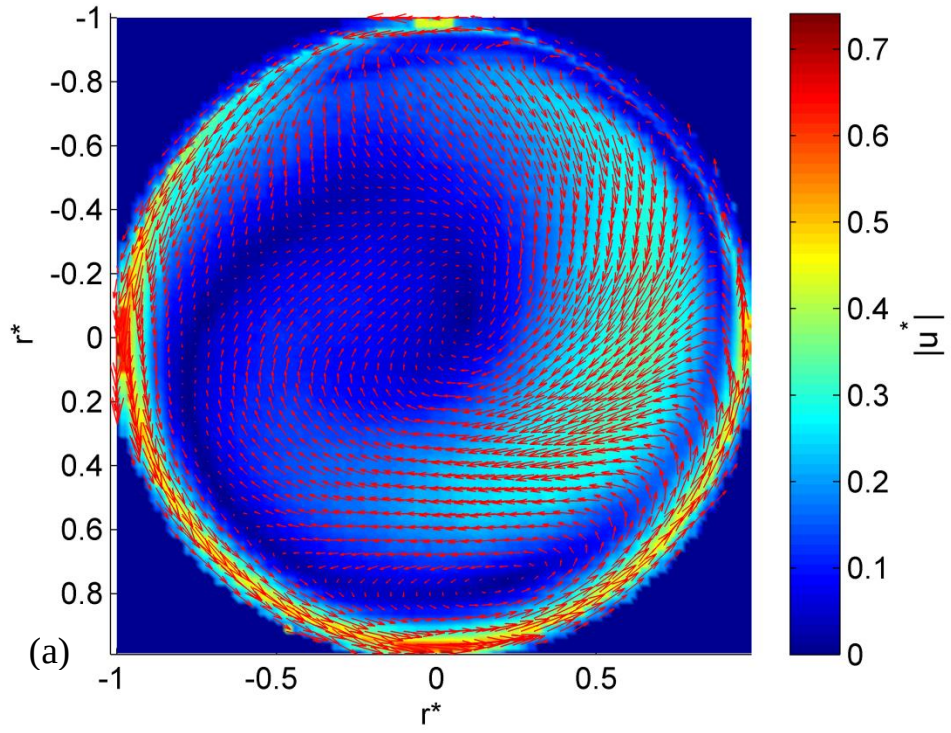
-1
-0.8
-0.6
-0.4
-0.2
0
0.2
0.4
0.6
0.8
r*
-1
-0.5
0
0.5
r*
0.7
0.6
0.5
0.4
0.3
0.2
0.1
0
|u*|

(a)

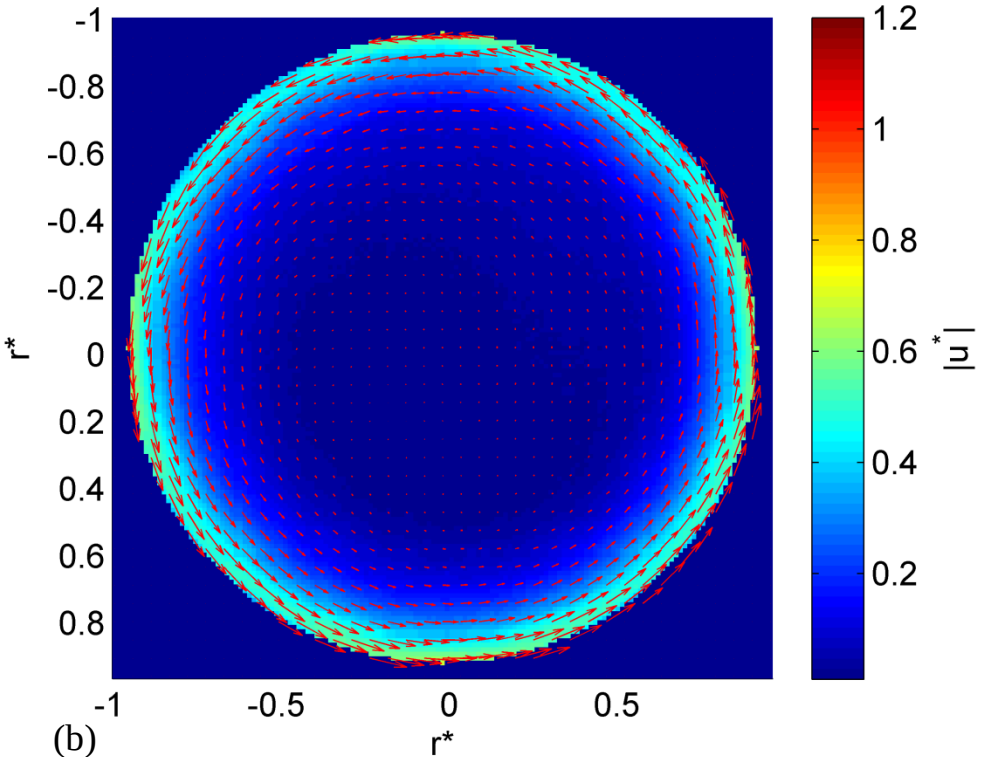
-1
-0.8
-0.6
-0.4
-0.2
0
0.2
0.4
0.6
0.8
r*
-1
-0.5
0
0.5
r*
1.2
1
0.8
0.6
0.4
0.2
|u*|

(b)

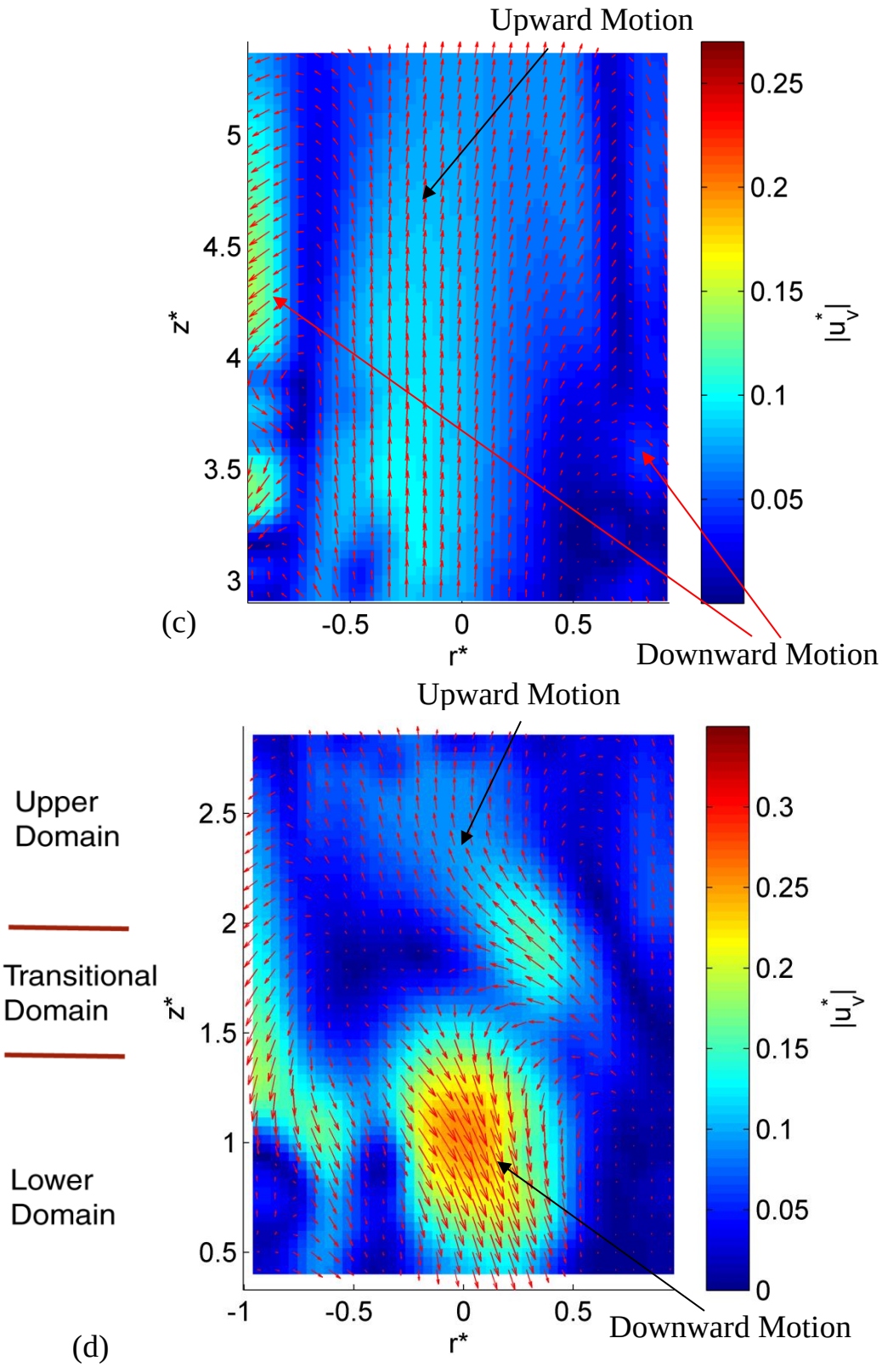

Figure 6.14 The velocity vector and magnitude field for the Counter-Rotating Flow: $\Omega_w^* = 1.5$, $\Omega_d^* = -1.6$ when

(a) $z^* = 1$ and (b) $z^* = 5$, and (c), (d): vertical planes

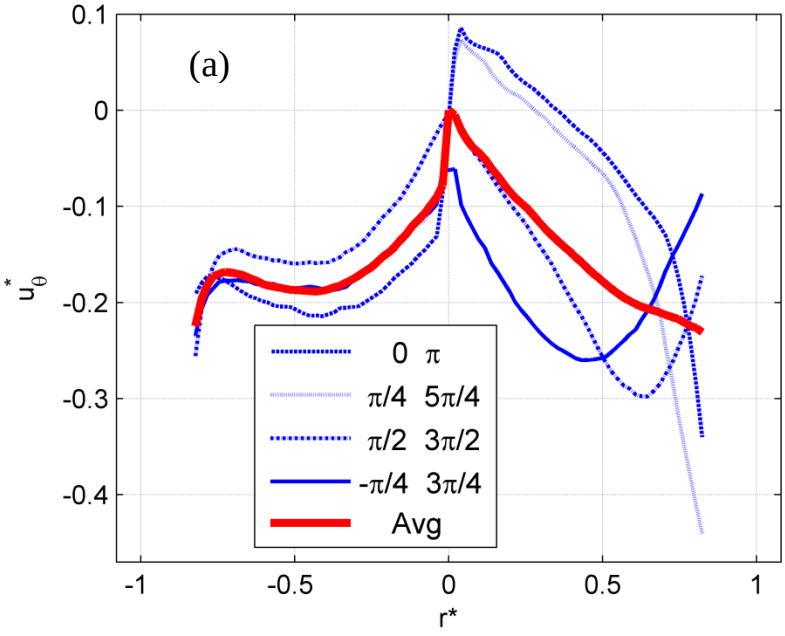
(a)
0.1
0
-0.1
-0.2
-0.3
-0.4
u_θ^*
-1
-0.5
0
0.5
1
r*
0 π
π/4 5π/4
π/2 3π/2
-π/4 3π/4
Avg

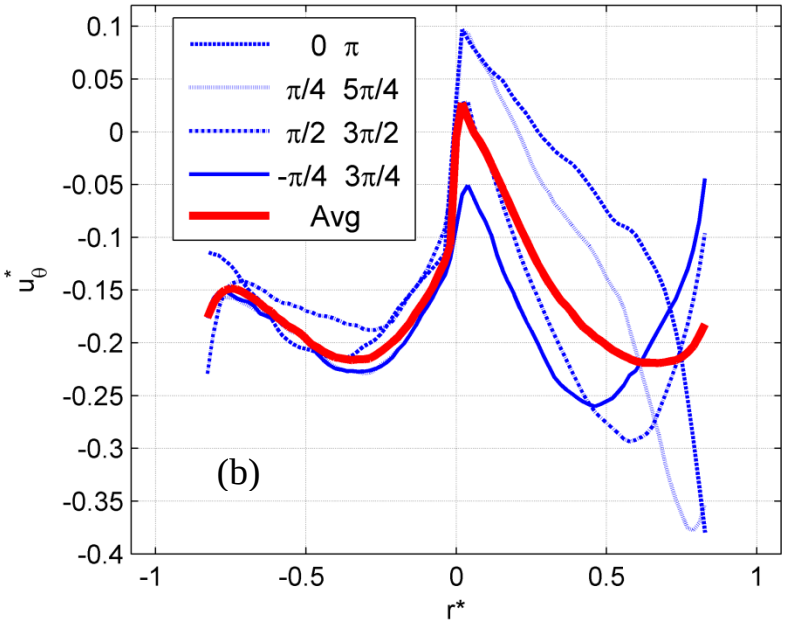
0.1
0.05
0
-0.05
-0.1
-0.15
-0.2
-0.25
-0.3
-0.35
-0.4
u_θ^*
-1
-0.5
0
0.5
1
r*
0 π
π/4 5π/4
π/2 3π/2
-π/4 3π/4
Avg
(b)

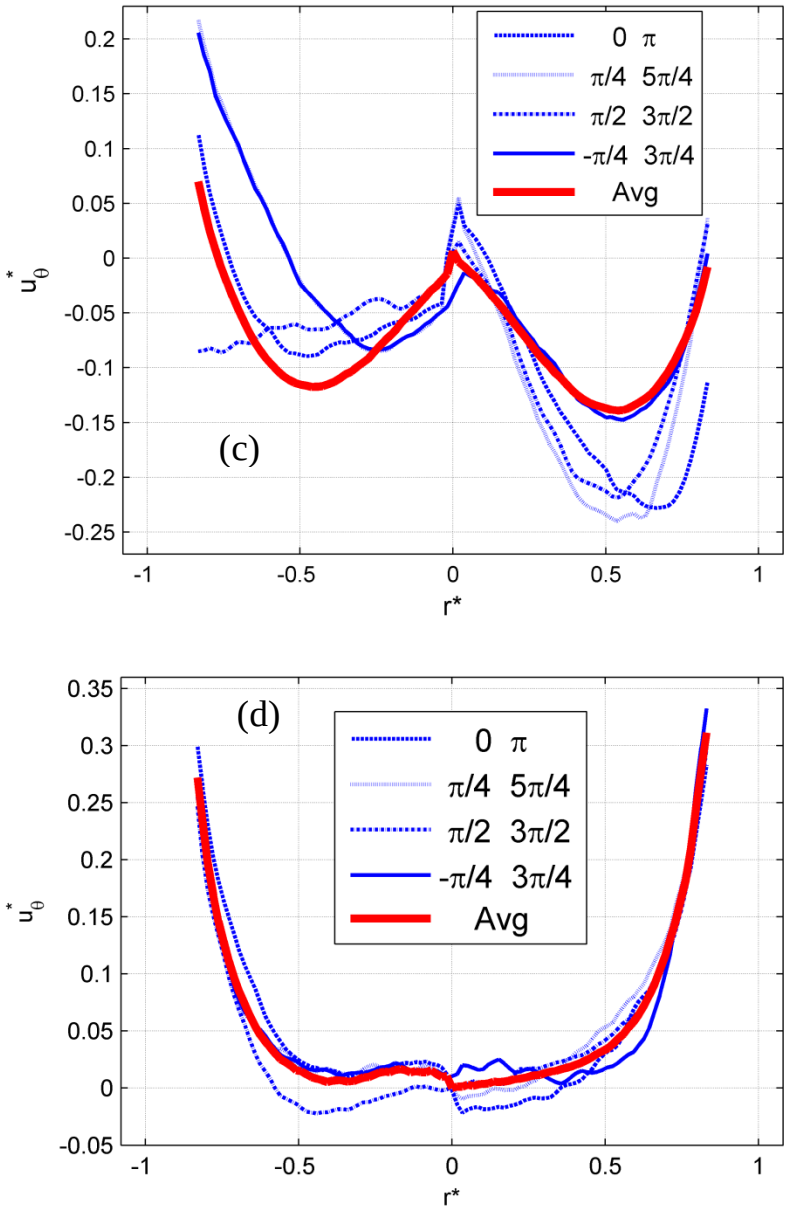

Figure 6.15 Normalized azimuthal velocity profile averaged over the half-circle-sectors and selected profiles across four radial sections for the Counter-Rotating flow when: $\Omega_w^* = 1.5$, $\Omega_d^* = -1.6$ when (a): $z^* = 0.67$, (b) $z^* = 1$, (c): $z^* = 1.5$ and (d): $z = 2.83$

Figure 6.15-a, b, c and d demonstrate the azimuthal component of the velocity profiles for the three lower heights as well as $z^* = 2.83$. Figures a and b are very similar with negative value for the most part which implies the clock-wise rotation (lower domain). In half of the plane

all section curves and the average curve are in good agreement while in the other half those curves are distinctly far from each other. However, in the figure c, in which the effect of wall on the flow become stronger (beginning of the transitional domain), the inner region has negative value and the outer region is positive. This confirms the existence of two concentric vortices that was seen previously.

The next disk spin rate is $\Omega_d^* = -1.8$ and velocity vector fields are presented in figures 6.16-a and b. Since all heights need to be discussed in this case, unlike the previous cases, seven studied heights are divided in two figures. This way the angle of view from the horizon that graphs are plotted with can be larger and more detail in figures can be demonstrated. In three lower heights flow is rotating clock-wise (lower domain) but in the third height there is a small region that rotates in the opposite direction (beginning of transitional domain). It can be visually seen that the structure of flow in these three heights is different. From $z^* = 0.67$ to $z^* = 1.5$ velocity in the larger radii decreases and the vortex at the center become stronger. At $z^* = 1.5$ center of vortex is not at the centerline of the cylinder.

In the lowest height of figure b ($z^* = 2.17$) the overall direction of flow changes to counter-clock-wise (beginning of upper domain) and it shows that the transition between the two rotations is happening at $1.5 < z^* < 2.17$. Yet, some clock-wise rotating structure can be seen at this height. At $z^* = 2.83$ and higher flow structure is similar and a high velocity, narrow ring close to the wall surrounds a much lower velocity core. This ring seems to be getting wider as the height increases.

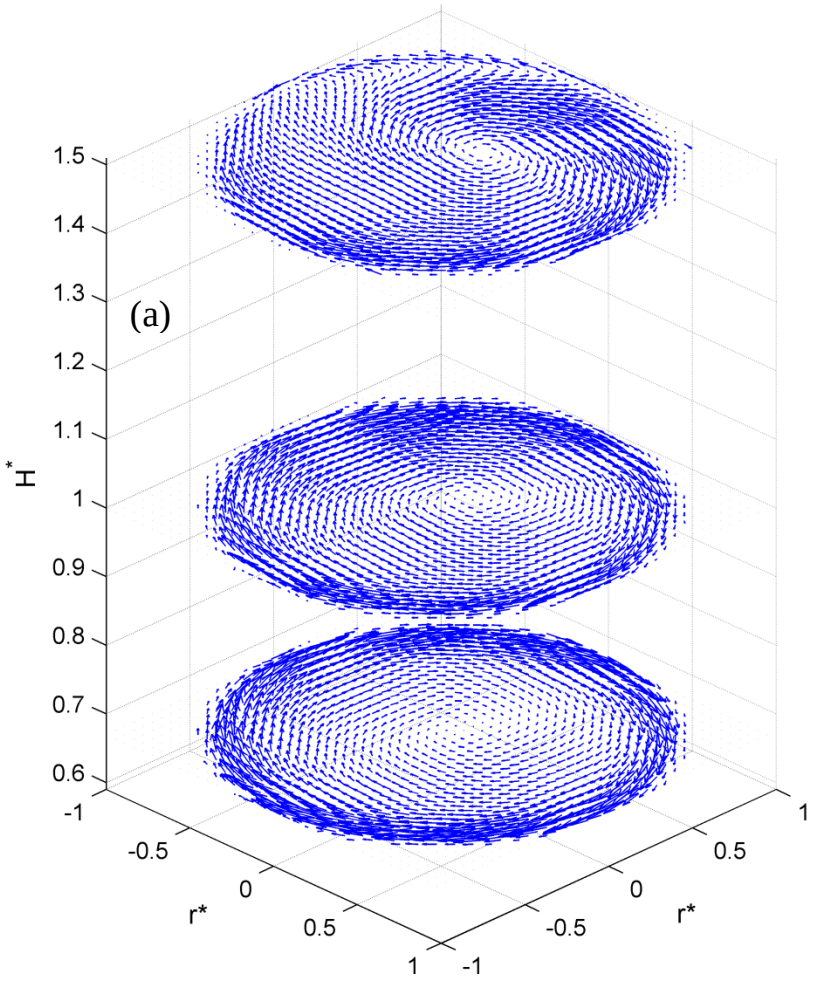
(a)
H*
1.5
1.4
1.3
1.2
1.1
1
0.9
0.8
0.7
0.6
-1
-0.5
0
0.5
1
r*
-1
-0.5
0
0.5
1
r*

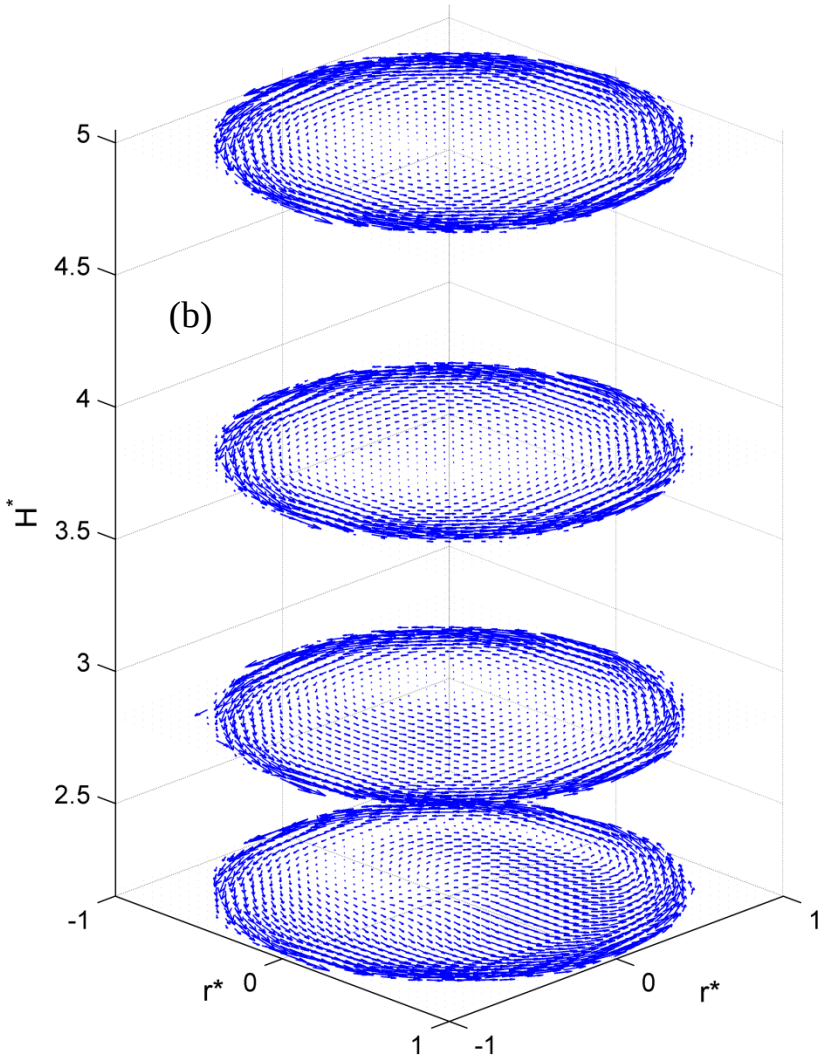

Figure 6.16 Velocity vector field for (a) three lower studied heights and (b) four higher ones for one Counter-Rotating flow case: with wall spin rate $\Omega_w^* = 1.5$ and disk spin rate $\Omega_d^* = -1.8$

Figure 6.17 shows the velocity vector/magnitude field for five lower heights of the aforementioned case. The main difference between the first three heights in the lower domain is that the high velocity region at $z^* = 0.67$ is very close to wall. This high velocity region at $z^* = 1$ and $z^* = 1.5$ becomes wider and the magnitude of velocity in the inner region becomes larger. Comparing figures c and d clearly shows that the transition occurs in between these two heights. Two higher heights are similar to figure e and are not presented here.

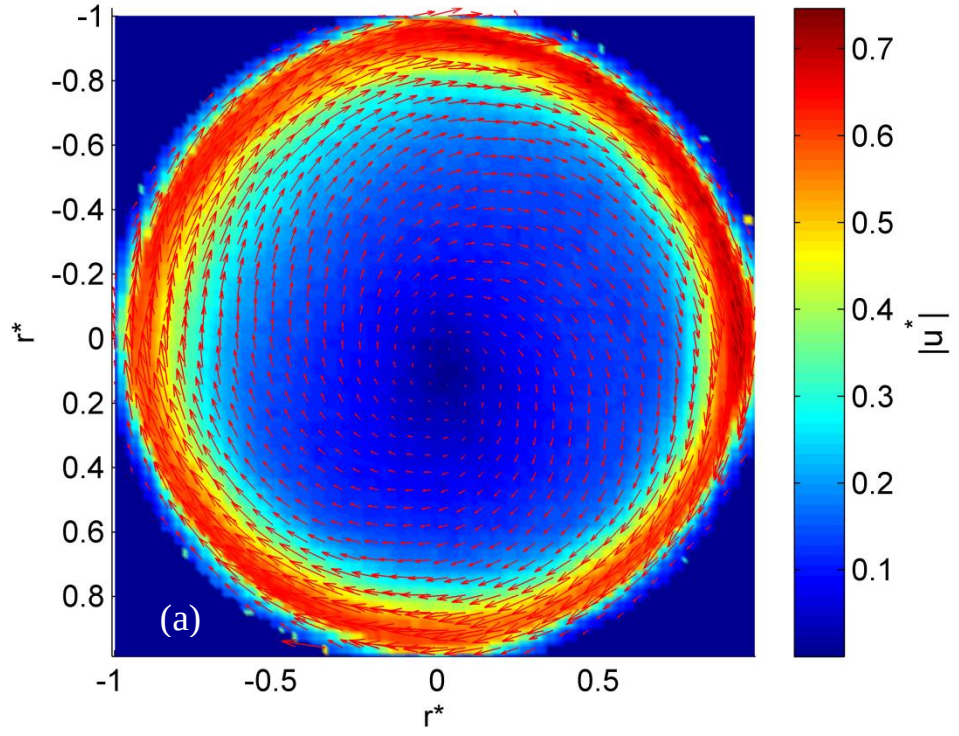
(a)
r*
r*
|u*|
-1
-0.8
-0.6
-0.4
-0.2
0
0.2
0.4
0.6
0.8
-0.5
0.5
0.7
0.6
0.5
0.4
0.3
0.2
0.1

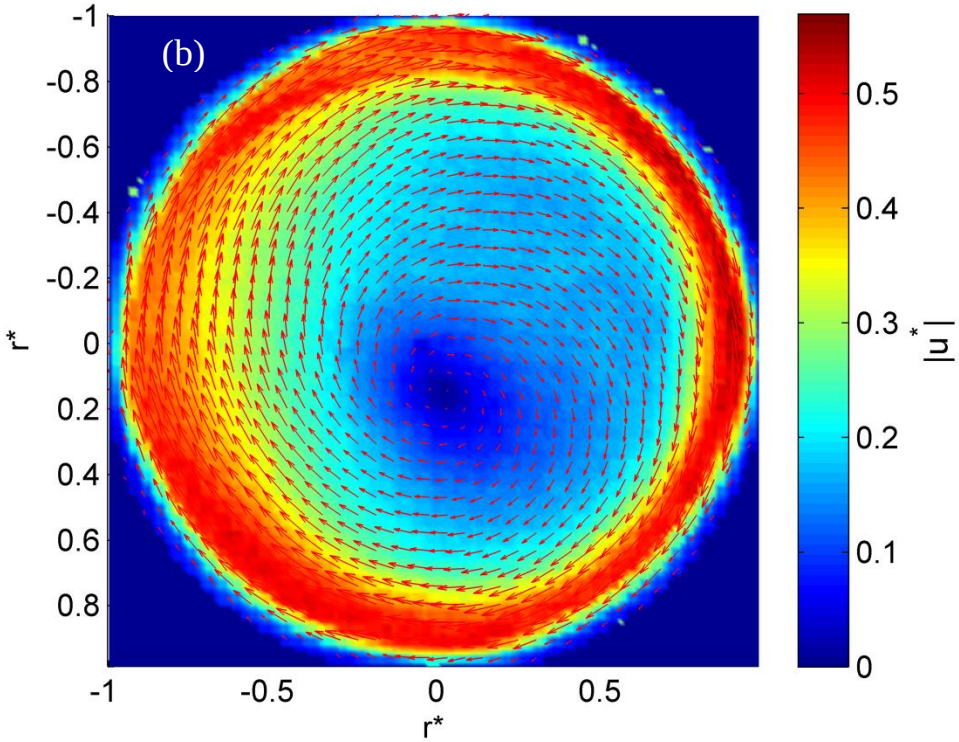
(b)
r*
r*
|u*|
-1
-0.8
-0.6
-0.4
-0.2
0
0.2
0.4
0.6
0.8
-0.5
0.5
0.5
0.4
0.3
0.2
0.1
0

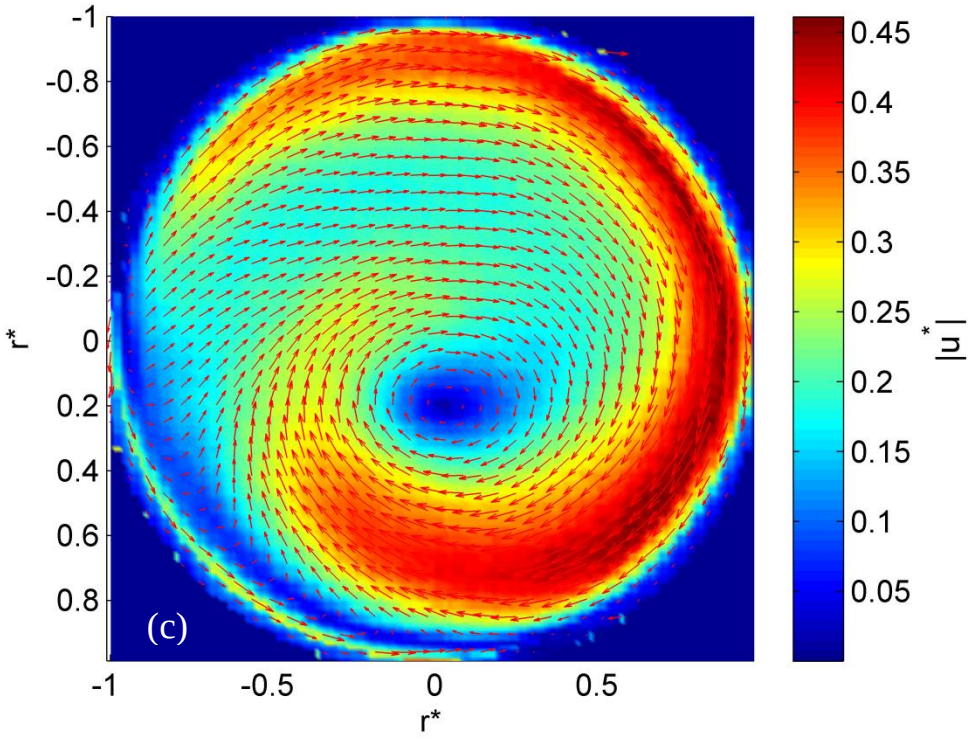
(c)
r*
r*
|u*|
-1
-0.8
-0.6
-0.4
-0.2
0
0.2
0.4
0.6
0.8
-1
-0.5
0
0.5
0.45
0.4
0.35
0.3
0.25
0.2
0.15
0.1
0.05

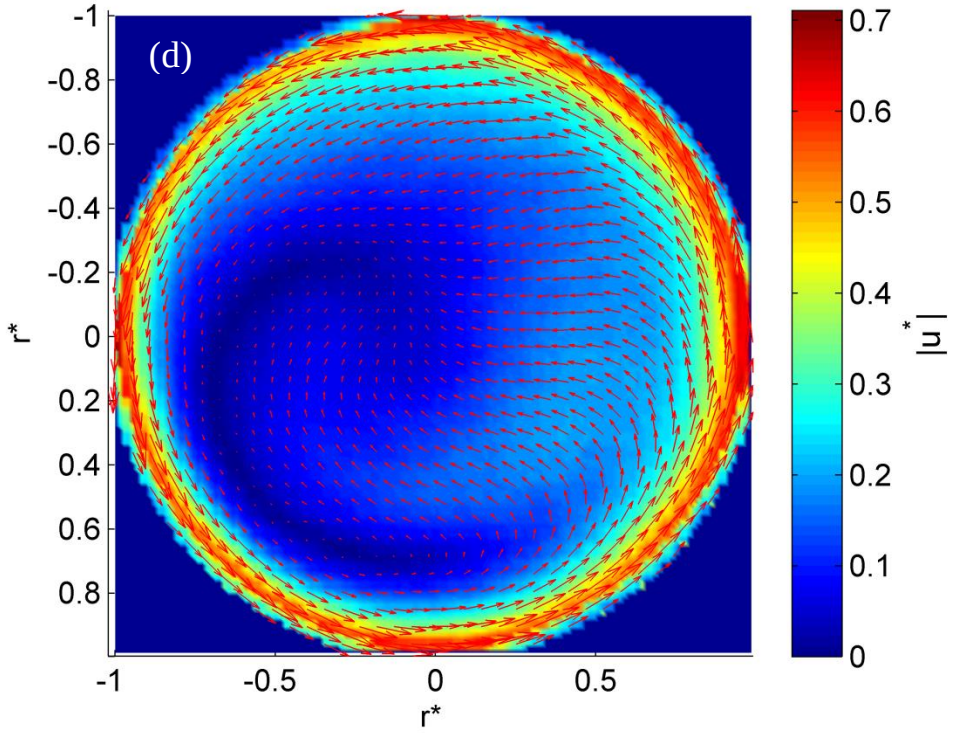
(d)
r*
r*
|u*|
-1
-0.8
-0.6
-0.4
-0.2
0
0.2
0.4
0.6
0.8
-1
-0.5
0
0.5
0.7
0.6
0.5
0.4
0.3
0.2
0.1
0

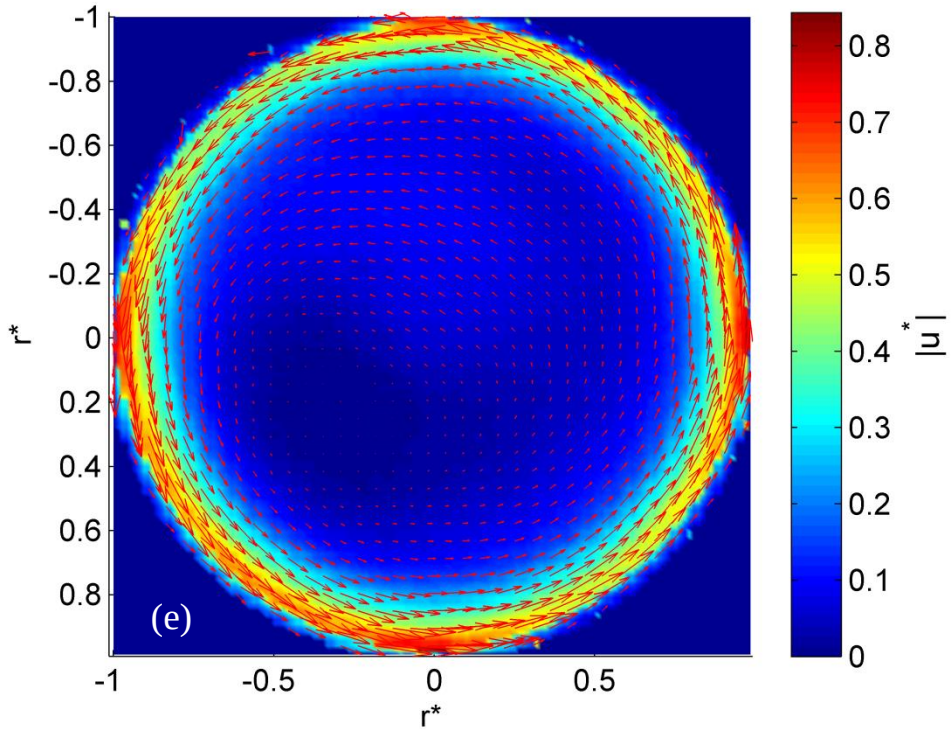

Figure 6.17 The velocity vector and magnitude field for the Counter-Rotating Flow: $\Omega_w^* = 1.5$, $\Omega_d^* = -1.8$ when (a): $z^* = 0.67$, (b): $z^* = 1$, (c): $z^* = 1.5$, (d): $z^* = 2.17$ and (e): $H^* = 2.83$

Figure 6.18-a, and b demonstrate the azimuthal component of the velocity profiles for the two heights just above and below the transitional domain: $z^* = 1.5$ and $z^* = 2.17$. Negative values of figure a and positive values in figure b clearly show the direction change in between. Also, a considerable difference between the four sections and the average is observed in both heights which are in a good agreement with k^* curves of these two heights in figure 6.2-e. Two curves corresponding to these heights in figure 6.2-e also have larger k^* values since they are close to the transition height. In both heights some sections show more symmetric behavior and some do not. Nonetheless, the average curves are not symmetric.

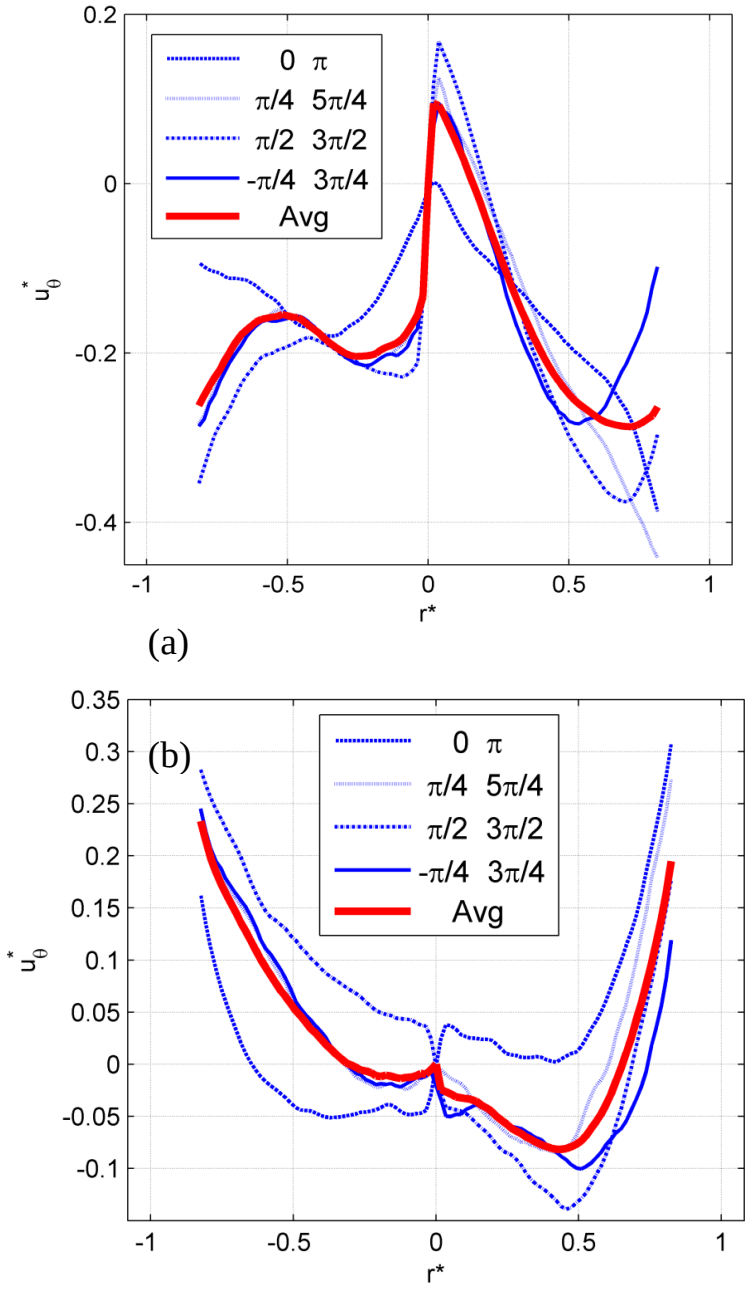

Figure 6.18 Normalized azimuthal velocity profile averaged over the half-circle-sectors and selected profiles across four radial sections for the Counter-Rotating Flow when: $\Omega_w^* = 1.5$, $\Omega_d^* = -1.8$ when (a): $z^* = 1.5$ and (c): $z^* = 2.17$

The largest studied disk spin rate is $\Omega_d^* = -2$ and velocity vector fields are presented in figures 6.19-a and b. The lower three heights are in the lower domain and mainly follow the disk-rotating direction. The rotation direction changes in the fourth height ($z^* = 2.17$, the first

height in figure b) and fifth height (where transitional domain is); higher ones are rotating counter-clock-wise with the wall. Flow structure at the fourth height is very interesting because there is not any clear direction for the rotation. It seems that this height is located within the transitional domain. Compared to lower disk spin rate cases, as discussed before, in higher disk spin rate this transition occurs in higher heights. For instance in $\Omega_d^* = -1$ the transition height was lower that the lowest studied height ($< z^* = 0.67$) and in $\Omega_D^* = -2$ the transition seems to be around the fourth studied height ($z^* = 2.17$).

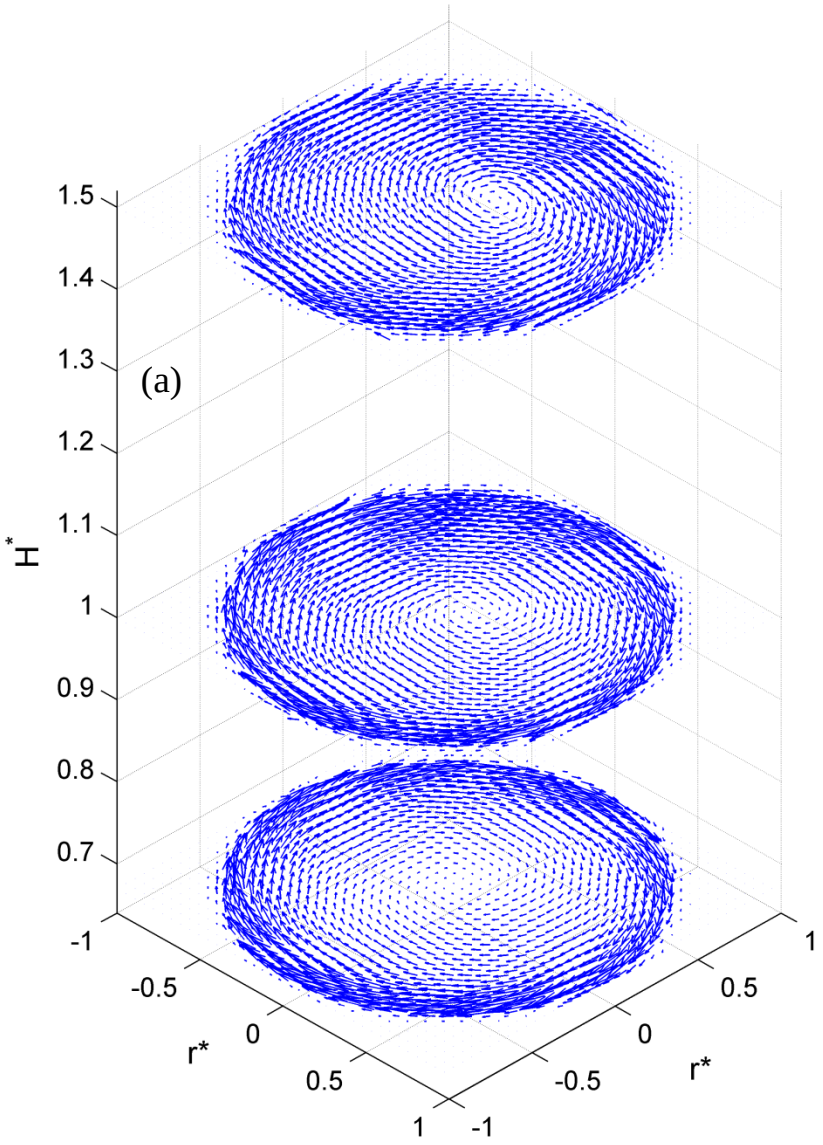

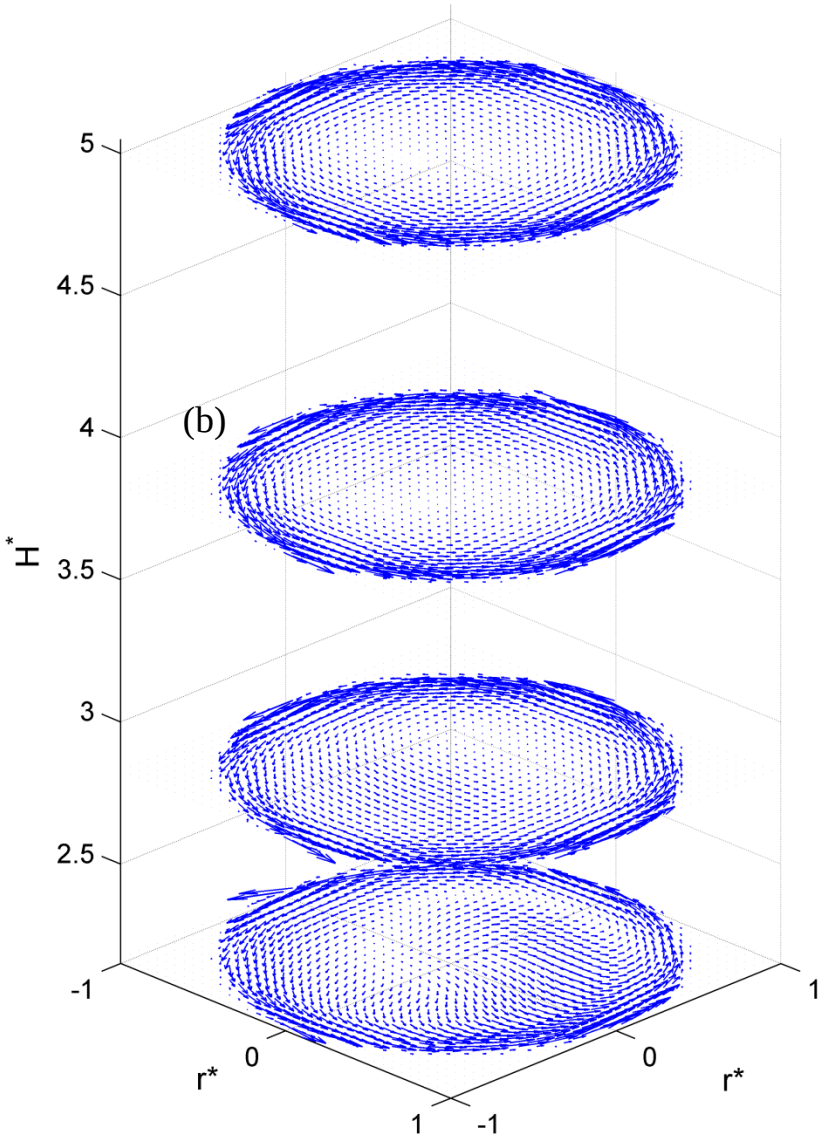

Figure 6.19 Velocity vector field for (a) three lower studied heights and (b) four higher ones for one Counter-Rotating flow case: with the wall spin rate $\Omega_w^* = 1.5$ and the disk spin rate $\Omega_d^* = -2$

Figure 6.20 shows the velocity vector/magnitude fields for all studied heights of the highest disk spin rate in the counter rotating flow experiments. The lowest height, $z^* = 0.67$, shows a high velocity ring in the outer range and a relatively lower velocity region in the inner region. Although this structure seems similar to higher heights (in opposite direction), the inner region behaves differently, rotates much more predictably and follows the disk-rotating direction

and the outer ring. This ring becomes wider at $z^* = 1$ and the inner regain has a higher magnitude of velocity. As the height increases, at $z^* = 1.5$, inner region in not rotating much slower than the outer ring and the velocity magnitude in the entire domain does not vary as it does in lower heights. Moreover, in this height unlike the previous disk spin rate, flow is still following the disk-rotating direction in the entire domain.

At $z^* = 2.17$, figure d, the velocity magnitude for the entire domain is significantly less than other heights. This seems to be due to equal impact of disk and wall at this height (just above the transitional domain). Therefore, flow does not have a clear direction of rotation. At $z^* = 2.83$ and above, figures e, f and g, a narrow ring of high velocity region surrounds a very low velocity region in the middle. This structure is similar to higher heights of previous cases with lower disk spin rates (upper domain).

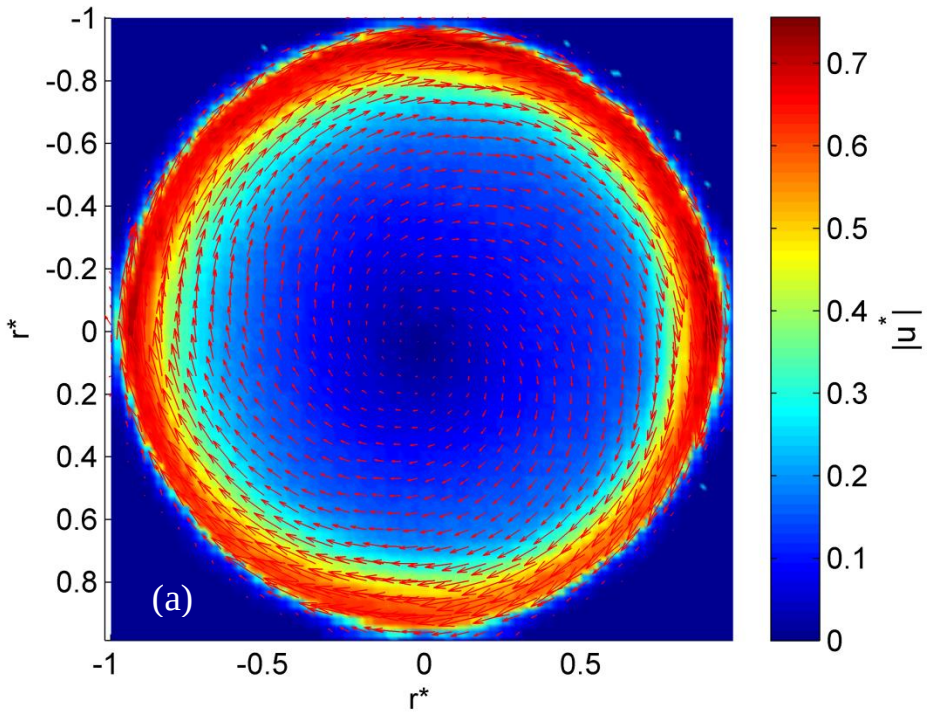

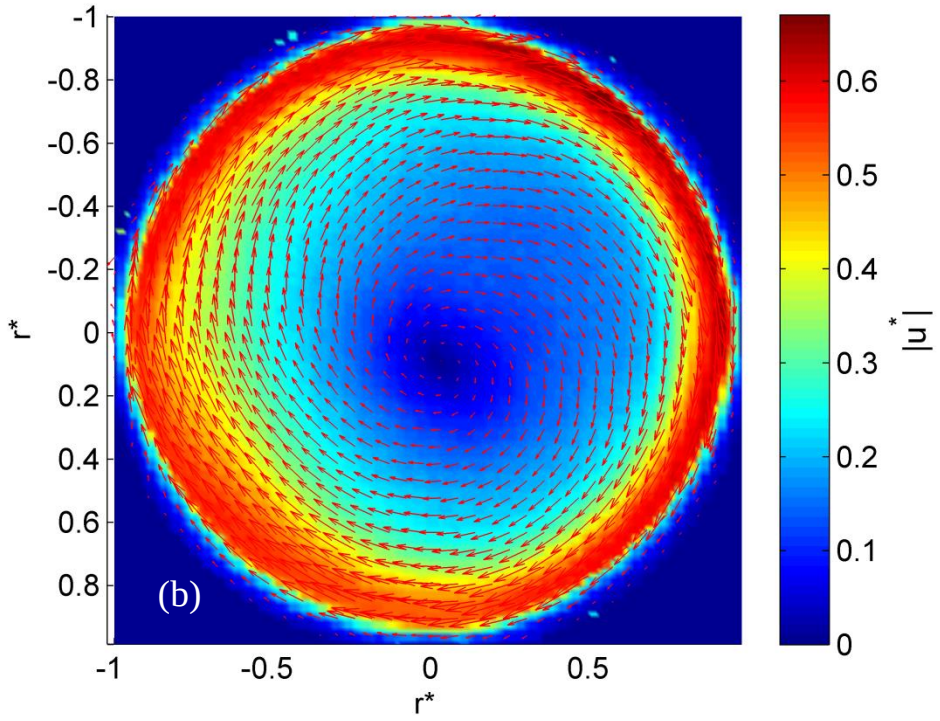
(b)
r*
r*
|u*|
-1
-0.8
-0.6
-0.4
-0.2
0
0.2
0.4
0.6
0.8
-0.5
0.5
0.1
0.3

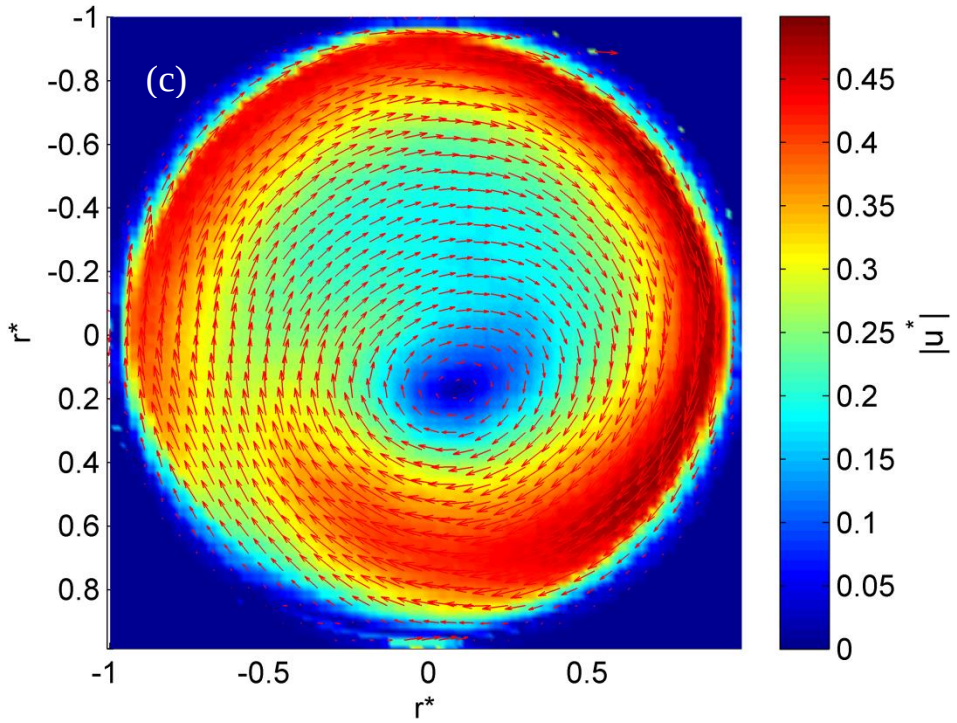
(c)
r*
r*
|u*|
-1
-0.8
-0.6
-0.4
-0.2
0
0.2
0.4
0.6
0.8
-0.5
0.5
0.45
0.4
0.35
0.3
0.25
0.15
0.1
0.05

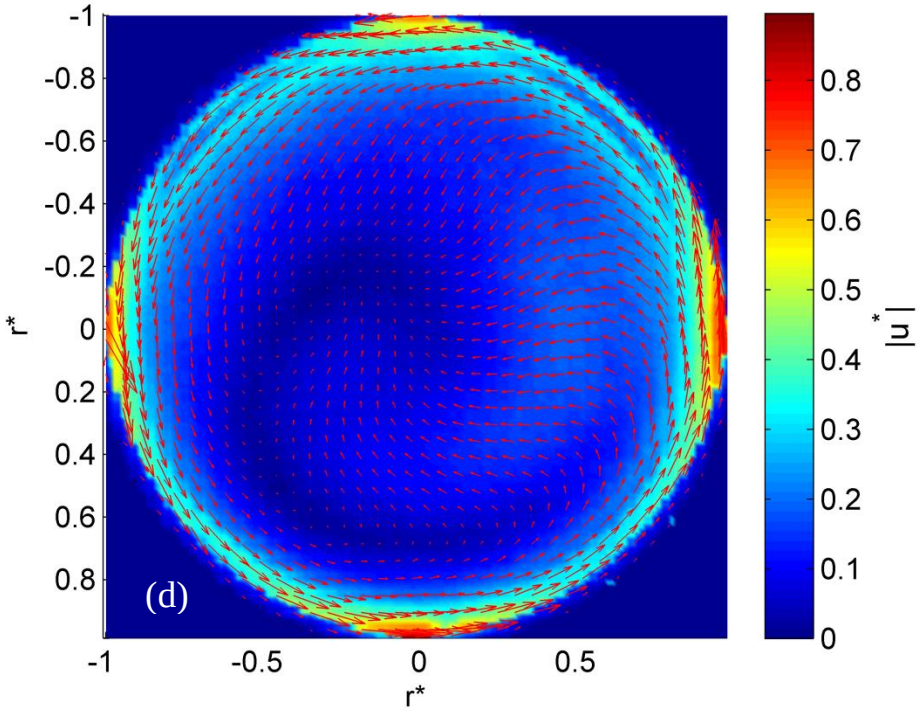
(d)
r*
r*
|u*|
-1
-0.8
-0.6
-0.4
-0.2
0
0.2
0.4
0.6
0.8
-1
-0.5
0
0.5
0.1
0.3
0.7
0.9

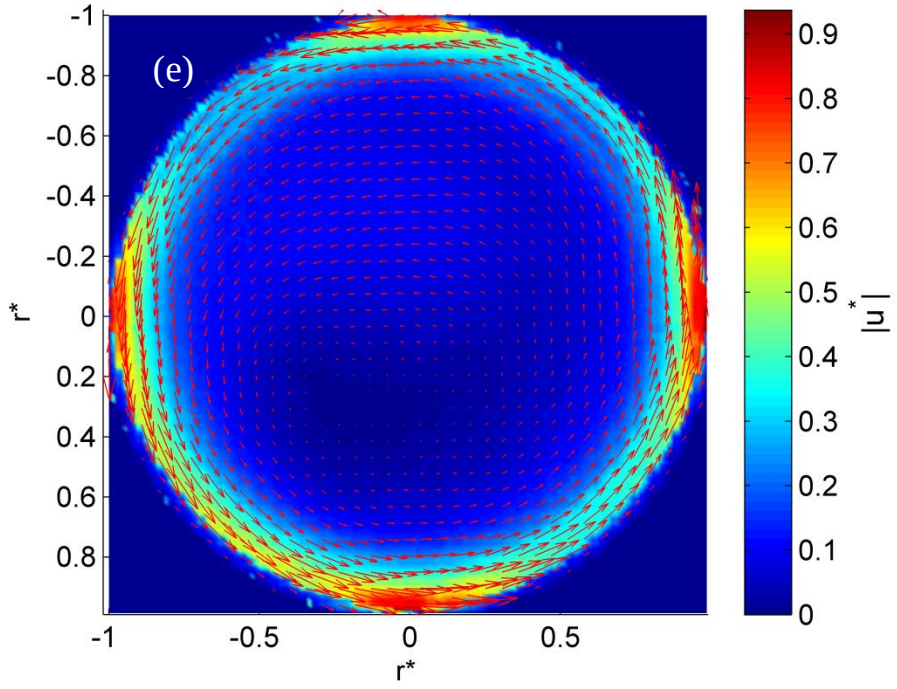
(e)
r*
r*
|u*|
-1
-0.8
-0.6
-0.4
-0.2
0
0.2
0.4
0.6
0.8
-1
-0.5
0
0.5
0.1
0.3
0.7
0.9

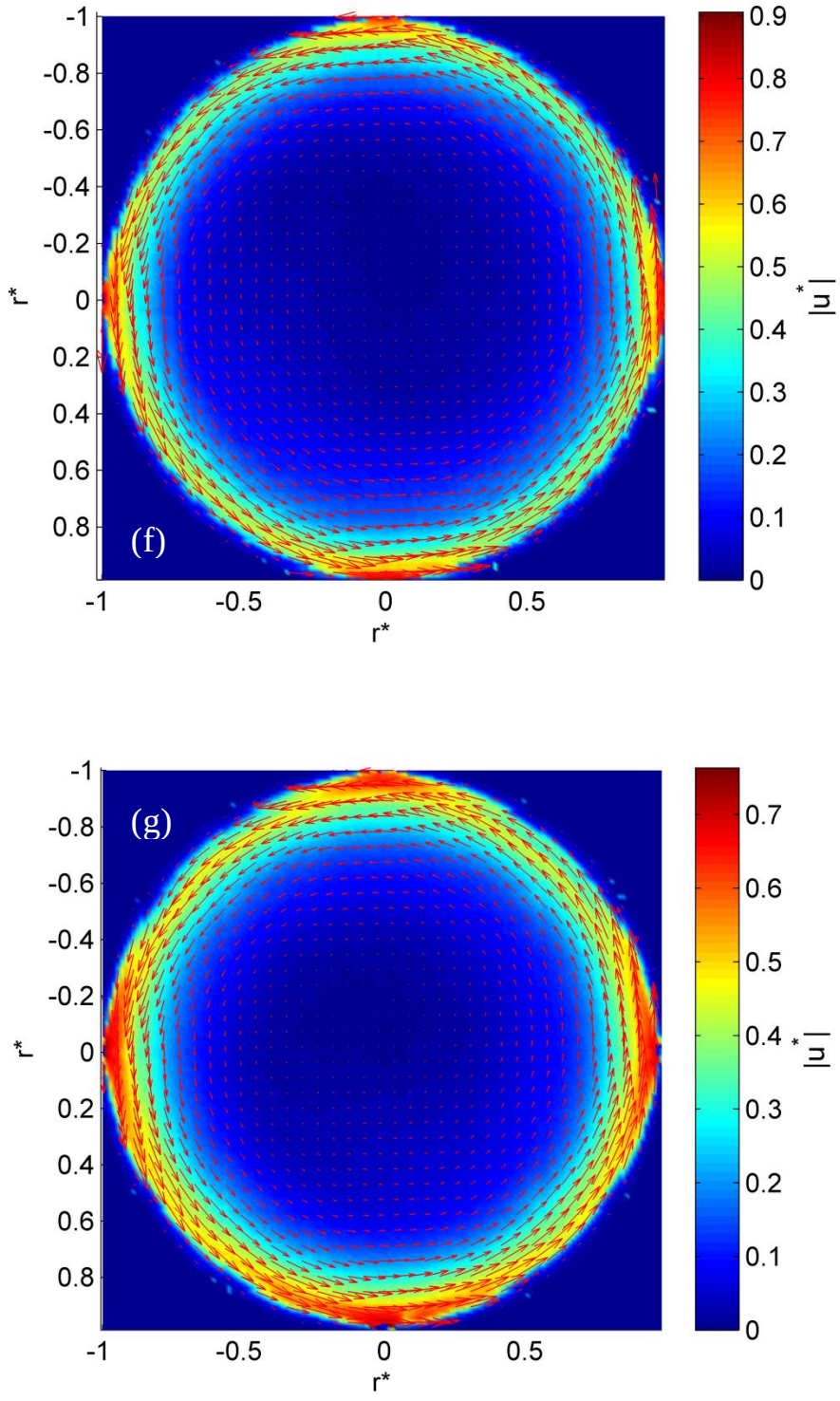

Figure 6.20 The velocity vector and magnitude field for the Counter-Rotating Flow: $\Omega_w^* = 1.5$, $\Omega_D^* = -2$ when (a): $H^* = 0.67$, (b): $H^* = 1$, (c): $H^* = 1.5$, (d): $H^* = 2.17$, (e): $H^* = 2.83$,(f): $H^* = 3.83$ and (g): $H^* = 5$

Figure 6.21 demonstrate the azimuthal component of the velocity profiles for all studied heights with $\Omega_d^* = -2$. The difference between the four sections and the average curve in all heights shows the symmetric behavior of the flow. At $z^* = 0.67$ all five curves are almost merges and show a very symmetric behavior. At $z^* = 1$, although the average curve is close to symmetric, other sections show different velocity profiles. Unlike the first two heights, figure c shows an axisymmetric behavior for the average curve. However, except for a small portion of the domain, azimuthal velocity is still negative in the rest of domain which implies the clock-wise rotation. The sign of velocity changes in the next height in figure d and the average curve is axisymmetric and low velocity, although the magnitude of velocity is less than all other height. The two reasons (rotation direction change and small magnitude of velocity for domain) show that the transition is taking place close to this height as explained before. Above this height, in figure e, f and g flow becomes smoother and more symmetric as the height increases.

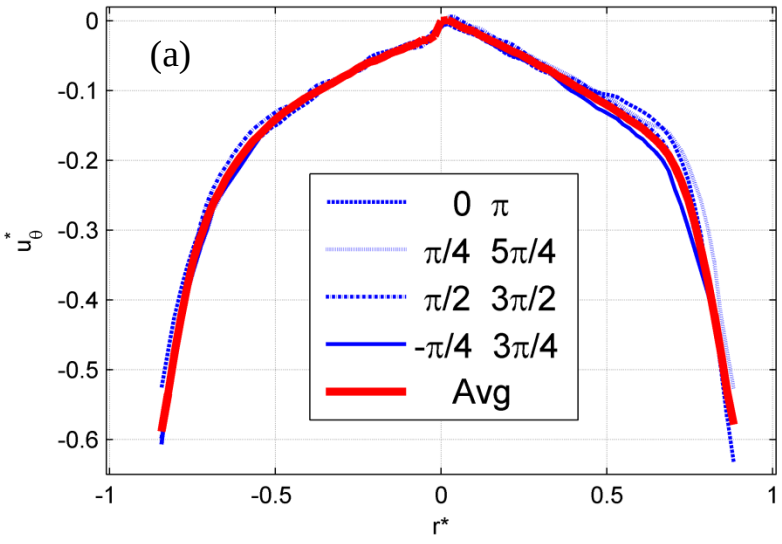
(a)
0 π
π/4 5π/4
π/2 3π/2
-π/4 3π/4
Avg
u^*_θ
r*

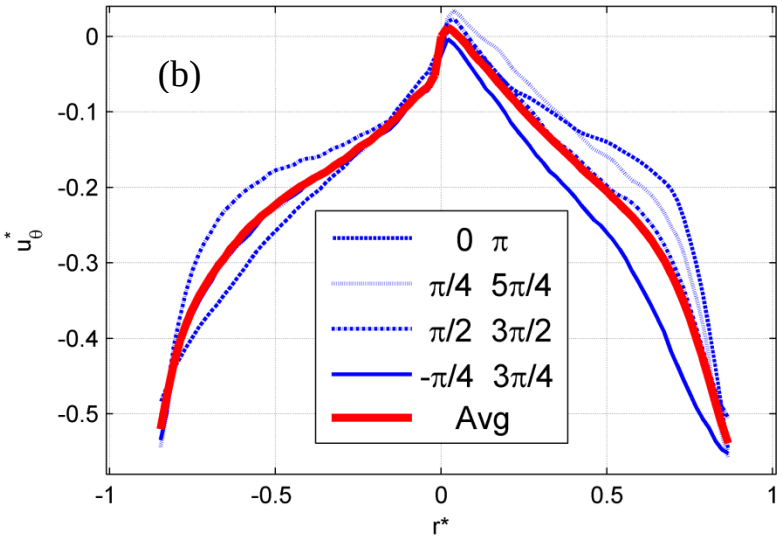
(b)
0 π
π/4 5π/4
π/2 3π/2
-π/4 3π/4
Avg
u^*_θ
r*

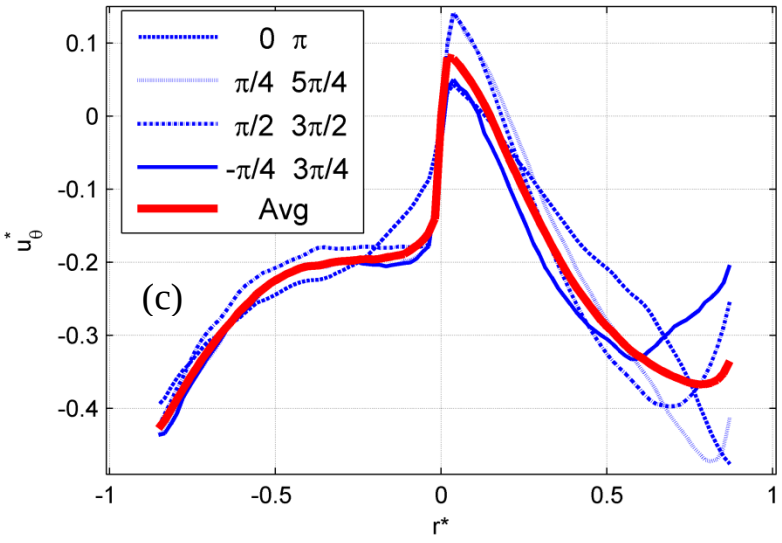
(c)
0 π
π/4 5π/4
π/2 3π/2
-π/4 3π/4
Avg
u^*_θ
r*

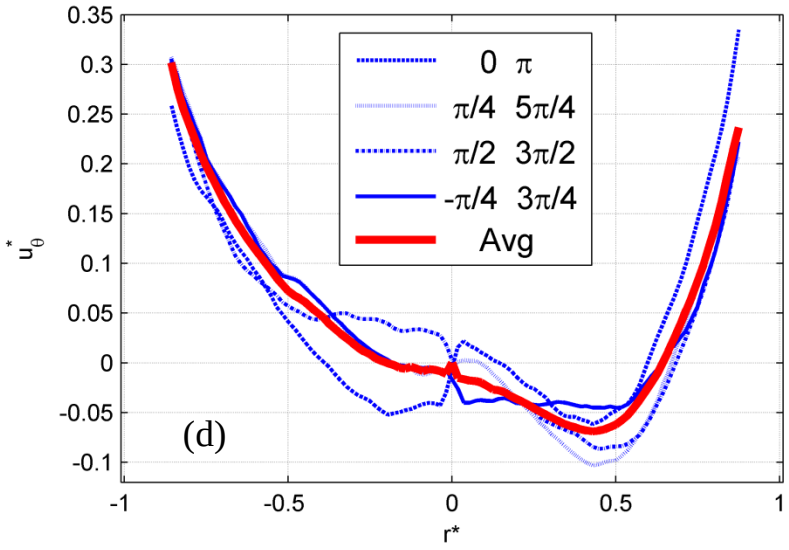
0.35
0.3
0.25
0.2
0.15
0.1
0.05
0
-0.05
-0.1
-1
-0.5
0
0.5
1
r*
u_θ^*
0 π
π/4 5π/4
π/2 3π/2
-π/4 3π/4
Avg
(d)

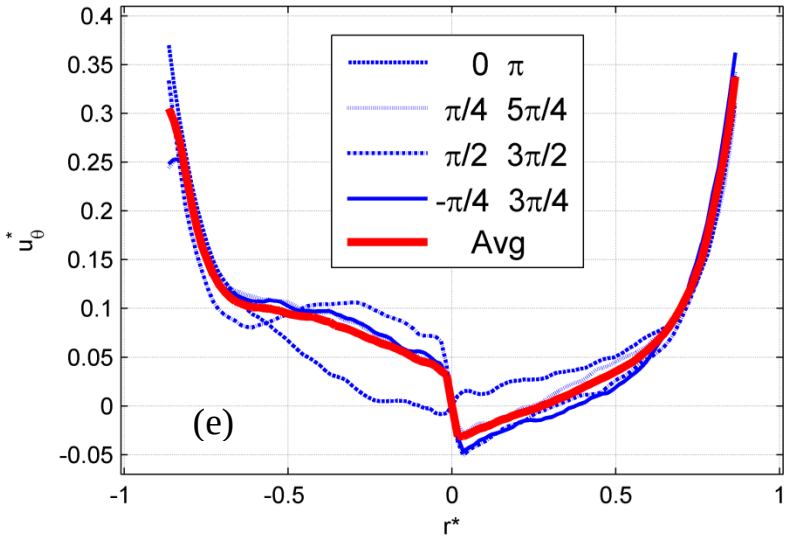
0.4
0.35
0.3
0.25
0.2
0.15
0.1
0.05
0
-0.05
-1
-0.5
0
0.5
1
r*
u_θ^*
0 π
π/4 5π/4
π/2 3π/2
-π/4 3π/4
Avg
(e)

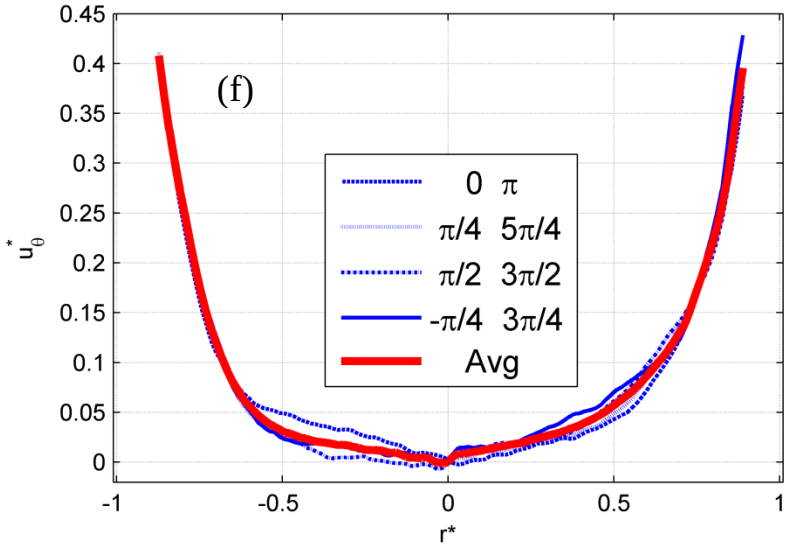
0.45
0.4
0.35
0.3
0.25
0.2
0.15
0.1
0.05
0
-1
-0.5
0
0.5
1
r*
u_θ^*
0 π
π/4 5π/4
π/2 3π/2
-π/4 3π/4
Avg
(f)

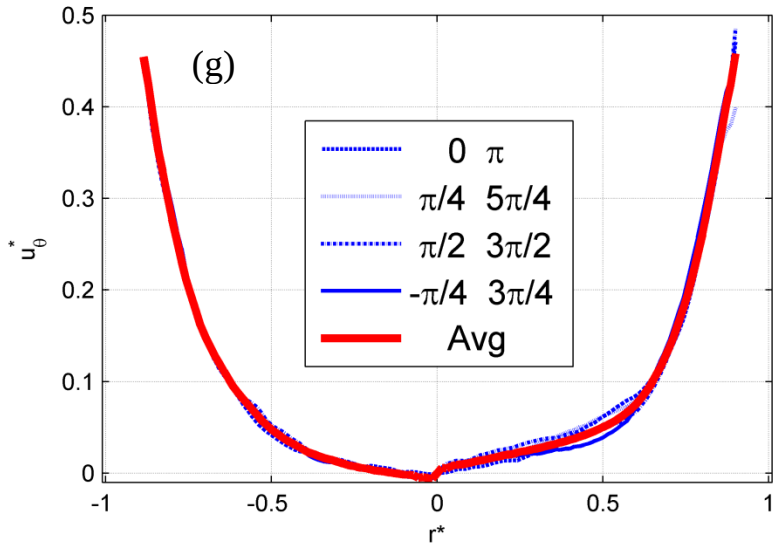

Figure 6.21 Normalized azimuthal velocity profile averaged over the half-circle-sectors and selected profiles across four radial sections for the Counter-Rotating flow when: $\Omega_w^* = 1.5$, $\Omega_d^* = -2$ when (a): $z^* = 0.67$, (b): $z^* = 1$, (c): $z^* = 1.5$, (d): $z^* = 2.17$, (e): $z^* = 2.83$, (f): $z^* = 3.83$ and (g): $z^* = 2.17$

Figure 6.22-a shows the profiles of k^* averaged over a cross-section as a function of z^* at $\Omega_w^* = 1.5$ and $\Omega_d^* = -1.6$ in the counter-rotating-cylinder-disk-flows for three Grashof numbers (including two other heated cases in the next chapter). There are the peak values (maxima) of k^* in all the cases. For example, in the case without disk heating ($Gr = 0$), the peak occurs at about $z^* = 1.5$, which approximately corresponds to the transitional domain. The circulation Γ at each cross-section is evaluated by integrating the vorticity field (ω_z) on the cross-section. Figure 6-22-b shows the normalized circulation $\Gamma^* = \Gamma / \Omega_w R^2$ as a function of z^*, indicating that Γ^* increases with z^* from the negative value (clockwise rotation driven by the disk) to the positive value (counter-clockwise rotation driven by the cylinder). There are the zero-crossing points in Γ^* which approximately correspond to the transitional domains. For $Gr = 0$, the zero-crossing point is at $z^* = 1.5$.

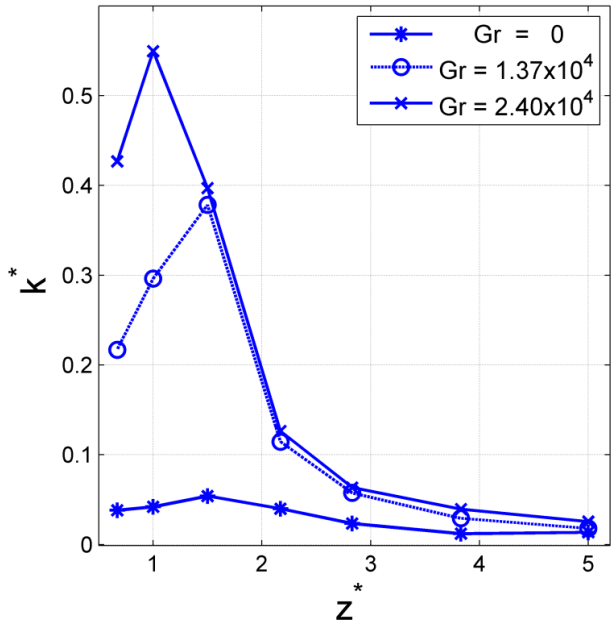

(a)

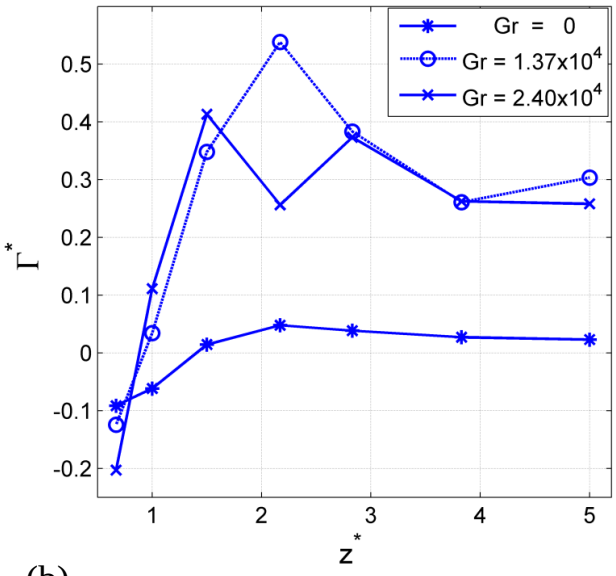

(b)

Figure 6.22 (a) Normalized turbulent kinetic energy averaged over a cross-section and (b) circulation as a function of z^* at $\Omega_w^* = 1.5$ and $\Omega_d^* = -1.6$ in the counter-rotating-cylinder-disk-flows for three Grashof numbers.

Figure 6.23 shows the peak value of k^* as a function of Ω_d^*. For $Gr = 0$, the peak value of k^* slightly decays and then approaches a constant as Ω_d^* increases. The averaged position of the transitional domain depends on the disk spinning rate Ω_d^* for a given value of Ω_w^*.

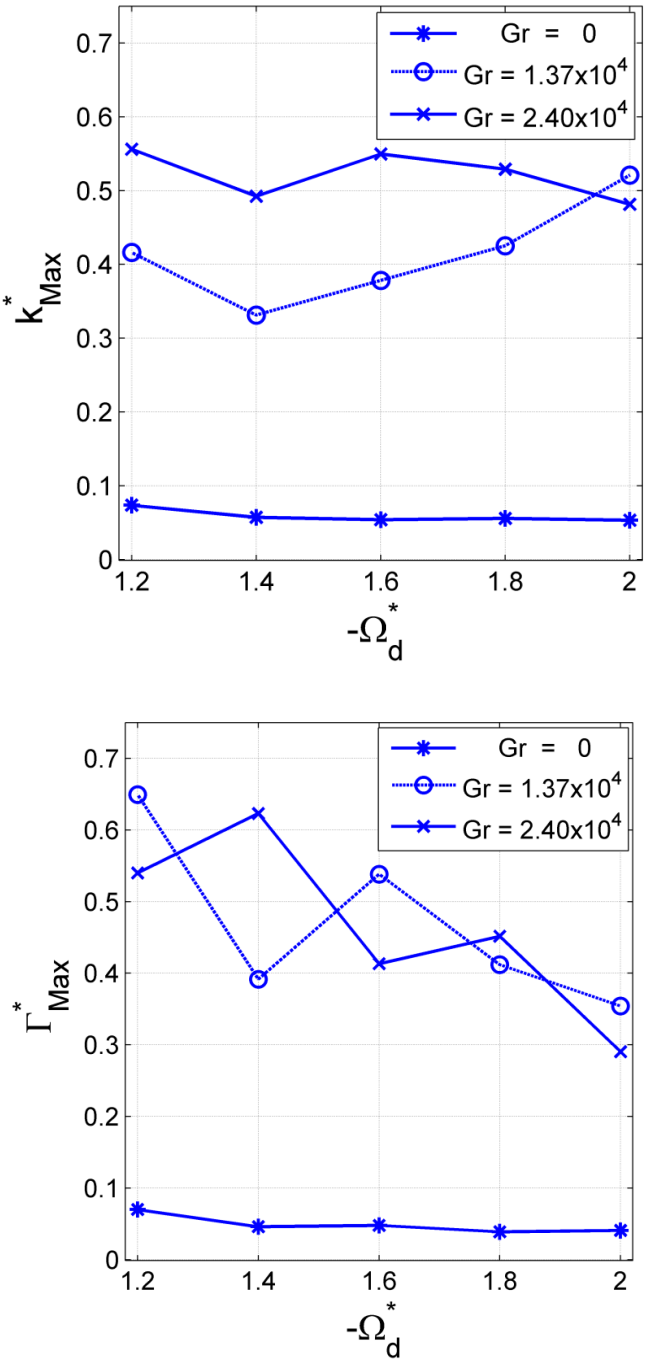

Figure 6.23 Peak values of (a) k^* and (b) Γ^* as a function of Ω_d^* at $\Omega_w^* = 1.5$ in the counter-rotating-cylinder-disk-flows for three Grashof numbers.

Figure 6.24 shows the positions of the transitional domain as a function of the disk spinning rate Ω_d^* at $\Omega_w^* = 1.5$ in the counter-rotating-cylinder-disk-flows for three Grashof

numbers. The error bars in Fig. 6.24 indicate the sizes of the transitional domains in these cases. In general, the vertical position of the transitional domain is increased with Ω_d^* because the influence of the counter-rotating disk propagates upward.

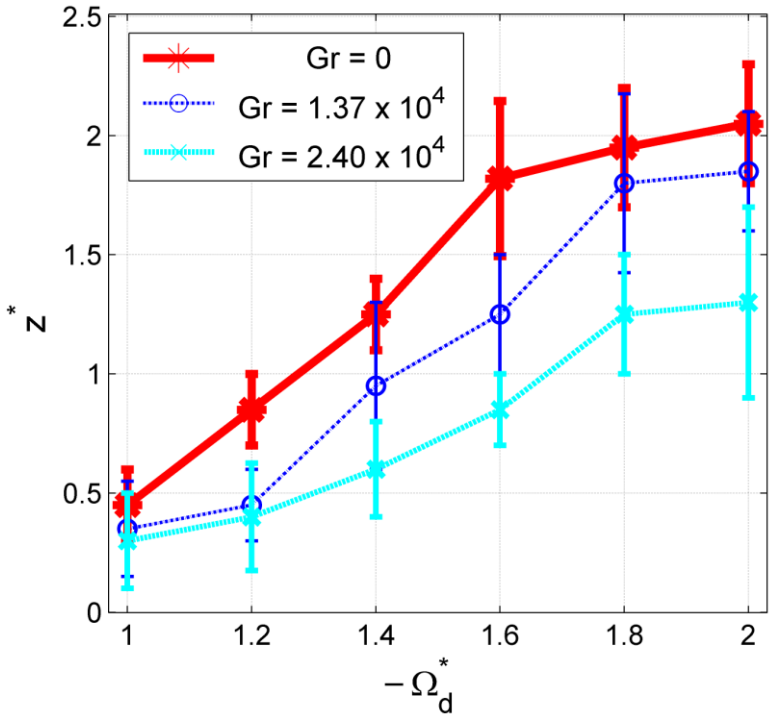

Figure 6.24 The positions of the transitional domain as a function of the disk spinning rate Ω_d^* at $\Omega_w^* = 1.5$ in the counter-rotating-cylinder-disk-flows for three Grashof numbers.

Based on the velocity measurements in the cross-sections and the vertical plane, the simplified 3D flow structures can be qualitatively reconstructed. The conjectured 3D flow structures are illustrated in Figure 6.25, which are the torus vortices wrapped by spiral streamlines. In the lower region, the flow on the torus vortex orthographically projected on the $\left(x^*, y^*\right)$ plane rotates clockwise around the z-axis as evidenced in Figure 6.2. Also, as indicated in Figure 6.25, the flow rotates clockwise around the axis of the torus relative to the screwing direction of the spiral streamlines. Accordingly, the downward flow is induced in the

center of the torus. In contrast, in the upper domain, the flow is associated with an array of the packed torus vortices that rotate counter-clockwise around both the z-axis and their axes, inducing the upward flow in the center of the array of the tori. The array of the torus vortices in the upper domain is similar that observed in the Taylor-Couette flow, except that there is the upward flow in the core of the tori in this case. The transitional domain is located between the counter-rotating tori in the lower and upper domains.

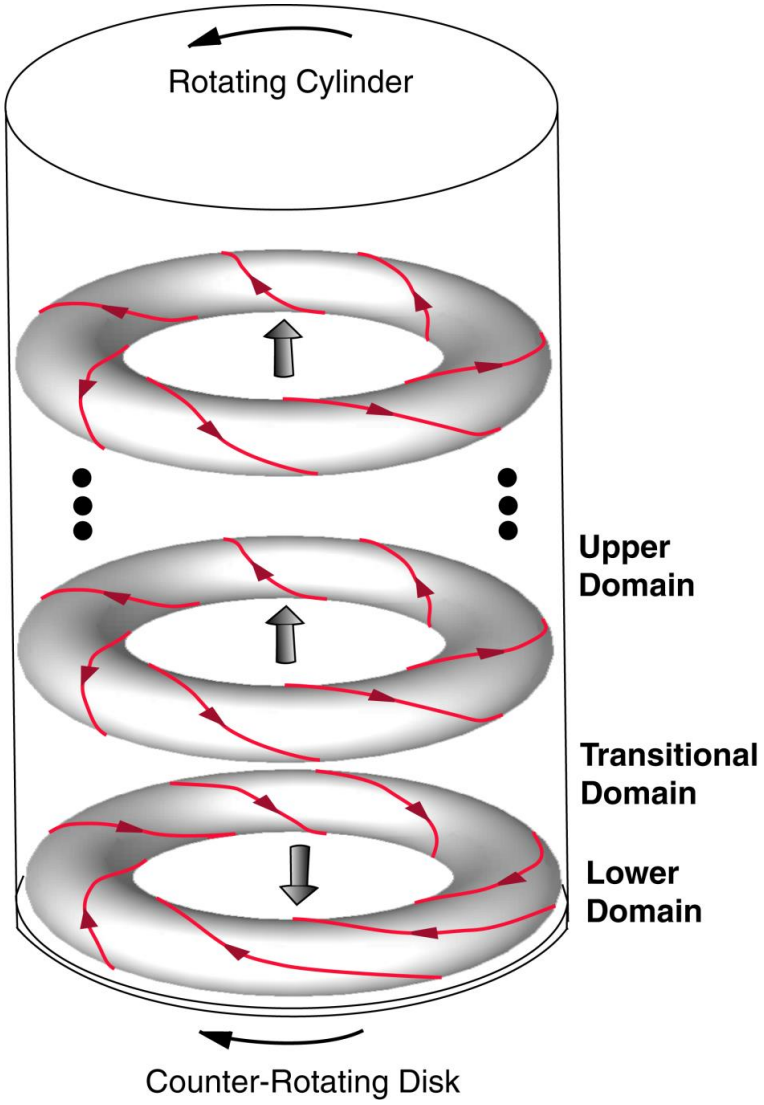

Figure 6.25 Conjectured 3D flow structures of the torus vortices.

7 Results and Discussion: Counter rotating flow, heated from bottom

Under the same rates of Ω_d^* and Ω_w^*, the flows in the rotating cylinder with the counter-rotating disk with disk heating were measured to understand the effects of the thermal buoyancy on the flow structures characterized by the Grashof number $Gr = R^3\beta\rho^2 g\Delta T / \mu^2$. The disk temperature differences were set at $\Delta T = T_d - T_0 = 25\,K$ and $50\,K$, and the corresponding Grashof numbers were $Gr = 1.37\times10^4$ and 2.4×10^4. Similar to figure 6.1, figure 7.1 displays $\left\langle u_\theta^* \right\rangle$-profile over the right and left circular sectors ($\theta = 0$ *to* π and $\theta = \pi$ *to* 2π) for all spin rates. The disk surface temperature is higher than the ambient temperature and it causes vertical flow due to buoyancy effect which increases the mixing in the flow. Since the area of wall is significantly larger than the disk, the dominant rotating condition is the wall. When mixing between the heights increase, the effect of wall is expected to be stronger in all heights. Therefore, flow is expected to become more similar to only-wall case as the disk temperature increases. Comparing figure 7.1-a, 7.2-a and 6.1-a for the lowest studied disk spin rate, $\Omega_d^* = -1$, shows that The values of $\left\langle u_\theta^* \right\rangle$ in the inner region ($-0.5 < r^* < 0.5$) is considerably higher than those in the case without disk heating. In other words, the vortex flow in the upper domain is less "hollow" due to the stronger influence induced by counter-clockwise rotating cylinder although the $\left\langle u_\theta^* \right\rangle$-profiles are still not linear.

In higher heights, $z^* > 2.17$, regardless of the disk spin rate, flow always rotates in same direction that the wall does (these heights are always in the upper domain). However, as the disk spin rate increases, so does the curvature of the velocity profile in those heights and value of

$\left\langle u_\theta^* \right\rangle$ increases. In lower heights, on the other hand, flow rotation direction in each height is dictated by three parameters: the height, the disk spin rate and the disk temperature. Previously, in no-heat section, it was shown that flow in lower heights, at a higher disk spin rate, tends to follow the disk rotation (lower domain). As was shown in figure 6.24, increasing the disk surface temperature to enhance the mixing decreases the chance of direction change in the rotation and following the disk in all heights (especially in lower ones). For instance comparing these three figures: 6.1-c, 7.1-c, 7.2-c shows that in all three of them, boundary conditions are the same except for the disk surface temperature which is $\Delta \mathrm{T} = 0^o C, 25^o C$ and $50^o C$ respectively and disk spin rate in all three is kept at $\Omega_{\mathrm{D}}^* = -1.4$. In figure 6.1-c two curves of $z^* = 0.67$ and $z^* = 1$ are separated from the rest and clearly follow the disk-rotating direction (lower domain). When the disk temperature is one step higher in figure 7.1-c, although three curves are separated from the others, only one at $z^* = 0.67$ is in lower domain. The curve corresponding with $z^* = 1$ is exactly where the impact of wall and disk are equal (transitional domain) and the value of is very small in all radii. For the higher disk temperature, in figure 7-2-c, only one curve is separated from the bunch of curves ($z^* = 0.67$) and even that one curve is above in the lower domain and in the transitional domain. Comparing figures for the other disk spin rates of the three studied surface temperature shows similar buoyancy effect. In a nutshell, the higher disk temperature leads to more mixing effects and a more dominant wall effect.

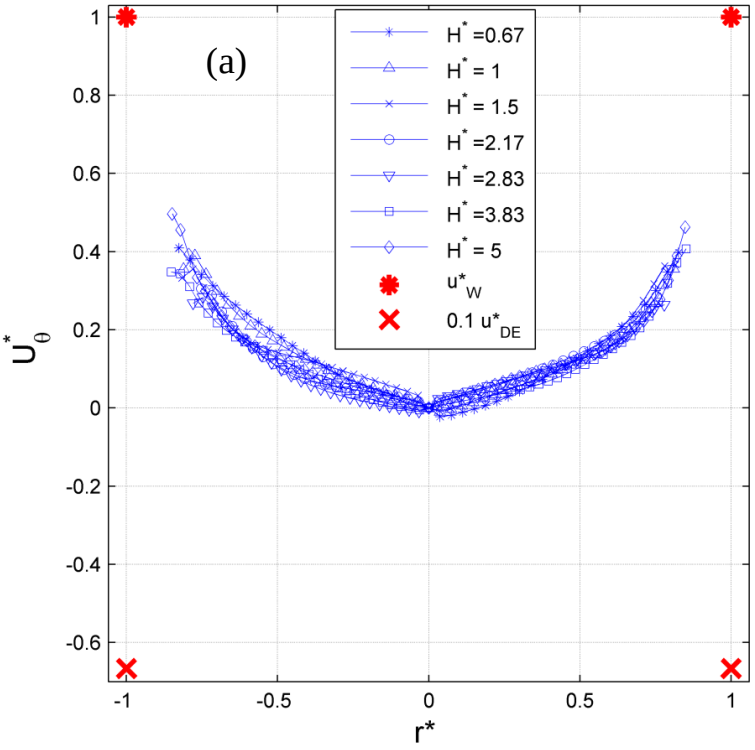
(a)
H* =0.67
H* = 1
H* = 1.5
H* =2.17
H* =2.83
H* =3.83
H* = 5
u*W
0.1 u*DE
U*θ
r*
1
0.8
0.6
0.4
0.2
0
-0.2
-0.4
-0.6
-1
-0.5
0
0.5
1

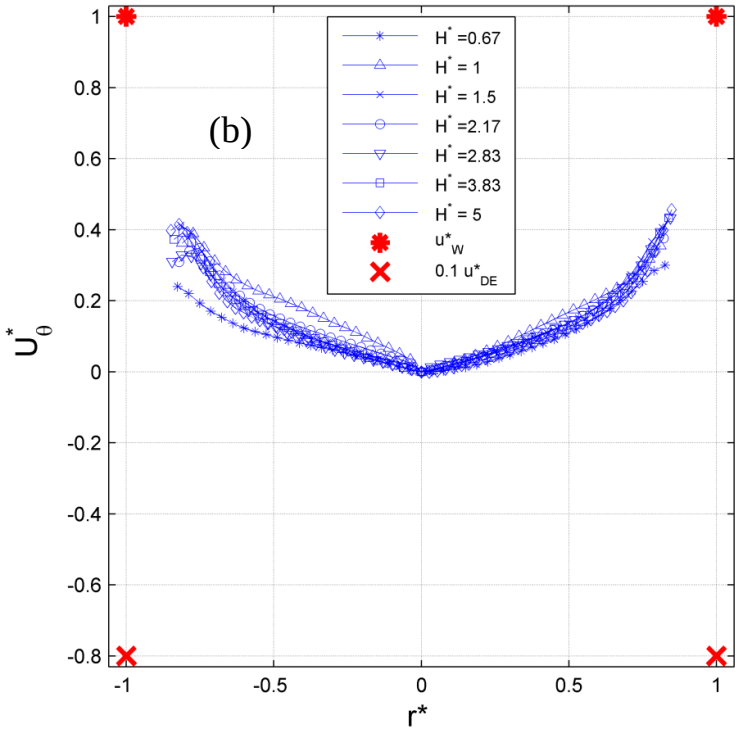
(b)
H* =0.67
H* = 1
H* = 1.5
H* =2.17
H* =2.83
H* =3.83
H* = 5
u*W
0.1 u*DE
U*θ
r*
1
0.8
0.6
0.4
0.2
0
-0.2
-0.4
-0.6
-0.8
-1
-0.5
0
0.5
1

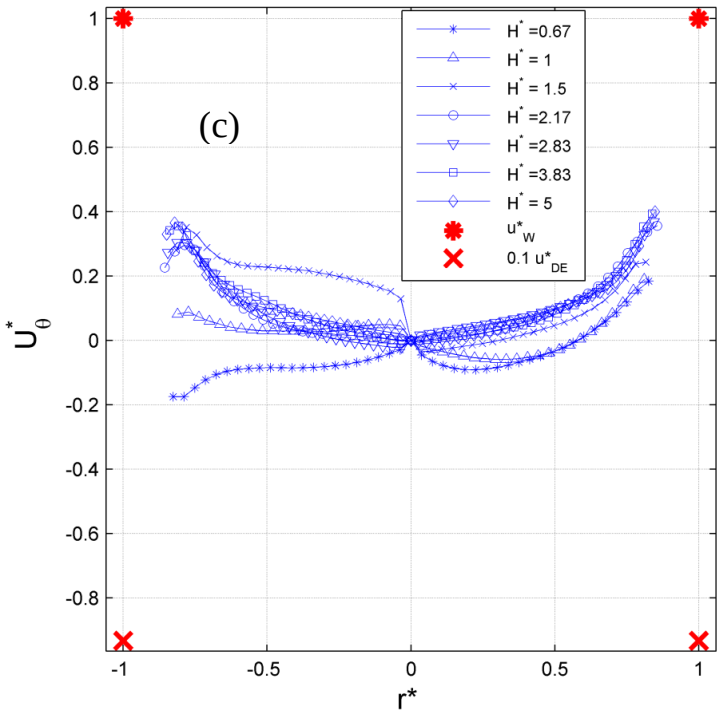
(c)
H* =0.67
H* = 1
H* = 1.5
H* =2.17
H* =2.83
H* =3.83
H* = 5
u*W
0.1 u*DE
U*θ
r*
1
0.8
0.6
0.4
0.2
0
-0.2
-0.4
-0.6
-0.8
-1
-0.5
0.5

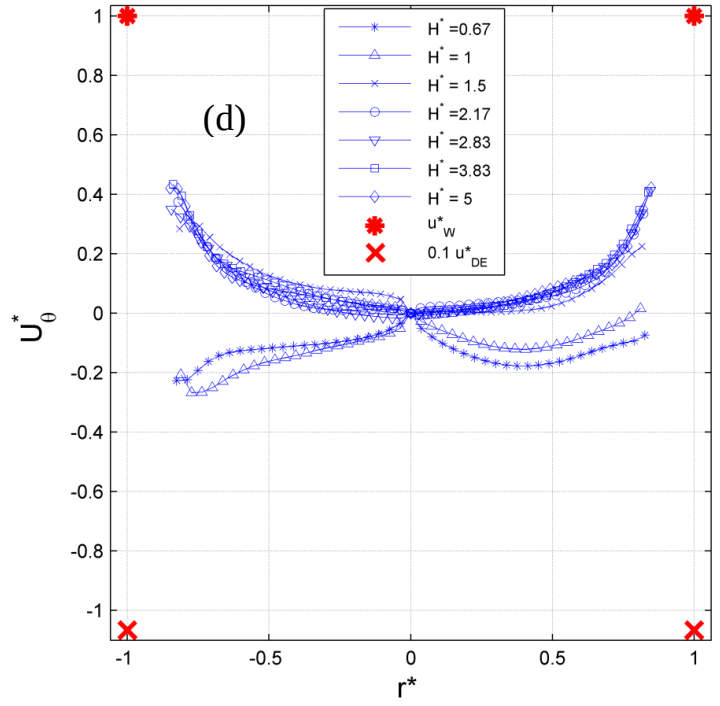
(d)
H* =0.67
H* = 1
H* = 1.5
H* =2.17
H* =2.83
H* =3.83
H* = 5
u*W
0.1 u*DE
U*θ
r*
1
0.8
0.6
0.4
0.2
0
-0.2
-0.4
-0.6
-0.8
-1
-0.5
0.5

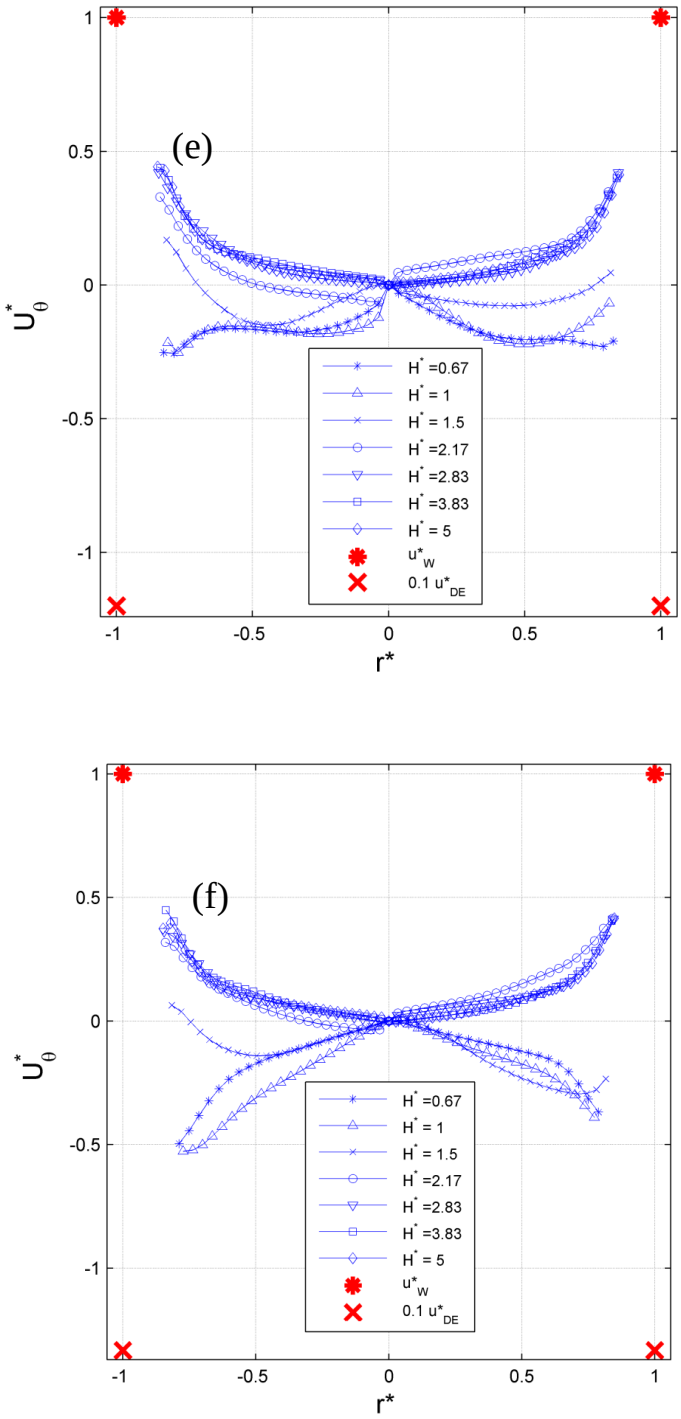

Figure 7.1 $\left\langle u_\theta^* \right\rangle$-profiles in all measured heights $\Delta T = 25^o C$ for the Co-Rotating Flow cases when the wall spinning rate is $\Omega_w^* = 1.5$ and the disk is spinning at rate of (a)$\Omega_D^* = -1$, (b)$\Omega_D^* = -1.2$, (c)$\Omega_D^* = -1.4$, (d)$\Omega_D^* = -1.6$, (e)$\Omega_D^* = -1.8$ and (f)$\Omega_D^* = -2$

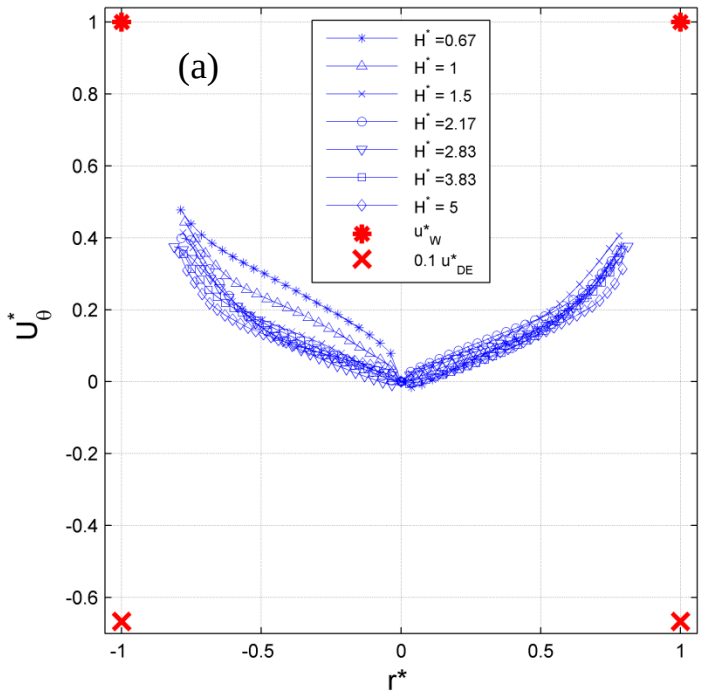
(a)
H* =0.67
H* = 1
H* = 1.5
H* =2.17
H* =2.83
H* =3.83
H* = 5
u*W
0.1 u*DE
U*θ
r*
1
0.8
0.6
0.4
0.2
0
-0.2
-0.4
-0.6
-1
-0.5
0
0.5
1

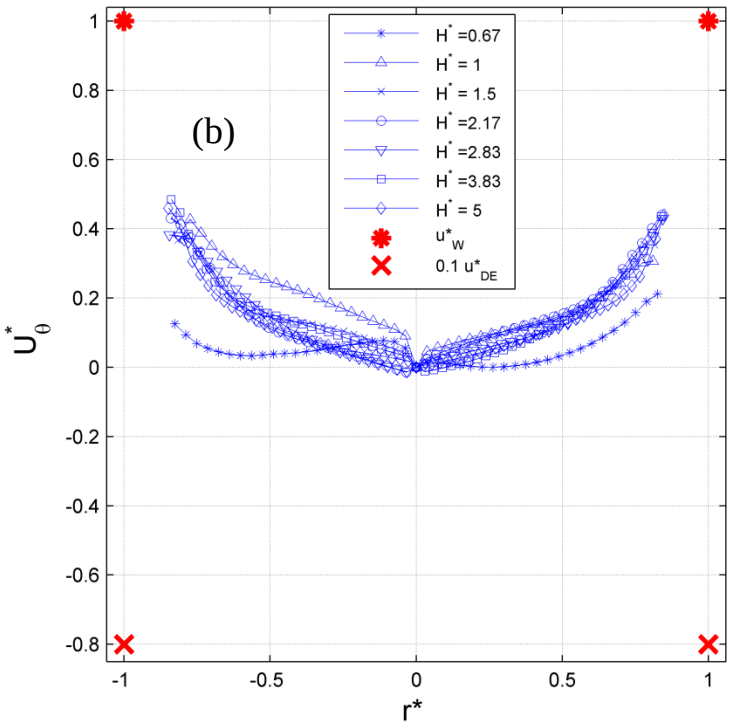
(b)
H* =0.67
H* = 1
H* = 1.5
H* =2.17
H* =2.83
H* =3.83
H* = 5
u*W
0.1 u*DE
U*θ
r*
1
0.8
0.6
0.4
0.2
0
-0.2
-0.4
-0.6
-0.8
-1
-0.5
0
0.5
1

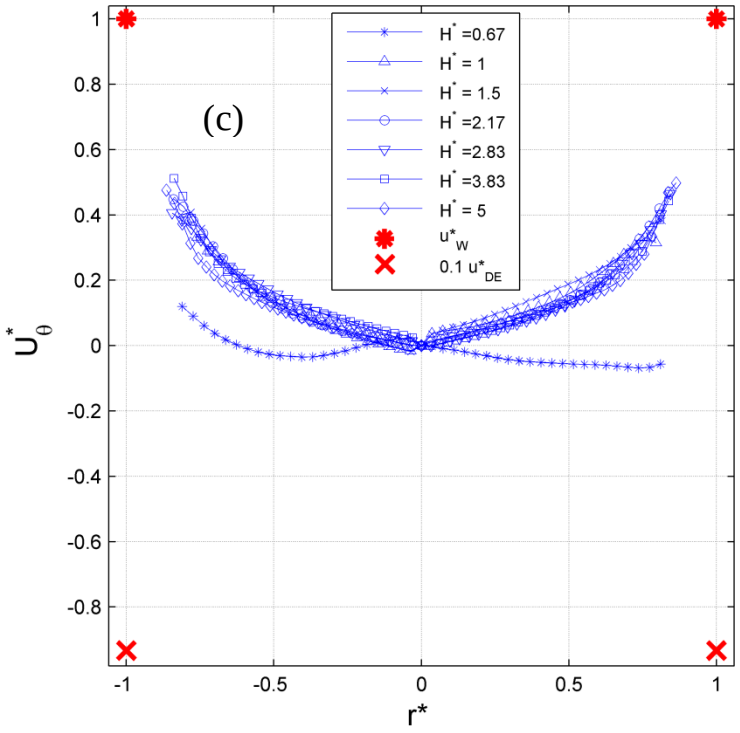
(c)
H* =0.67
H* = 1
H* = 1.5
H* =2.17
H* =2.83
H* =3.83
H* = 5
u*W
0.1 u*DE
U*θ
r*
1
0.8
0.6
0.4
0.2
0
-0.2
-0.4
-0.6
-0.8
-1
-0.5
0.5

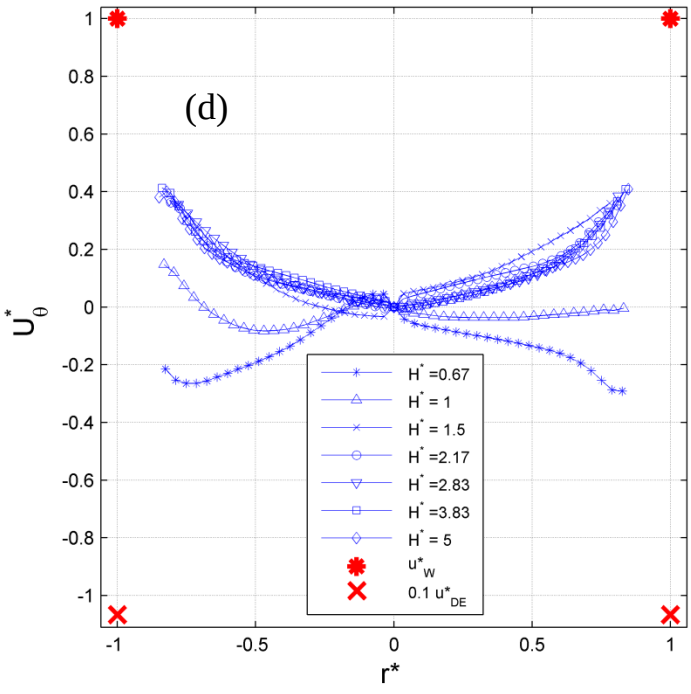
(d)
H* =0.67
H* = 1
H* = 1.5
H* =2.17
H* =2.83
H* =3.83
H* = 5
u*W
0.1 u*DE
U*θ
r*
1
0.8
0.6
0.4
0.2
0
-0.2
-0.4
-0.6
-0.8
-1
-0.5
0.5

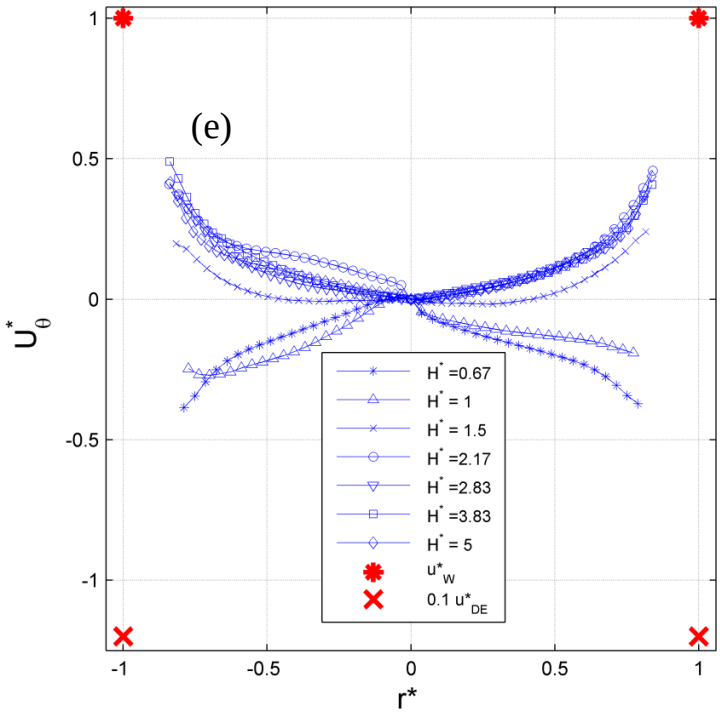

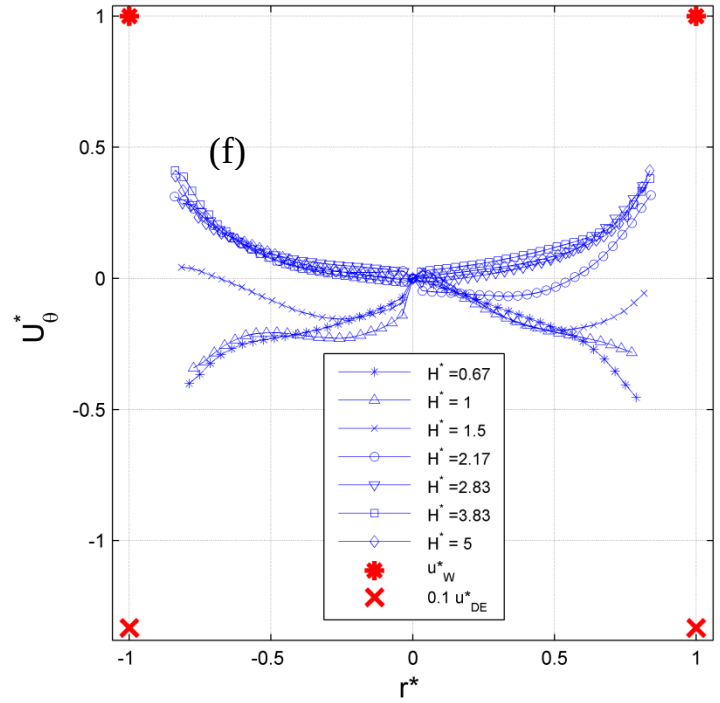

Figure 7.2 $\left\langle u_\theta^* \right\rangle$-profiles in all measured heights $\Delta T = 50^o C$ for the Co-Rotating Flow cases when the wall spinning rate is $\Omega_W^* = 1.5$ and the disk is spinning at rate of (a)$\Omega_d^* = -1$, (b)$\Omega_d^* = -1.2$, (c)$\Omega_d^* = -1.4$, (d)$\Omega_d^* = -1.6$, (e)$\Omega_d^* = -1.8$ and (f)$\Omega_d^* = -2$

Similar to un-heated cases, k^* profiles are calculated and presented here. All curves ($\Delta T = 25^o C$) show higher values of k^* compared to the corresponding curves of un-heated cases. Moreover, less noise and random results are observed in the heated cases. Since k^* is larger, it seems that less error in results is expected. In figure 7.3-a, showing the lowest studied disk spin rate, curves from the top to the bottom and studied heights have the same order. Also, all curves exhibit the convex property with the maximum near the center. As mentioned earlier, it is believed that the transitional domain at this case is below the lowest measured height ($z^* = 0.67$). As the disk spin rate increases in the second figure 7.3-b and transitional domain ascends, at least in a small region, the curves of $z^* = 0.67$ and $z^* = 1$ cross each other and show close results. Figures 7-3-h and 7-4-h shows the k_V^*-profiles in the upper and transitional/lower domains. It is found that the value of k_V^* in the vertical plane is considerably smaller than the value of k^* in the cross-section.

In higher disk spin rates, curves that locate within the transitional do not necessarily show convex property and the peak could be anywhere between $-1 < r^* < 1$. These curves in the transitional domain also show much larger k^* compared to the other curves and heights do not follow the descending order that is observed in figure 7.3-a. For instance, in figure 7.3-d, three curves associated with $z^* = 0.67$, $z^* = 1$ and $z^* = 1.5$, which are in or close to the transitional domain, are not convex (the negative second derivatives). These curves also have much higher values of k^*. Other four curves in figure 7.3-d are smoother with convex property and in descending order with respect to their heights in the similar fashion that was described in figure 7-1-a for the lowest disk spin rate. Figures 7.3-g and 7.4-g show k^* profiles in averaged in two domain below and above $z^* = 1.5$. It can clearly be seen that the value of k^* in the transitional

domain is much higher, and the k^*-profile in the upper domain exhibits the convex property with the maximum near the center. This indicates that the buoyancy effect due to disk heating considerably enhance the turbulent kinetic energy in the counter-rotating-cylinder-disk-flow. The more direct evidences for this observation are provided in Figure 6.22-a where k^* is plotted as a function of z^* for three Grashof numbers ($Gr = 0$, 1.37×10^4 and 2.4×10^4). The values of k^*, particularly the peak value of k^*, increase with Gr. As mentioned earlier, the locations where the peaks of k^* occur approximately correspond to the transitional domains. The peak value of k^* shown in Figure 6-23-a as a function of Ω_d^*, which indicates that the peak value of k^* increase with Gr in a range of Ω_d^*. In addition, as shown in Fig. Figure 6.22-b, the magnitude of the normalized circulation $\Gamma^* = \Gamma / \Omega_w R^2$ is considerably enhanced by disk heating, and it increases with Gr in a range of $z^* = 0.67 - 1.5$ even though the behavior of Γ^* in $z^* = 2.17 - 5$ needs to be further clarified. The peak value of Γ^* is shown in Figure 6.23-b as a function of Ω_d^* for three Grashof numbers, which are considerably increased for $Gr = 1.37 \times 10^4$ and 2.4×10^4. The value of $max(\Gamma^*)$ has a slightly decaying trend as Ω_d^* increases. Furthermore, as shown in Figure 7.15 and 7.33, it is found that the average location of the transitional domain moved downward to the disk as Gr increases.

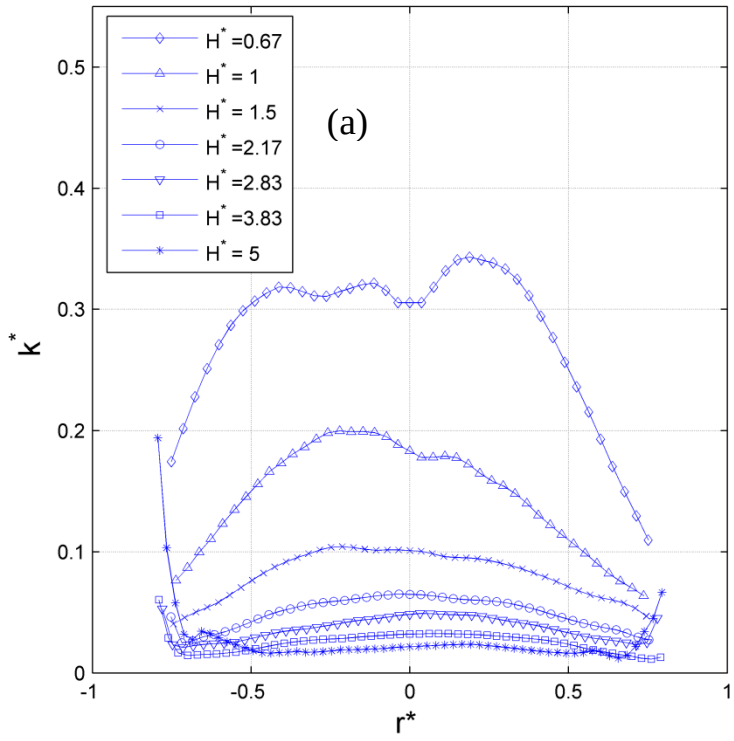
H* =0.67
H* = 1
H* = 1.5
H* =2.17
H* =2.83
H* =3.83
H* = 5
(a)
k*
r*
0
0.1
0.2
0.3
0.4
0.5
-1
-0.5
0
0.5
1

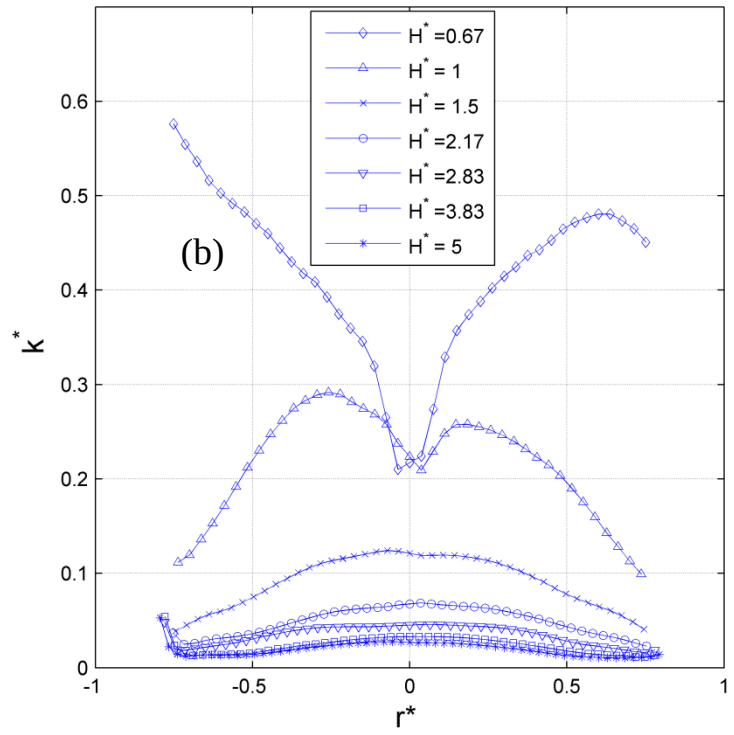
H* =0.67
H* = 1
H* = 1.5
H* =2.17
H* =2.83
H* =3.83
H* = 5
(b)
k*
r*
0
0.1
0.2
0.3
0.4
0.5
0.6
-1
-0.5
0
0.5
1

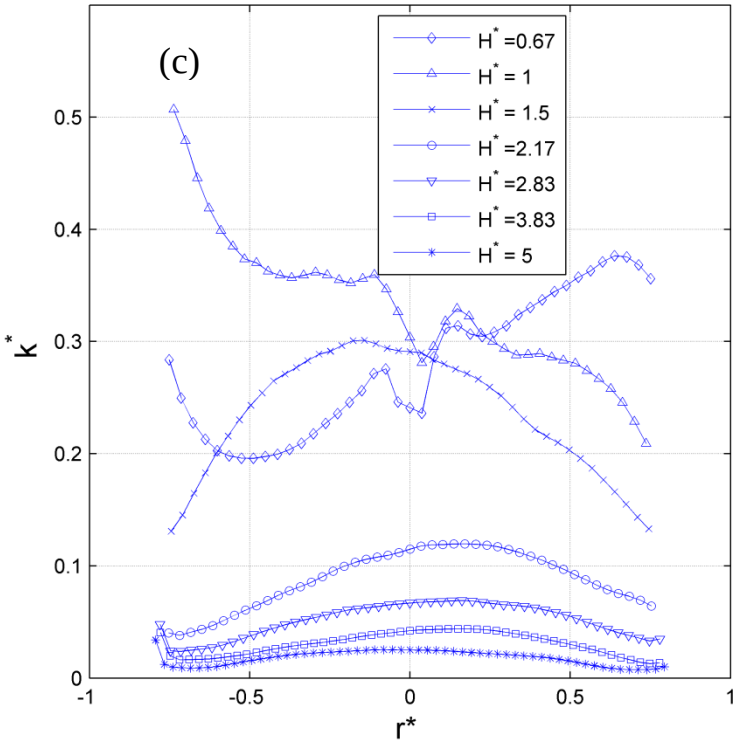
(c)
H* =0.67
H* = 1
H* = 1.5
H* =2.17
H* =2.83
H* =3.83
H* = 5
k*
r*
0
0.1
0.2
0.3
0.4
0.5
-1
-0.5
0
0.5
1

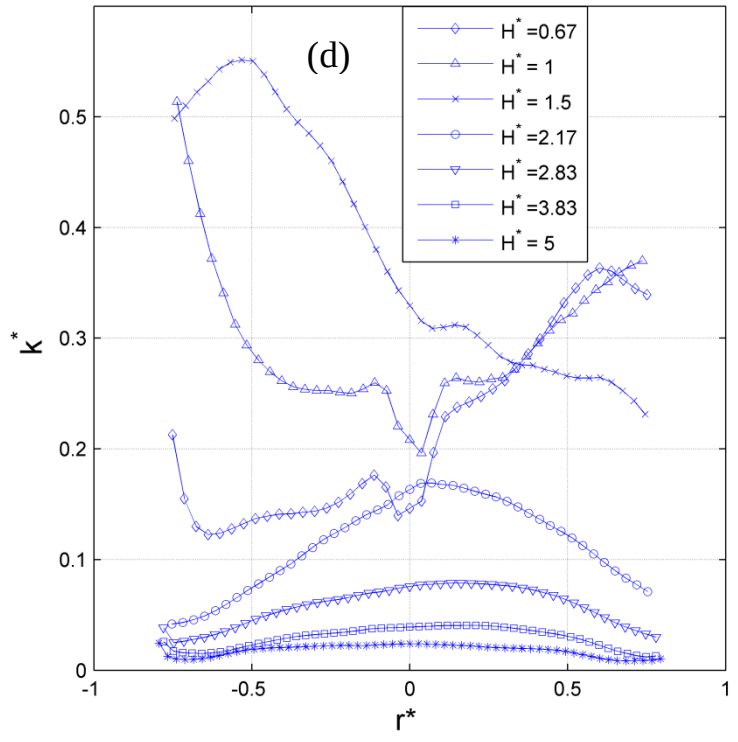
(d)
H* =0.67
H* = 1
H* = 1.5
H* =2.17
H* =2.83
H* =3.83
H* = 5
k*
r*
0
0.1
0.2
0.3
0.4
0.5
-1
-0.5
0
0.5
1

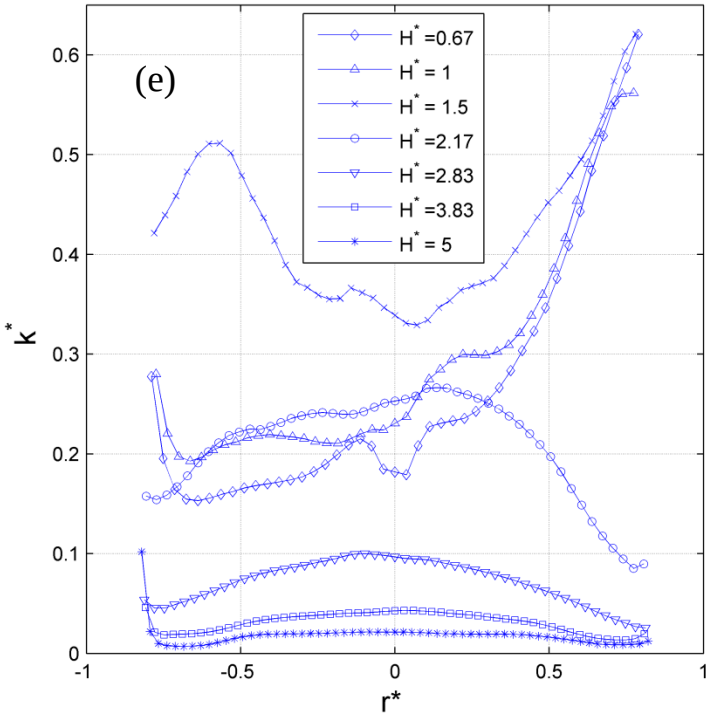
(e)
H* =0.67
H* = 1
H* = 1.5
H* =2.17
H* =2.83
H* =3.83
H* = 5
k*
r*
0.6
0.5
0.4
0.3
0.2
0.1
0
-1
-0.5
0
0.5
1

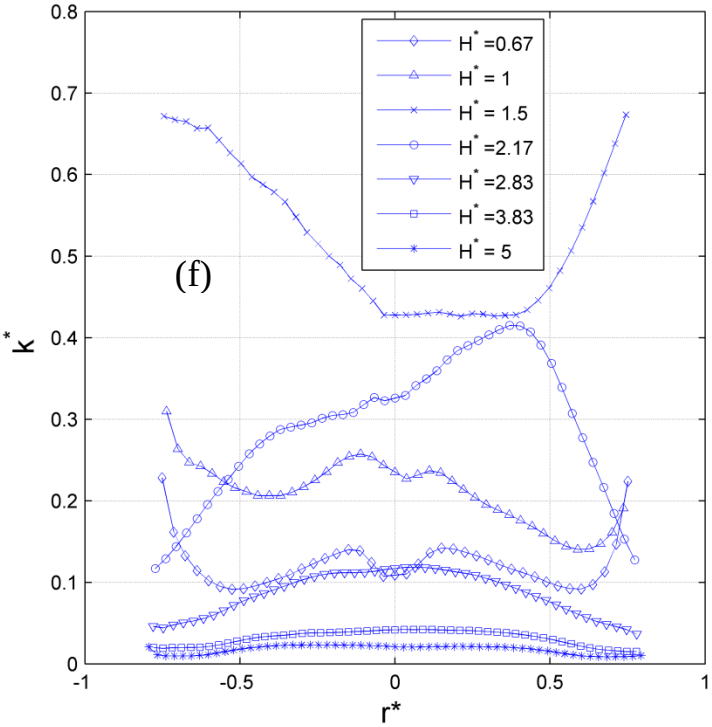
(f)
H* =0.67
H* = 1
H* = 1.5
H* =2.17
H* =2.83
H* =3.83
H* = 5
k*
r*
0.8
0.7
0.6
0.5
0.4
0.3
0.2
0.1
0
-1
-0.5
0
0.5
1

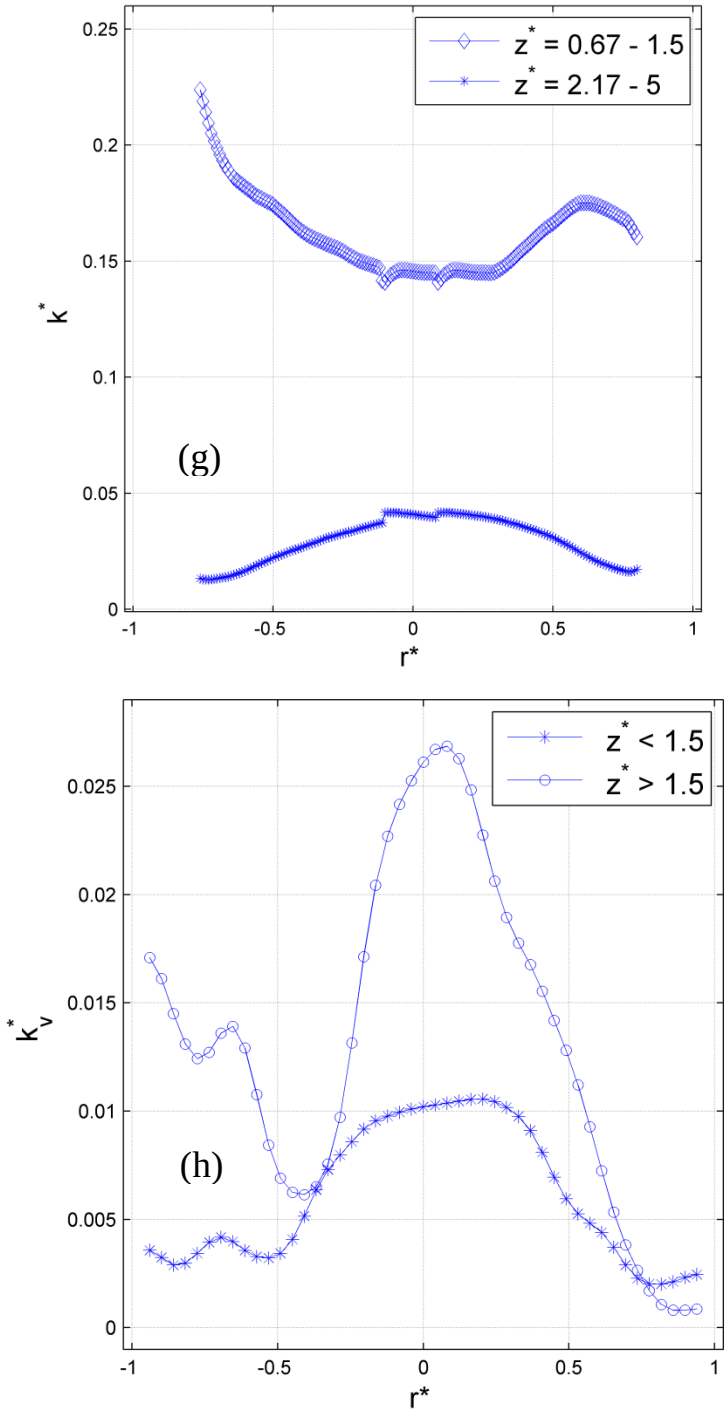

Figure 7.3 Normalized turbulent kinetic energy in all measured heights for one heated, Counter-Rotating flow case when $\Delta T = 25^{o}C$ $\Omega_w^* = 1.5$ (a) $\Omega_d^* = 1$, (b) $\Omega_d^* = 1.2$, (c) $\Omega_d^* = 1.4$, (d) $\Omega_d^* = 1.6$, (e) $\Omega_d^* = 1.8$, (f) $\Omega_d^* = 2$, (g) the upper and transitional domains at $\Omega_w^* = 1.5$ and $\Omega_d^* = -1.6$ and (h) k_V^* profiles in two domains

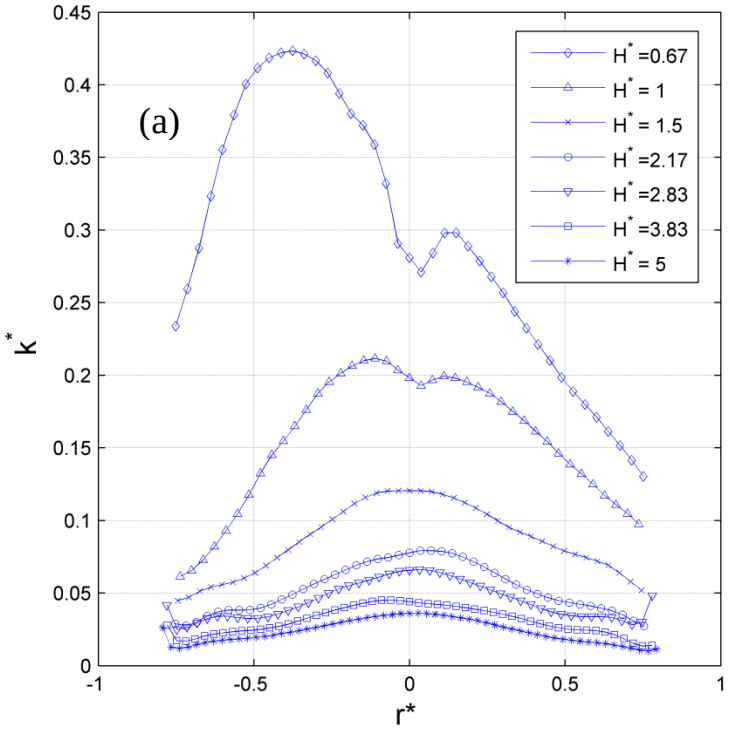
(a)
H* =0.67
H* = 1
H* = 1.5
H* =2.17
H* =2.83
H* =3.83
H* = 5
k*
r*
0.45
0.4
0.35
0.3
0.25
0.2
0.15
0.1
0.05
0
-1
-0.5
0
0.5
1

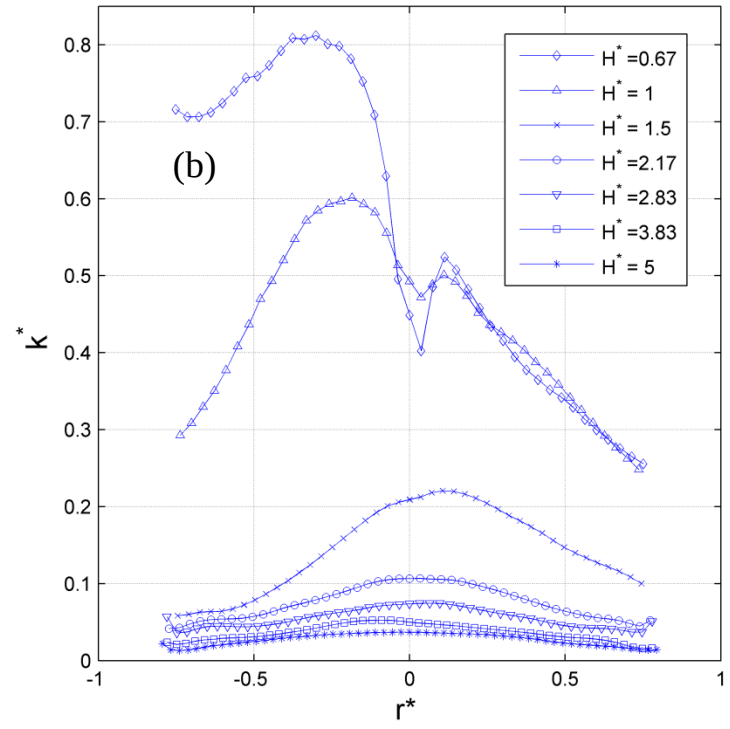
(b)
H* =0.67
H* = 1
H* = 1.5
H* =2.17
H* =2.83
H* =3.83
H* = 5
k*
r*
0.8
0.7
0.6
0.5
0.4
0.3
0.2
0.1
0
-1
-0.5
0
0.5
1

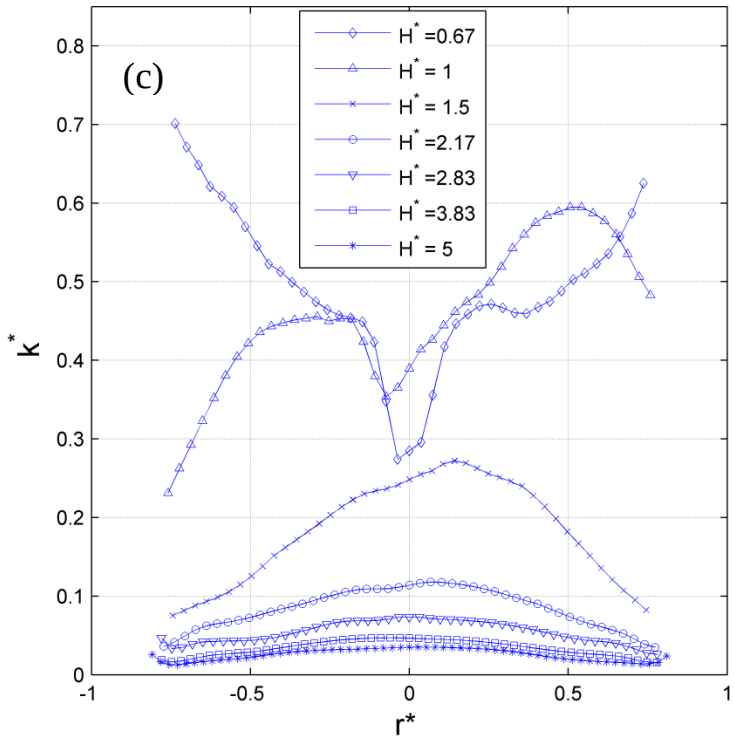
(c)
H* =0.67
H* = 1
H* = 1.5
H* =2.17
H* =2.83
H* =3.83
H* = 5
k*
r*
0
0.1
0.2
0.3
0.4
0.5
0.6
0.7
0.8
-1
-0.5
0
0.5
1

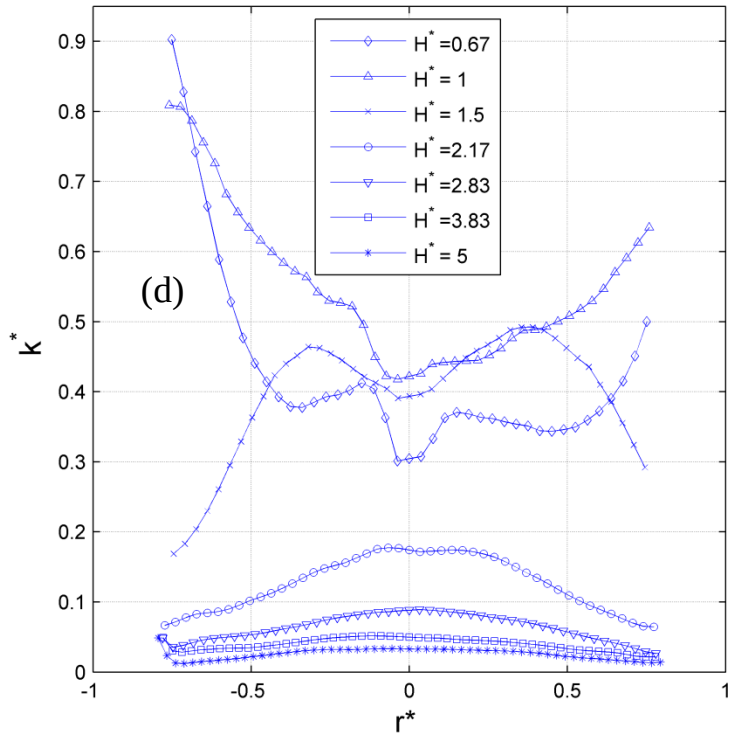
(d)
H* =0.67
H* = 1
H* = 1.5
H* =2.17
H* =2.83
H* =3.83
H* = 5
k*
r*
0
0.1
0.2
0.3
0.4
0.5
0.6
0.7
0.8
0.9
-1
-0.5
0
0.5
1

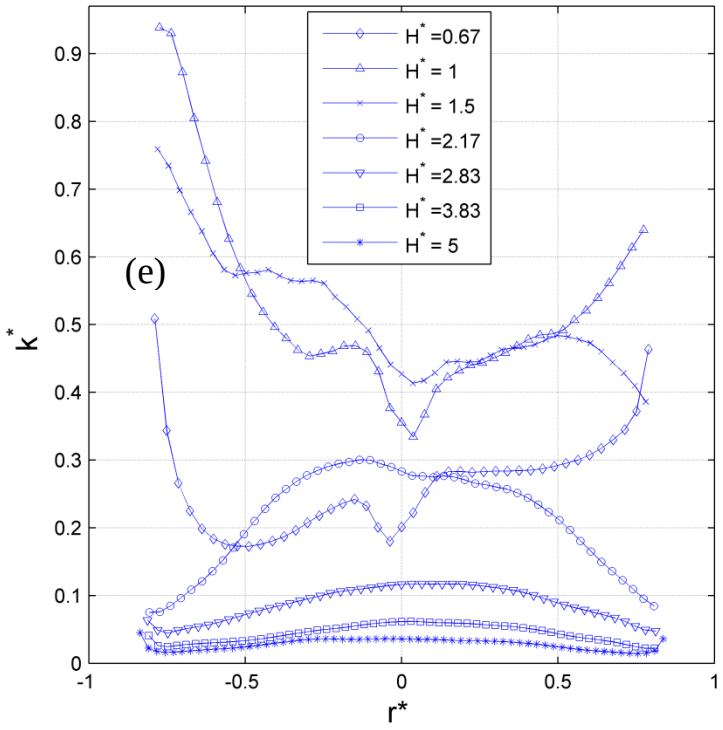
H* =0.67
H* = 1
H* = 1.5
H* =2.17
H* =2.83
H* =3.83
H* = 5
(e)
k*
r*
0
0.1
0.2
0.3
0.4
0.5
0.6
0.7
0.8
0.9
-1
-0.5
0
0.5
1

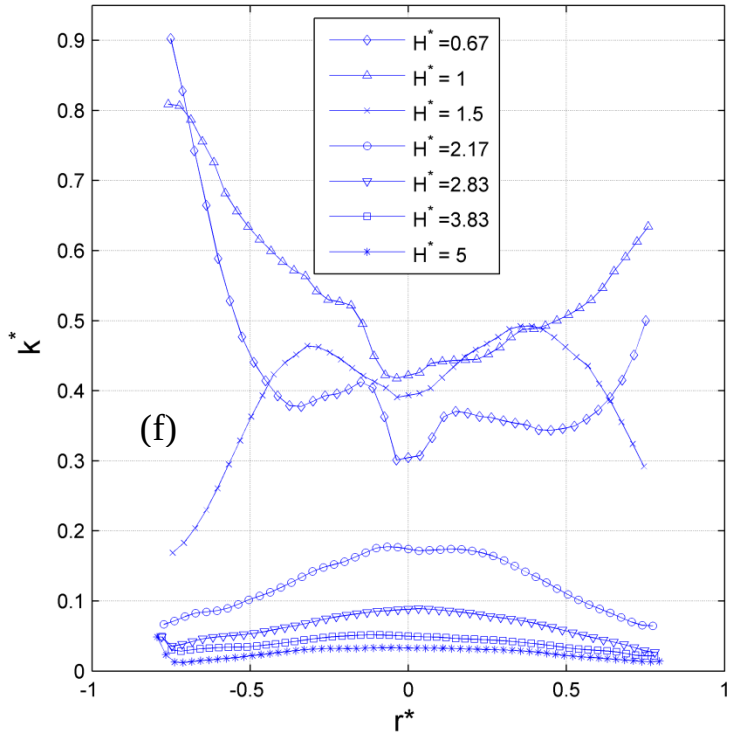
H* =0.67
H* = 1
H* = 1.5
H* =2.17
H* =2.83
H* =3.83
H* = 5
(f)
k*
r*
0
0.1
0.2
0.3
0.4
0.5
0.6
0.7
0.8
0.9
-1
-0.5
0
0.5
1

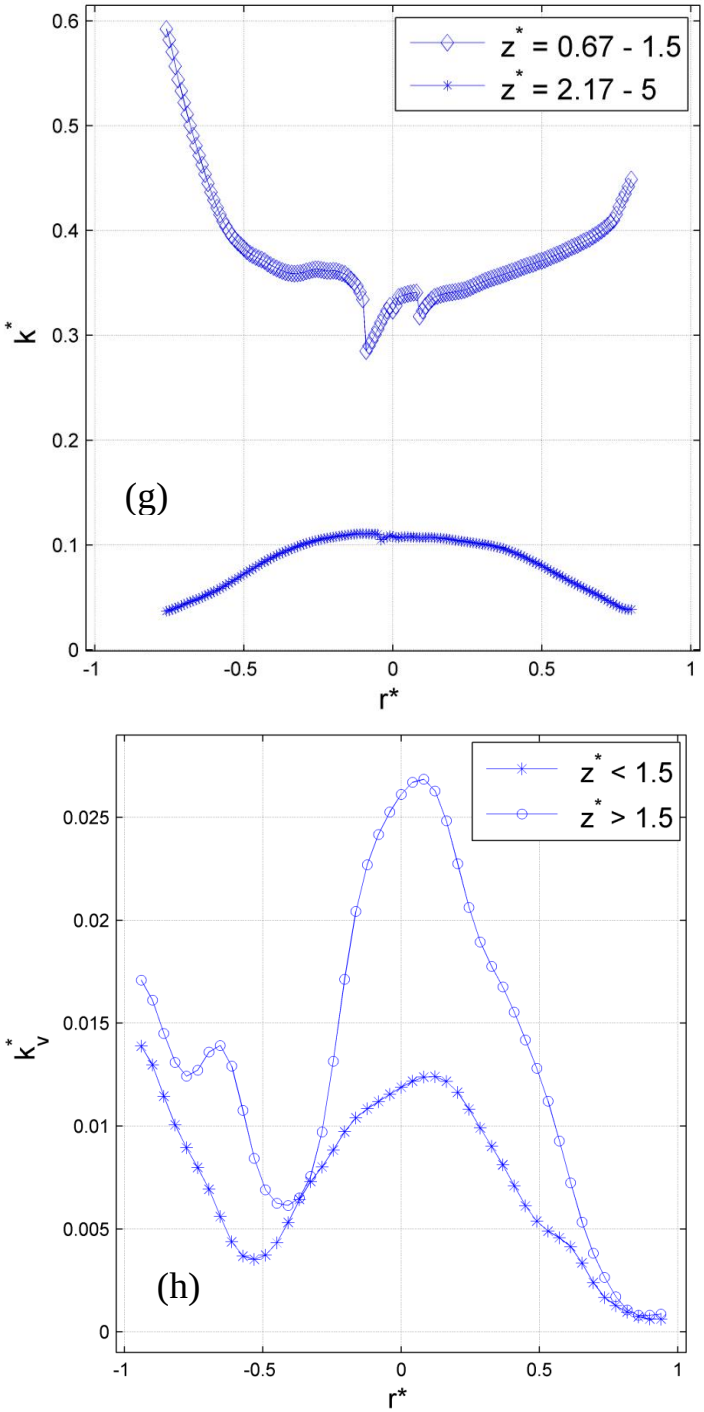

Figure 7.4 Normalized turbulent kinetic energy in all measured heights for one heated, Counter-Rotating Flow case when $\Delta T = 50^{o}C$ $\Omega_{w}^{*} = 1.5$ (a) $\Omega_{D}^{*} = 1$, (b) $\Omega_{D}^{*} = 1.2$, (c) $\Omega_{D}^{*} = 1.4$, (d) $\Omega_{D}^{*} = 1.6$, (e) $\Omega_{D}^{*} = 1.8$, (f) $\Omega_{D}^{*} = 2$, (g) the upper and transitional domains at $\Omega_{w}^{*} = 1.5$ and $\Omega_{d}^{*} = -1.6$, (h) k_{V}^{*} profiles in two domains

Similar to previous sections, details of the flow are presented for each disk spin rate. The focus is to show as much detail as possible from the transitional domain. figure 7.5 shows the

average of velocity vector fields for the Counter-Rotating case in different heights when the wall spin rate is $\Omega_w^* = 1.5$, disk spin rate is $\Omega_d^* = -1$and $\Delta T = 25^oC$ ($Gr = 1.37 \times 10^4$).This figure shows that all heights are rotating counter-clock-wise and following the wall.

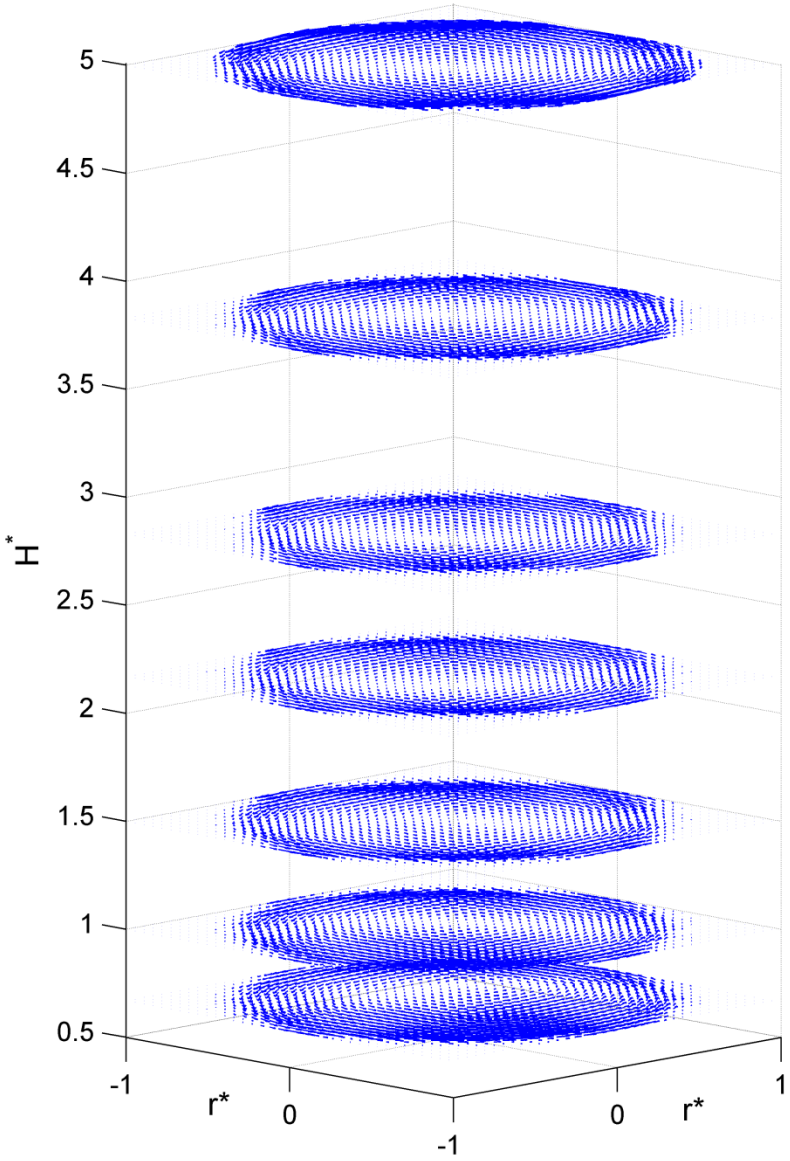

Figure 7.5 Velocity vector field for all studied heights for one Heated Counter-Rotating flow case: $\Delta T = 25^oC$ $\Omega_w^* = 1.5$ and the disk spin rate $\Omega_D^* = -1$

Clearly, the transitional domain has not reached the lowest studied height, $z^* = 0.67$. Velocity vector fields in higher heights are very similar and a high velocity ring surrounding the

large low velocity region. Vector field in some heights do not show clear results in very outer radii. As explained before, this uncertainty in larger radii is due to lack of particles and makes the results unreliable locally.

Velocity vector field superposed on magnitude field and azimuthal velocity component along several sections for the lowest studied height are shown in figures 7.6 and 7.7. Similar to some other cases in unheated Counter Rotating flow, center of vortex in this figure is not at the centerline of the cylinder as can be seen in figure 7.6. Therefore, different sections in figure 7.7 show different values for u_θ^*. In some sections the center (minimum of the curve) is at $r^* < 0$ and in others it is located at $r^* > 0$. In other heights vortex is not as off-center as it is at $z^* = 0.67$ and as a result velocity profile peak is closer to $r^* = 0$. Maximum velocity in figures 7.6 and 7.7 is about $u_{\theta,Max}^* = 0.45$ which is significantly lower than other heights. This value in other heights is usually $0.6 < u_{\theta,Max}^* < 0.8$. It can be due to being close to the disk and the influence of the transitional domain. In figure 7.6 and many other velocity vector / magnitude fields in the vicinity of four points that masked circle and surrounding square meet, velocity is slightly larger. It only happens very close to the wall and makes results seem locally unreliable. Since results near the wall are already deleted from all velocity profiles, the rest of curves do not seem to be affected by this error.

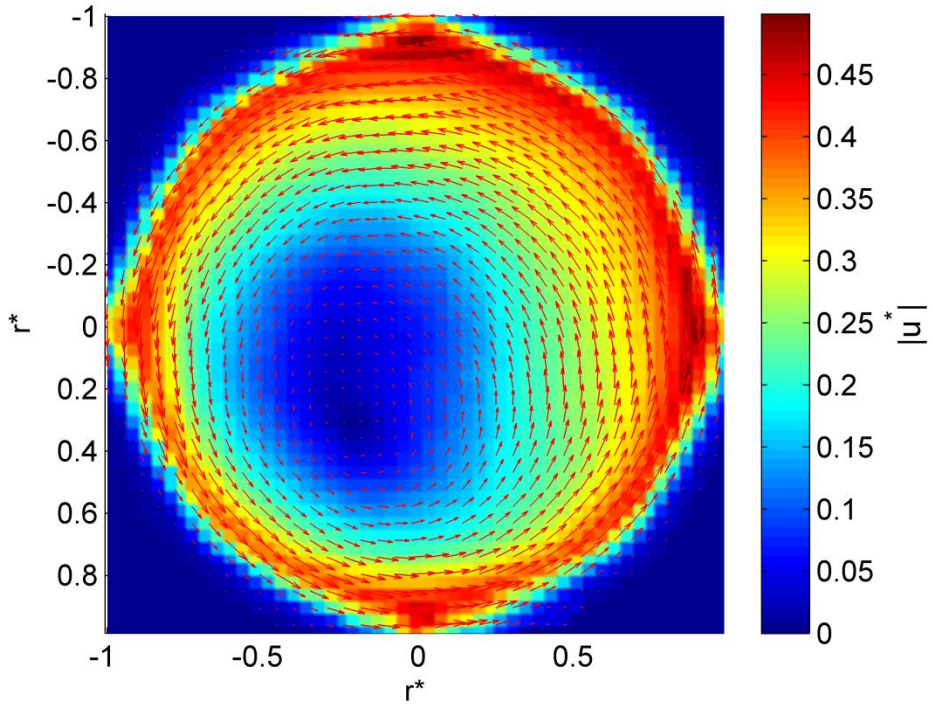

Figure 7.6 The velocity vector and magnitude field for the Heated Counter-Rotating Flow when: $\Delta T = 25^{o}C$, $\Omega_w^* = 1.5$, $\Omega_d^* = -1$for one height: $z^* = 0.67$

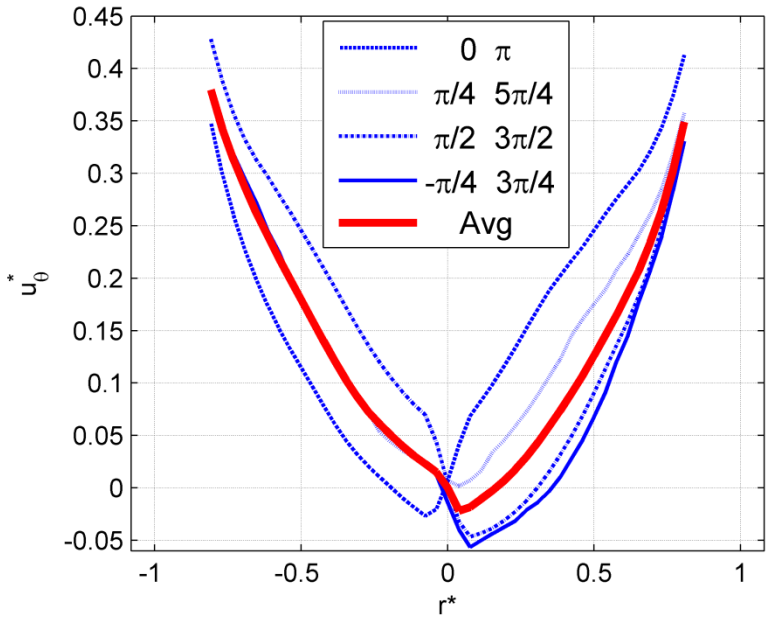

Figure 7.7 Normalized azimuthal velocity profile averaged over the half-circle-sectors and selected profiles across four radial sections for the Heated Counter-Rotating flow when: $\Delta T = 25^{o}C$, $\Omega_w^* = 1.5$, $\Omega_z^* = -1$, $z^* = 0.67$

The next disk speed is $\Omega_d^* = -1.2$ and other conditions are kept the same. Velocity vector fields are demonstrated in figures 7.8 a and b. Again, three lower heights and four higher ones are shown separately to display more detail in each figure. Although the flow pattern in the second and the third heights are slightly different from other heights, all six higher heights are more or less similar with the high velocity ring and low velocity region in the middle.

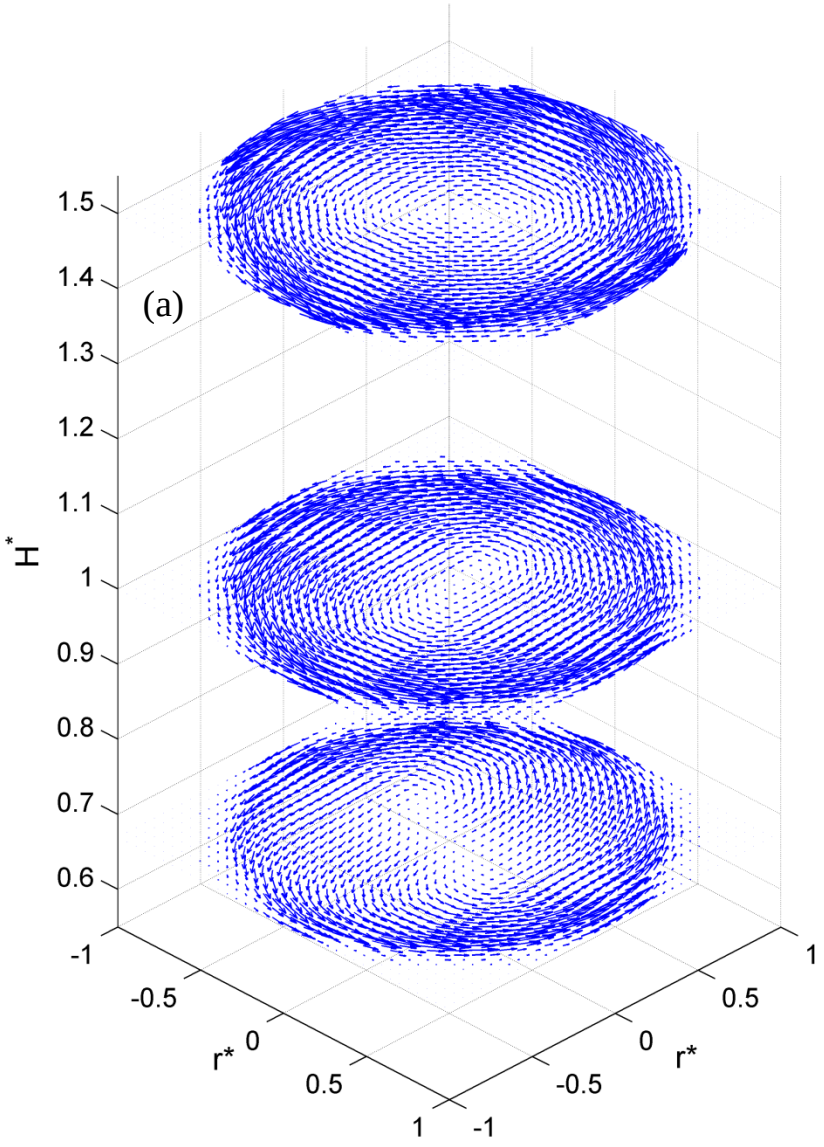

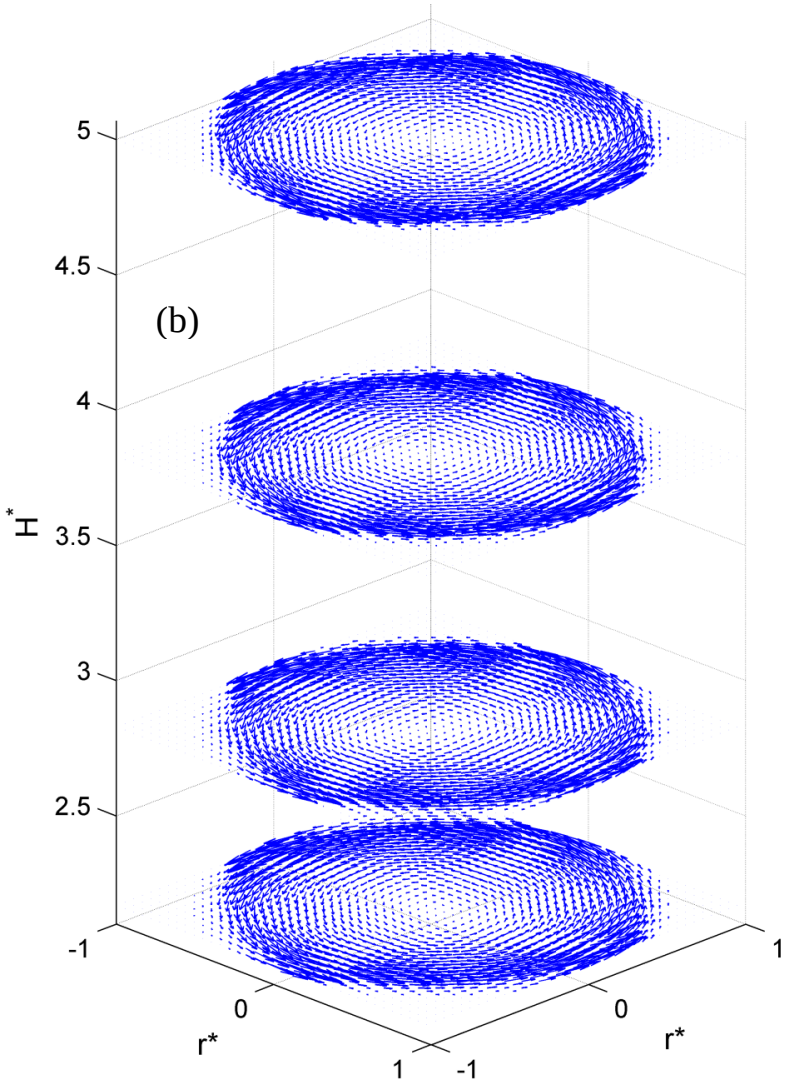

Figure 7.8 Velocity vector field for one Heated Counter-Rotating flow case: $\Delta T = 25^{o}C$ $\Omega_w^* = 1.5$ and the disk spin rate $\Omega_d^* = -1.2$ for (a): three lower studied heights and (b) four higher ones

In addition, at the first height, $z^* = 0.67$, flow pattern is quite different. At this height flow at the center is not rotating in the same direction that it does in the outer region. It seems that two clockwise vortices next to each other exist. Due to the disk effect those two vortices are not colliding although they rotate in the same direction and relatively close to each other. Vortex at the center of the second height, $z^* = 1$, is more like an oval rather than being circular. Also, the size of vectors in figure a clearly shows that magnitude of velocity in the third height is

considerably larger than this value in the first two heights. Although all vector/magnitude fields are not presented here, it has been seen that above the first two heights velocity magnitude increases remarkably. Velocity vector / magnitude fields of these two heights are presented in figure 7.9 a and b.

Figure 7.9 shows more detail about the flow for the two lower heights of the second studied disk spin rate, $\Omega_d^* = -1.2$. Two counter rotating vortices next to each other can be seen in figure a. At 2 and 8 O'clock these two vortices are closer to the wall which makes the flow speed larger close to the wall. However, maximum velocity in this height is significantly smaller than other ones, even compared to the same height in previous disk speed. In figure b height has increased and two vortices are merged and formed an oval shape. Maximum velocity is larger but still less than higher heights. Unlike the unheated case, the transitional domain at this disk spin rate is still below the lowest measured height.

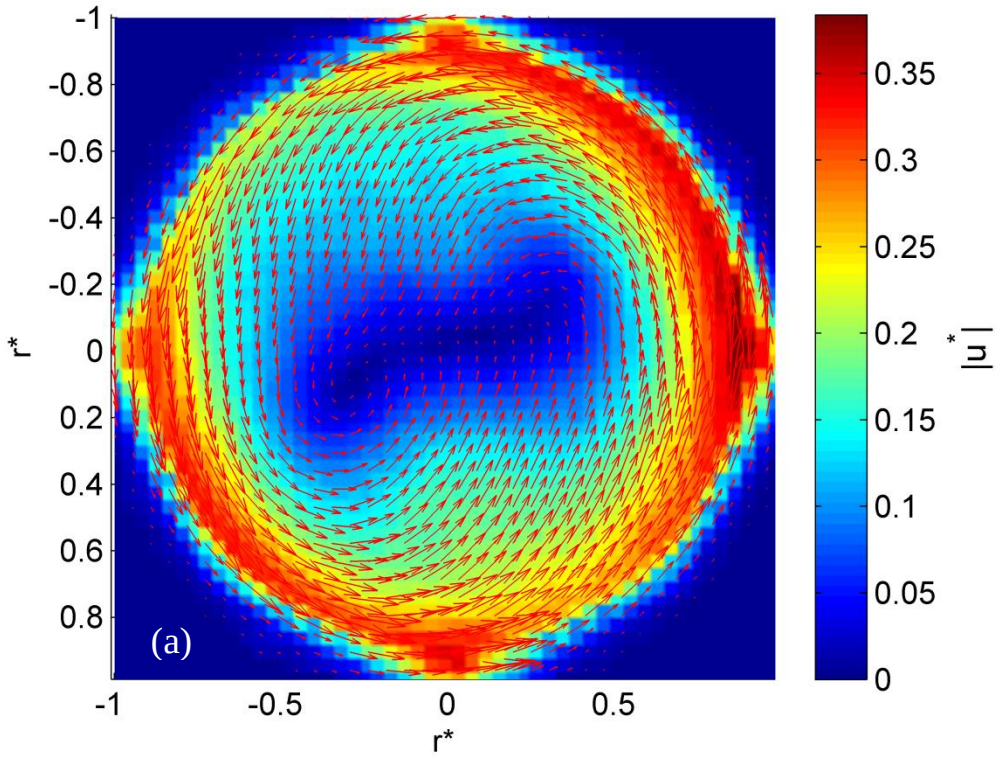

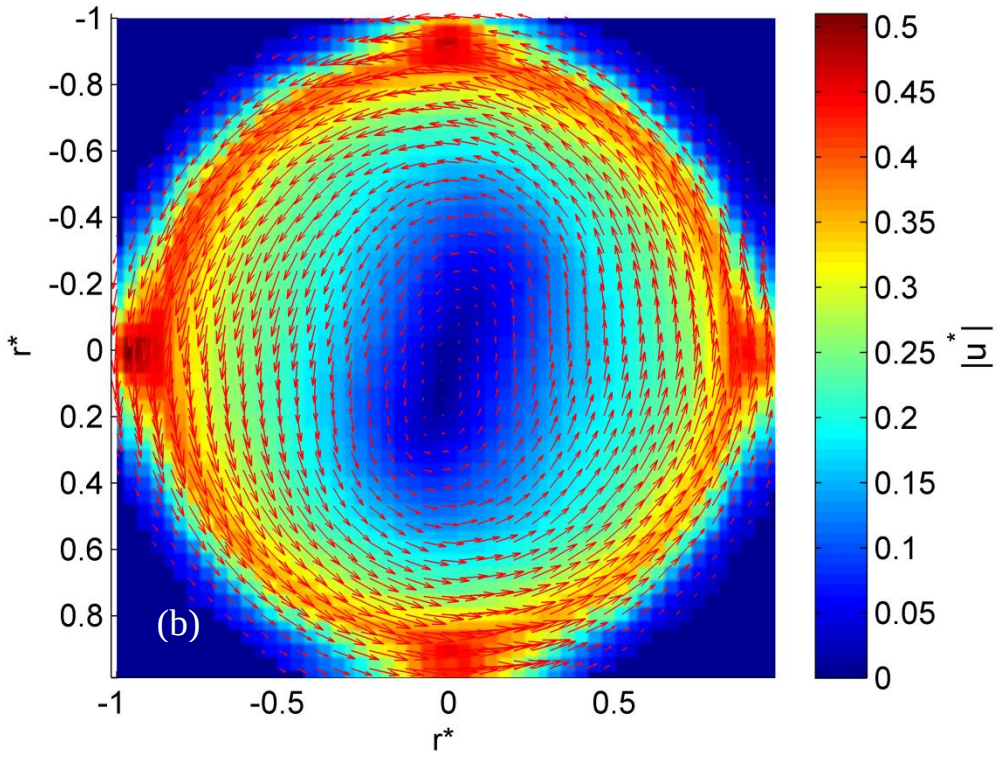

Figure 7.9 The velocity vector and magnitude field for the Heated Counter-Rotating Flow when: $\Delta T = 25^{o}C$, $\Omega_w^* = 1.5$, $\Omega_d^* = -1.2$ for heights (a): $z^* = 0.67$and (b): $z^* = 1$

Velocity profile sections are shown in figure 7.10 for those two heights. Due to non-axisymmetric behavior of flow in the first height, the difference between sections is more than other cases. Also, it can be seen that the magnitude of velocity at $z^* = 0.67$ in any radius is smaller compared to $z^* = 1$.

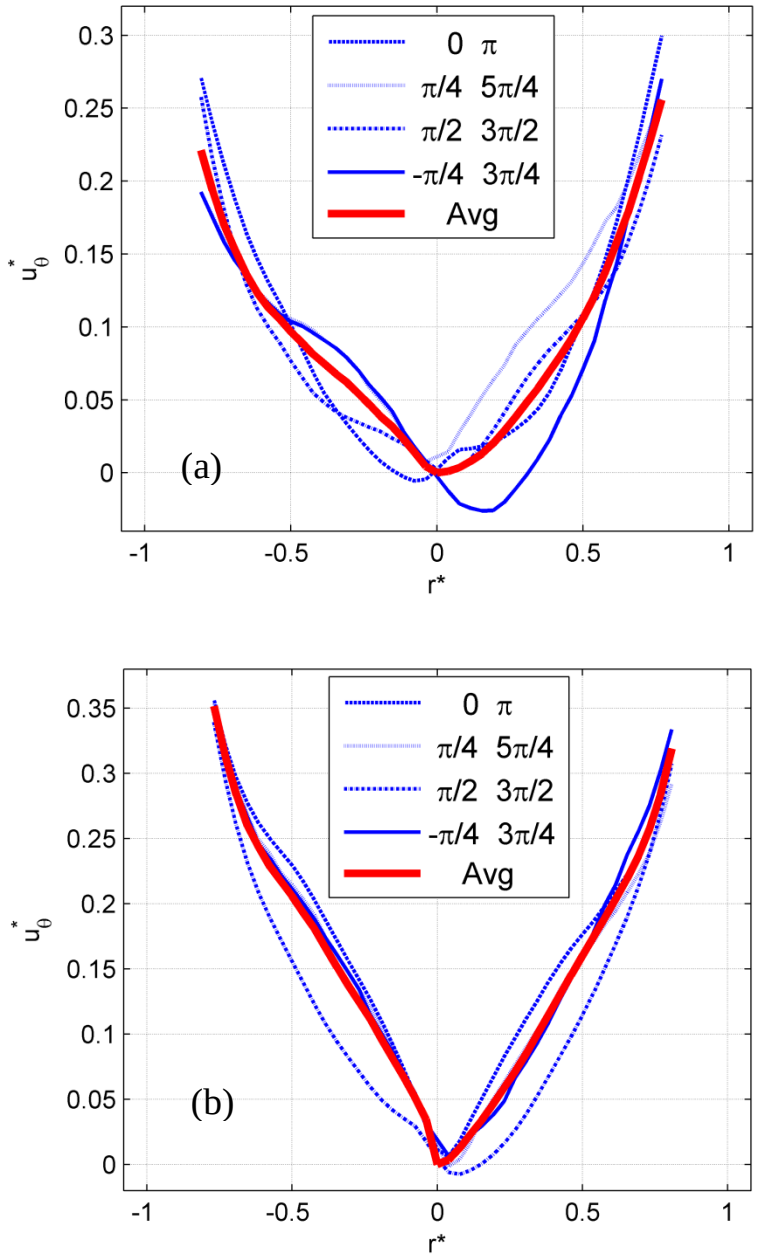

Figure 7.10 Normalized azimuthal velocity profile averaged over the half-circle-sectors and selected profiles across four radial sections for the Heated Counter-Rotating flow when: $\Delta T = 25^o C$, $\Omega_w^* = 1.5$, $\Omega_d^* = -1.2$ when (a): $z^* = 0.67$, (b): $z^* = 1$

Next disk spin rate is $\Omega_d^* = -1.4$ and figure 7.11 shows the vector fields for the different heights. Flow pattern that is shown in three lower heights of figure a is different with the previous disk spin rate. Unlike that case, in the lower height of this case there is a strong clock-wise in the center that follows the disk (lower domain). Also, flow in two lower heights is not

similar to those heights in lower disk speeds. Nonetheless, in four higher heights in figure b flow pattern in more or less similar to previous case with a high velocity ring near the wall and low velocity core. In the higher heights direction of rotation is always same with the wall (upper domain).

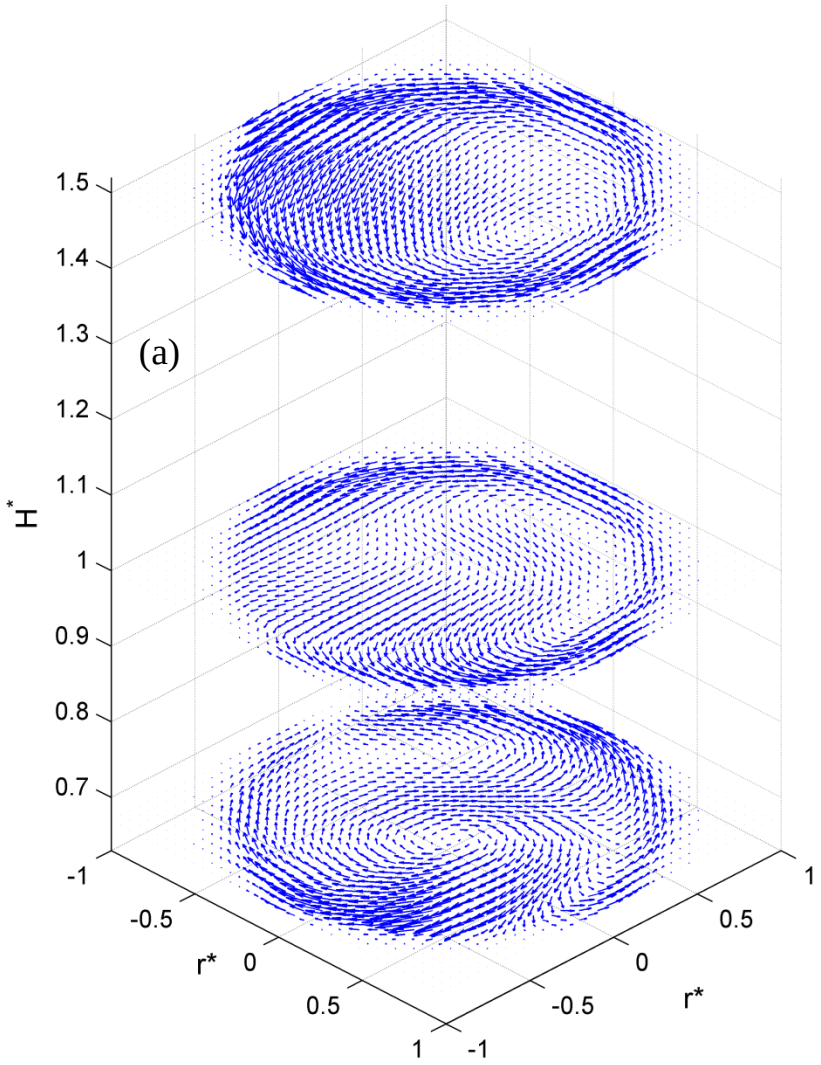

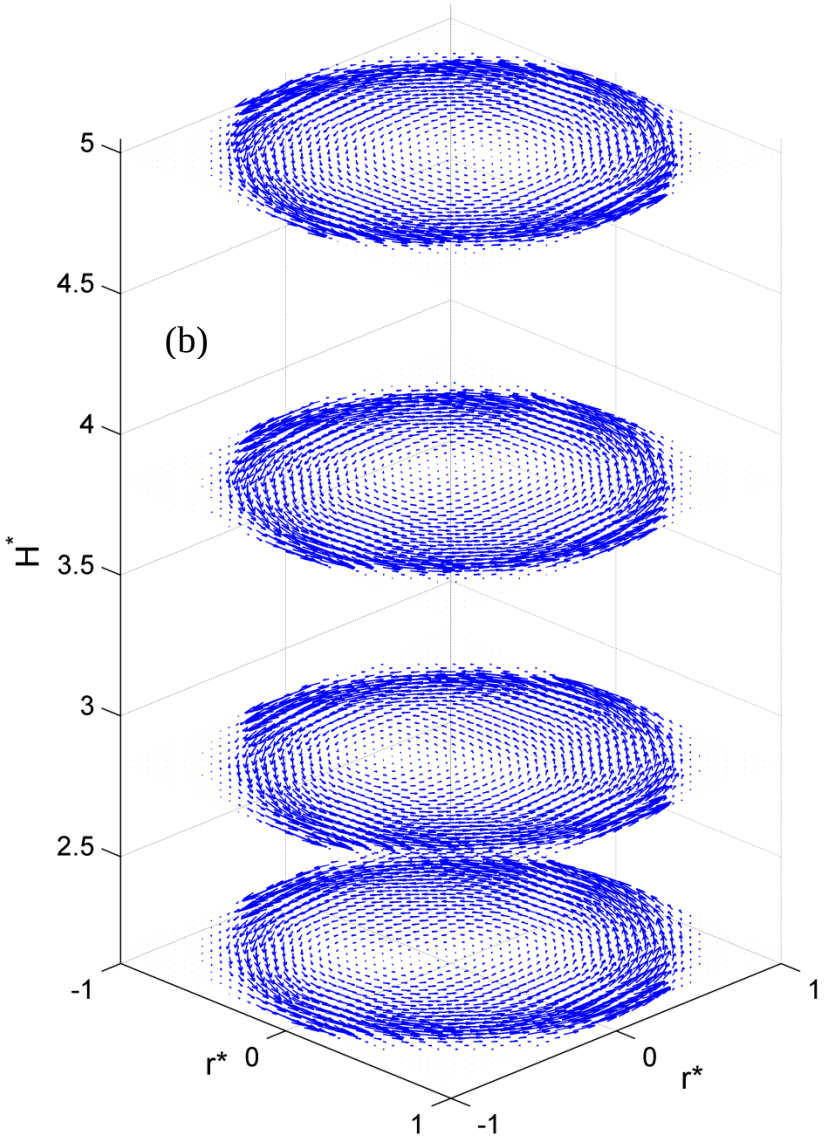

Figure 7.11 Velocity vector field for one Heated Counter-Rotating flow case: $\Delta T = 25^{o}C$ $\Omega_w^* = 1.5$ and the disk spin rate $\Omega_d^* = -1.4$ for (a): three lower studied heights and (b) four higher ones

Velocity magnitude/vector field of the three lower heights are shown in figure 7.12. In the first height, near the wall, flow has two opposite rotating directions in lower and higher halves of the section. Flow pattern is complex but overall follows the disk rotation (lower domain). In the second height flow is neither clock-wise nor counter-clock-wise (transitional domain). Finally in the third height, the wall rotation effect becomes dominant and flow is

rotating counter-clock-wise. However, this flow is not symmetric and center of flow is close to 3 O'clock (beginning of upper domain).

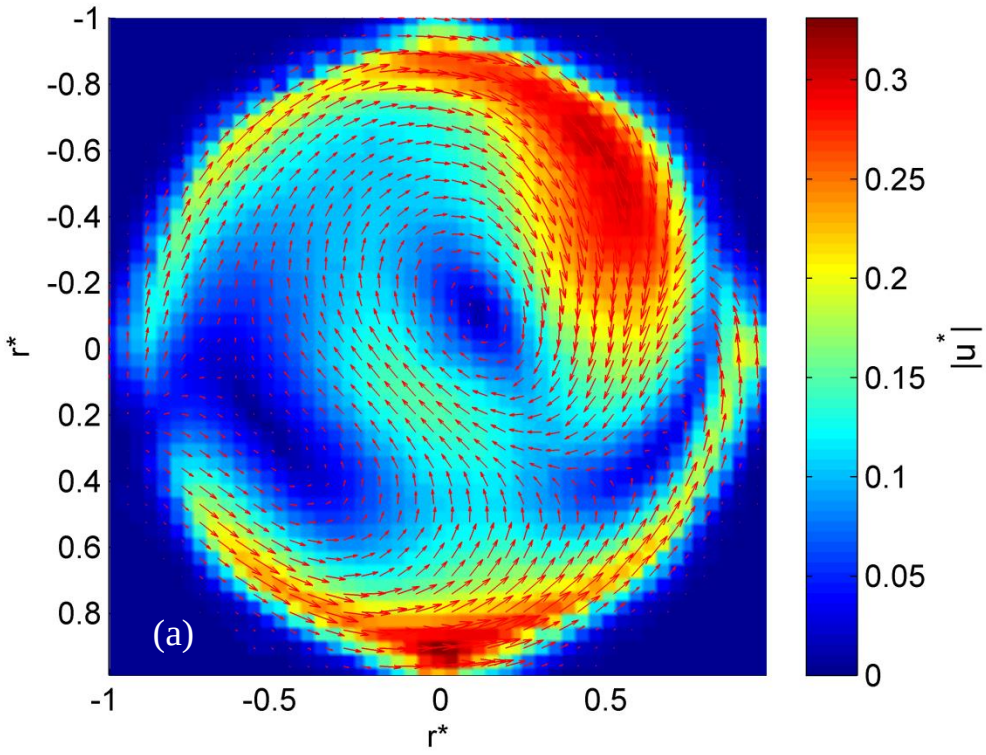

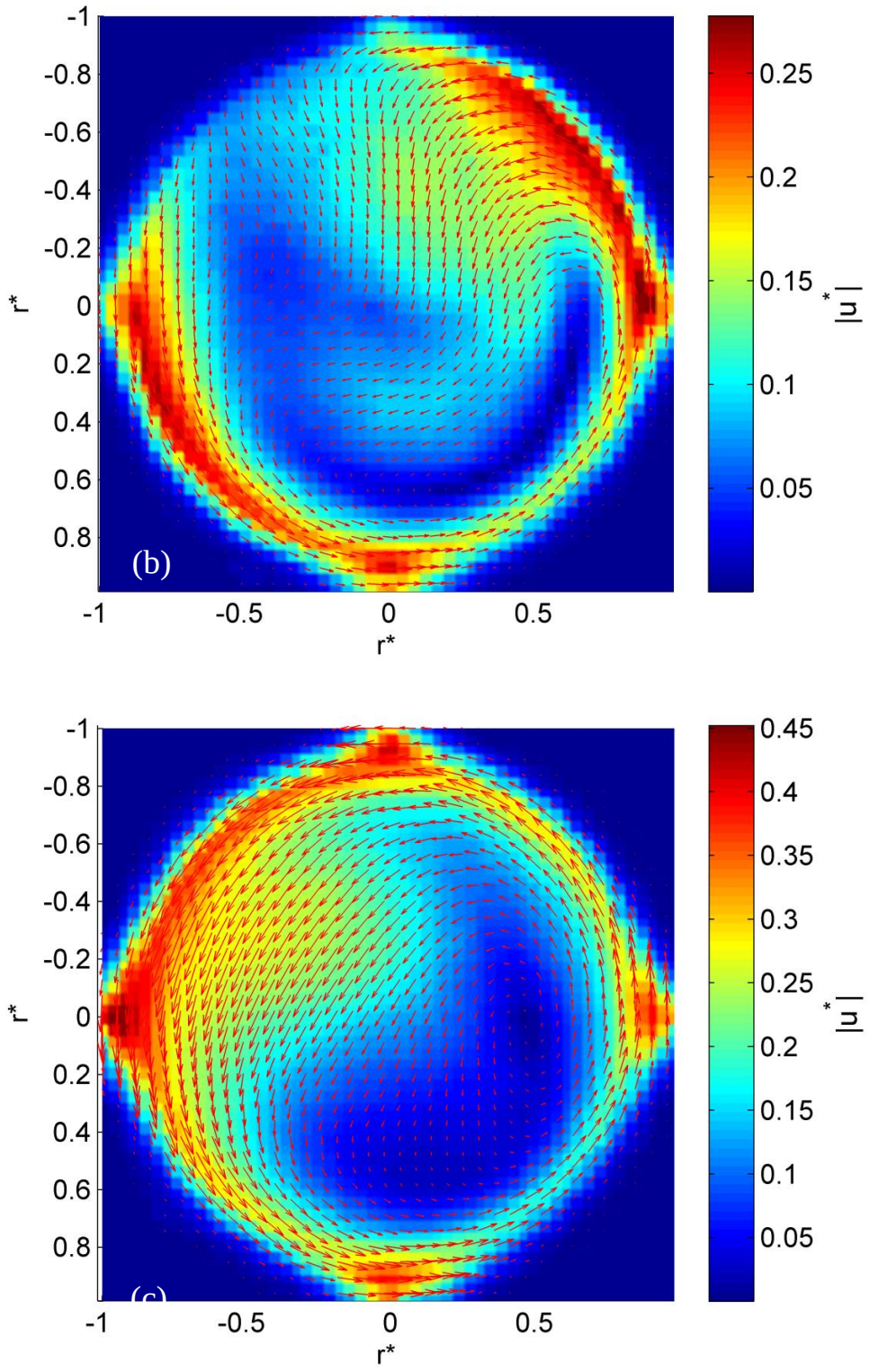

Figure 7.12 The velocity vector and magnitude field for the Heated Counter-Rotating Flow when: $\Delta T = 25^{o}C$, $\Omega_w^* = 1.5$, $\Omega_d^* = -1.4$ for heights (a): $z^* = 0.67$, (b): $z^* = 1$ and (c): $z^* = 1.5$

The axisymmetric and complex behavior of the flow for the first three heights can be seen in the figure 7.13. In the first height curves of different sections behave completely differently and the sign of u_θ^* changes multiple times in some sections (especially in the horizontal and vertical section: $0 - \pi$ and $\pi/2\_3\ \pi/2$). Maximum magnitude of azimuthal velocity for the average curve in this height is not much more than 0.15. In the second height although the maximum value is close the first height, the pattern of flow seems to be completely different. Section curves compared to the average curve behave differently but their sign do not change in a similar fashion with the first height. Figure c shows that flow start to follow the wall, maximum value becomes significantly larger and curve in different section begin to become more similar. All three figures 7.11, 7.12 and 7.13 indicate that the transitional domain is located around $z^* = 1$ in this disk spin rate.

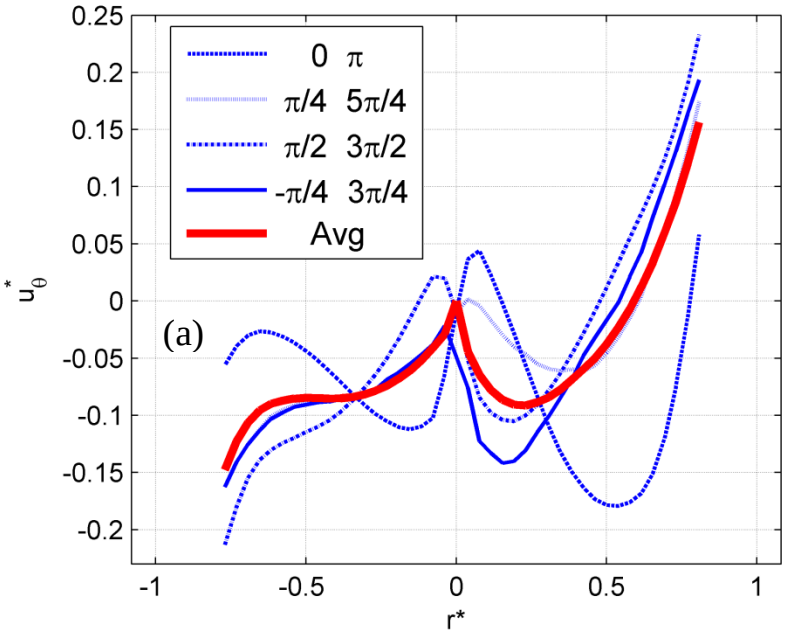

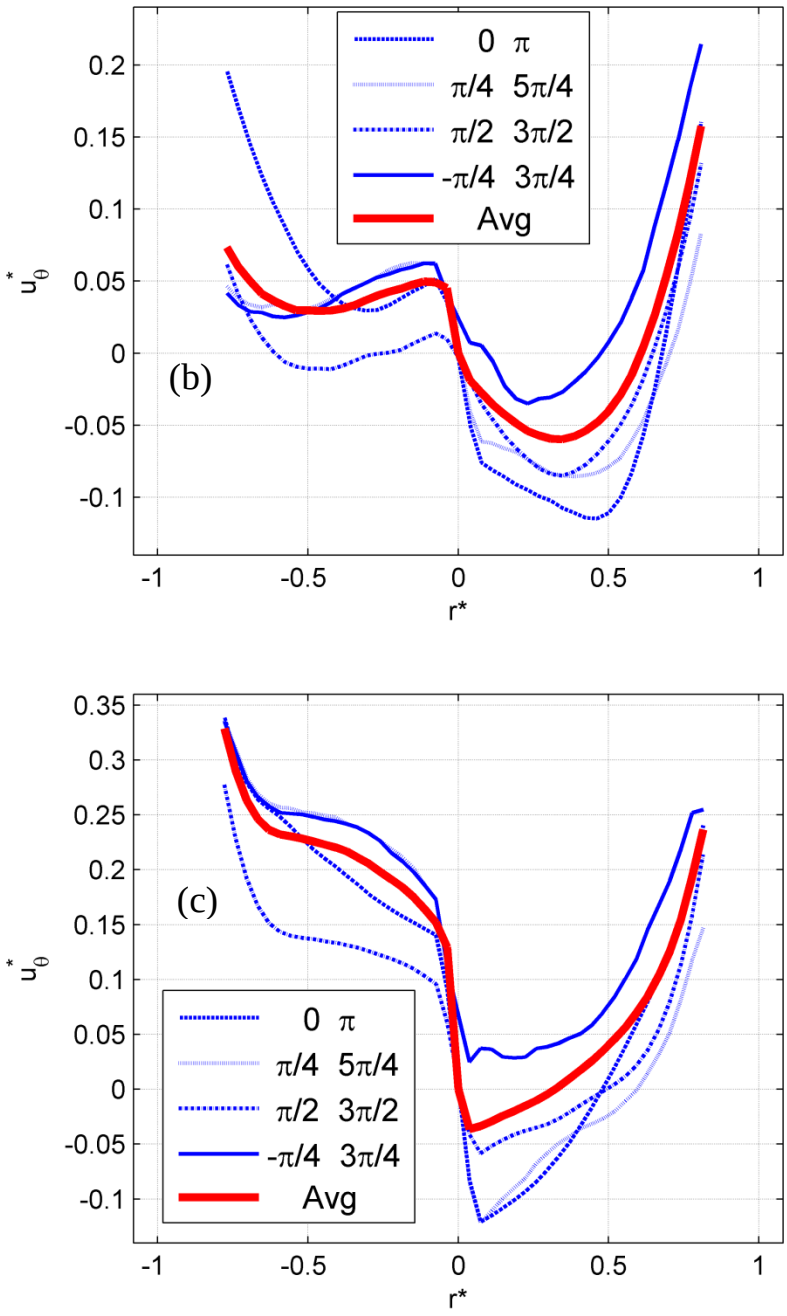

Figure 7.13 Normalized azimuthal velocity profile averaged over the half-circle-sectors and selected profiles across four radial sections for the Heated Counter-Rotating flow when: $\Delta T = 25^o C$, $\Omega_w^* = 1.5$, $\Omega_{dD}^* = -1.4$ when (a): $z^* = 0.67$, (b): $z^* = 1$and (c): $z^* = 1.5$

In the next disk spin rate where $\Omega_d^* = -1.6$, similar to unheated case, more details and figures are presented. In this case vertical velocity vector fields are also extracted. The rotation direction in the first two heights has become mostly clock-wise and disk has dominant effect

which can be seen in figure 7.14-a (lower domain). Nonetheless in the second height, outer ring at some points follow the wall and flow is not completely clock-wise (beginning of transitional domain). The third height, however, has a clock-wise rotating outer ring. In the middle of this ring the direction of rotation varies from one point to another. Above this height flow pattern is similar to higher heights of previous cases with the high velocity, narrow ring and low velocity inner core (upper domain). Compared to previous disk spin rate, disk has stronger effect in all first three heights.

Figure 7.15 demonstrates the velocity vector/magnitude field of the first four heights. As was shown in previous figure, disk effect in the first two heights is dominant and a relatively strong clock-wise vortex exists in both figure a and b. In outer region of figure b between 3 O'clock and 7 O'clock a narrow counter-clock-wise rotating flow distinguishes this figure from figure a. Just between this counter-clock-wise and the inner clock-wise vortex there is a narrow band with very low velocity magnitude. This narrow band becomes remarkably larger in the next height ($z^* = 1$), central vortex vanishes and flow pattern changes completely. However, there are still some points that flow in clock-wise. It appears that transition starts to happen close to this height($z^* = 1$) and probably just beneath it. Above this height flow pattern is closer to a symmetrical shape and there is no clock-wise flow (transitional domain). Maximum of velocity magnitude seems to decrease as the height increase until it passes the transition height and just after this height maximum of velocity increases.

Vertical plane in figures 7.15-e and f are very similar to unheated case (figure 6-14-c and d). However, the upward and downward flows are stronger and transitional domain is narrower and in lower location. Two dark bands of low velocity region is clearly observed in the upper domain.

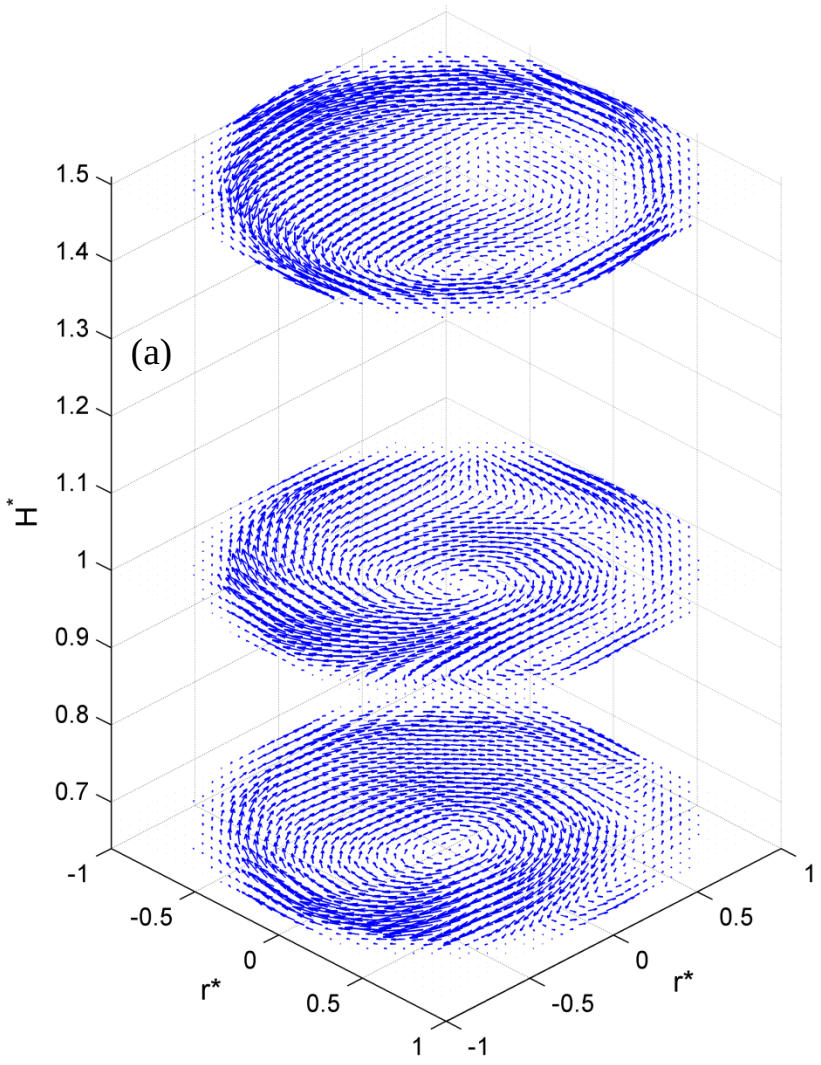
(a)
H*
1.5
1.4
1.3
1.2
1.1
1
0.9
0.8
0.7
-1
-0.5
0
0.5
1
r*
1
0.5
0
-0.5
-1
r*

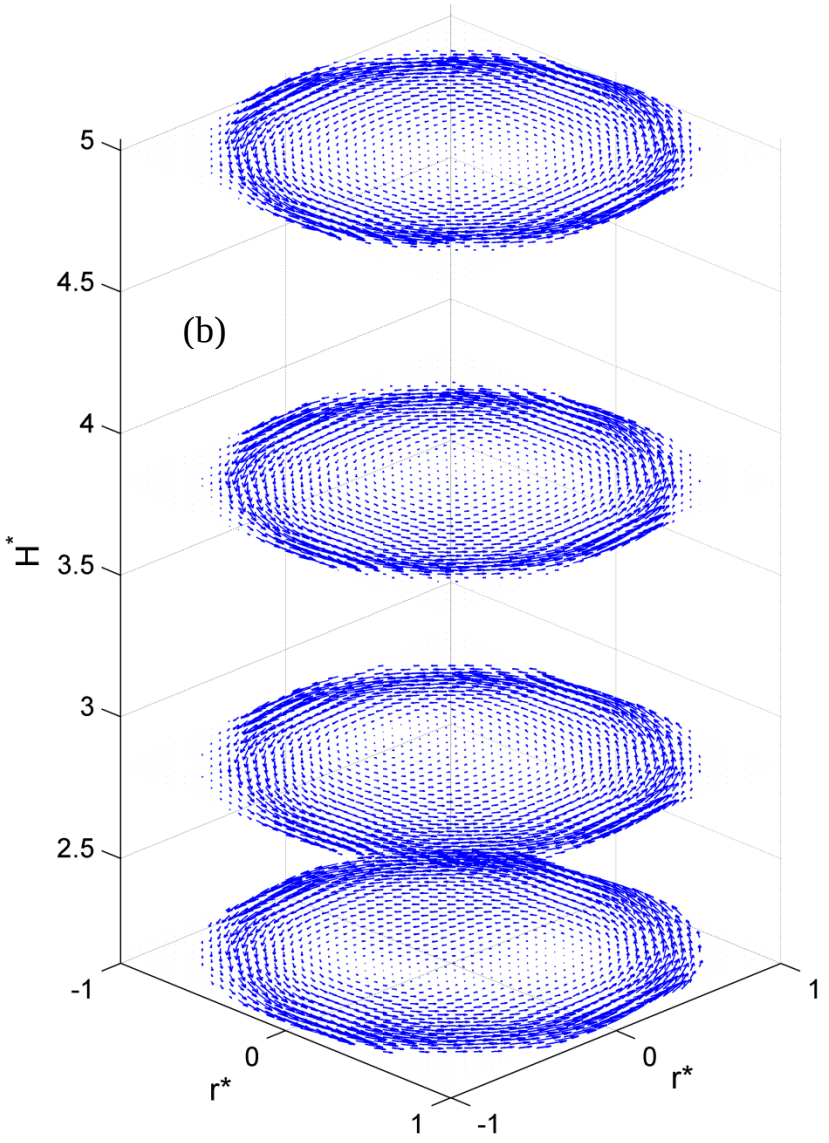

Figure 7.14 Velocity vector field for one Heated Counter-Rotating flow case: $\Delta T = 25^{o}C$ $\Omega_w^* = 1.5$ and the disk spin rate $\Omega_d^* = -1.6$ for (a): three lower studied heights and (b) four higher ones

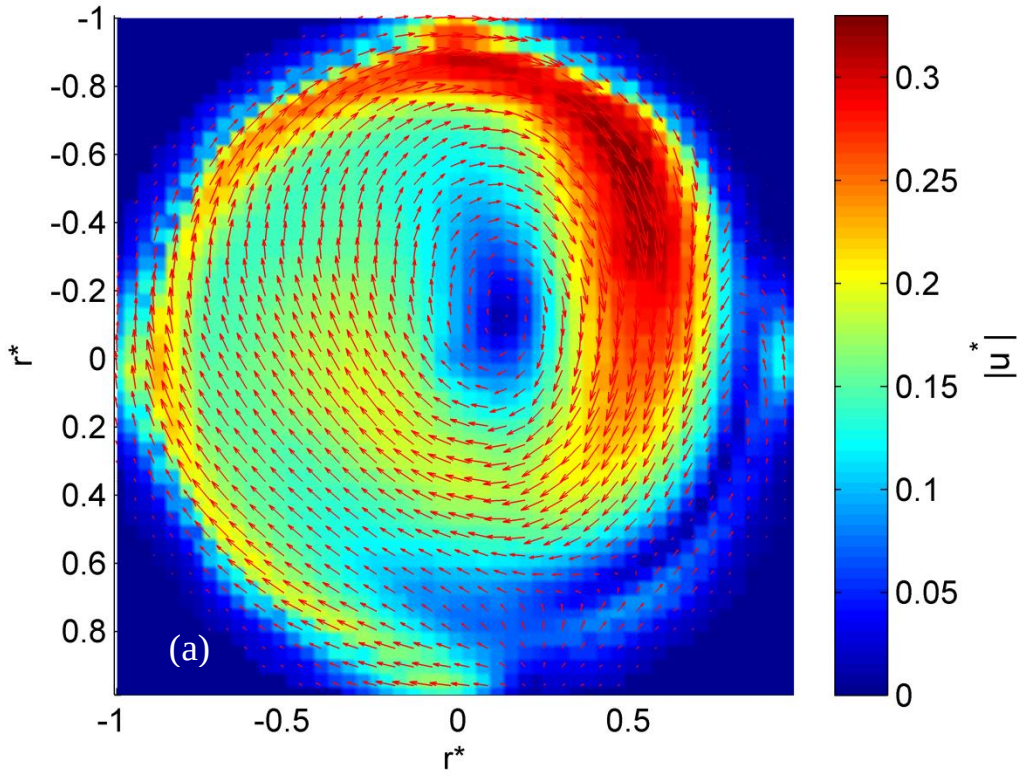
-1
-0.8
-0.6
-0.4
-0.2
0
0.2
0.4
0.6
0.8
r*
-1
-0.5
0
0.5
r*
(a)
0.3
0.25
0.2
0.15
0.1
0.05
0
|u*|

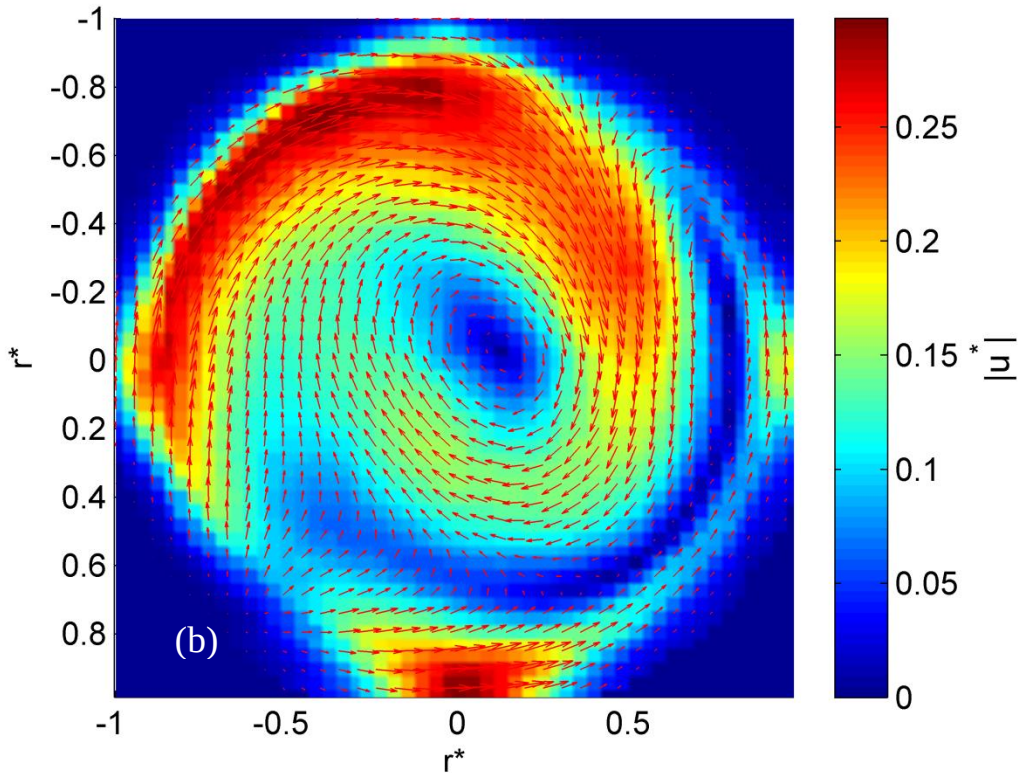
-1
-0.8
-0.6
-0.4
-0.2
0
0.2
0.4
0.6
0.8
r*
-1
-0.5
0
0.5
r*
(b)
0.25
0.2
0.15
0.1
0.05
0
|u*|

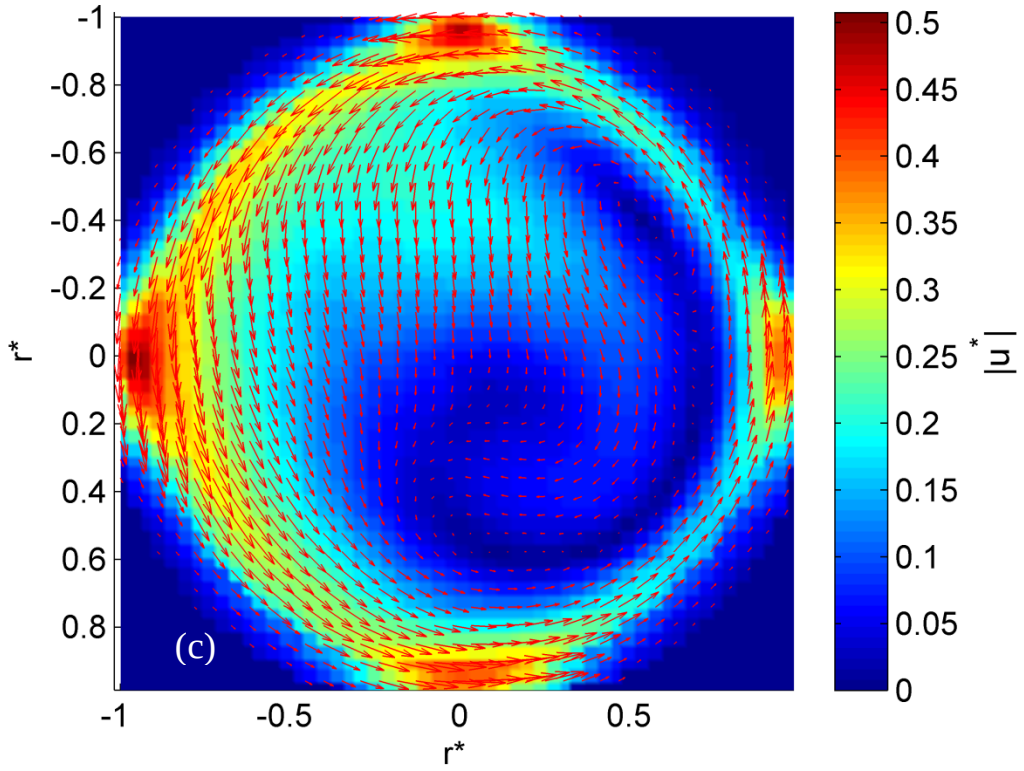
(c)
r*
r*
|u*|
-1
-0.8
-0.6
-0.4
-0.2
0
0.2
0.4
0.6
0.8
-1
-0.5
0
0.5
0.5
0.45
0.4
0.35
0.3
0.25
0.2
0.15
0.1
0.05
0

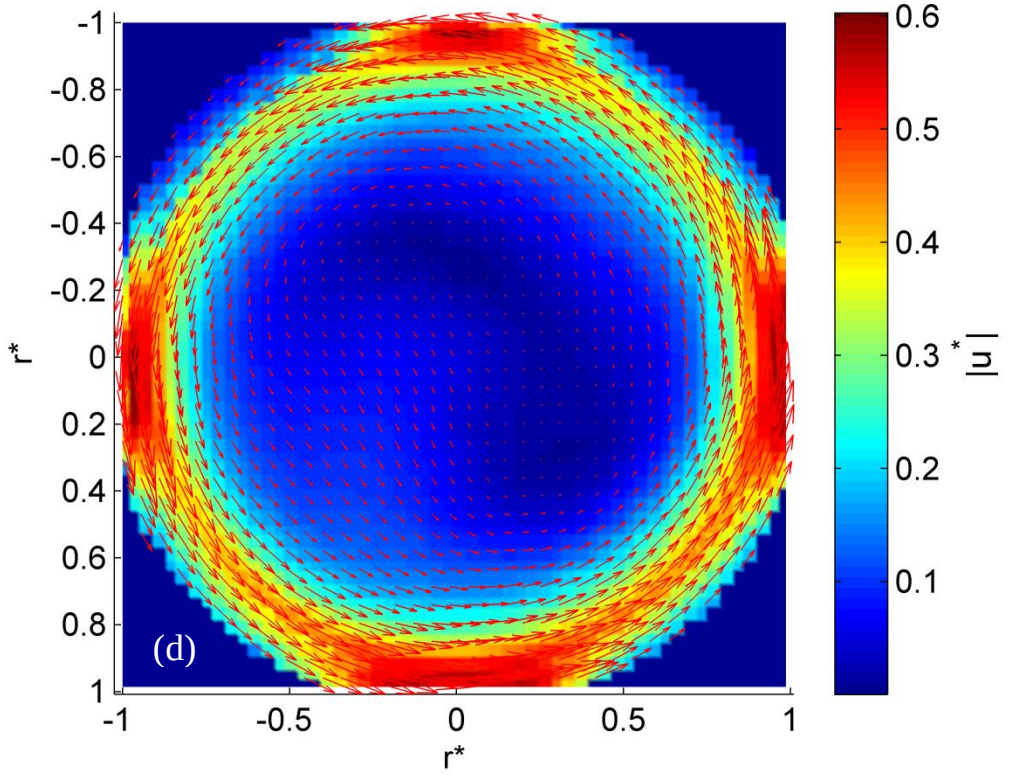
(d)
r*
r*
|u*|
-1
-0.8
-0.6
-0.4
-0.2
0
0.2
0.4
0.6
0.8
1
-1
-0.5
0
0.5
1
0.6
0.5
0.4
0.3
0.2
0.1

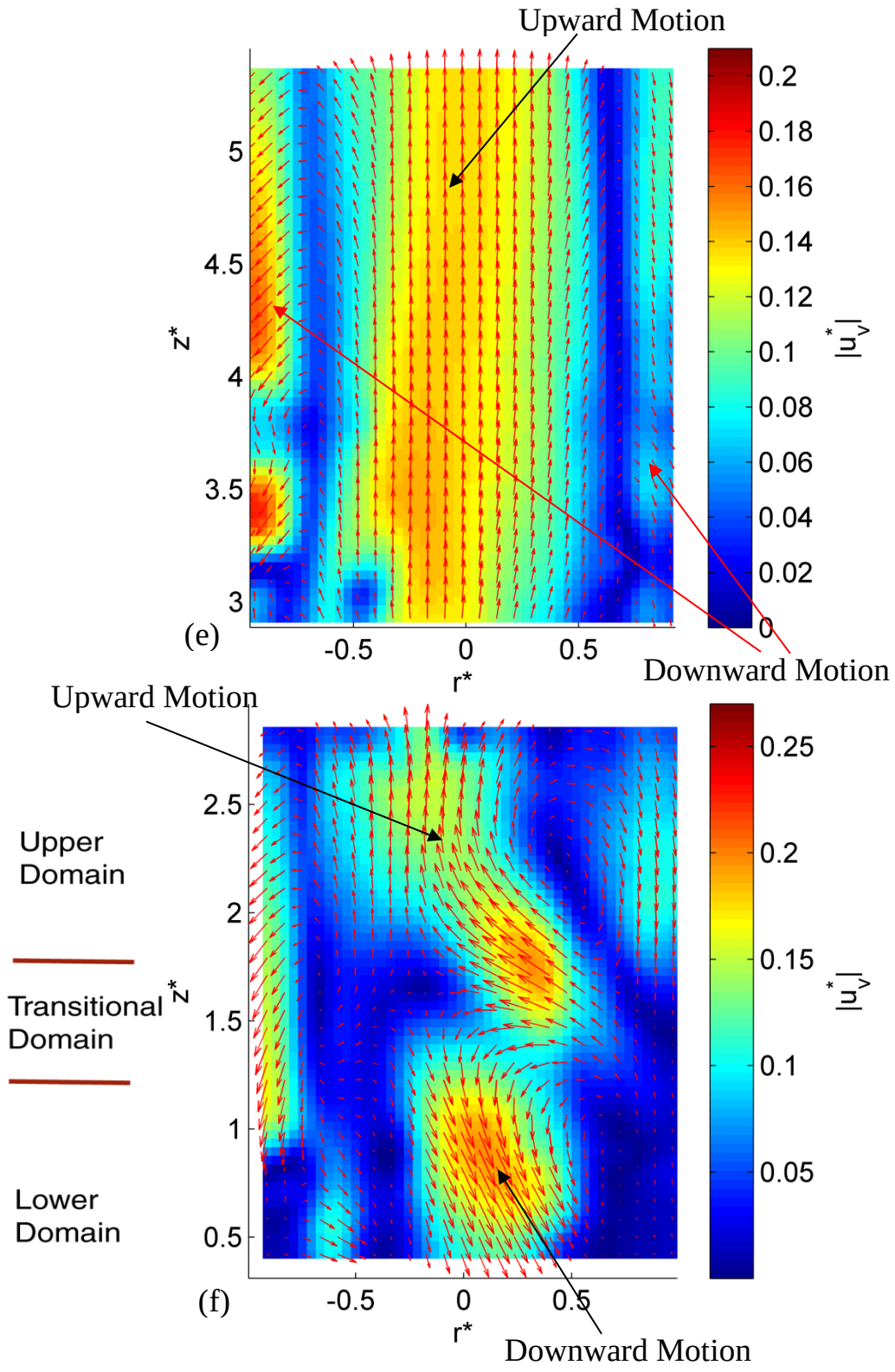

Figure 7.15 The velocity vector and magnitude field for the Heated Counter-Rotating flow when: $\Delta T = 25^{o}C$, $\Omega_w^* = 1.5$, $\Omega_d^* = -1.6$ for heights (a): $z^* = 0.67$, (b): $z^* = 1$, (c): $z^* = 1.5$, (d): $z^* = 2.17$ (e):and (f): vertical planes

Figure 7.16 demonstrates the azimuthal velocity profile sections. The axisymmetric behavior of the flow in lower heights can be seen in the difference between the section curves and average curve. This difference becomes less and less as the height increases. The value is mostly negative in figures a and b and positive in figures c and d which confirms that transition happens between $z^* = 1$ and $z^* = 1.5$.

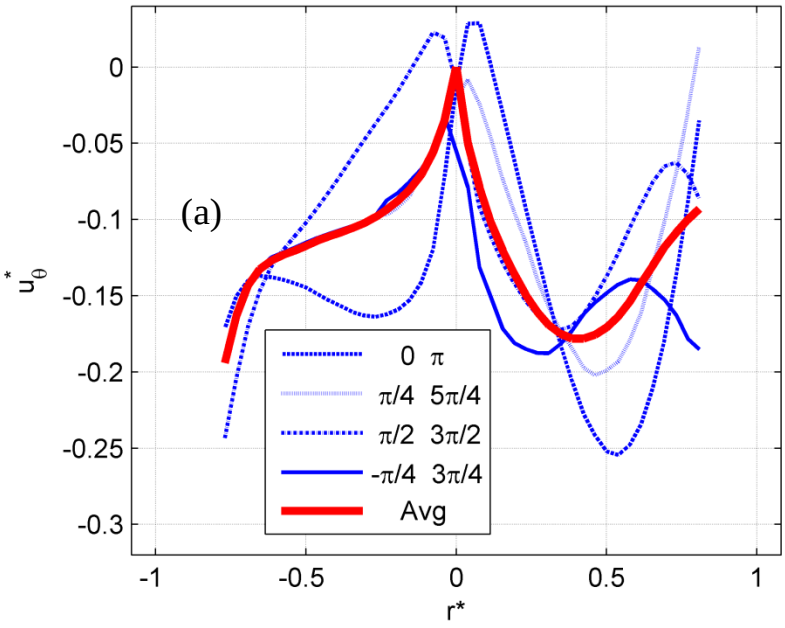

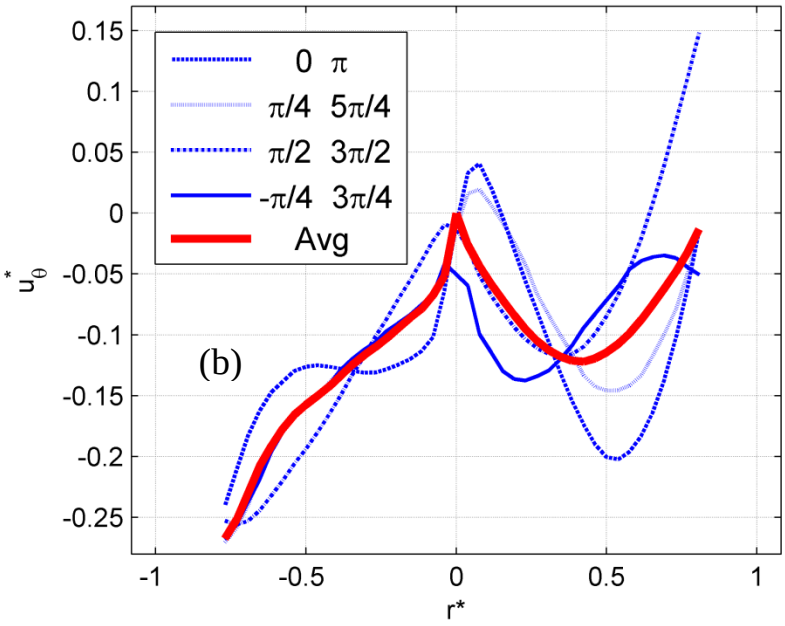
0.15
0.1
0.05
0
-0.05
-0.1
-0.15
-0.2
-0.25
-1
-0.5
0
0.5
1
r*
u_θ^*
0 π
π/4 5π/4
π/2 3π/2
-π/4 3π/4
Avg
(b)

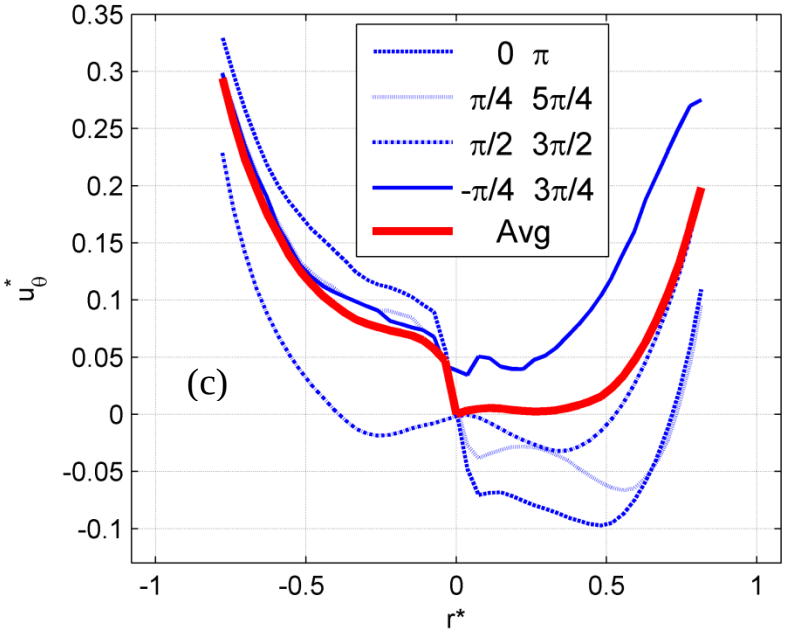
0.35
0.3
0.25
0.2
0.15
0.1
0.05
0
-0.05
-0.1
-1
-0.5
0
0.5
1
r*
u_θ^*
0 π
π/4 5π/4
π/2 3π/2
-π/4 3π/4
Avg
(c)

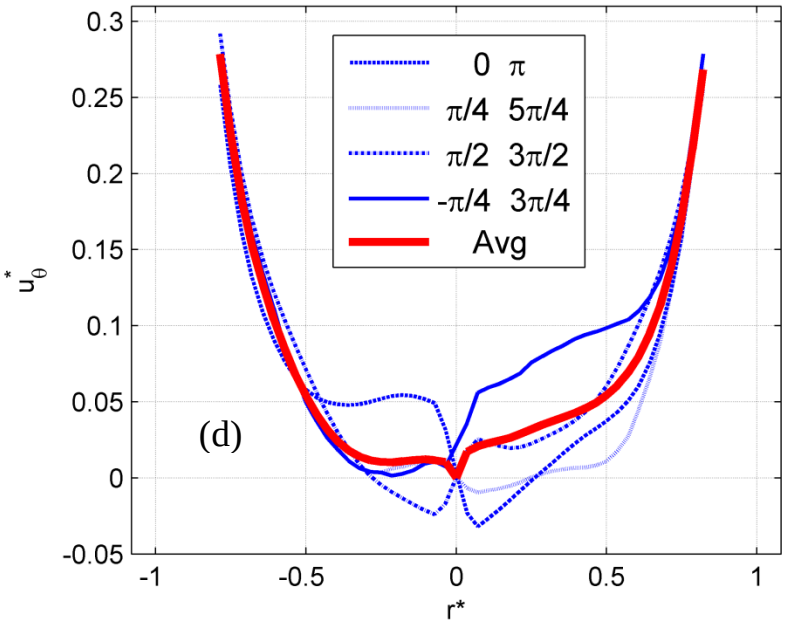

Figure 7.16 Normalized azimuthal velocity profile averaged over the half-circle-sectors and selected profiles across four radial sections for the Heated Counter-Rotating flow when: $\Delta T = 25^{o}C$, $\Omega_w^* = 1.5$, $\Omega_d^* = -1.6$ when (a): $z^* = 0.67$, (b): $z^* = 1$, (c): $z^* = 1.5$ and (d): $z^* = 2.17$

$\Omega_d^* = -1.8$ is the next disk spin rate. As shown in figure 7.17, as the the Ω_d^* increases, effect of disk becomes stronger in all lower heights. The two lower heights are still showing clock-wise rotation and the small region of counter-clock-wise rotation in the second height for previous case has become weaker in this one. A comparison between the third height of this case and previous one clearly shows the effect of increase in disk speed. At the center there is still a strong vortex spinning in the disk-rotating direction while in previous case this vortex at this height is totally vanished. Although three higher heights show the similar results, the fourth one from bottom is quite different with previous case.

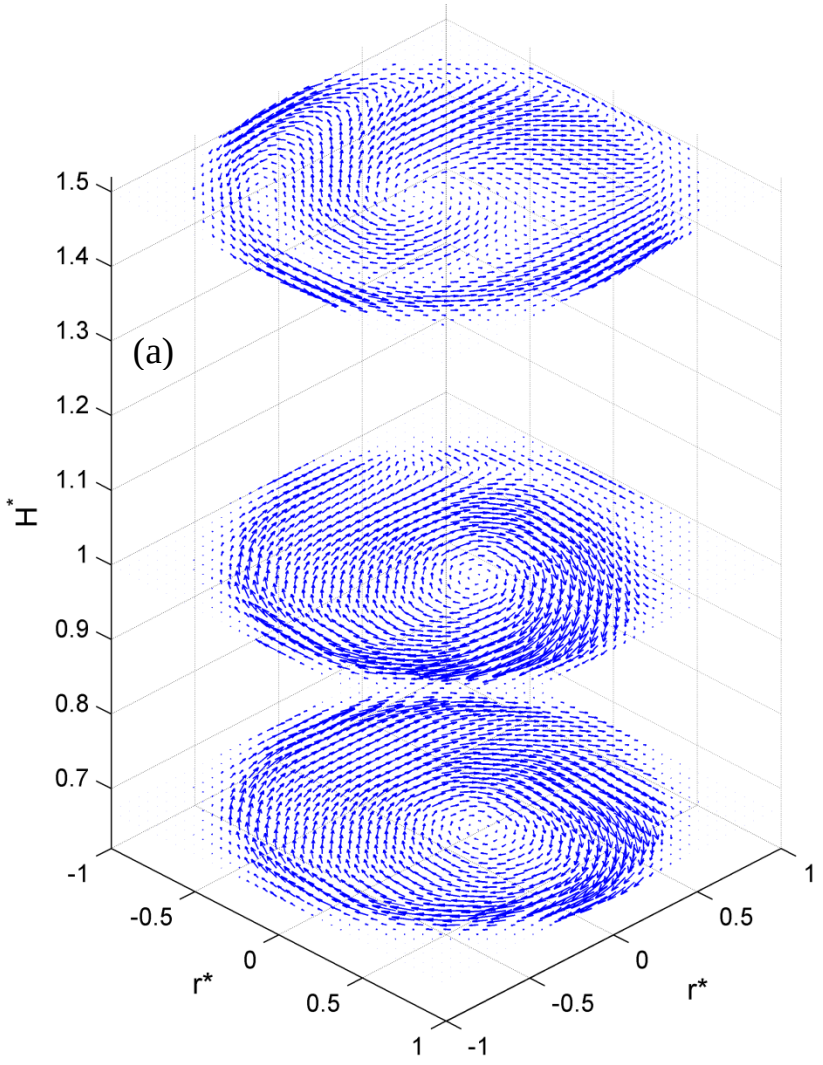
(a)
H*
1.5
1.4
1.3
1.2
1.1
1
0.9
0.8
0.7
-1
-0.5
0
0.5
1
r*
-1
-0.5
0
0.5
1
r*

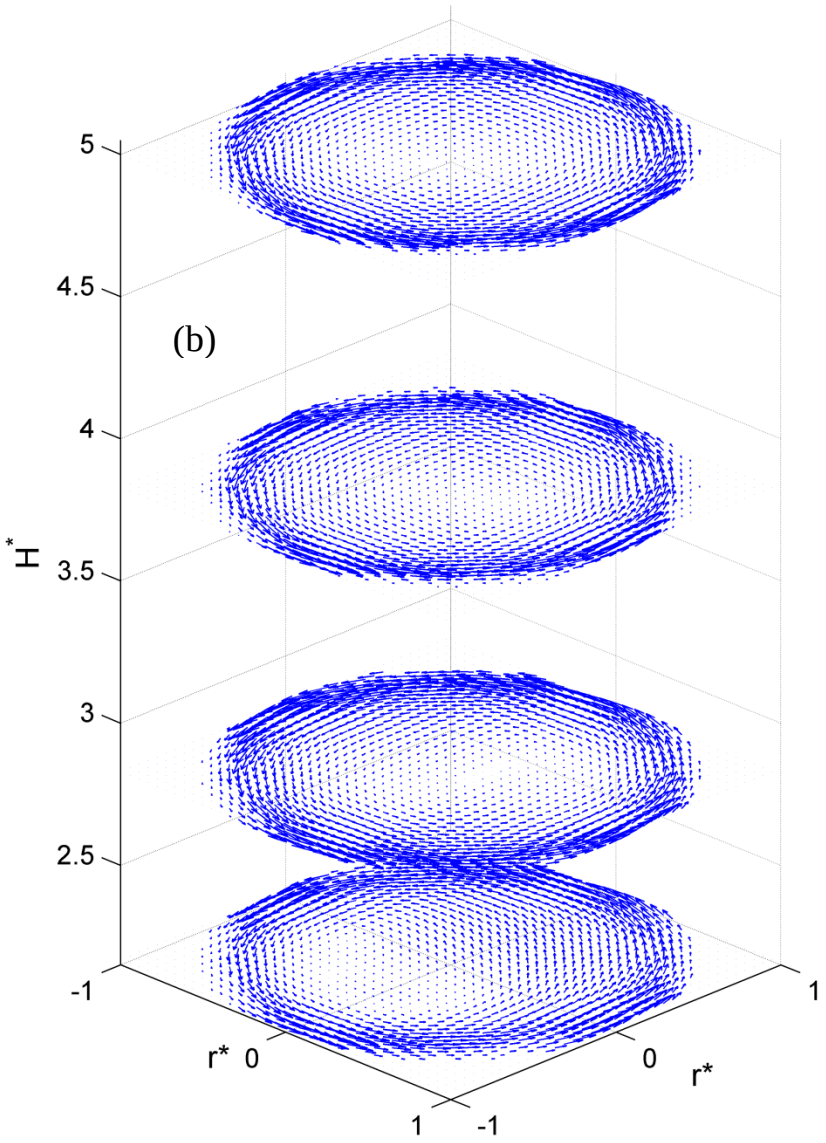

Figure 7.17 Velocity vector field for one heated Counter-Rotating flow case: $\Delta T = 25^{o}C$ $\Omega_w^* = 1.5$ and the disk spin rate $\Omega_d^* = -1.8$ for (a): three lower studied heights and (b) four higher ones

Figure 7.18 show the velocity vector/magnitude field of first four heights. The magnitude of velocity in the first two heights has increased compared to $\Omega_d^* = -1.6$. The transition height appears to be very close to (or even include) the third height ($z^* = 1.5$). In this height one ring of counter-clock-wise vortex surround another clock-wise in close to center. In the fourth height center of vortex is close to 12 O'clock and flow still does not seem symmetric.

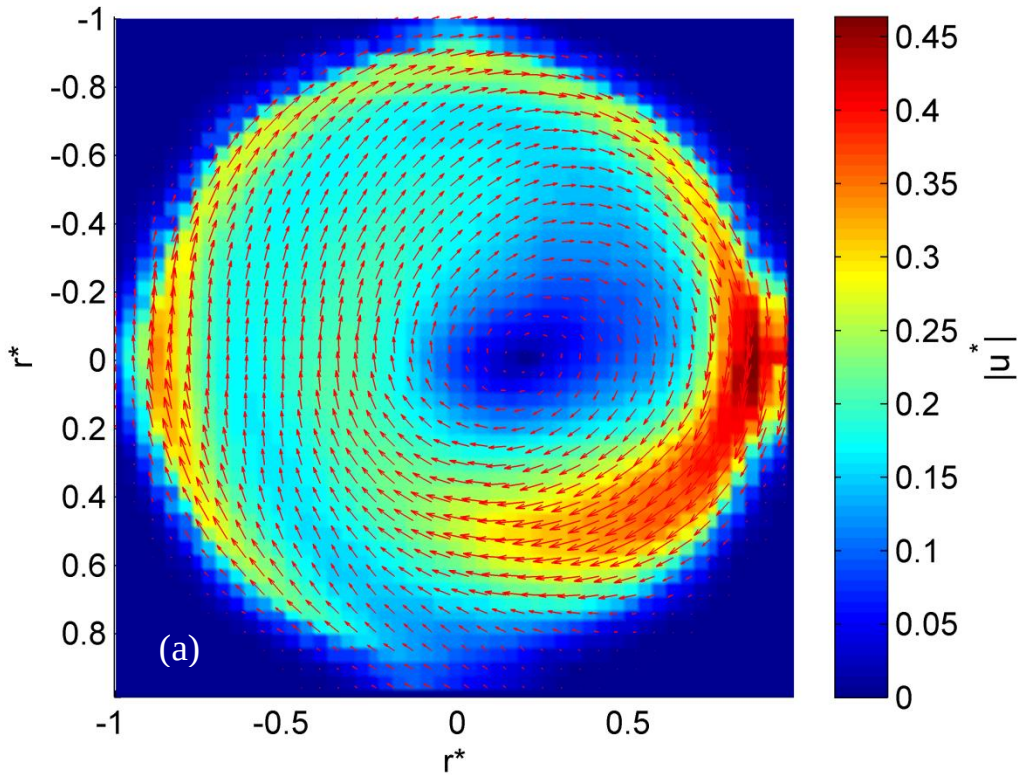
-1
-0.8
-0.6
-0.4
-0.2
0
0.2
0.4
0.6
0.8
r*
(a)
-1
-0.5
0
0.5
r*
0.45
0.4
0.35
0.3
0.25
0.2
0.15
0.1
0.05
0
|u*|

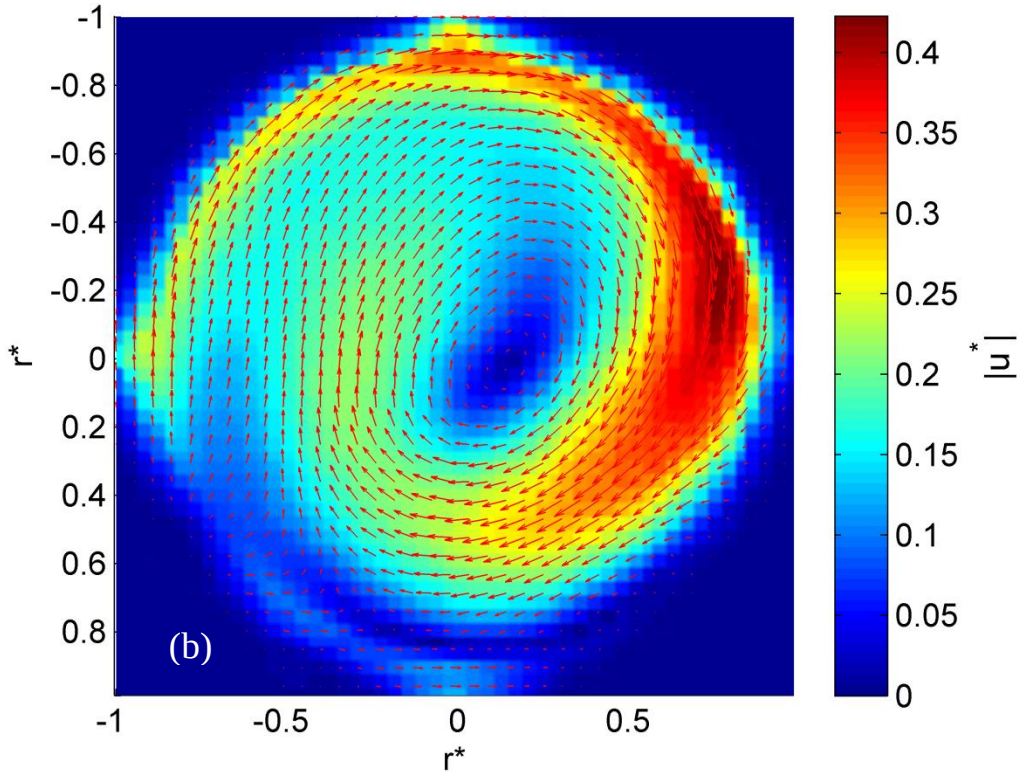
-1
-0.8
-0.6
-0.4
-0.2
0
0.2
0.4
0.6
0.8
r*
(b)
-1
-0.5
0
0.5
r*
0.4
0.35
0.3
0.25
0.2
0.15
0.1
0.05
0
|u*|

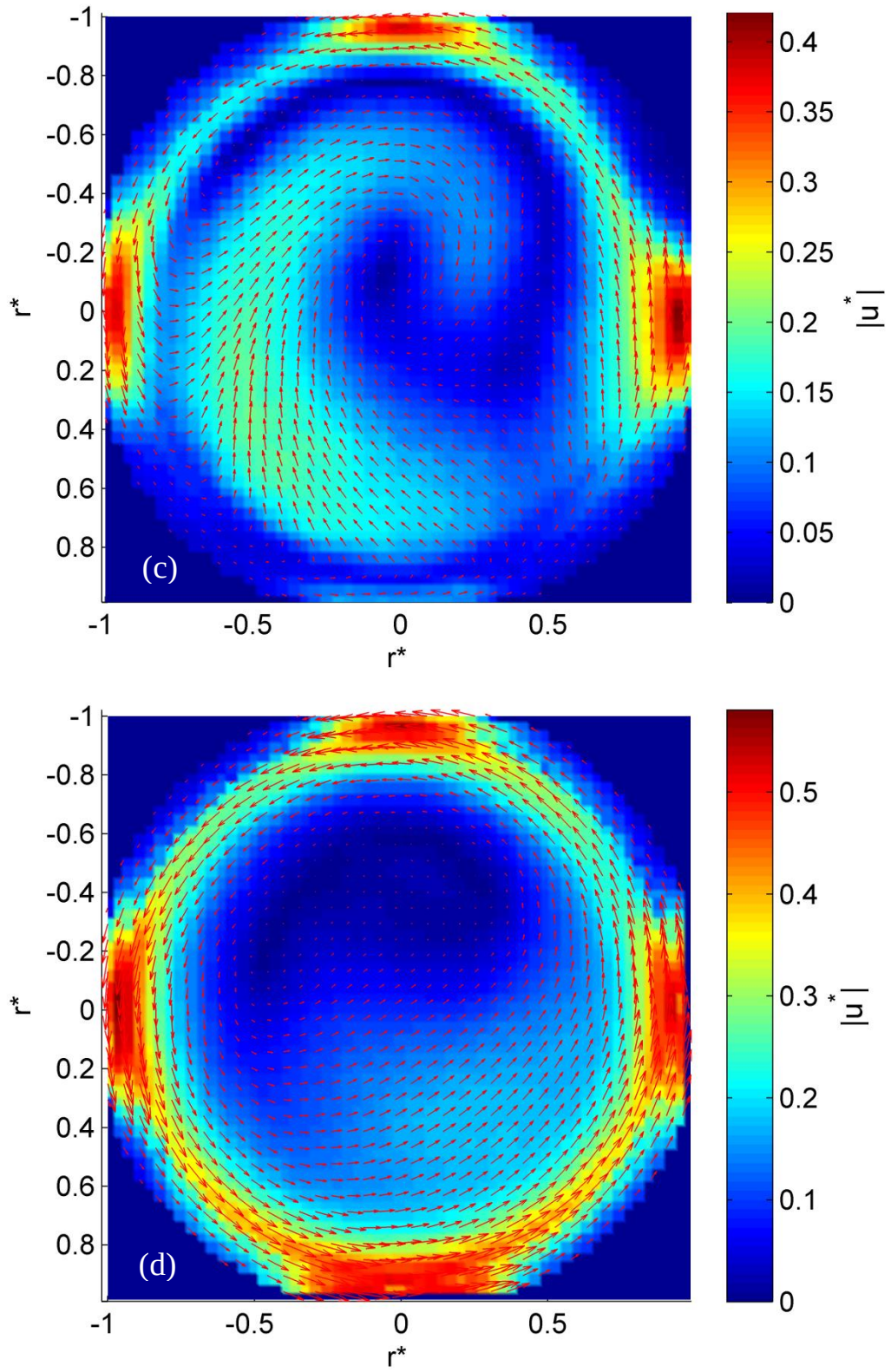

Figure 7.18 The velocity vector and magnitude field for the Heated Counter-Rotating Flow when: $\Delta T = 25^{o}C$, $\Omega_w^* = 1.5$, $\Omega_d^* = -1.8$ for heights (a): $z^* = 0.67$, (b): $z^* = 1$, (c): $z^* = 1.5$ and (d): $z^* = 2.17$

Profiles of velocity azimuthal component in this disk speed are shown in figure 7.19. First two heights show non-axisymmetric, clock-wise rotations. Average profiles in these two heights are more or less similar (unlike the previous disk speed). This means that the disk effect remains dominant at least up to $z^* = 1$. At the third height, although flow is clock-wise near the center, the flow pattern has changed obviously and two concentric vortices co-exist. Above this height wall effect becomes dominant and flow pattern gradually shows axisymmetric behavior.

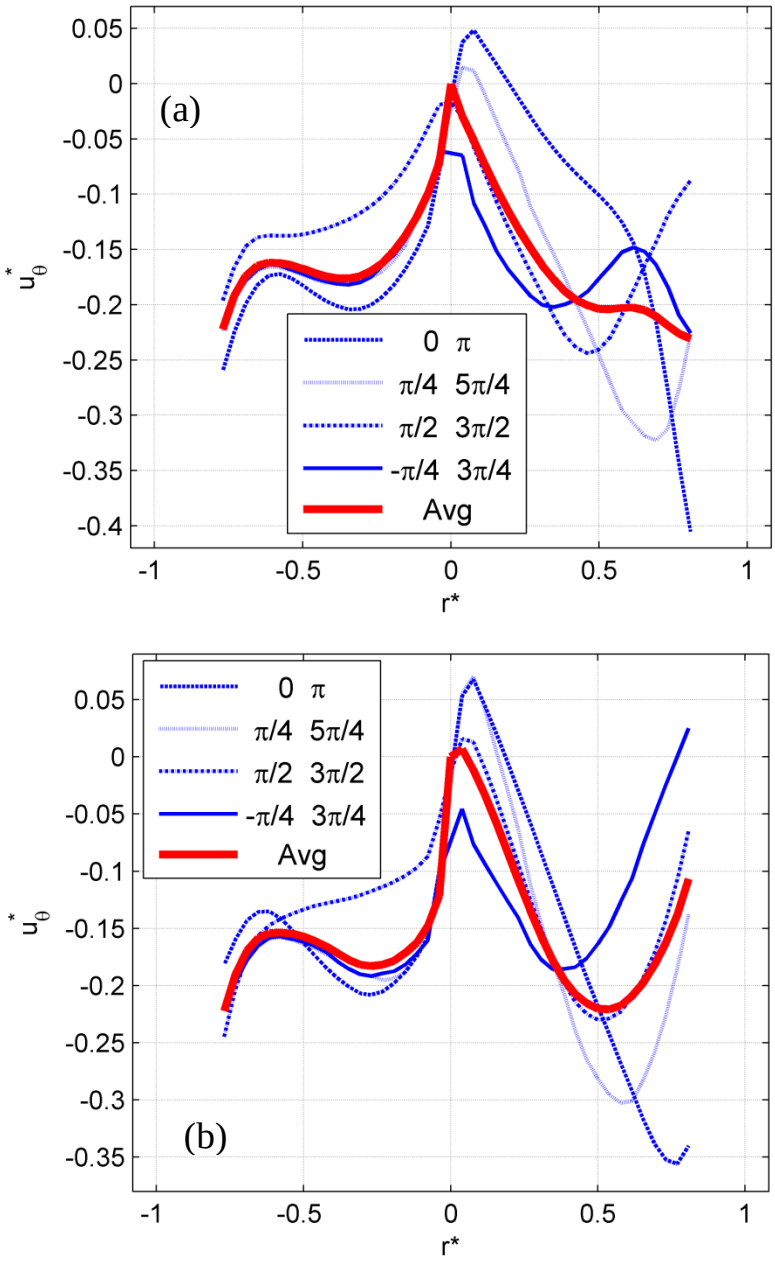

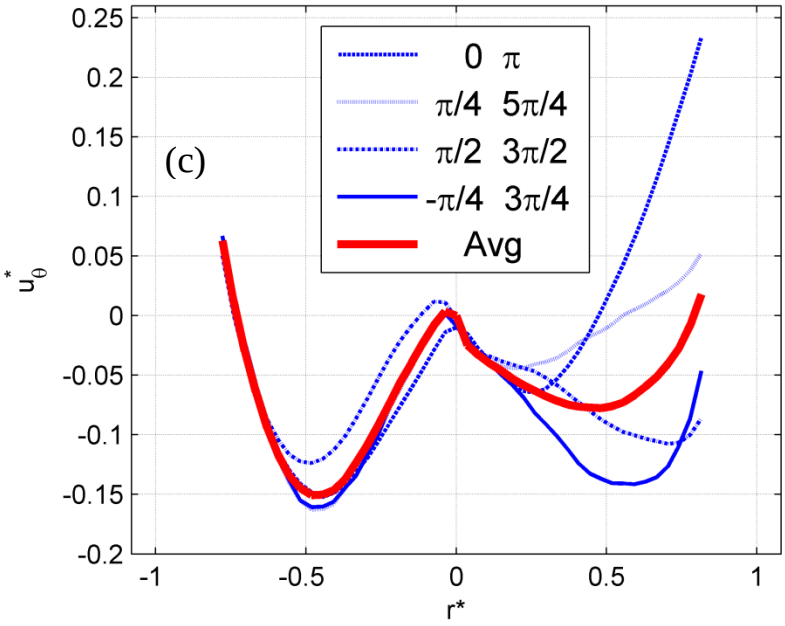
(c)
0 π
π/4 5π/4
π/2 3π/2
-π/4 3π/4
Avg
u_θ^*
r*

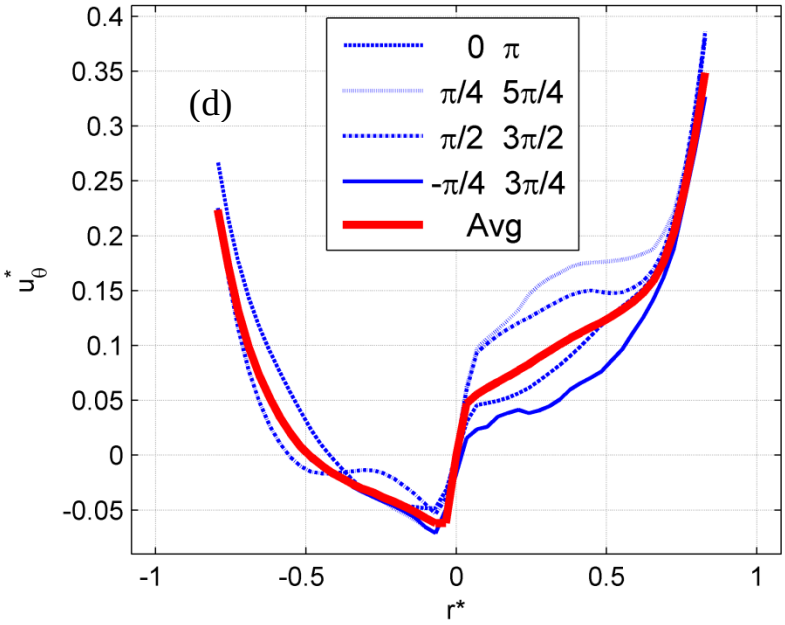
(d)
0 π
π/4 5π/4
π/2 3π/2
-π/4 3π/4
Avg
u_θ^*
r*

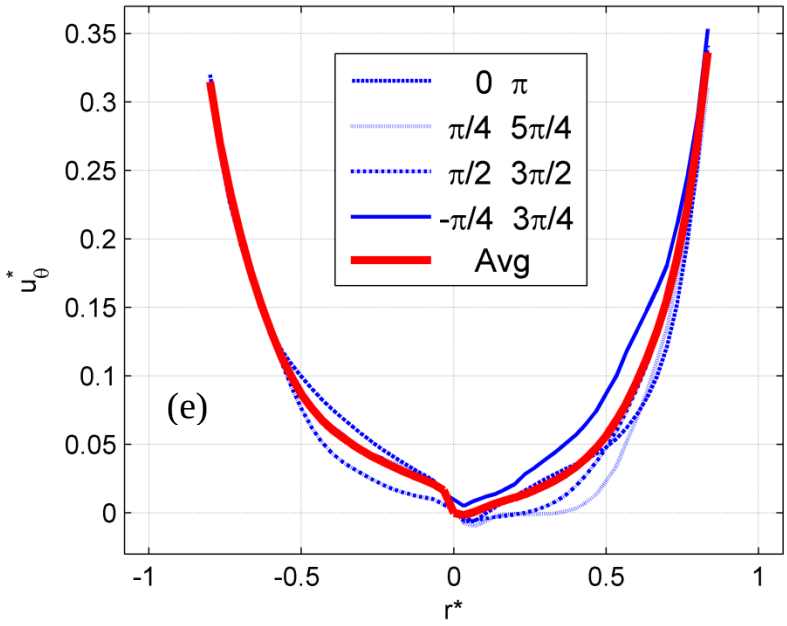

Figure 7.19 Normalized azimuthal velocity profile averaged over the half-circle-sectors and selected profiles across four radial sections for the Heated Counter-Rotating Flow when: $\Delta T = 25^o C$, $\Omega_w^* = 1.5$, $\Omega_d^* = -1.8$ when (a): $z^* = 0.67$, (b): $z^* = 1$, (c): $z^* = 1.5$, (d): $z^* = 2.17$ and (e): $z^* = 2.83$

In the next and last disk spin rate, $\Omega_d^* = -2$, the disk effect has reached even higher heights, as expected. The three first heights show clock-wise rotation and the four higher one are rotating counter-clock-wise. The first two heights show stronger vector compared to the previous disk speeds. The third height of this case and the previous one are quite different. It seems that the transition domain has risen and it is completely above the third height and beneath the fourth one. The vortex in the fourth height is clearly off-centered, unlike the higher ones.

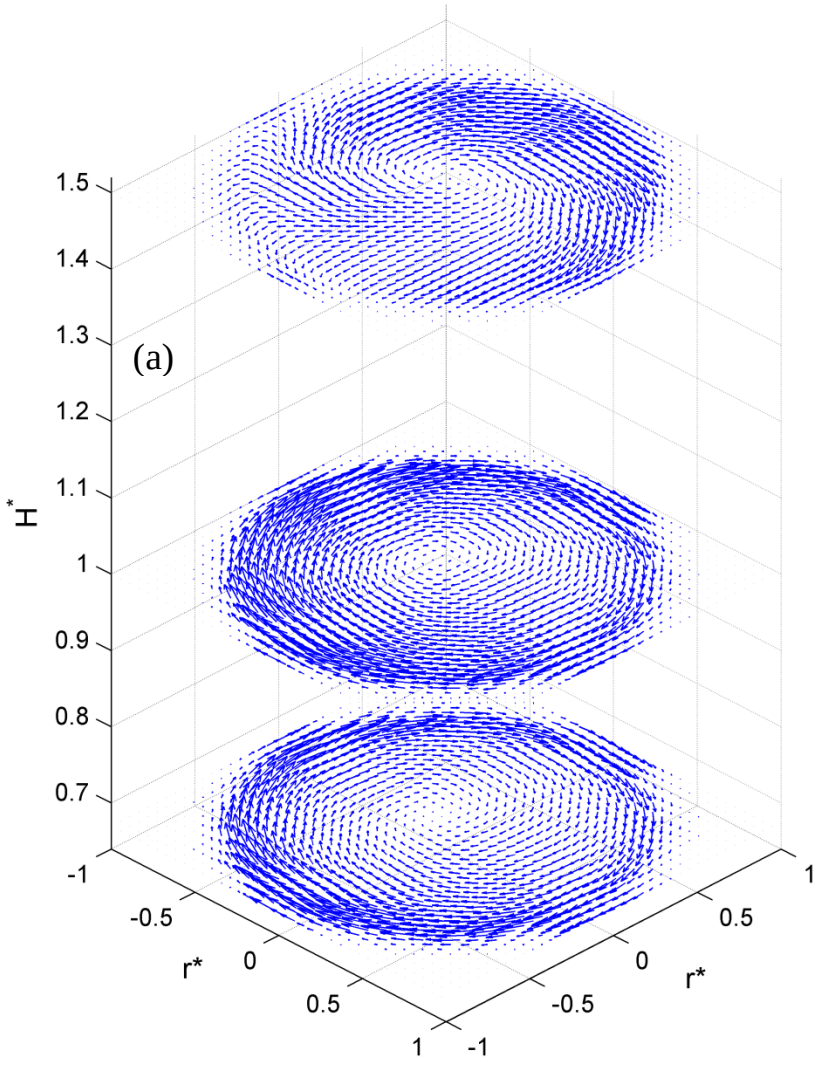
(a)
H*
1.5
1.4
1.3
1.2
1.1
1
0.9
0.8
0.7
-1
-0.5
0
0.5
1
r*
-1
-0.5
0
0.5
1
r*

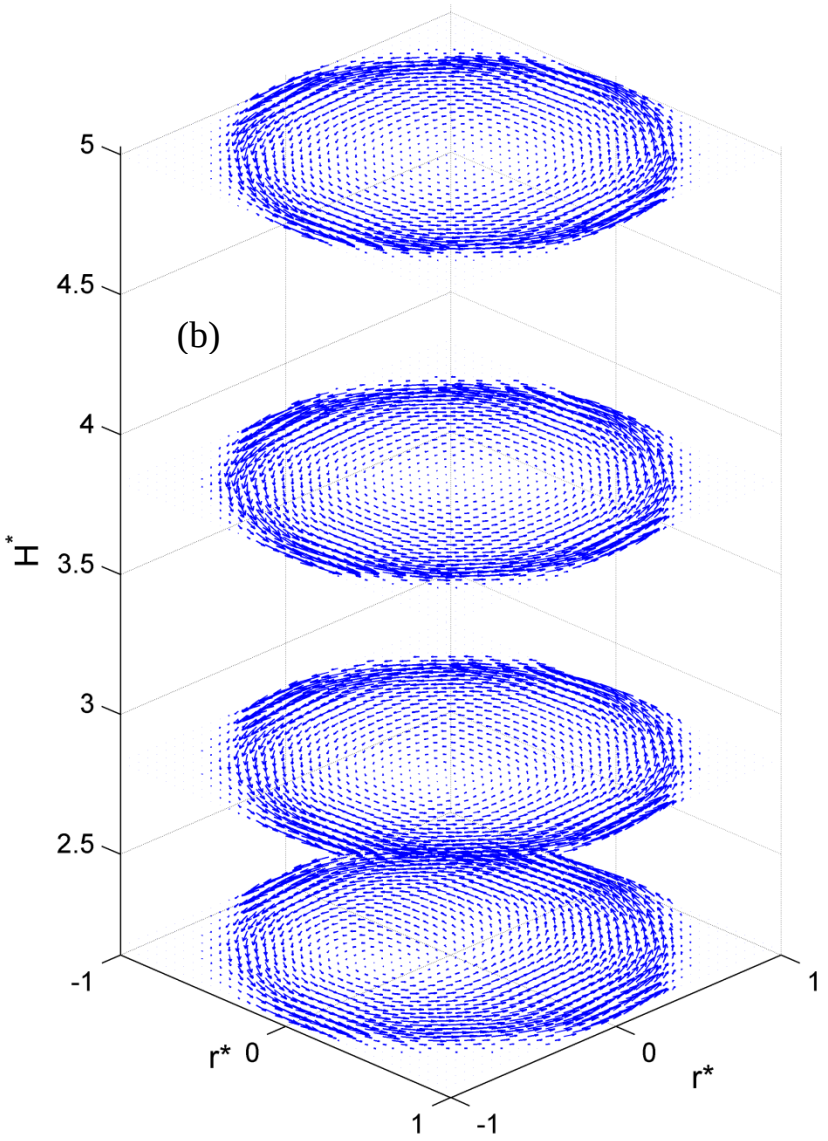

Figure 7.20 Velocity vector field for one Heated Counter-Rotating flow case: $\Delta T = 25^{o}C$ $\Omega_w^* = 1.5$ and the disk spin rate $\Omega_d^* = -2$ for (a): three lower studied heights and (b) four higher ones

Figure 7.21 shows more detail of velocity field for this case. The main difference between the first and the second height in this case is that in the first height flow in outer ring is much faster than inner region while in the second height this difference is considerably less. In the third height although the whole flow is clock-wise, in the upper half of outer ring does not have a clear direction of rotation. Maximum of speed magnitude at this height is less than this

value in higher and lower height (because the transition occurs at these heights). Finally at the fourth height and above that flow is counter-clock-wise.

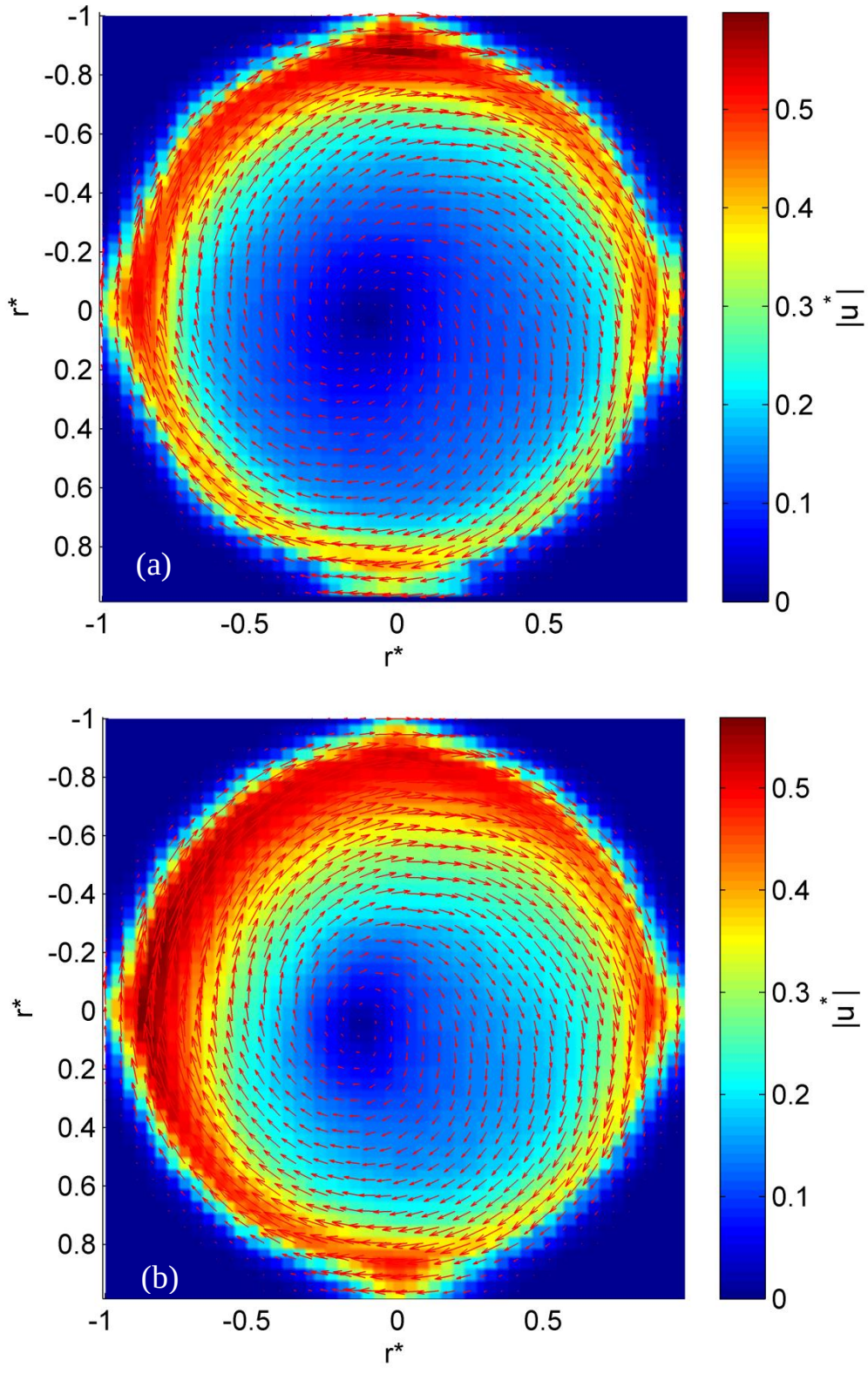

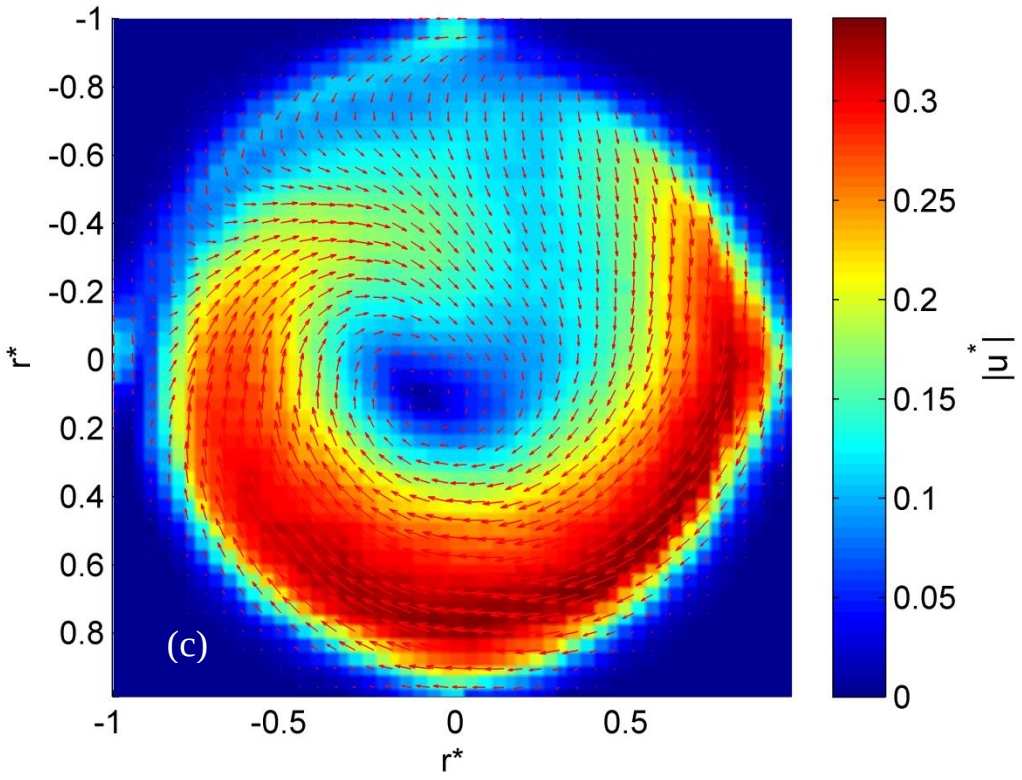
(c)
r*
r*
|u*|
-1
-0.8
-0.6
-0.4
-0.2
0
0.2
0.4
0.6
0.8
-0.5
0.5
0.3
0.25
0.2
0.15
0.1
0.05

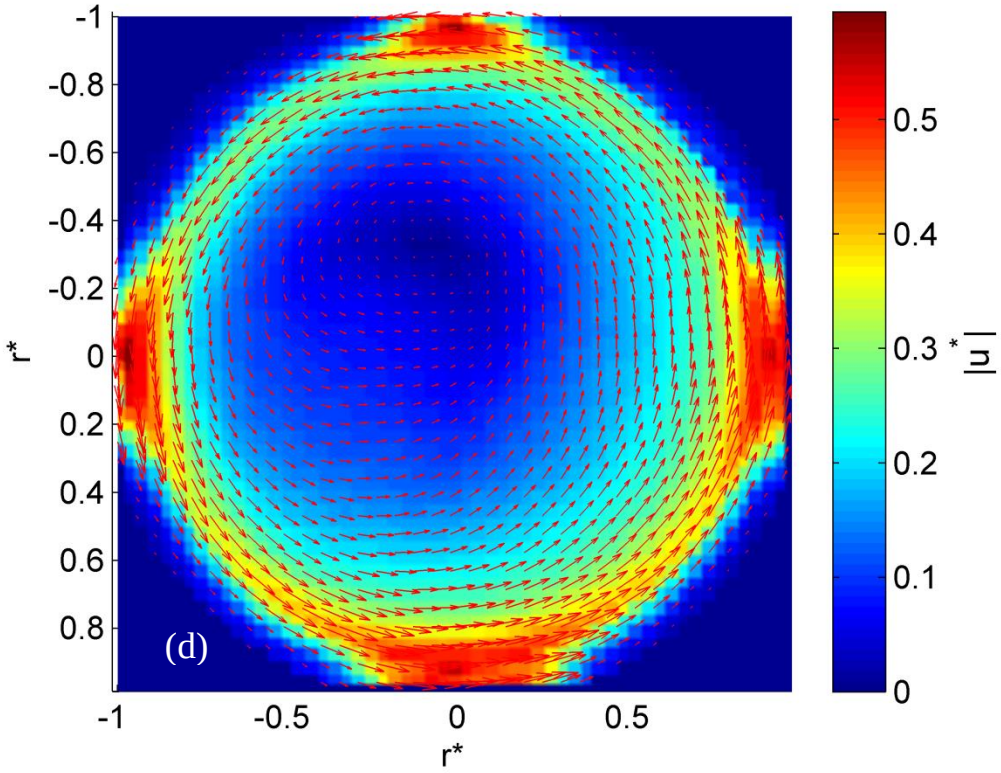
(d)
r*
r*
|u*|
-1
-0.8
-0.6
-0.4
-0.2
0
0.2
0.4
0.6
0.8
-0.5
0.5
0.5
0.4
0.3
0.2
0.1

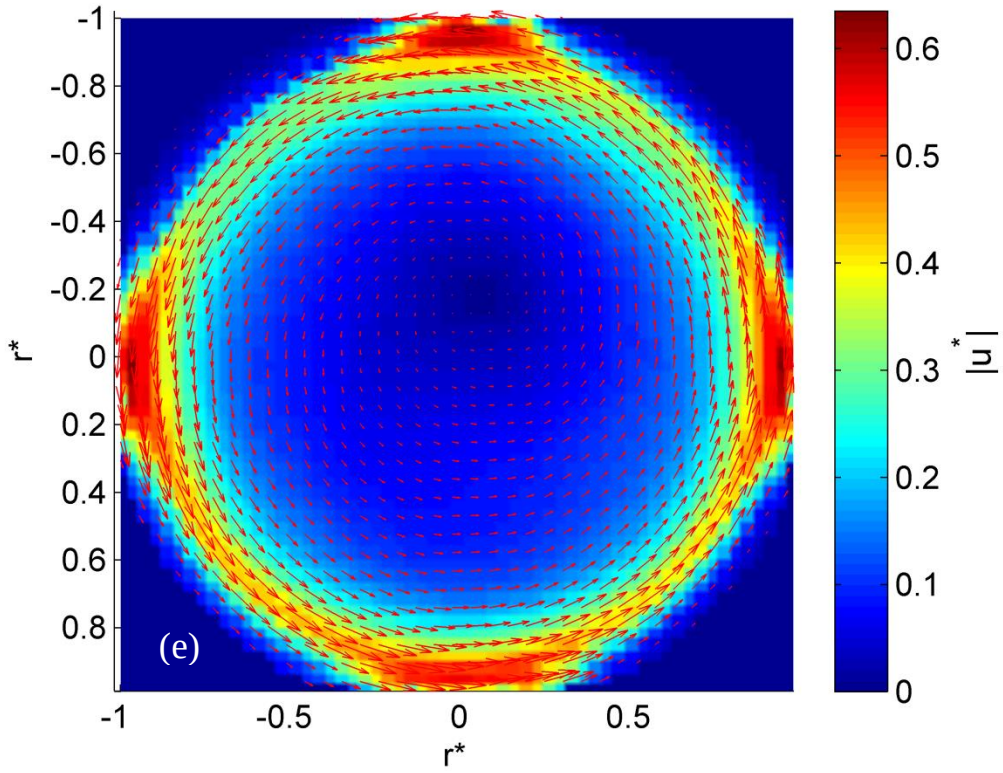

Figure 7.21 The velocity vector and magnitude field for the Heated Counter-Rotating Flow when: $\Delta T = 25^{o}C$, $\Omega_w^* = 1.5$, $\Omega_d^* = -2$ for heights (a): $z^* = 0.67$, (b): $z^* = 1$, (c): $z^* = 1.5$, (d): $z^* = 2.17$ and (e): $z^* = 2.8$.

The azimuthal component of the velocity is shown in figure 7.22. There is a clear difference between the shapes of curves in the first height of this case and all other cases. It seems that as the disk speed increases and reaches $\Omega_d^* = -2$, the first height curve becomes parabolic. The transition from this negative parabolic curve in lowest height to the positive parabolic shape in three higher heights can be seen in this figure. Another difference between this case and previous ones is symmetricity of flow in all heights. Unlike previous cases, flow looks more symmetric in all heights except where transition takes place ($z^* = 1.5$). In other words, the curves of four sections and the average curve are very close to each other in all heights except for the third one. This behavior from the curve is different in other disk spin rates.

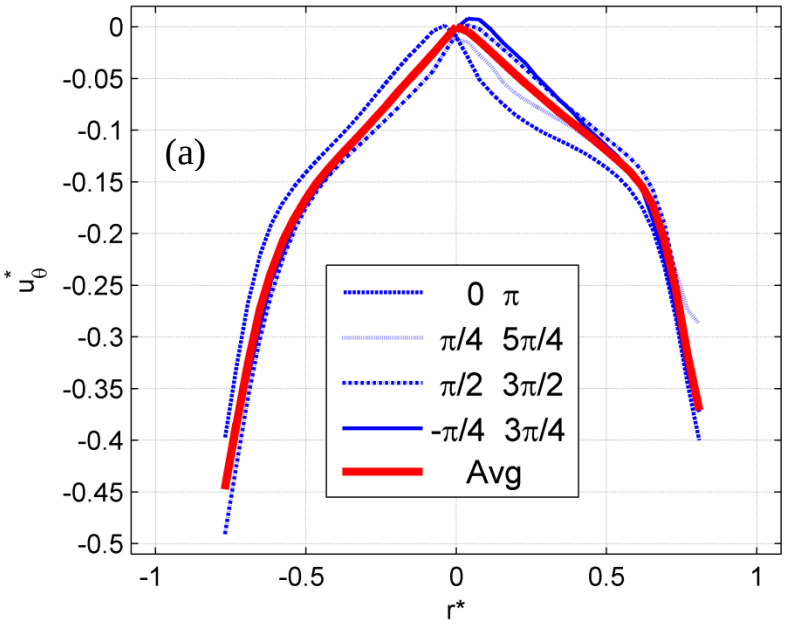
(a)
0
-0.05
-0.1
-0.15
-0.2
-0.25
-0.3
-0.35
-0.4
-0.45
-0.5
-1
-0.5
0
0.5
1
r*
u_θ^*
0 π
π/4 5π/4
π/2 3π/2
-π/4 3π/4
Avg

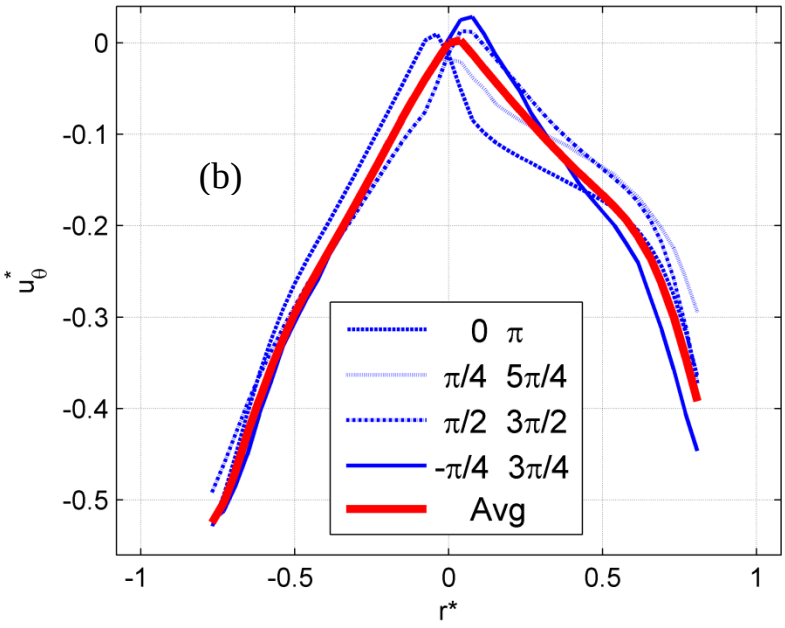
(b)
0
-0.1
-0.2
-0.3
-0.4
-0.5
-1
-0.5
0
0.5
1
r*
u_θ^*
0 π
π/4 5π/4
π/2 3π/2
-π/4 3π/4
Avg

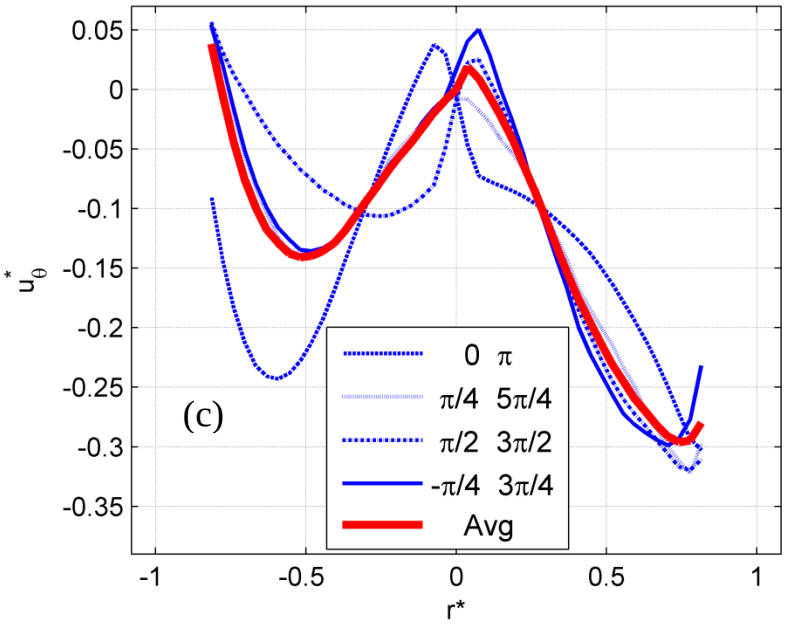
0.05
0
-0.05
-0.1
-0.15
-0.2
-0.25
-0.3
-0.35
u_θ^*
(c)
0 π
π/4 5π/4
π/2 3π/2
-π/4 3π/4
Avg
-1
-0.5
0
0.5
1
r*

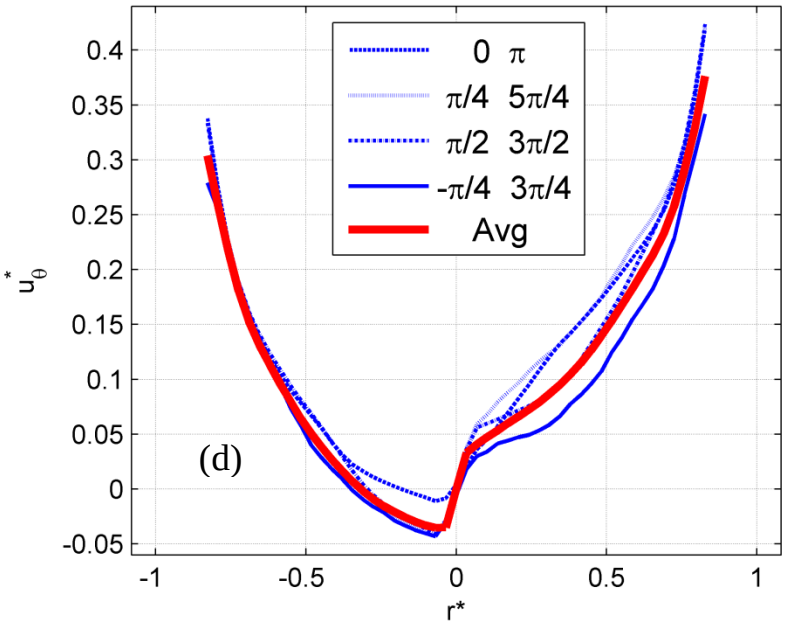
0.4
0.35
0.3
0.25
0.2
0.15
0.1
0.05
0
-0.05
u_θ^*
(d)
0 π
π/4 5π/4
π/2 3π/2
-π/4 3π/4
Avg
-1
-0.5
0
0.5
1
r*

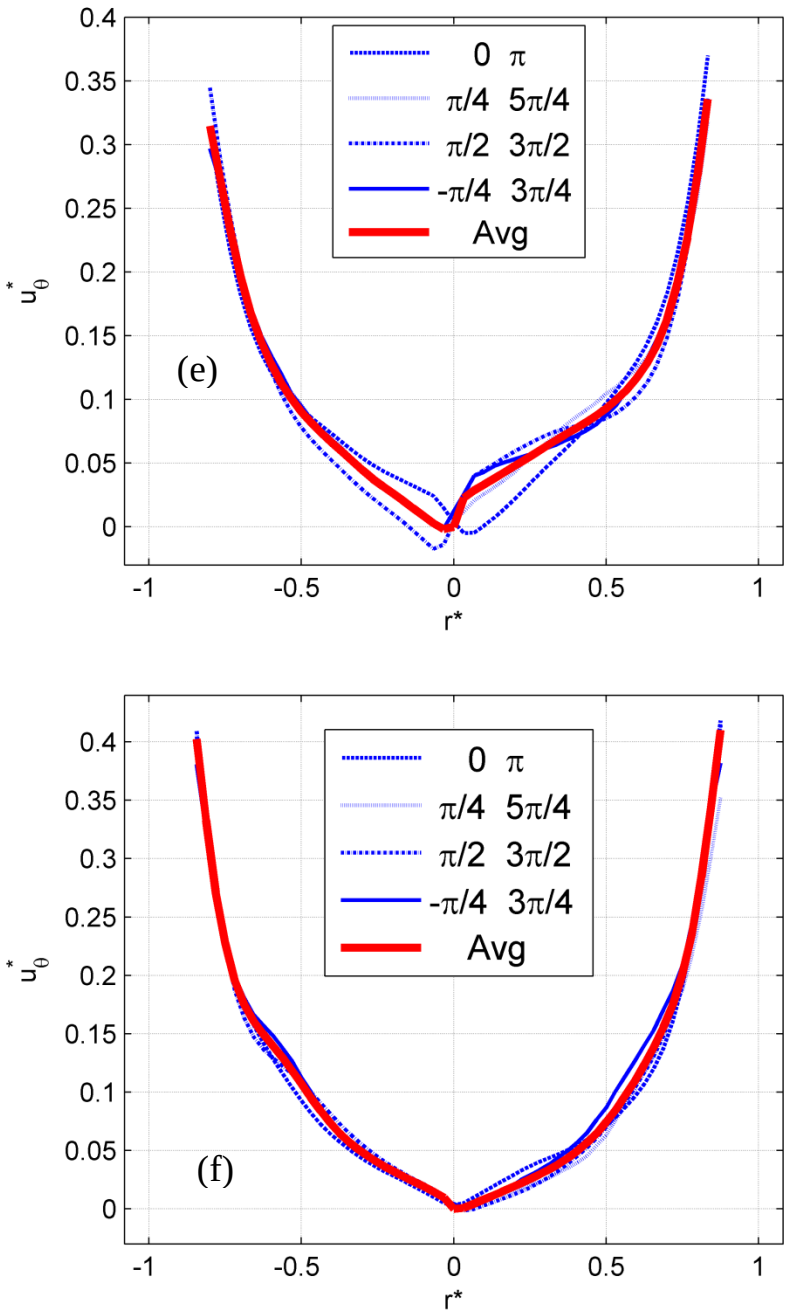

Figure 7.22 Normalized azimuthal velocity profile averaged over the half-circle-sectors and selected profiles across four radial sections for the Heated Counter-Rotating flow when: $\Delta T = 25^o C$, $\Omega_w^* = 1.5$, $\Omega_d^* = -2$ when (a): $z^* = 0.67$, (b): $z^* = 1$, (c): $z^* = 1.5$, (d): $z^* = 2.17$, , (e): $z^* = 2.83$ and (f): $z^* = 3.83$

Similar to the results that is shown for the counter rotating flow with : $\Delta T = 25^o C$ is also presented for : $\Delta T = 50^o C$ ($Gr = 0$, 1.37×10^4 and 2.4×10^4). For each disk spin rate velocity

vector fields of all measured heights, velocity vector/magnitude fields and profiles of azimuthal components of velocity are presented below. For the first step disk spin rate is set at $\Omega_d^* = -1$. Figure 7-23 shows that flow in all heights is counter-clock-wise.

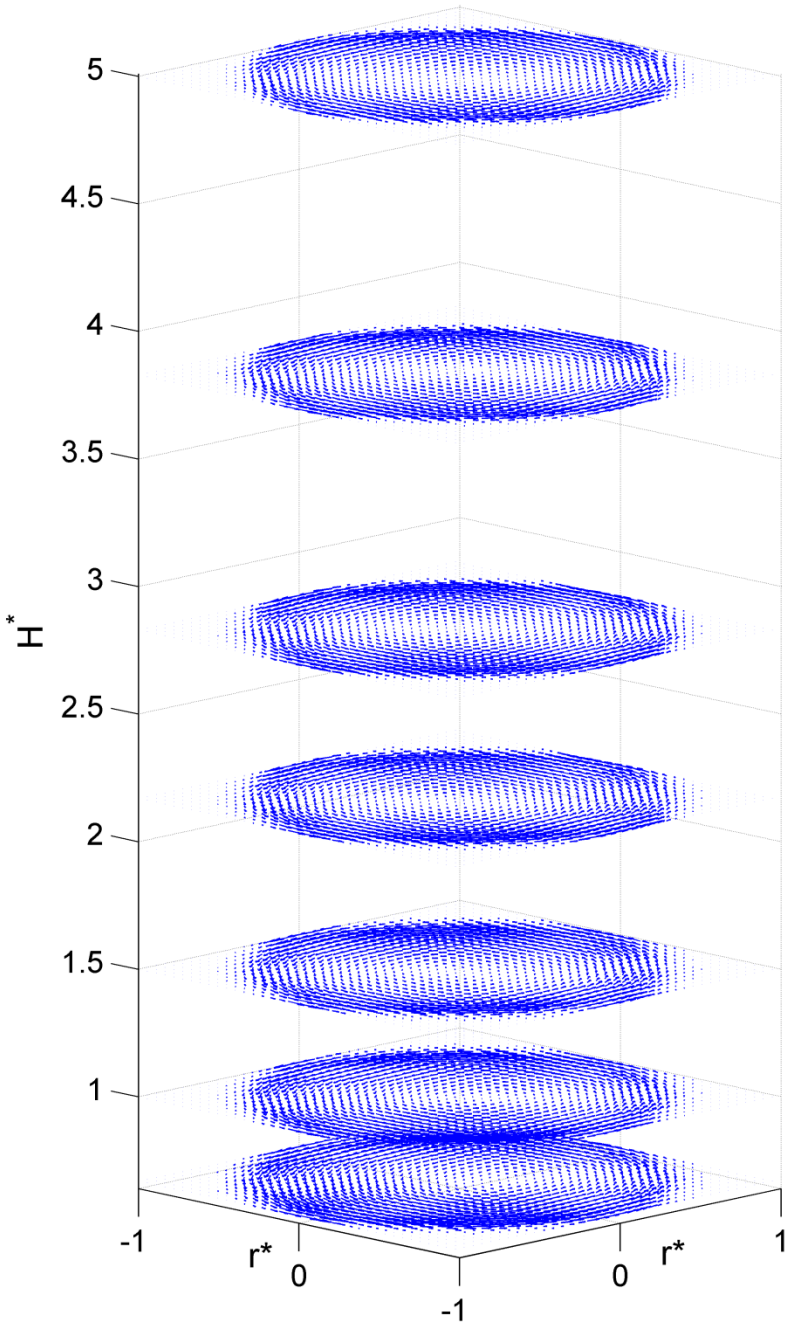

Figure 7.23 Velocity vector field for all studied heights for one Heated Counter-Rotating flow case: $\Delta T = 50^o C$ $\Omega_w^* = 1.5$ and the disk spin rate $\Omega_d^* = -1$

In similar situation with $\Delta T = 25^{o}C$ it was shown that the transition occurs below this height. Same thing happens in this thermal condition and it seems that transitional domain is lower than $z^{*} = 0.67$.

Velocity vector/magnitude fields of the first two heights in figure 7.24 also confirm that flow is counter-clock-wise and very similar to previous case (with $\Delta T = 25^{o}$) in the lower two heights. Compared to the lower disk temperature cases, the high velocity ring and large, low velocity core does not exist anymore and the pattern of velocity magnitude shows that it changes along the radius more gradually. Flow in the second height seems more symmetric that the first height. The maximum of velocity is $10 - 15\%$ larger than previous thermal condition in figure 7-6. This means that as the mixing of flow increases (due to the buoyancy effect in higher disk spin rates) flow in lower heights not only can reach higher speeds, but also has a more uniform flow pattern.

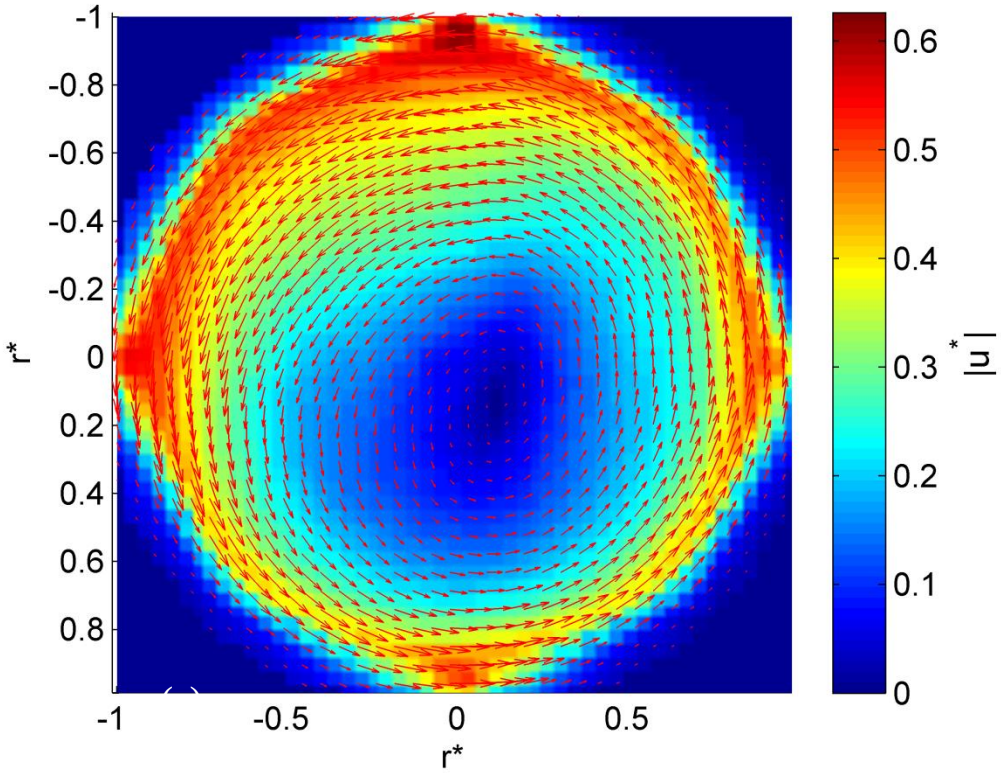

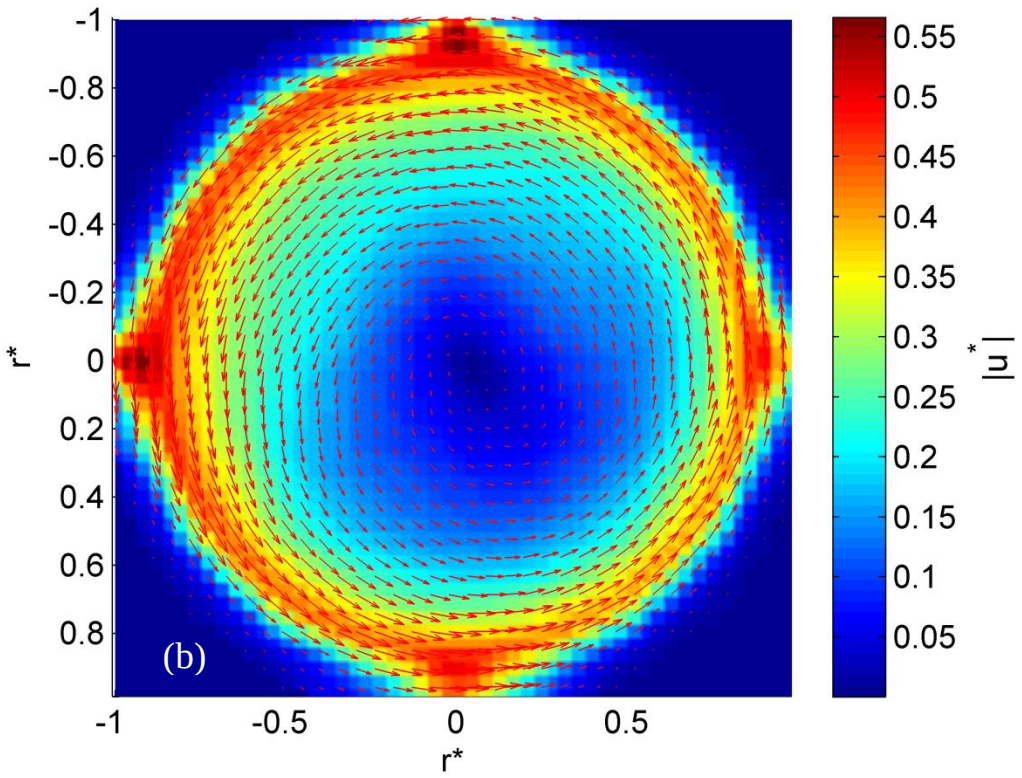

Figure 7.24 The velocity vector and magnitude field for the Heated Counter-Rotating flow when: $\Delta T = 50^{o}C$, $\Omega_w^* = 1.5$, $\Omega_d^* = -1$ for heights (a): $z^* = 0.67$and (b): $z^* = 1$

Profiles of azimuthal velocity are shown in figure 7.25. Both average curves show that profiles' behavior is very closer to linear in this thermal condition compared to figure 7.7. Also, flow pattern in this thermal condition is more symmetric and the difference between section curves and average curve is less than figure 7.7.

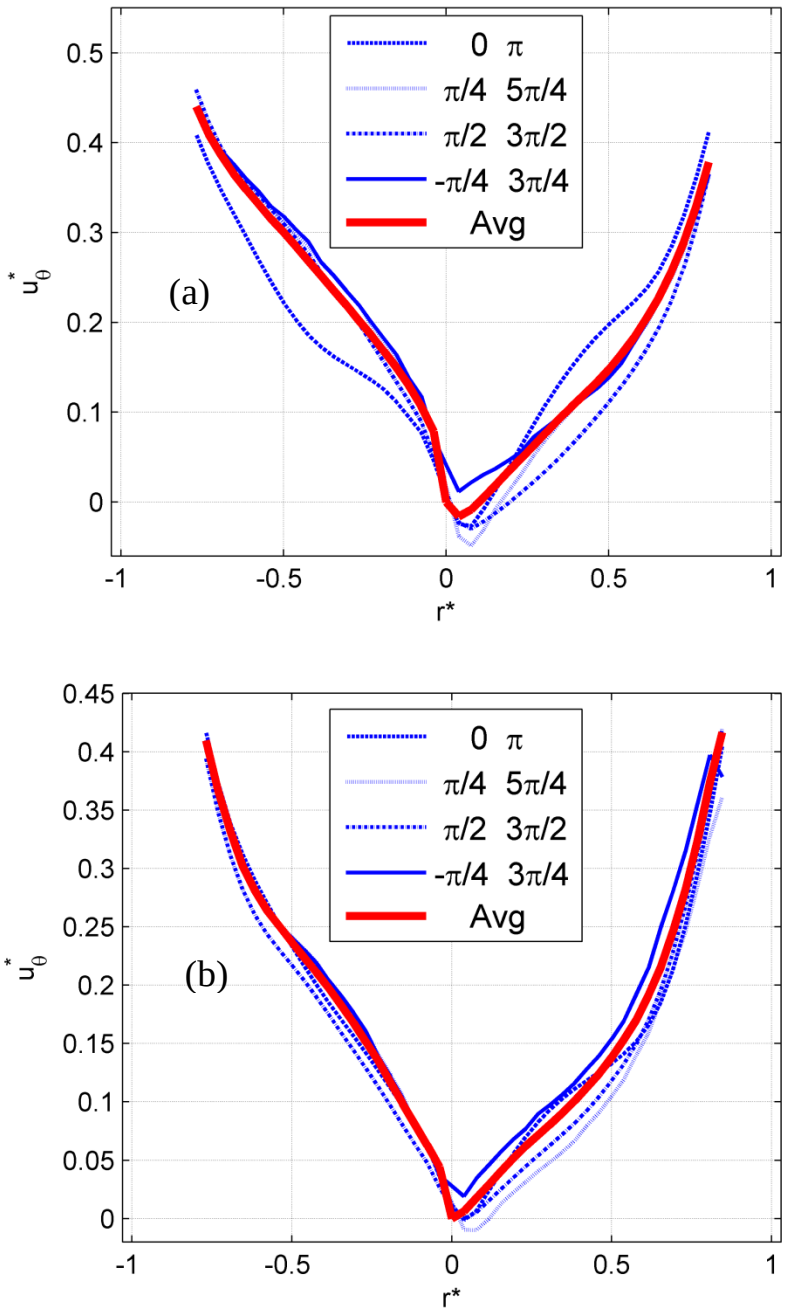

Figure 7.25 Normalized azimuthal velocity profile averaged over the half-circle-sectors and selected profiles across four radial sections for the Heated Counter-Rotating flow when: $\Delta T = 50^o C$, $\Omega_w^* = 1.5$, $\Omega_d^* = -1$ when (a): $z^* = 0.67$ and (b): $z^* = 1$

Next disk spin rate is $\Omega_d^* = -1.2$ and height by height vector fields are shown in figure 7.26. Flow pattern in the first two heights have changed. In the first one flow is not completely counter-clock-wise. Although for the most parts flow follows the wall-rotating direction, two

small vortices. Moreover, in the second height flow is less symmetric than previous disk rate. In the third height and above that flow is similar to previous disk spin rate. It seems that the transition happened just below (or even includes) the second height and has ascended from the previous disk spin rate.

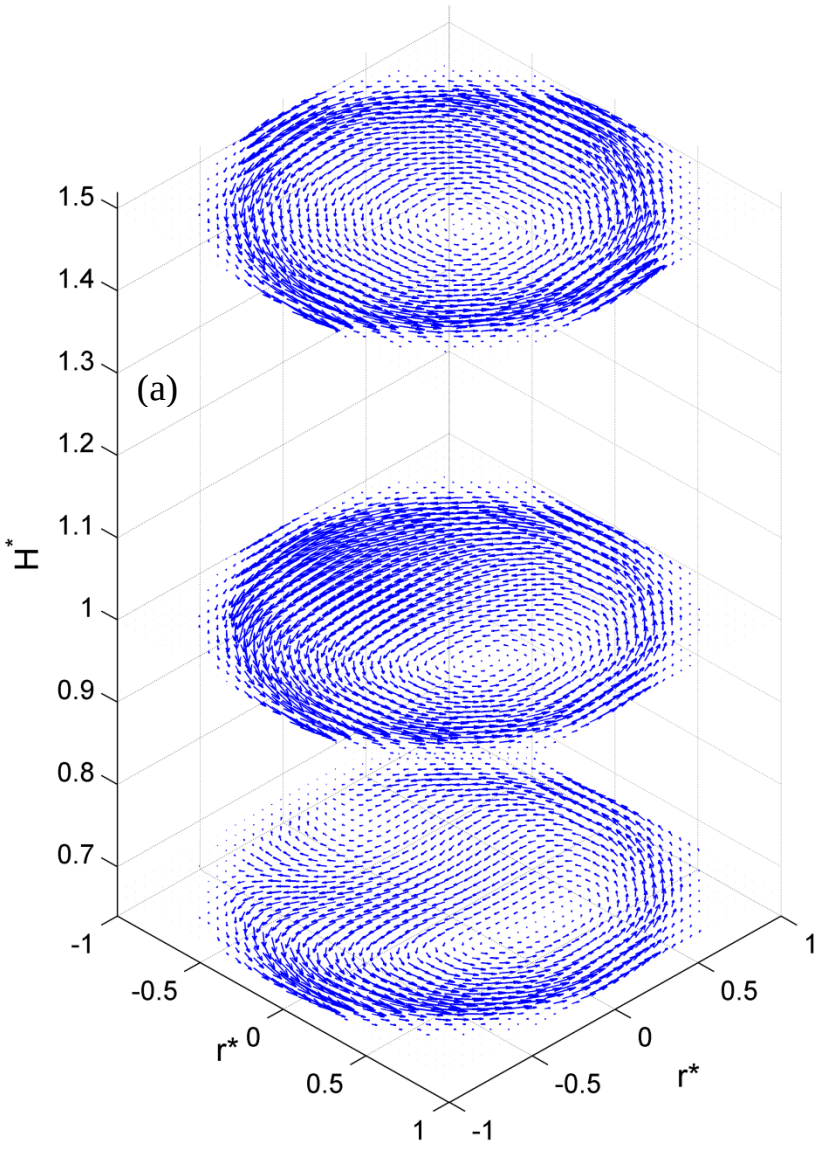

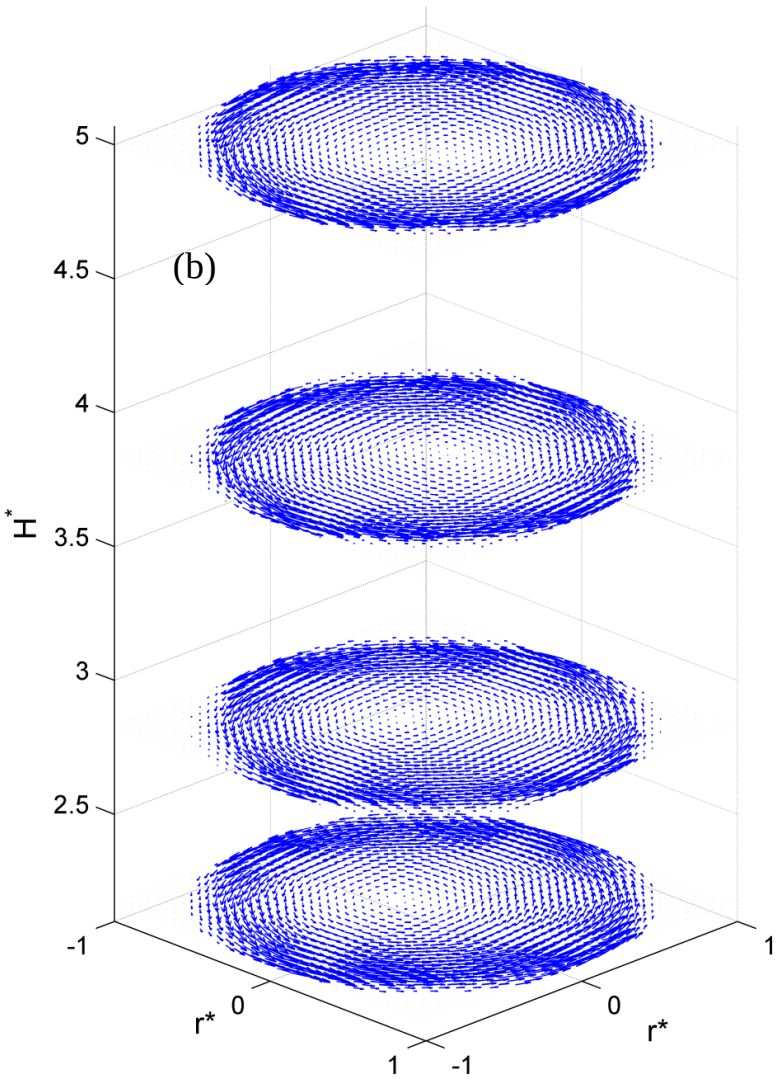

Figure 7.26 Velocity vector field for one Heated Counter-Rotating flow case: $\Delta T = 50^{o}C$ $\Omega_w^* = 1.5$ and the disk spin rate $\Omega_d^* = -1.2$ for (a): three lower studied heights and (b) four higher ones

Velocity vector/magnitude fields of the first two heights are shown in figure 7.27. Although even in the first height flow is mostly rotating counter-clock-wise and following the wall, between 8 and 10 O'clock there is a weak opposite rotating vortex and flow behavior is quite different. It seems that the transitional domain is just below $z^* = 0.67$. At the same region in the higher height rotation becomes strongly counter-clock-wise. In both first heights flow is not symmetric and center of vortex in close to 3 O'clock.

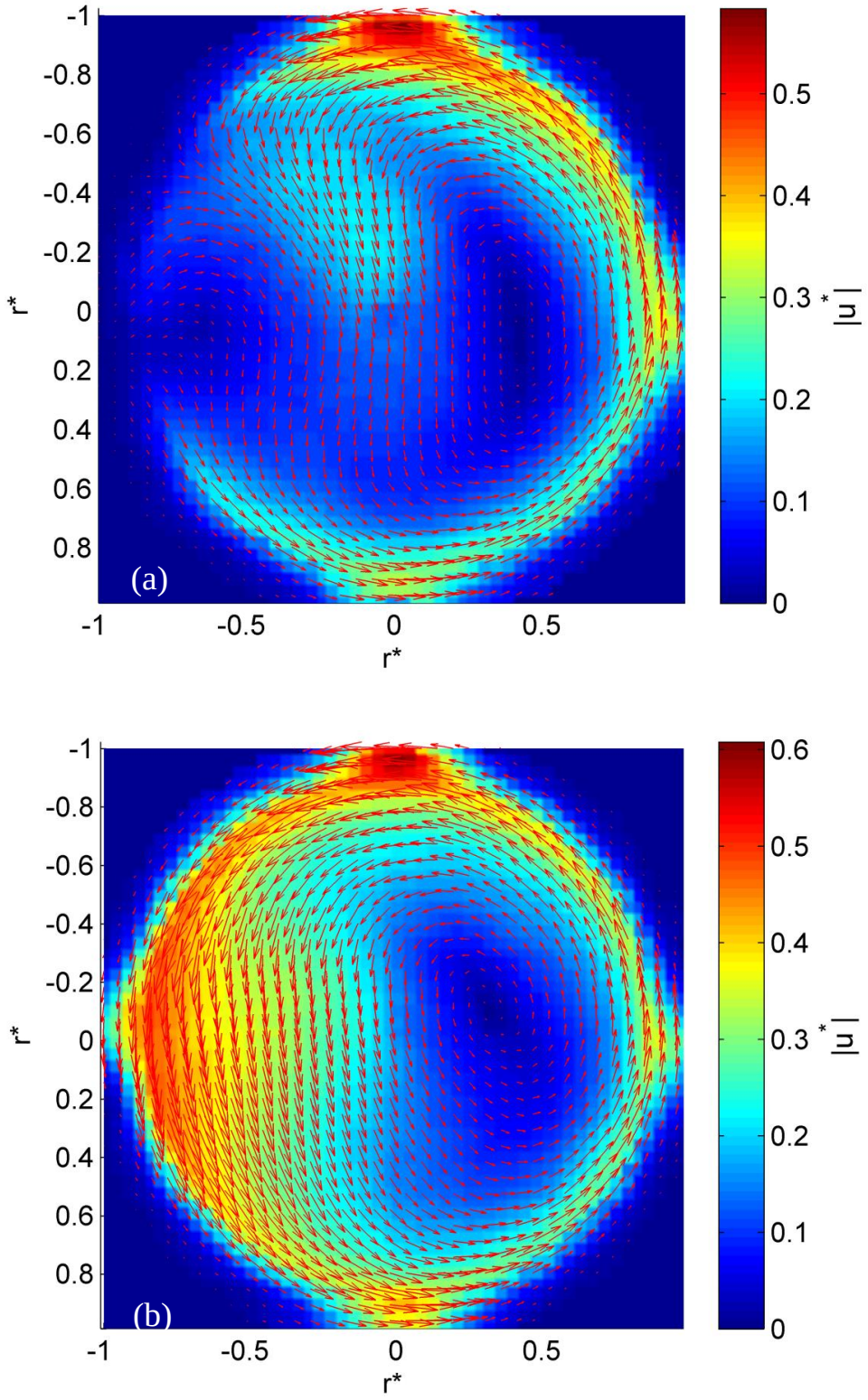

Figure 7.27 The velocity vector and magnitude field for the Heated Counter-Rotating flow when: $\Delta T = 50^{o}C$, $\Omega_w^* = 1.5$, $\Omega_d^* = -1.2$ for heights (a): $z^* = 0.67$and (b): $z^* = 1$

Comparing the azimuthal component of the velocity in the first three heights shows that in the first layer this value is much less than the other two ones and as the height increases, the difference between height decreases and flow become more symmetric. As said for the previous figure, this one also shows that flow in most of the region in the first height is positive (counter-clock-wise) and this value increases in higher heights.

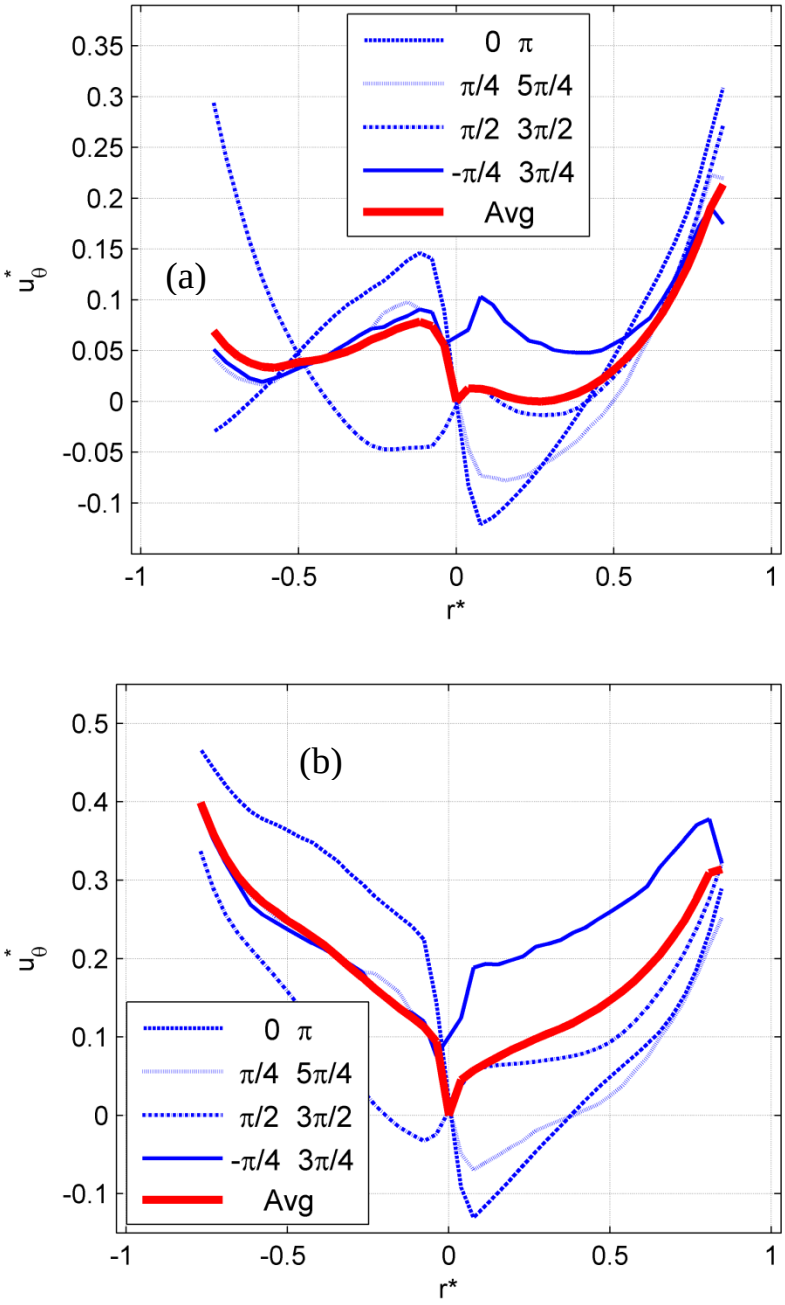

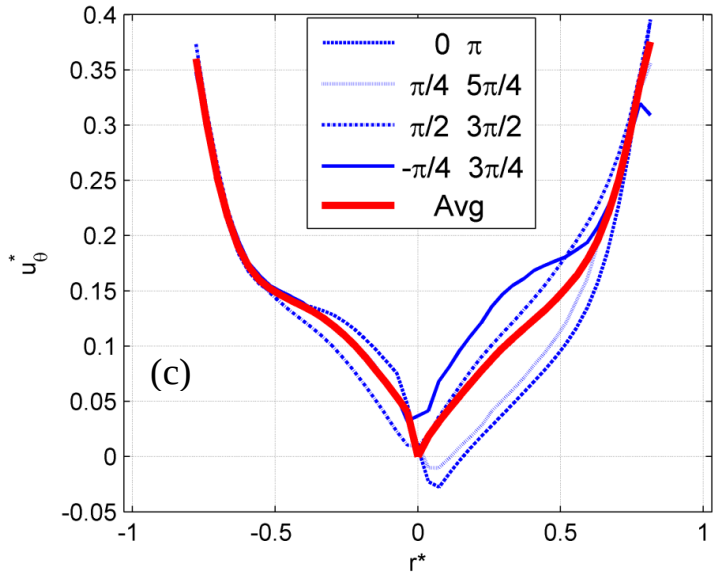

Figure 7.28 Normalized azimuthal velocity profile averaged over the half-circle-sectors and selected profiles across four radial sections for the Heated Counter-Rotating flow when: $\Delta T = 50^o C$, $\Omega_w^* = 1.5$, $\Omega_d^* = -1.2$ when (a): $z^* = 0.67$, (b): $z^* = 1$ and (c): $z^* = 1.5$

In the next disk spin rate, $\Omega_d^* = -1.4$, flow pattern in the first height has significantly changed due to presence of transitional domain. In the second height and above flow follows the wall-rotating direction (upper domain). Flow in the first height does not have a clear spinning direction. Obviously, the magnitude of vectors in the first height is smaller than that in other heights due to equal effect of the two opposite rotating vortices above and below the transitional domain. Another fact is the center of vortex in the second height is not at the centerline. Moreover, in all of the heights above the second height, unlike the similar cases in lower disk temperature with the ring of high velocity and large low velocity region at the center, velocity from the wall to the center does not change so drastically. In other words, velocity near the center in this case is larger than velocity in the previous thermal conditions. Nonetheless, in five higher heights flow pattern is more or less similar.

In figure 7.30 velocity magnitude/vector fields of the flow in the first three heights are demonstrated. Interestingly, at the first height domain is divided to two halves in which flow has

two opposite directions. Maximum velocity, as mentioned before is smaller than other heights and flow does not seem axisymmetric at all. Clearly, the transition is taking place in this height and the effect of disk and wall has almost same strengths. At the second height flow is following the wall-rotating direction even though the maximum velocity is slightly less than higher heights (upper domain). Also, the center of vortex leaning toward 2 O'clock and flow is not completely axisymmetric. Although even at the third height center of vortex is close to 12 O'clock, at this height and above flow seems more axisymmetric and follows the wall-rotating direction. Both velocity of flow near the wall and the maximum velocity have increased from the second height to the third one.

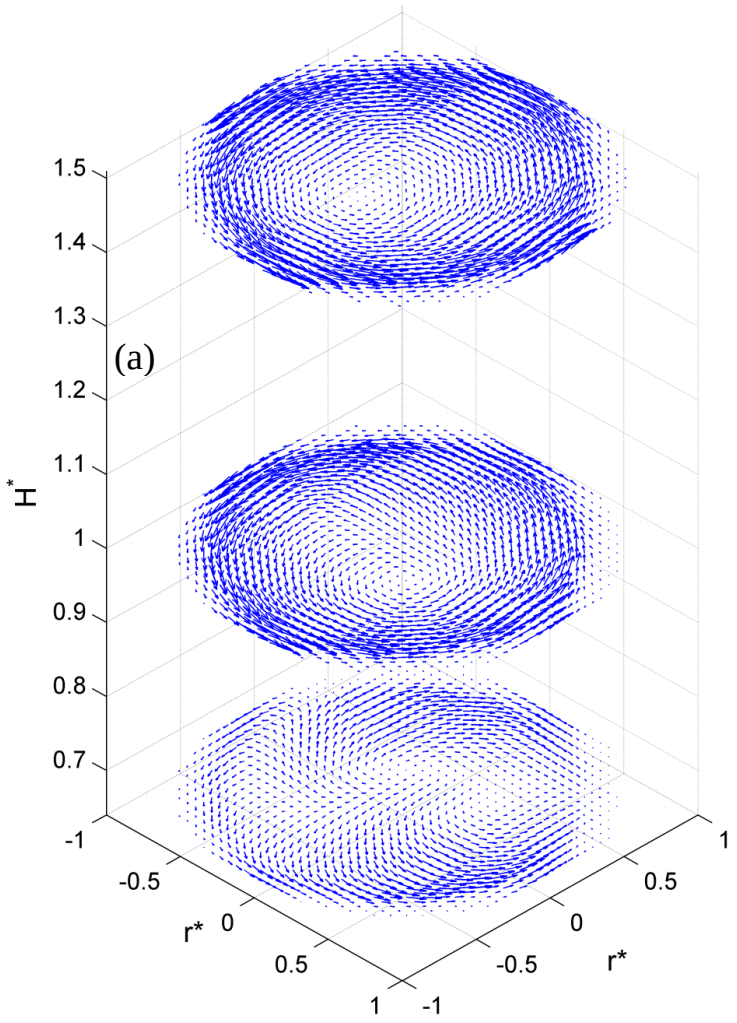

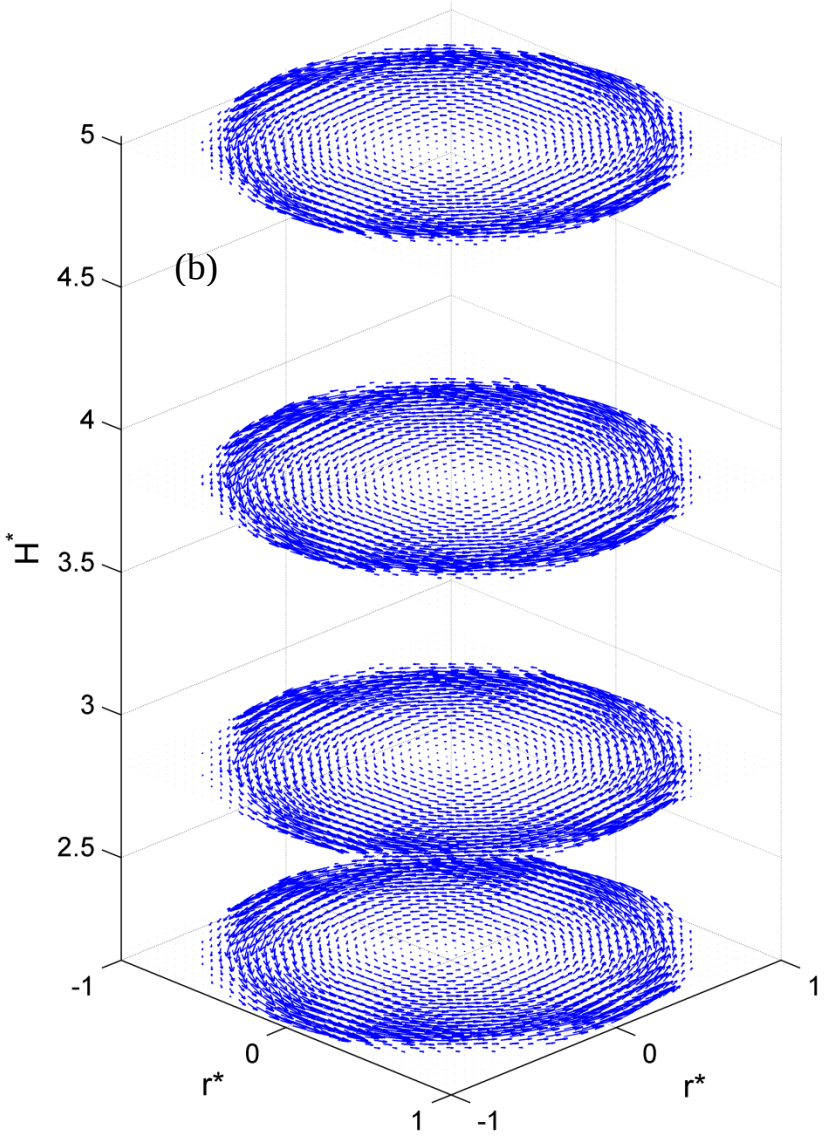

Figure 7.29 Velocity vector field for one Heated Counter-Rotating flow case: $\Delta T = 50^{o}C$ $\Omega_w^* = 1.5$ and the disk spin rate $\Omega_d^* = -1.4$ for (a): three lower studied heights and (b) four higher ones

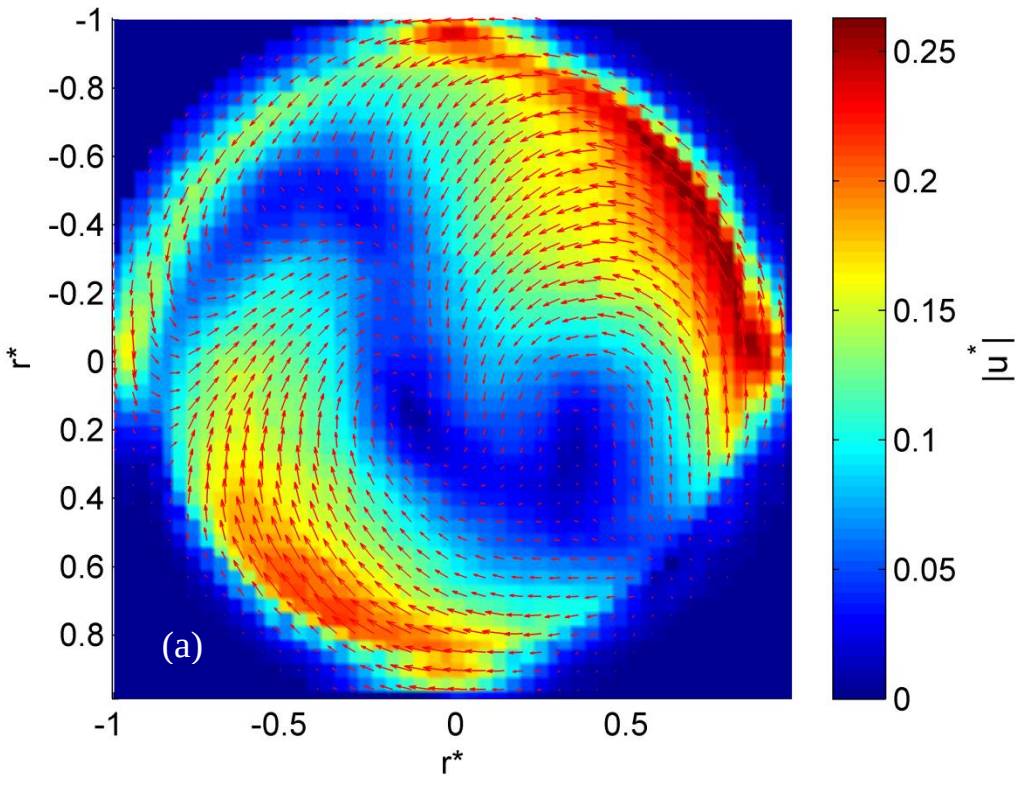
-1
-0.8
-0.6
-0.4
-0.2
0
0.2
0.4
0.6
0.8
r*
(a)
-1
-0.5
0
0.5
r*
0.25
0.2
0.15
0.1
0.05
0
|u*|

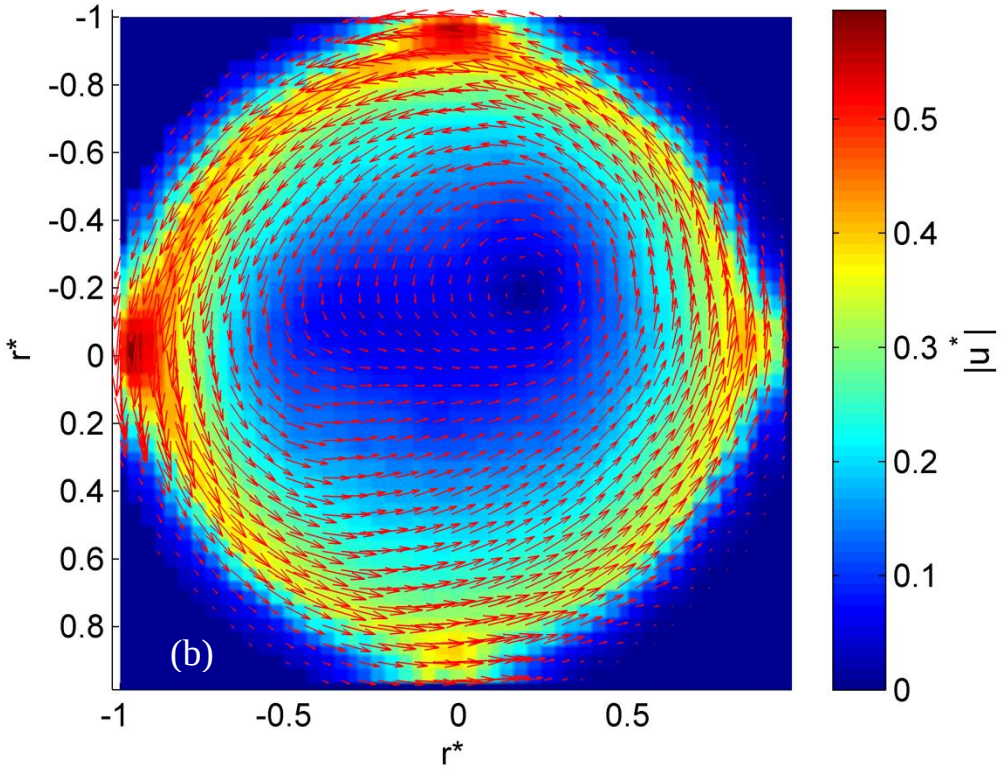
-1
-0.8
-0.6
-0.4
-0.2
0
0.2
0.4
0.6
0.8
r*
(b)
-1
-0.5
0
0.5
r*
0.5
0.4
0.3
0.2
0.1
0
|u*|

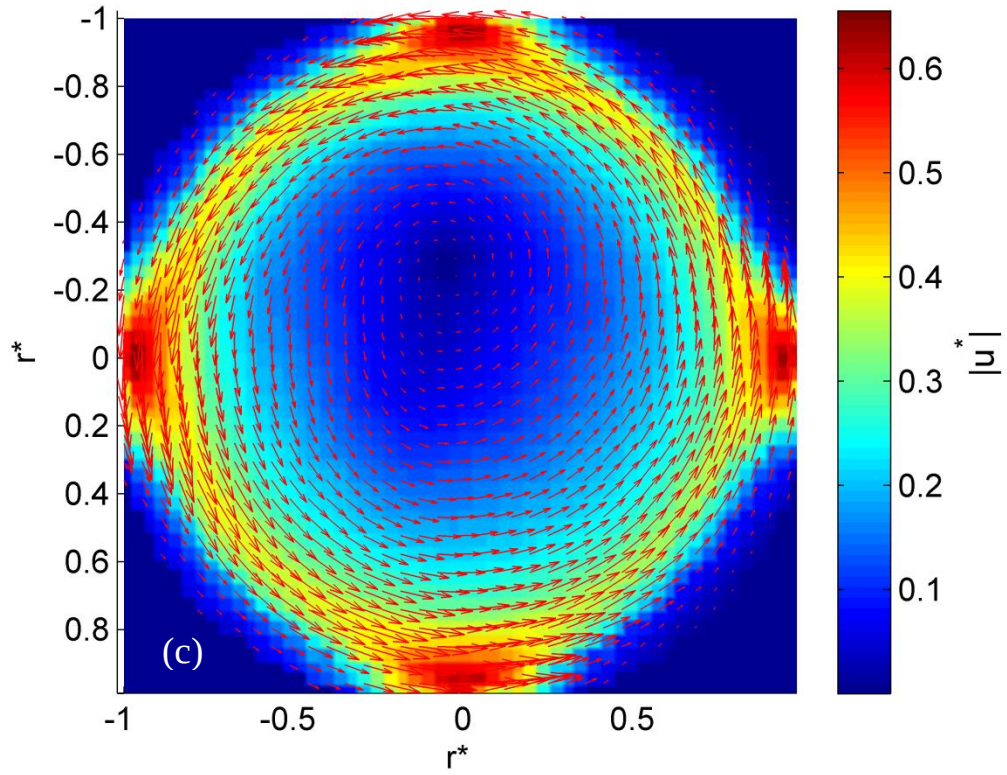

Figure 7.30 The velocity vector and magnitude field for the Heated Counter-Rotating flow when: $\Delta T = 50^{o}C$, $\Omega_w^* = 1.5$, $\Omega_d^* = -1.4$ for heights (a): $z^* = 0.67$, (b): $z^* = 1$ and (c): $z^* = 1.5$

The azimuthal component of velocity for the first three heights in figure 7.31 clearly demonstrates that at the first height flow is completely different. In this height the average curve shows a very low magnitude and other sections are very significantly different because flow does not behave axisymmetrically. Above this height velocity almost linearly increases from the center to the wall and as the height increases it become more symmetric.

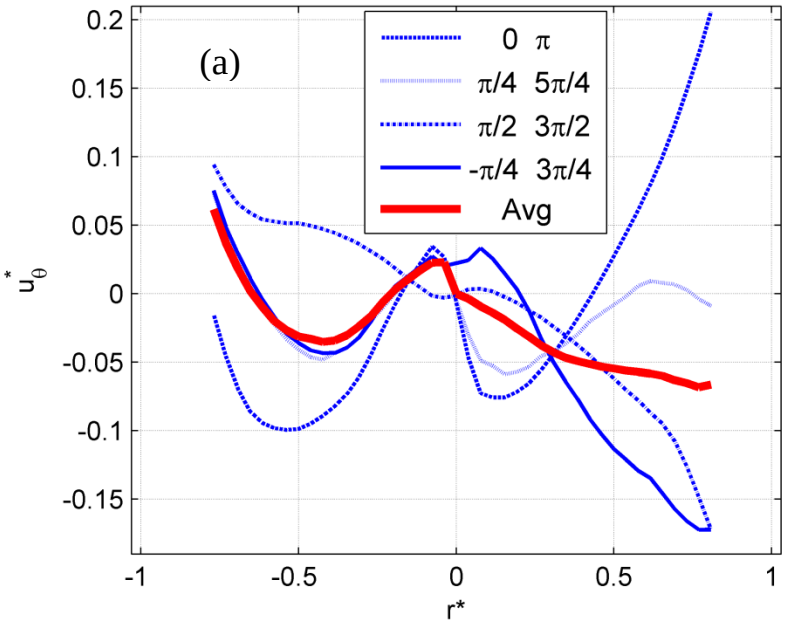
(a)
0 π
π/4 5π/4
π/2 3π/2
-π/4 3π/4
Avg
0.2
0.15
0.1
0.05
0
-0.05
-0.1
-0.15
-1
-0.5
0
0.5
1
r*
u*θ

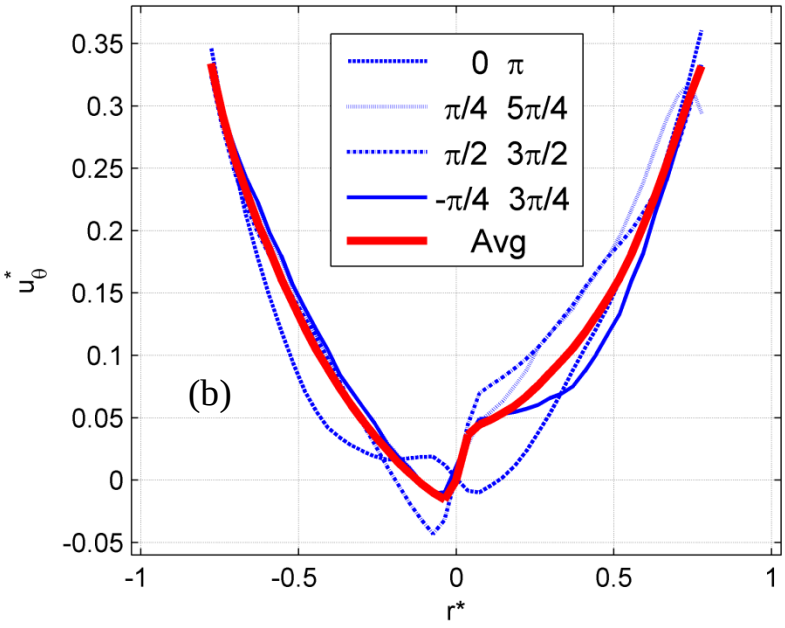
(b)
0 π
π/4 5π/4
π/2 3π/2
-π/4 3π/4
Avg
0.35
0.3
0.25
0.2
0.15
0.1
0.05
0
-0.05
-1
-0.5
0
0.5
1
r*
u*θ

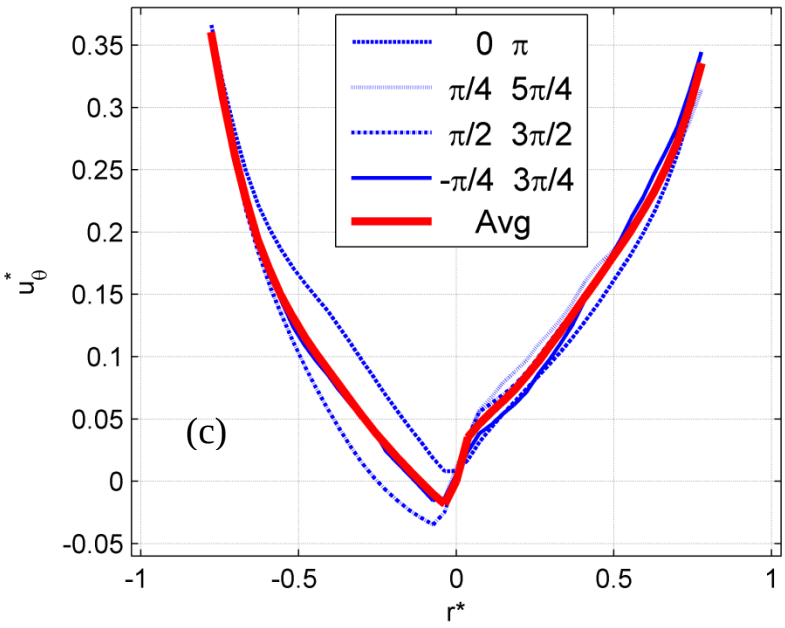

Figure 7.31 Normalized azimuthal velocity profile averaged over the half-circle-sectors and selected profiles across four radial sections for the Heated Counter-Rotating Flow when: $\Delta T = 50^o C$, $\Omega_w^* = 1.5$, $\Omega_d^* = -1.4$ when (a): $z^* = 0.67$, (b): $z^* = 1$ and (c): $z^* = 1.5$

In the next disk spin rate, $\Omega_d^* = -1.6$, transition from the clock-wise rotating flow to the opposite direction has moved upward and locates close to the second height. As figure 7.32 shows, the first height disk is in the lower domain and the third is the upper one. It seems that disk's and wall's effects have the same strength at the second height (transitional domain). Although at the third height flow is following the wall rotation, this flow is not axisymmetric and center of vortex is far from centerline. Above the third height flow is similar to previous cases and simply following the wall-rotating direction with more axisymmetric behavior compared to the lower heights. This figure also shows the direction of rotation next to the azimuthal velocity profile and can be compared with figure 6.2 in which conditions are similarly designed expect for the disk temperature ($\Delta T = 0^o C$ for that case).

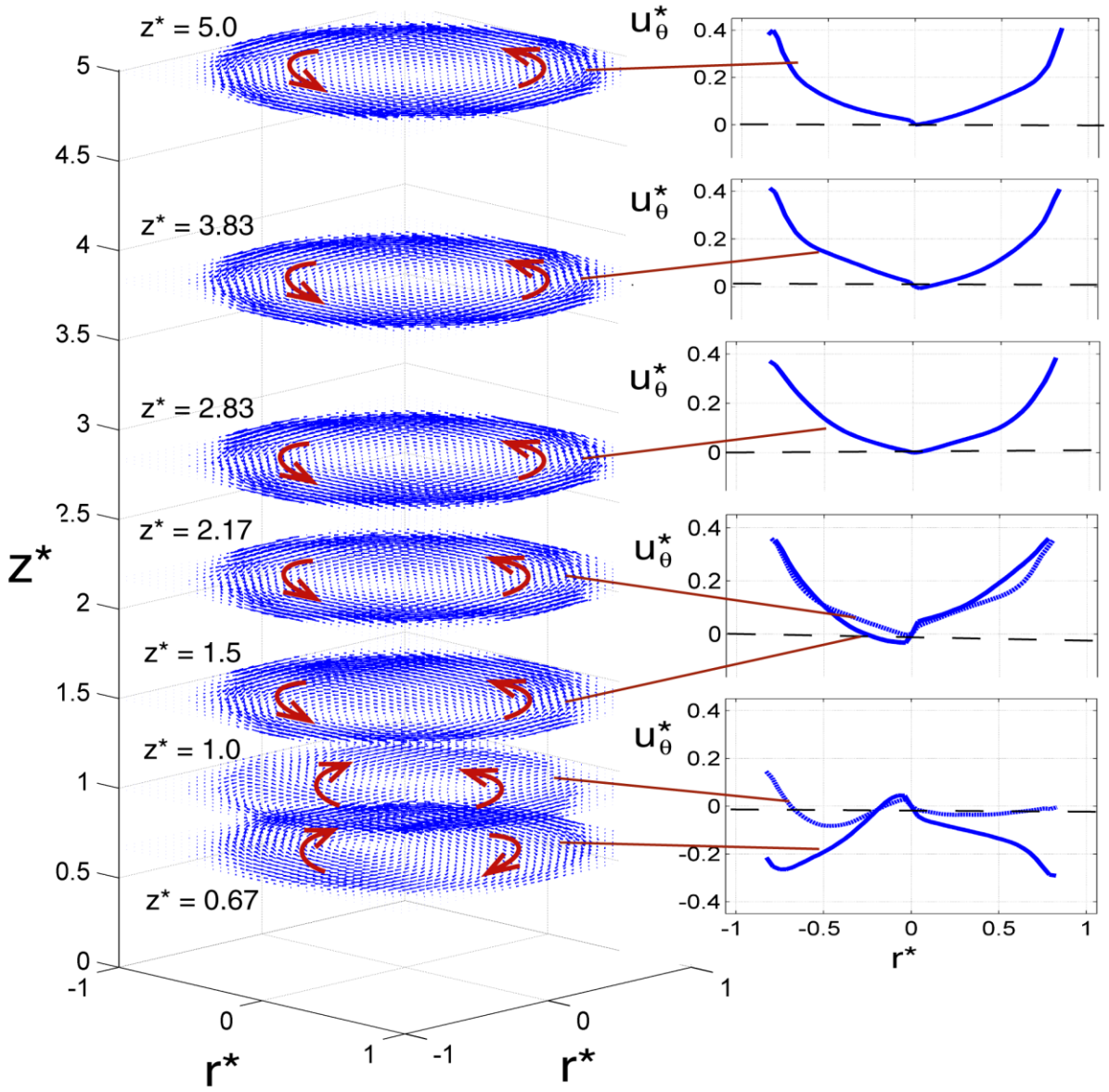

Figure 7.32 Velocity vector field for one Heated Counter-Rotating flow case: $\Delta T = 50^{o}C$ $\Omega_w^* = 1.5$ and the disk spin rate $\Omega_d^* = -1.6$ along with the normalized azimuthal velocity

In figure 7.33 velocity magnitude/vector fields for the first three heights are presented. The clock-wise rotation of the first height can be clearly seen in the figure-a (lower domain) as well as the two opposite rotating flows in the two halves of domain at the second height (upper domain). The counter-clock-wise rotation, however, seems slightly stronger. At the first and third heights the centers of vortex are close to 1 and 10 O'clock respectively and are far from the

centerline. Since these two heights are close the transition domain height flow, similar to other cases, the flow does not behave axi-symmetrically. Moreover, maximum of velocity above the transition height, in the third height, increases (compared to two lower heights). The main difference between the vertical plane (Figures d and e) in this case and previous cases with lower *Gr* number is the vertical location of the transitional domain. Obviously, this domain has descended in this case and its height is about half of this height in unheated case. Upward and downward motions are slightly stronger and the two dark bands of low velocity region in previous cases in even clearer.

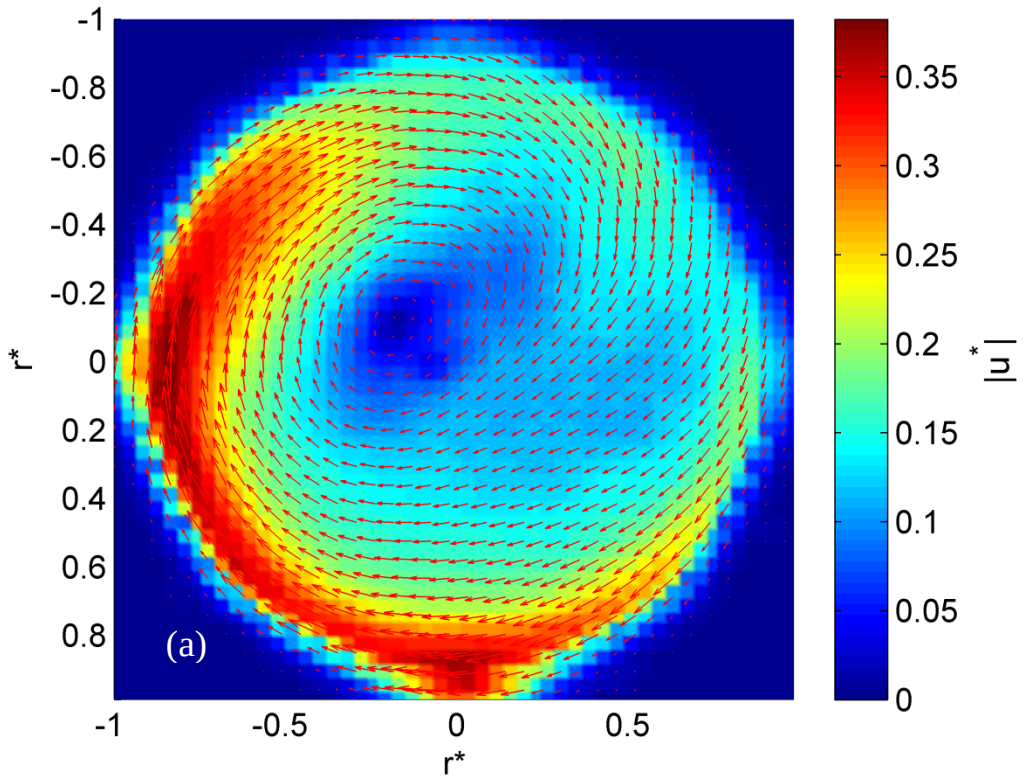

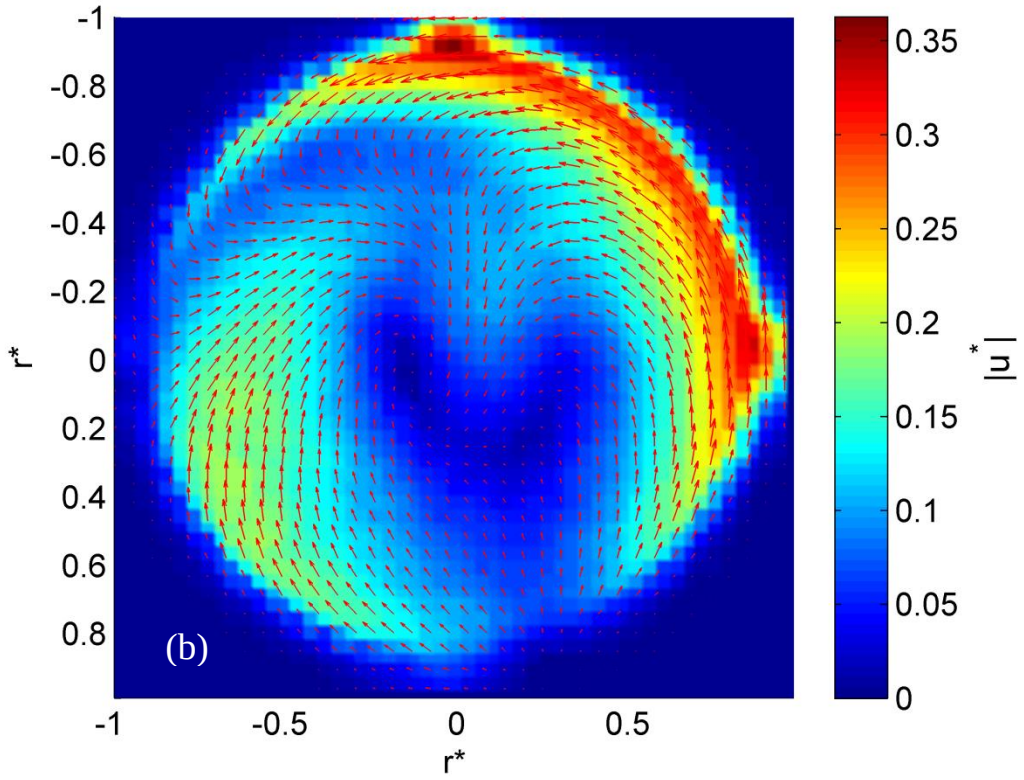
-1
-0.8
-0.6
-0.4
-0.2
0
0.2
0.4
0.6
0.8
r*
(b)
-1
-0.5
0
0.5
r*
0.35
0.3
0.25
0.2
0.15
0.1
0.05
0
|u*|

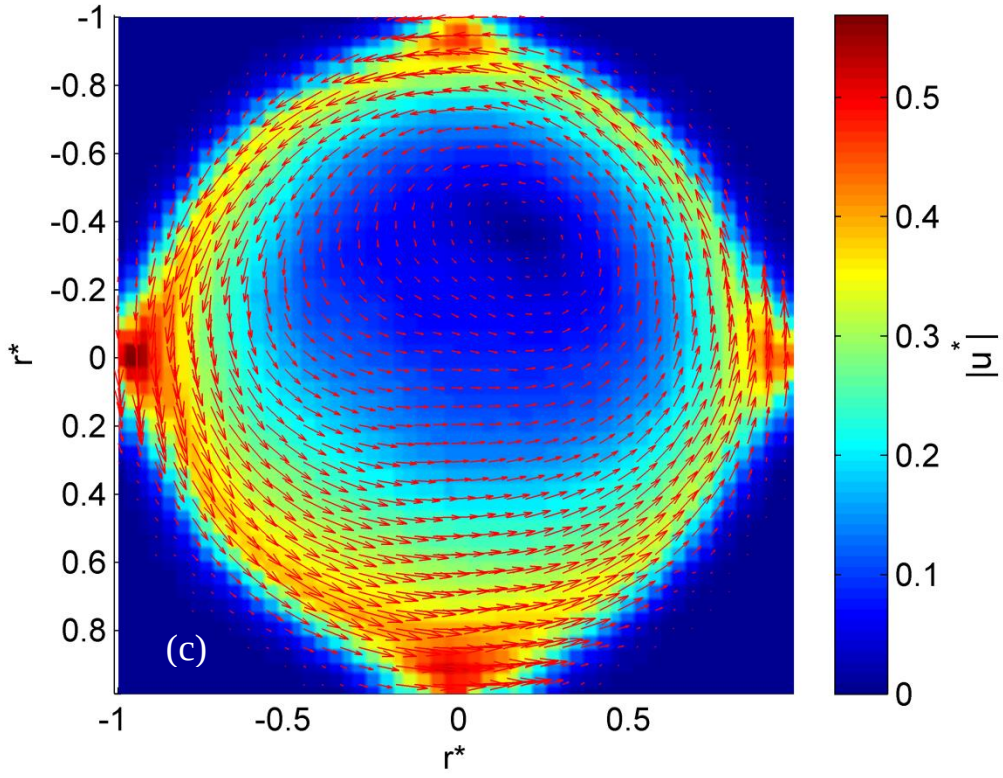
-1
-0.8
-0.6
-0.4
-0.2
0
0.2
0.4
0.6
0.8
r*
(c)
-1
-0.5
0
0.5
r*
0.5
0.4
0.3
0.2
0.1
0
|u*|

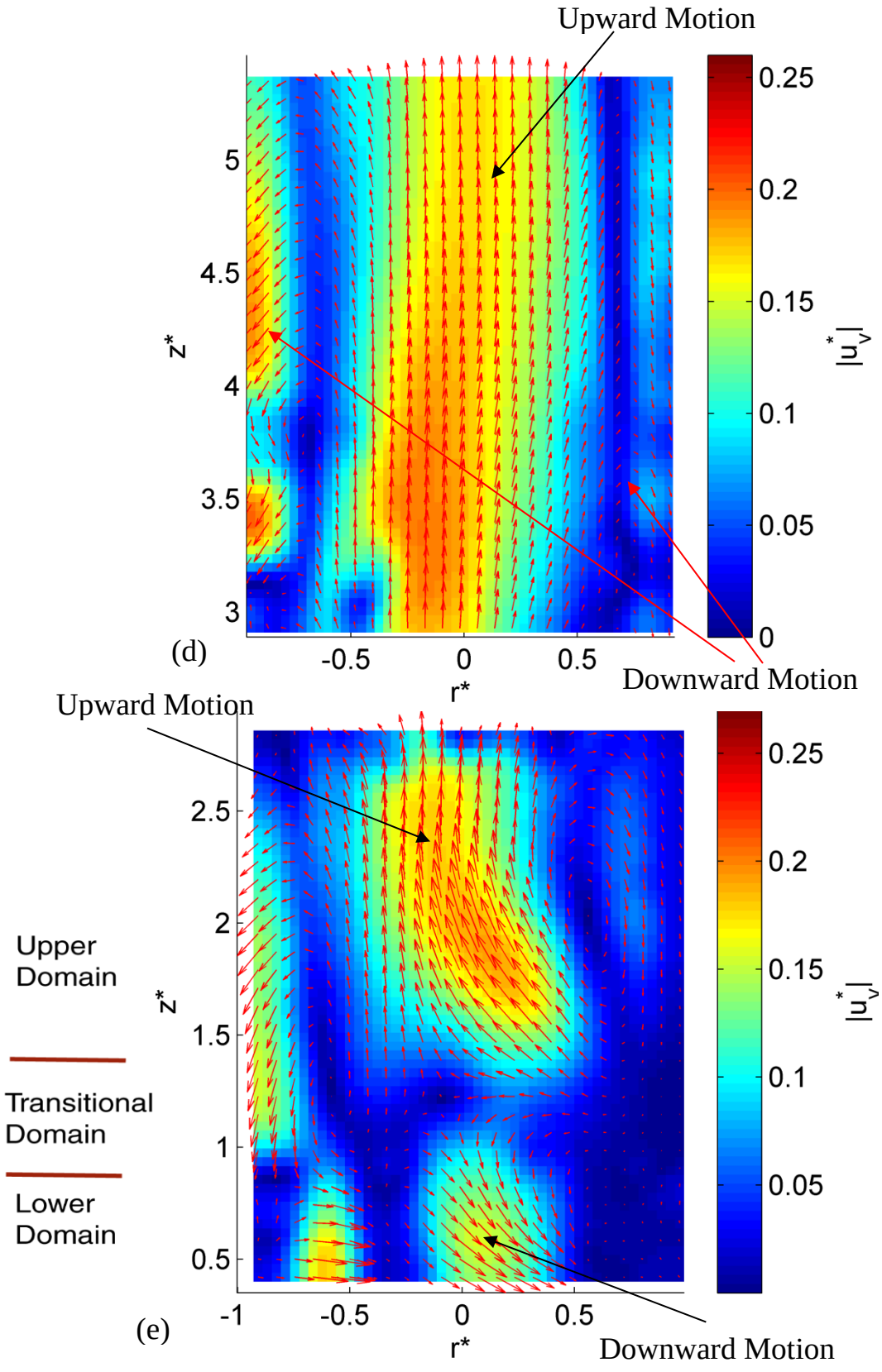

Figure 7.33 The velocity vector and magnitude field for the Heated Counter-Rotating flow when: $\Delta T = 50^{o}C$, $\Omega_w^* = 1.5$, $\Omega_d^* = -1.6$ for heights (a): $z^* = 0.67$, (b): $z^* = 1$,(c): $z^* = 1.5$ and (b) and (b): vertical planes

The azimuthal velocity component in figure 7.34 also shows that at the second height transition is taking place. The value of the average curve in this height is very smaller than other heights. The difference between 4 sections and the average curve in the first three height show that flow is not quite axisymmetric in any of them (Especially in the second height).

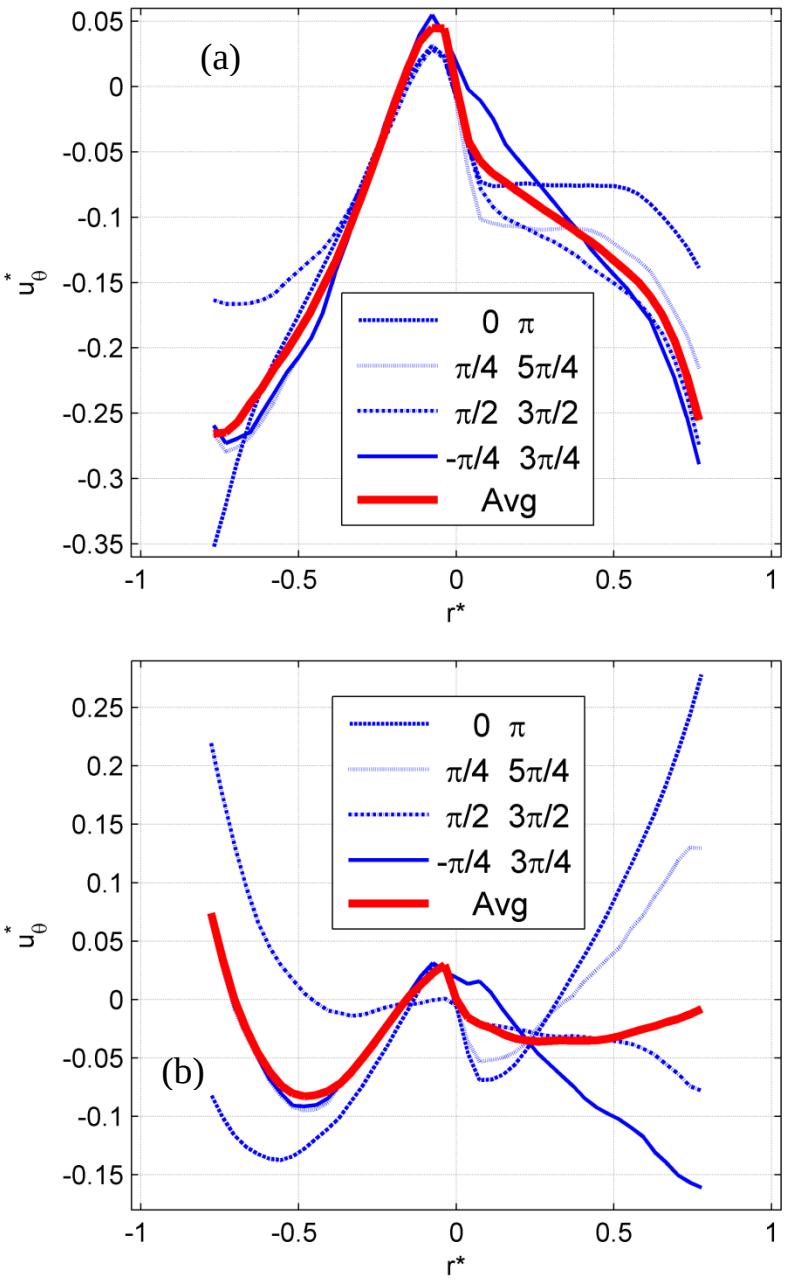

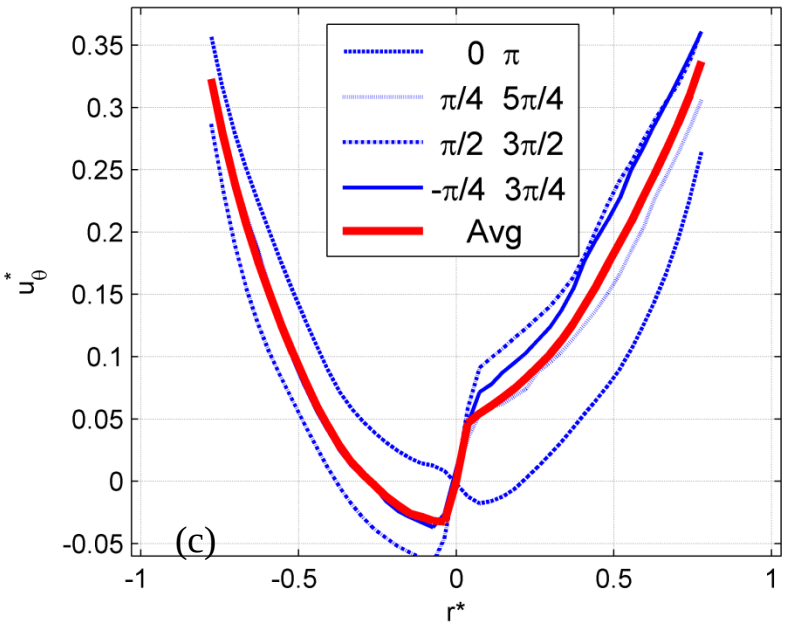

Figure 7.34 Normalized azimuthal velocity profile averaged over the half-circle-sectors and selected profiles across four radial sections for the Heated Counter-Rotating Flow when: $\Delta T = 50^o C$, $\Omega_w^* = 1.5$, $\Omega_d^* = -1.6$ when (a): $z^* = 0.67$, (b): $z^* = 1$ and (c): $z^* = 1.5$

In the next disk spin rate, $\Omega_d^* = -1.8$, two first heights are spinning clock-wise as shown in figure 7.35 (lower domain). In the third height flow rotation becomes mostly counter-clock-wise, however, some opposite rotating flows are observed in the inner region (beginning of upper domain). It seems that the transition is taking place just below the third height. Magnitudes of vectors in the first height seem to be larger than the second one. Flow in the fourth height is not as axisymmetric as flow at this height in lower disk spin rate. Velocity magnitude/vector fields in figure 7.36 also show that the dominant clock-wise rotation in the first height begins to change in the second one. Inner region of the third height does not show a particular direction of rotation and at the fourth height center of vortex leaning towards 4 O'clock.

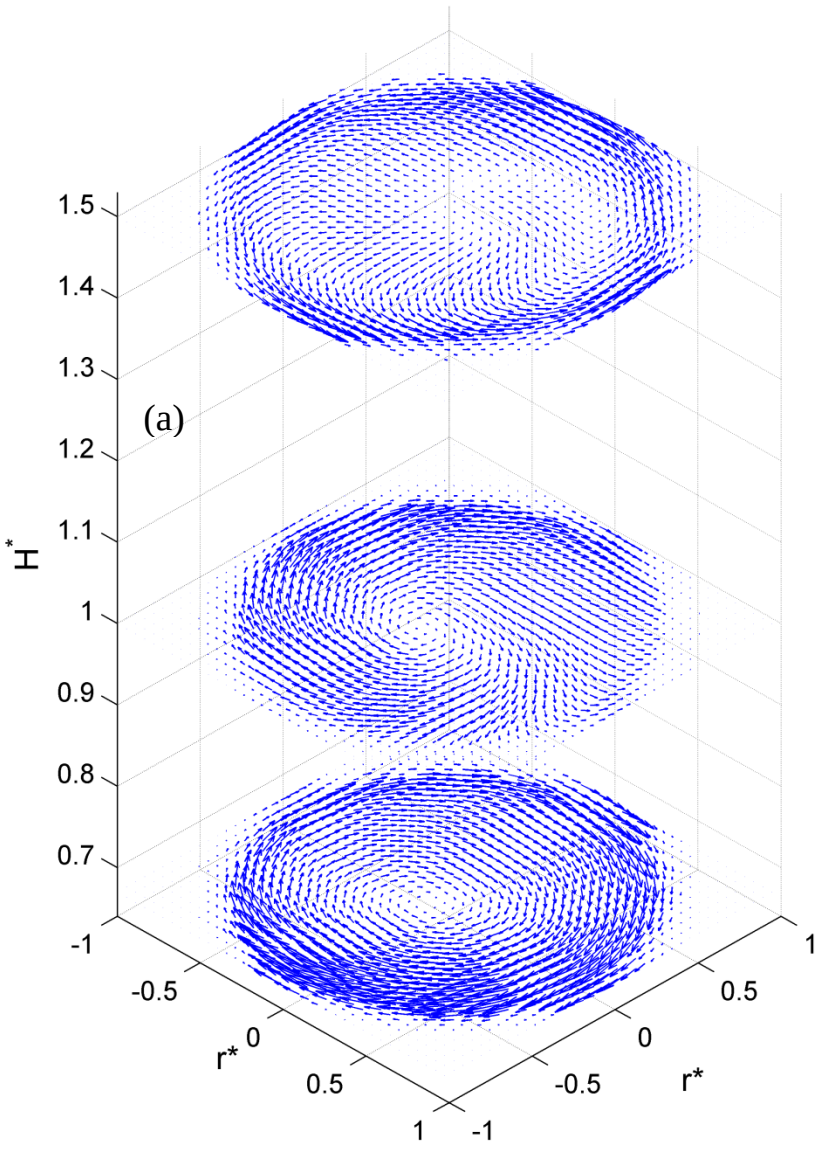
(a)
H*
1.5
1.4
1.3
1.2
1.1
1
0.9
0.8
0.7
-1
-0.5
0
0.5
1
r*
-1
-0.5
0
0.5
1
r*

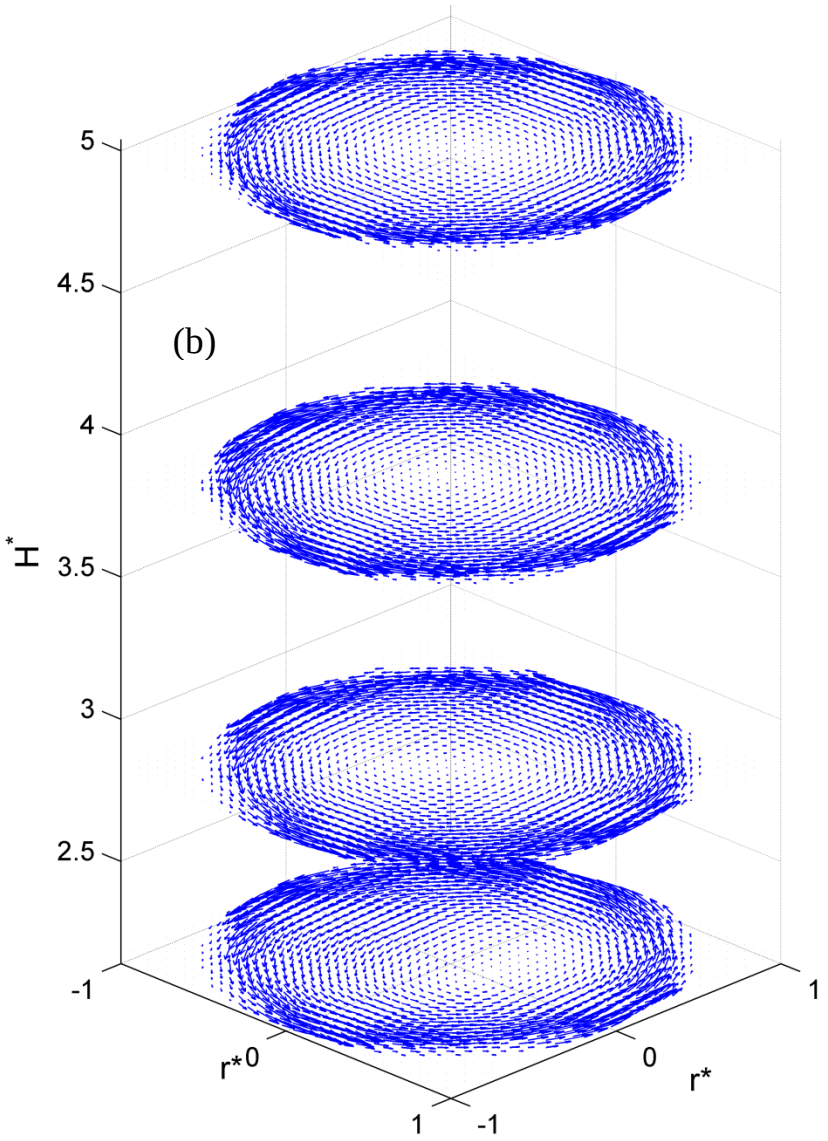

Figure 7.35 Velocity vector field for one Heated Counter-Rotating flow case: $\Delta T = 50^{o}C$ $\Omega_w^* = 1.5$ and the disk spin rate $\Omega_d^* = -1.8$ for (a): three lower studied heights and (b) four higher one

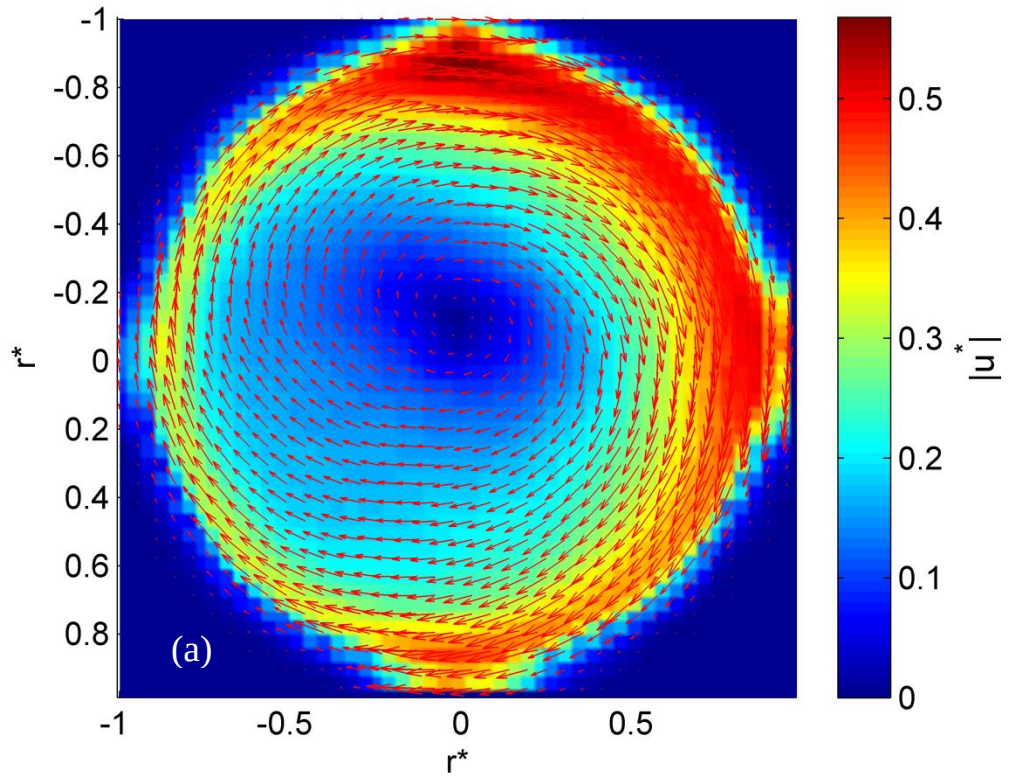
-1
-0.8
-0.6
-0.4
-0.2
0
0.2
0.4
0.6
0.8
r*
(a)
-1
-0.5
0
0.5
r*
0.5
0.4
0.3
0.2
0.1
0
|u*|

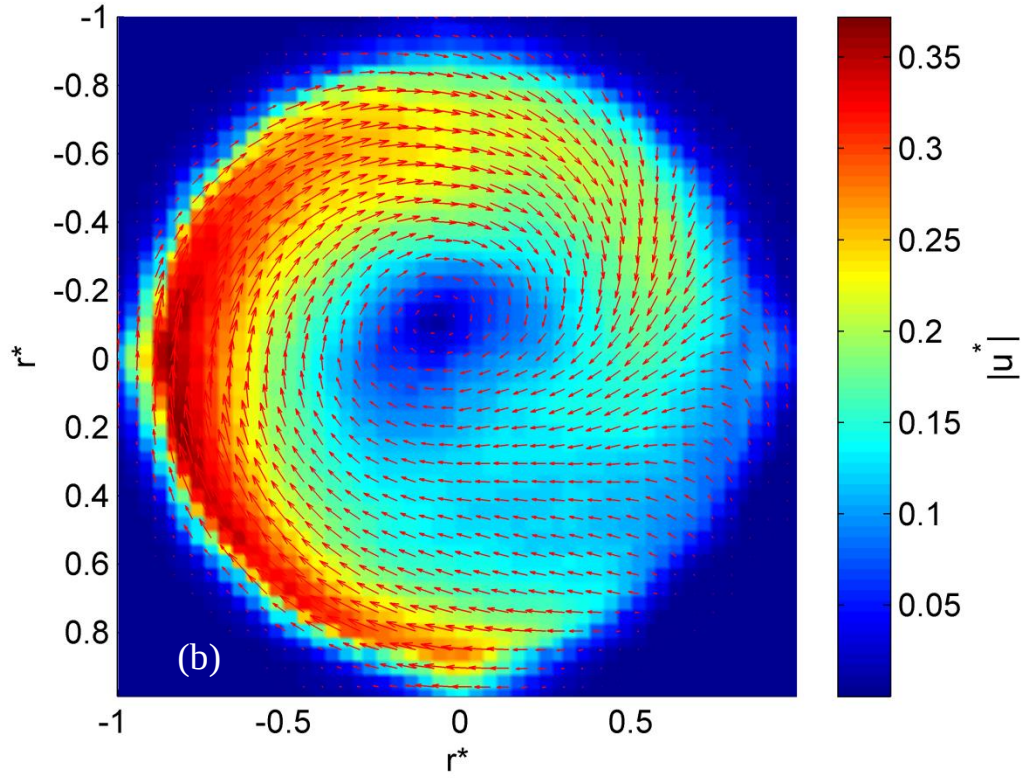
-1
-0.8
-0.6
-0.4
-0.2
0
0.2
0.4
0.6
0.8
r*
(b)
-1
-0.5
0
0.5
r*
0.35
0.3
0.25
0.2
0.15
0.1
0.05
|u*|

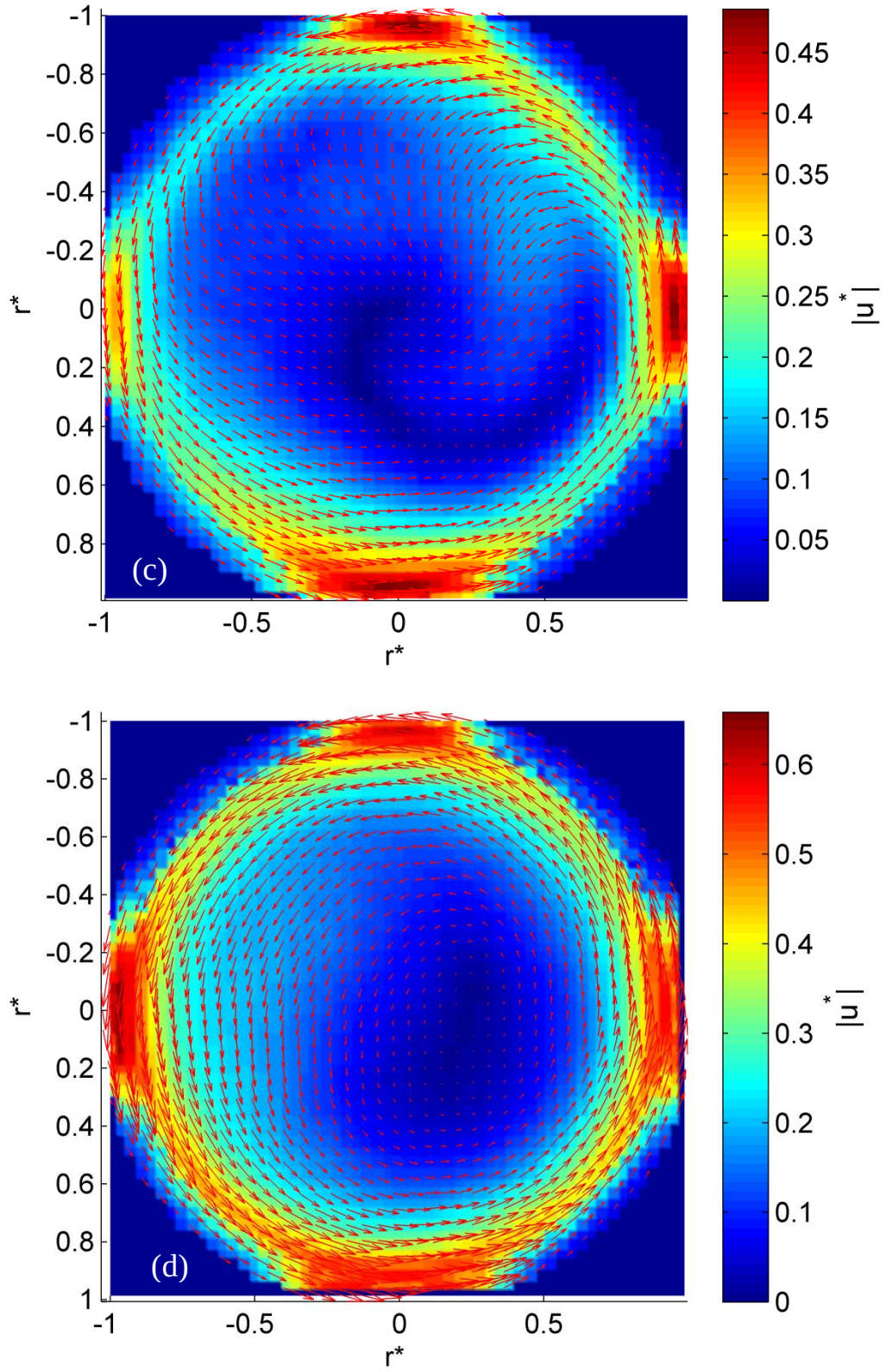

Figure 7.36 The velocity vector and magnitude field for the Heated Counter-Rotating Flow when: $\Delta T = 50^{o}C$, $\Omega_w^* = 1.5$, $\Omega_d^* = -1.8$ for heights (a): $z = 0.67$, (b): $z^* = 1$, (c): $z^* = 1.5$, and (d): $z^* = 2.17$

$\left\langle u_\theta^* \right\rangle$-profiles in the first five heights in figure 7.37 show that transition occurs between the second and the third heights. The least axisymmetric behavior is observed in the third height in which difference between the four sections and the average curve is relatively larger.

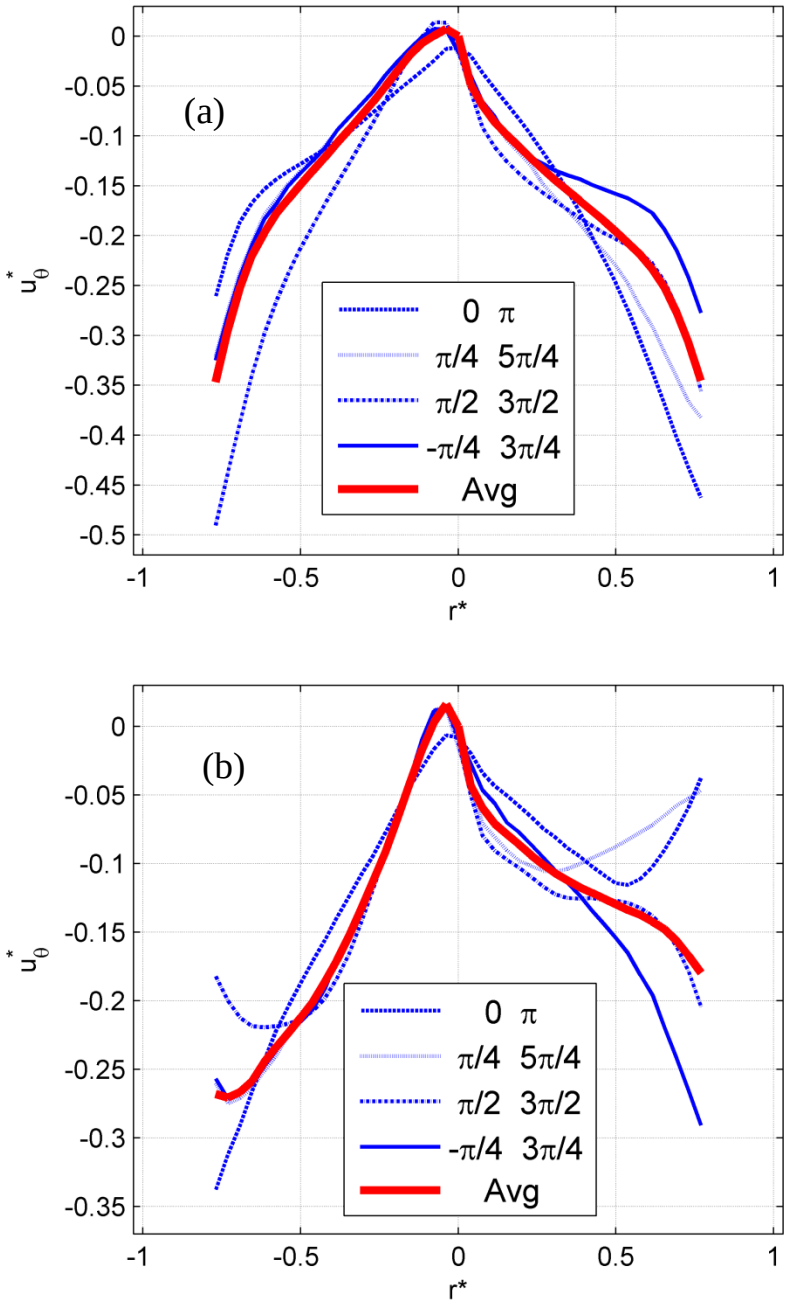

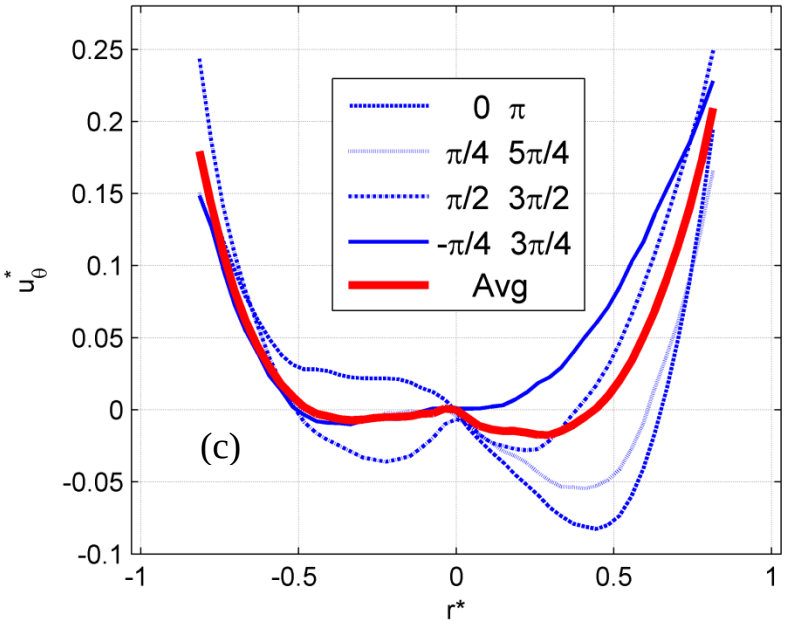
0.25
0.2
0.15
0.1
0.05
0
-0.05
-0.1
-1
-0.5
0
0.5
1
r*
u_θ^*
0 π
π/4 5π/4
π/2 3π/2
-π/4 3π/4
Avg
(c)

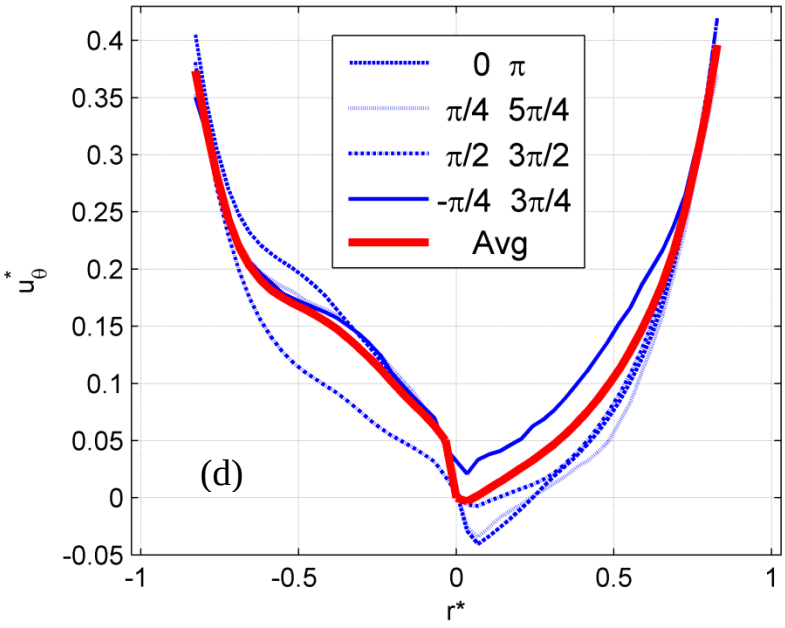
0.4
0.35
0.3
0.25
0.2
0.15
0.1
0.05
0
-0.05
-1
-0.5
0
0.5
1
r*
u_θ^*
0 π
π/4 5π/4
π/2 3π/2
-π/4 3π/4
Avg
(d)

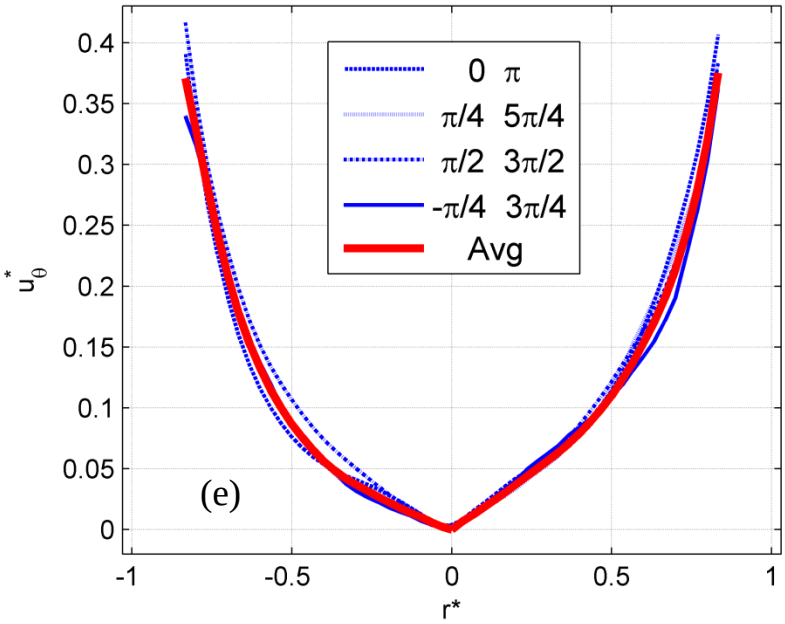

Figure 7.37 Normalized azimuthal velocity profile averaged over the half-circle-sectors and selected profiles across four radial sections for the Heated Counter-Rotating flow when: $\Delta T = 50^o C$, $\Omega_w^* = 1.5$, $\Omega_d^* = -1.8$ when (a): $z^* = 0.67$, (b): $z^* = 1$, (c) $z^* = 1.5$, (d): $z^* = 2.17$ and (e): $z^* = 2.83$

The last and largest studied disk spin rate is $\Omega_d^* = -2$. In this case, as shown in figure 7.38, at the first two heights flow is clock-wise. Even in the third height the dominant flow is clock-wise, yet in a portion of domain flow rotation is different (beginning of the transitional domain). The exact opposite thing happen in the fourth height and most parts of domain (especially outer ring) show counter-clock-wise rotation and in some points of the inner region flow is still clock-wise (end of the transitional domain). As expected, above this height flow is completely following the wall-rotating direction (upper domain). It appears that the transition takes place between the third and the fourth heights.

In the next figure, similar to other cases, velocity vector/magnitude fields are presented. Comparing figures 7.39-a and b shows that velocity magnitude decreases as the height increases. In the third height, as mentioned before, half of the outer ring has the opposite direction of flow

rotation. Flow in the inner region of fourth height is not axisymmetric and even between 6 and 9 O'clock rotates in opposite direction.

Figure 7.40 shows that the least axisymmetric behavior is observed in the second, third and fourth heights. Especially comparing figures 7.40-c and d and difference between the sections and average curves clearly shows that transition is happening in $1.5 < z^* < 2.17$. Also, the sign of $\langle u_\theta^* \rangle$-profiles between these two heights changes in most parts of the domain.

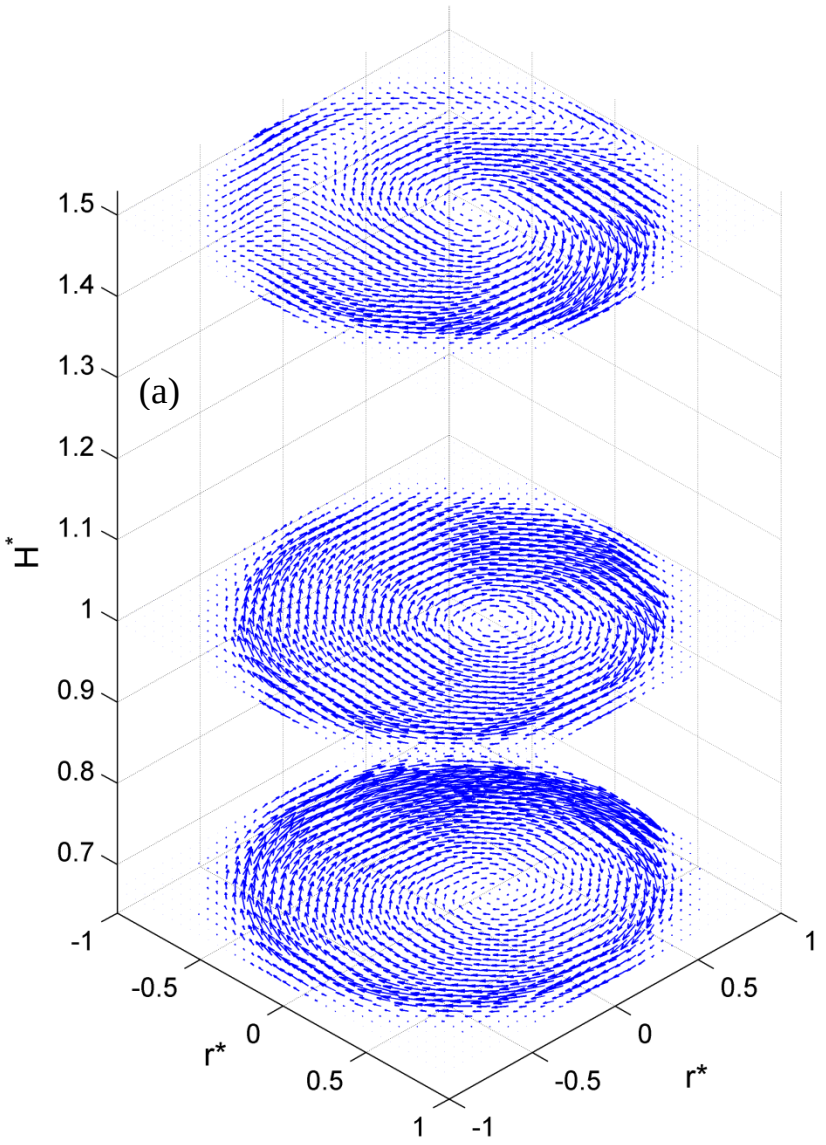

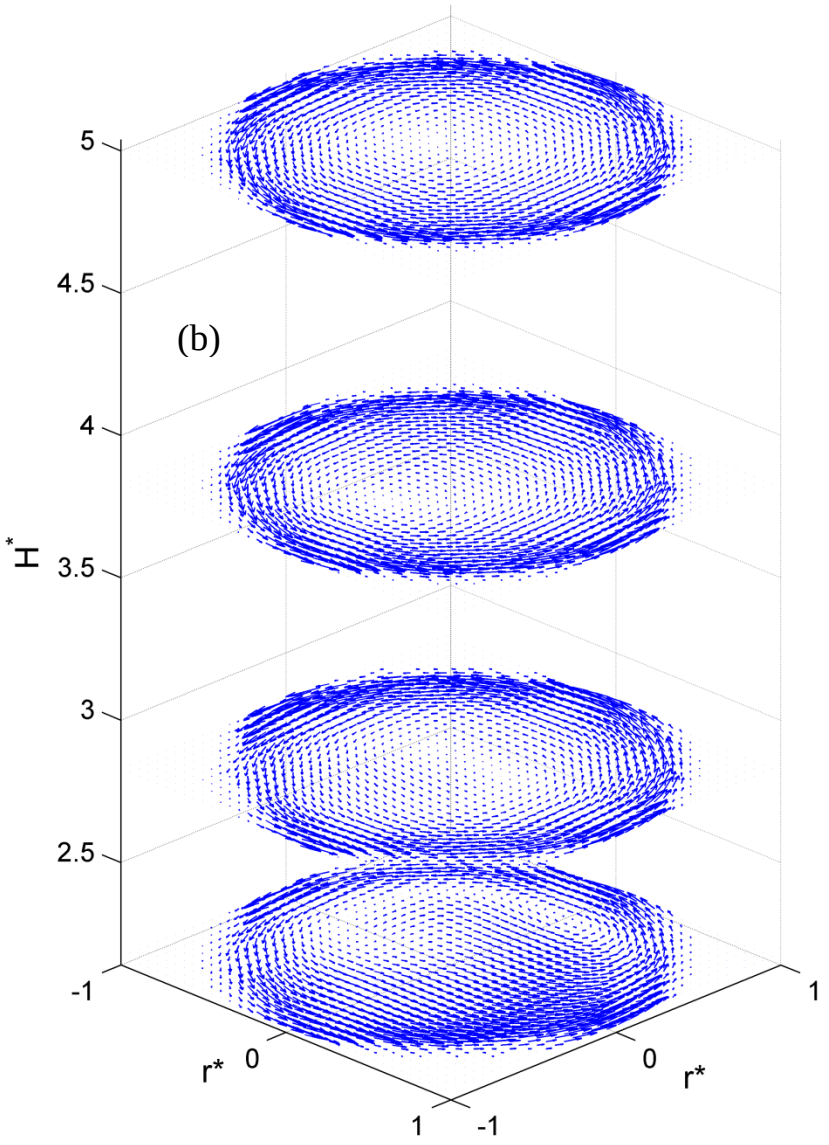

Figure 7.38 Velocity vector field for one Heated Counter-Rotating flow case: $\Delta T = 50^{o}C$ $\Omega_w^* = 1.5$ and the disk spin rate $\Omega_d^* = -2$ for (a): three lower studied heights and (b) four higher one

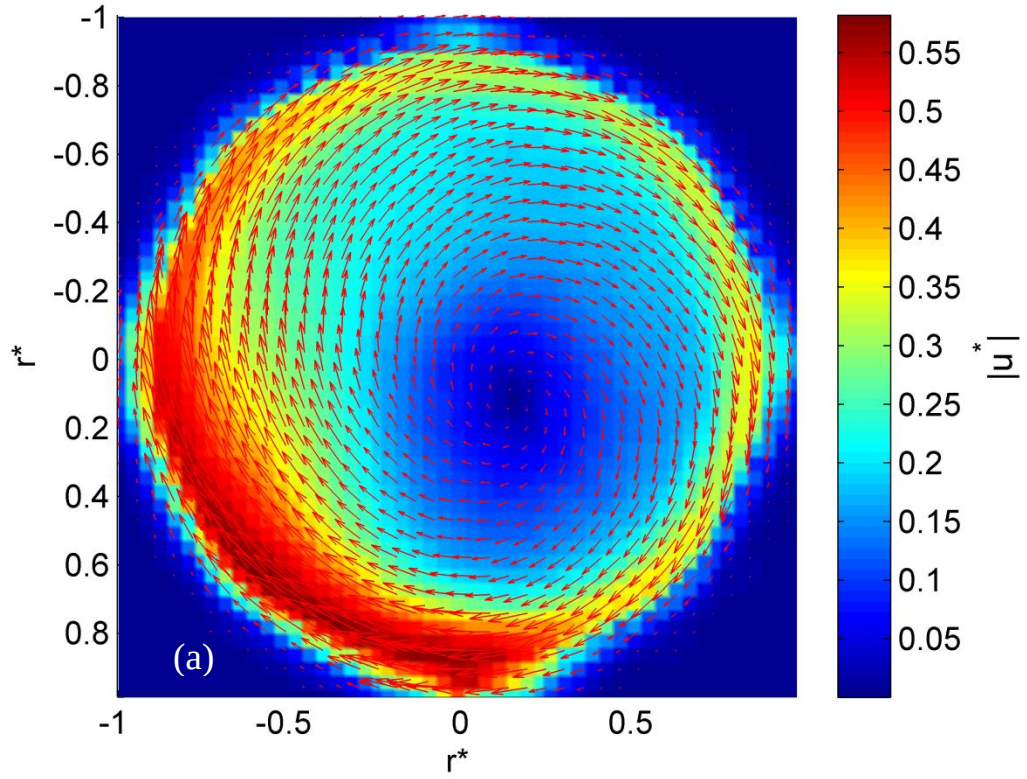
-1
-0.8
-0.6
-0.4
-0.2
0
0.2
0.4
0.6
0.8
r*
-1
-0.5
0
0.5
r*
(a)
0.55
0.5
0.45
0.4
0.35
0.3
0.25
0.2
0.15
0.1
0.05
|u*|

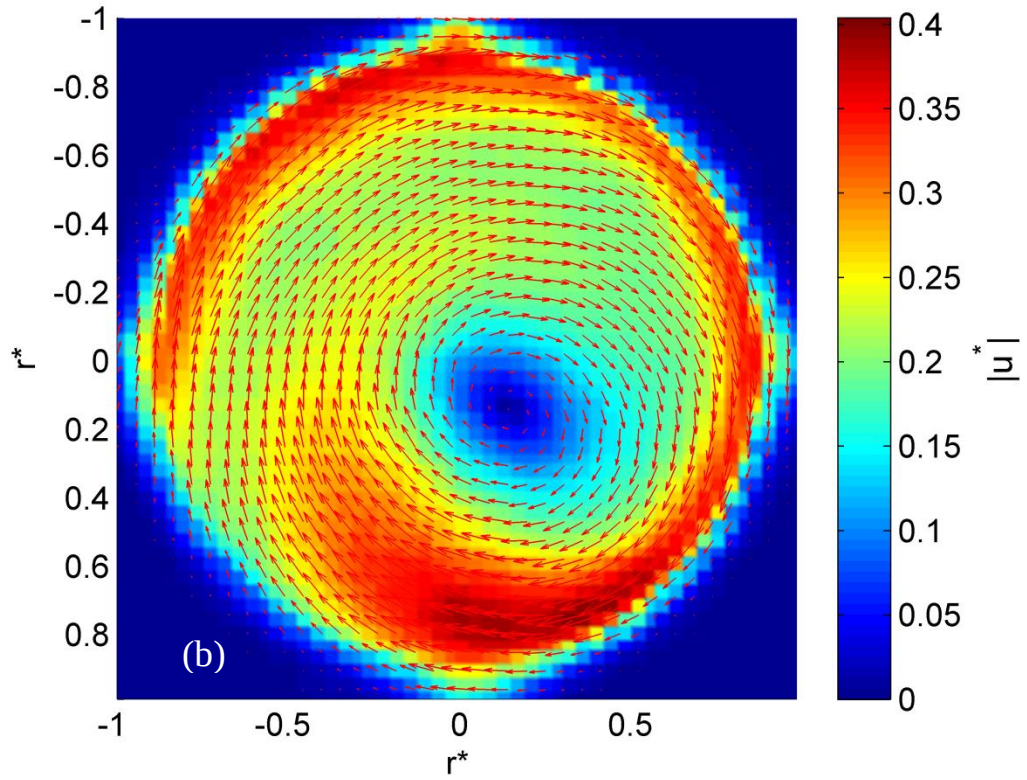
-1
-0.8
-0.6
-0.4
-0.2
0
0.2
0.4
0.6
0.8
r*
-1
-0.5
0
0.5
r*
(b)
0.4
0.35
0.3
0.25
0.2
0.15
0.1
0.05
0
|u*|

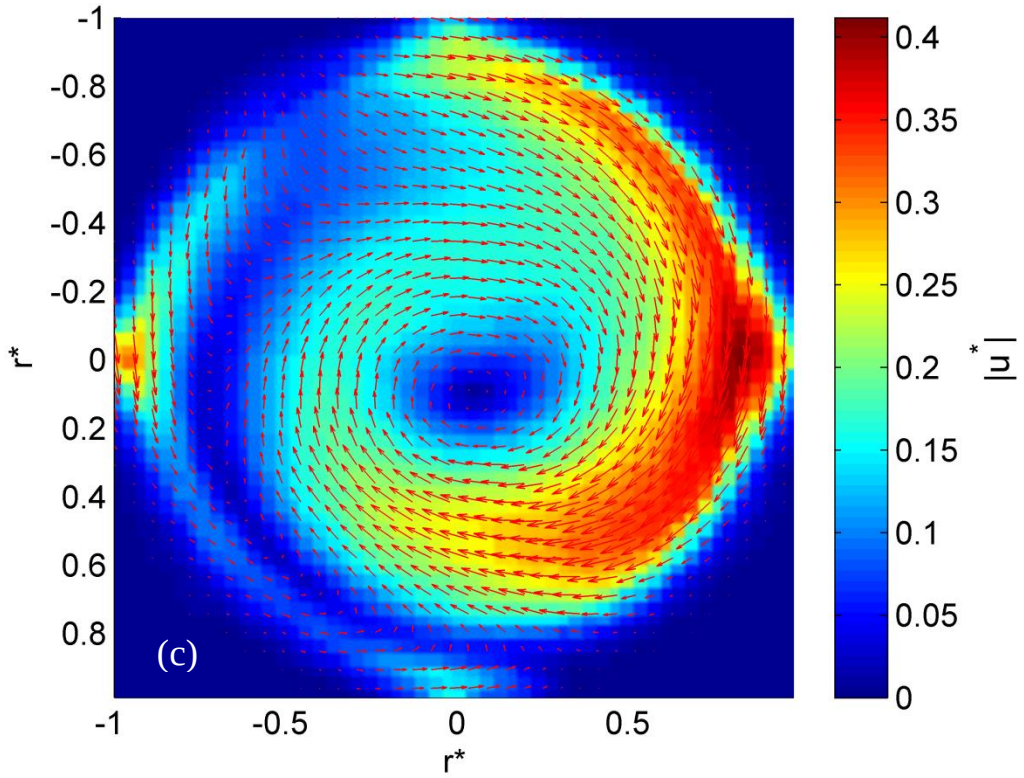
-1
-0.8
-0.6
-0.4
-0.2
0
0.2
0.4
0.6
0.8
r*
(c)
-1
-0.5
0
0.5
r*
0.4
0.35
0.3
0.25
0.2
0.15
0.1
0.05
0
|u*|

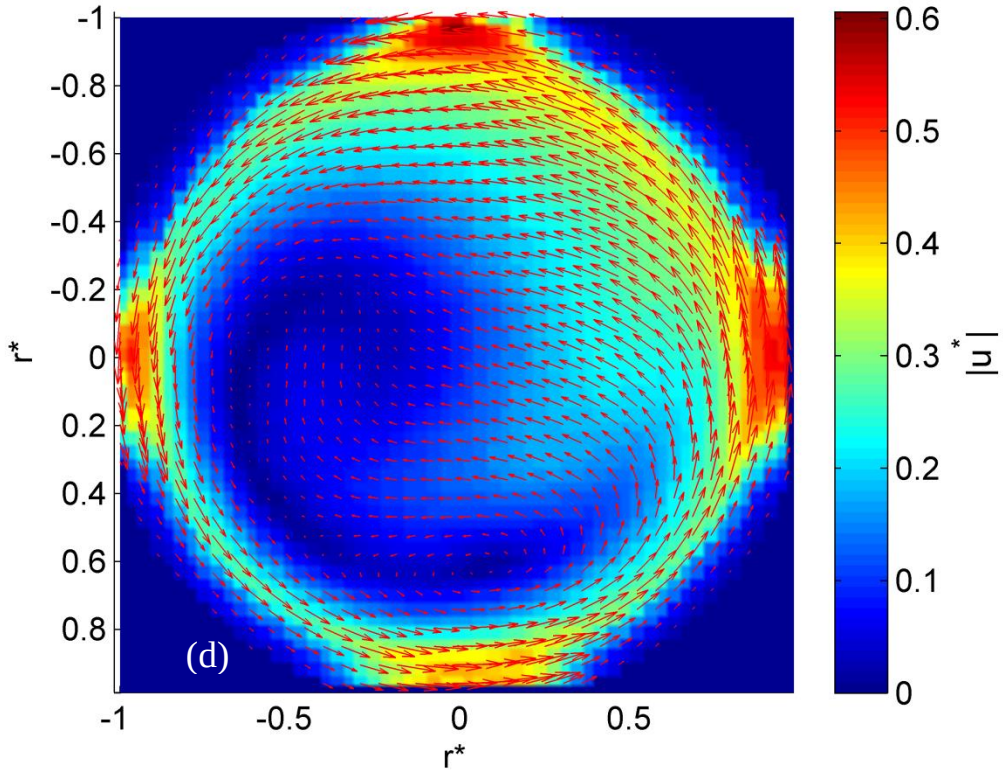
-1
-0.8
-0.6
-0.4
-0.2
0
0.2
0.4
0.6
0.8
r*
(d)
-1
-0.5
0
0.5
r*
0.6
0.5
0.4
0.3
0.2
0.1
0
|u*|

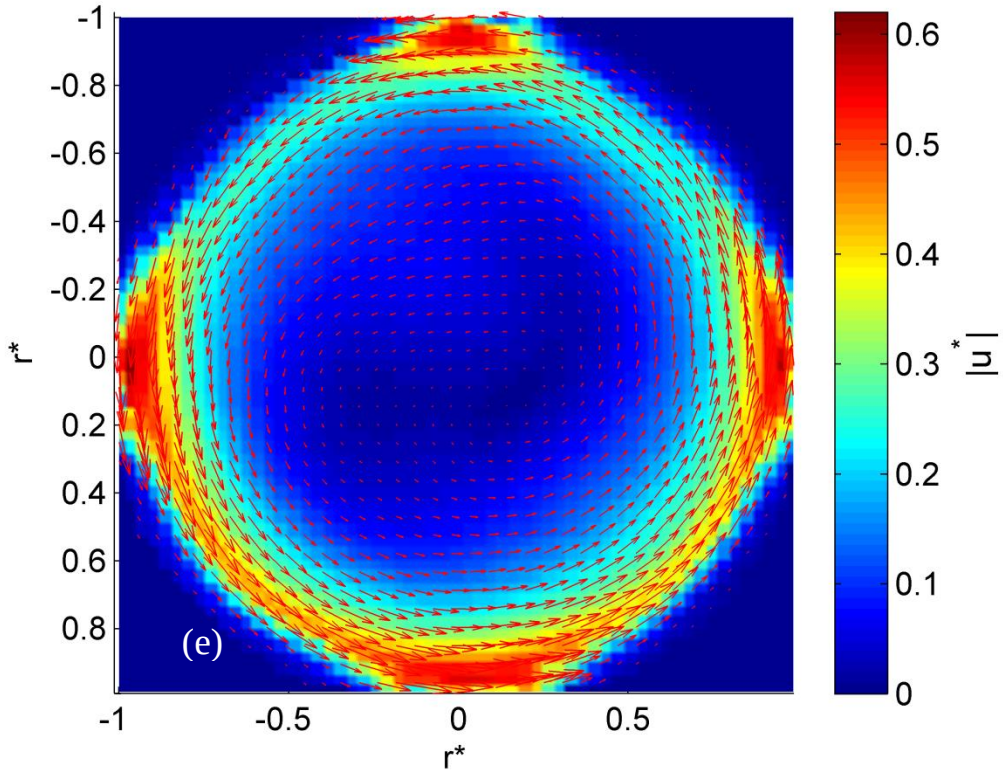

Figure 7.39 The velocity vector and magnitude field for the Heated Counter-Rotating flow when: $\Delta T = 50^{o}C$, $\Omega_w^* = 1.5$, $\Omega_d^* = -2$ for heights (a): $z^* = 0.67$, (b): $z^* = 1$, (c): $z^* = 1.5$, (d): $z^* = 2.17$ and (e): $z^* = 2.83$

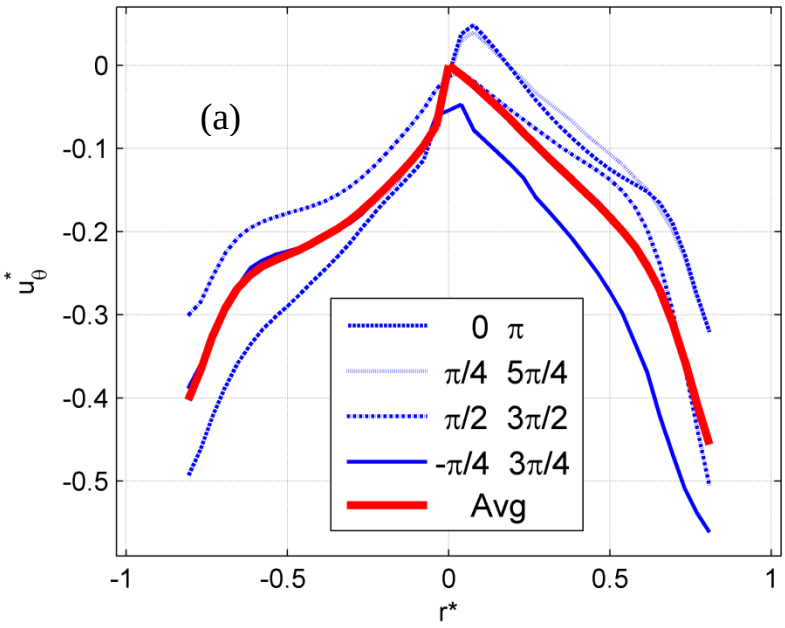

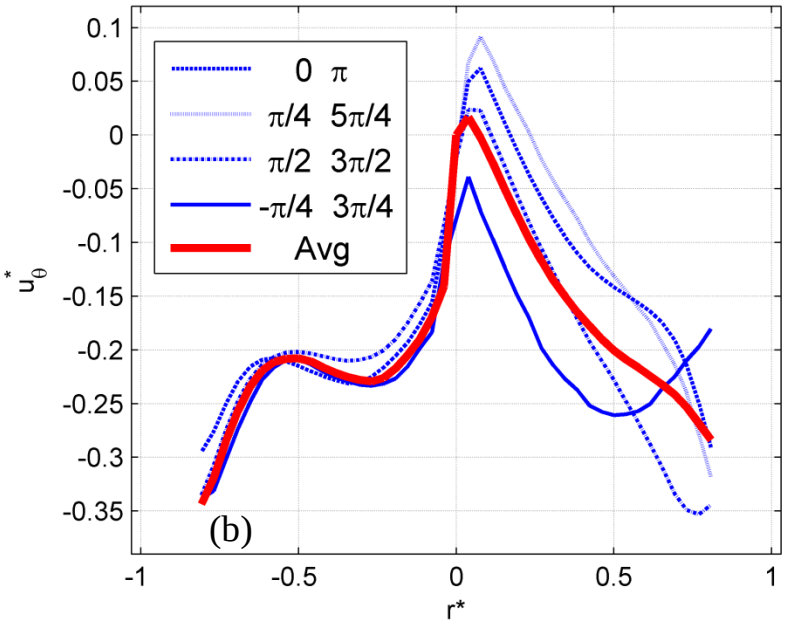
0.1
0.05
0
-0.05
-0.1
-0.15
-0.2
-0.25
-0.3
-0.35
u_θ^*
0 π
π/4 5π/4
π/2 3π/2
-π/4 3π/4
Avg
(b)
-1
-0.5
0
0.5
1
r*

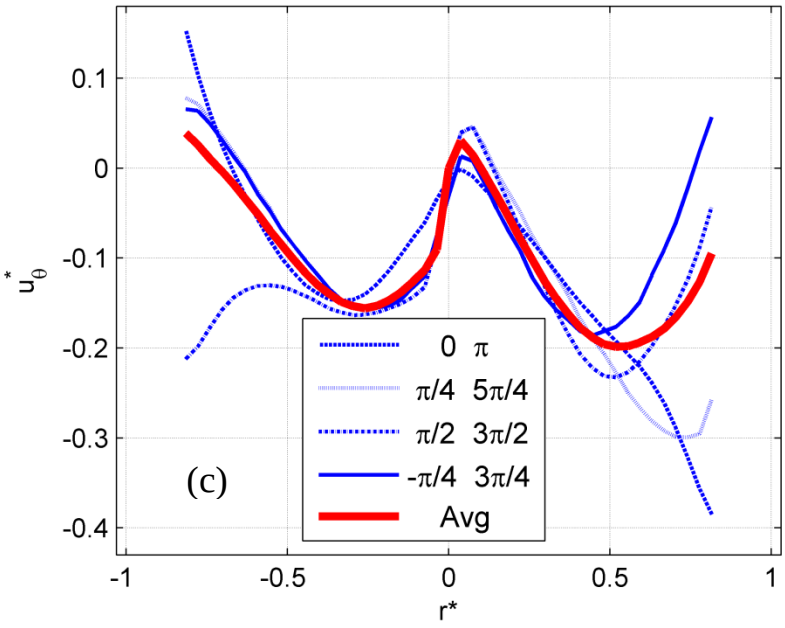
0.1
0
-0.1
-0.2
-0.3
-0.4
u_θ^*
0 π
π/4 5π/4
π/2 3π/2
-π/4 3π/4
Avg
(c)
-1
-0.5
0
0.5
1
r*

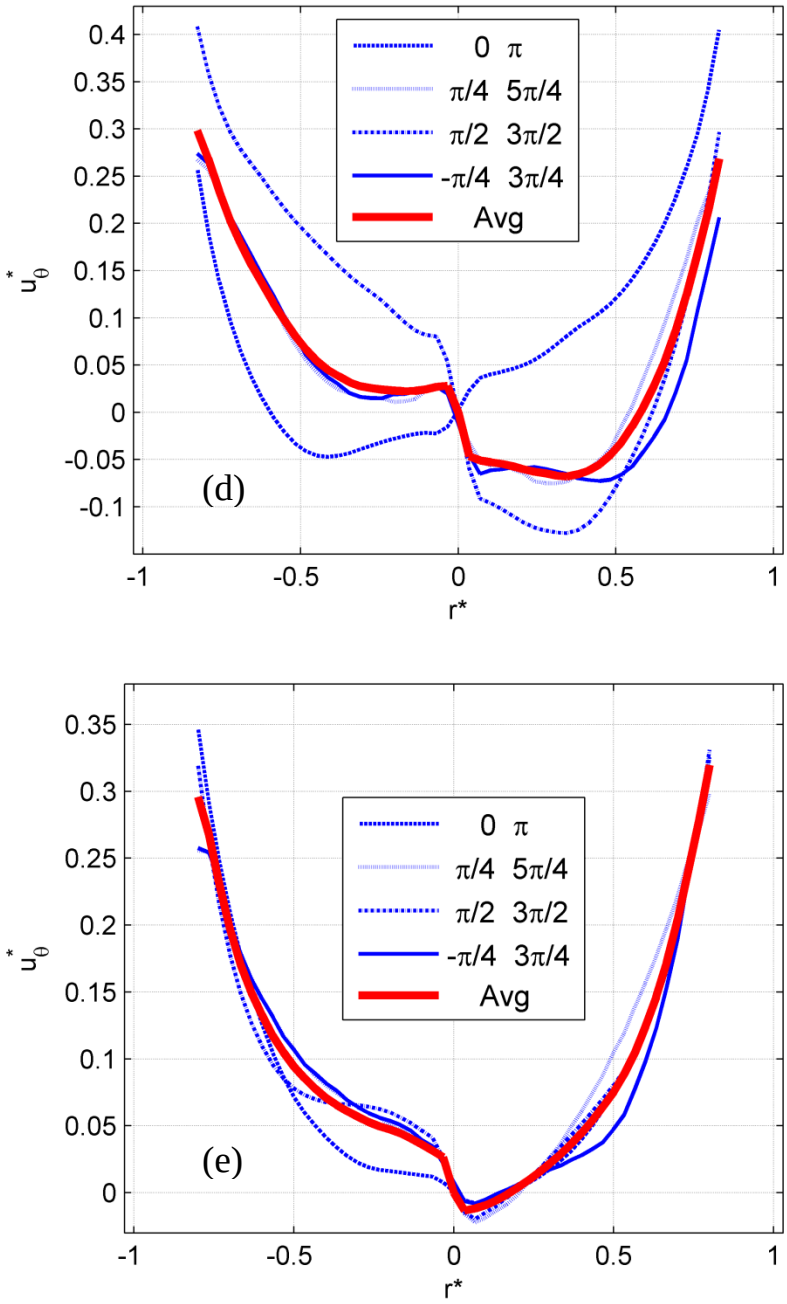

Figure 7.40 Normalized azimuthal velocity profile averaged over the half-circle-sectors and selected profiles across four radial sections for the Heated Counter-Rotating flow when: $\Delta T = 50^{o}C$, $\Omega_w^* = 1.5$, $\Omega_d^* = -2$ when (a): $z^* = 0.67$, (b): $z^* = 1$, (c) $z^* = 1.5$, (d): $H^* = 2.17$ and (e): $z^* = 2.83$

8 Results and Discussion: Co-rotating flow

In this chapter one of the Baseline-Flow I cases are combined with all Baseline-Flow II cases that was presented in previous chapter. Nonetheless, in this flow, which is named Co-Rotating flow, the disk and the wall are rotating in the same direction. The wall spin rate remains constant at $\Omega_w^* = 1.5$ (150 RPM in counter-clock-wise) and experiments are performed at these disk spin rates: $\Omega_d^* = 1$, $\Omega_d^* = 1.2$, $\Omega_d^* = 1.4$, $\Omega_d^* = 1.6$, $\Omega_d^* = 1.8$ and $\Omega_d^* = 2$. Similar to Baseline-Flow II cases in previous chapter, three azimuthal velocity profiles, in which the disk is spinning at rates of $\Omega_d^* = 1.2$, $\Omega_d^* = 1.6$ and $\Omega_d^* = 2$, are extracted and shown in Figures 8-1-a, b and c. These figures show that when Ω_d^* increases from 1.2 to 2 all curves slightly shift upward and only less than 10% increase in u_θ^* is observed. Another interesting fact that the curves at different heights in Figures 8-1-a, b and c are different from those in figure 5-3-a b and c, in which only the wall spins. It can be seen that curves in $r^* > 0.5$ are completely behaving more or less linearly, whereas the behavior of curves in $r^* < 0.5$ is not close to linear. During all of the experiments of Co-Rotating flow, it was observed that injecting particles through the region of $r^* < 0.5$ was difficult and concentration of particles inside was significantly less than outside of this region. This is exactly where two regions of linear and non-linear behavior of velocity profile in all disk speeds can be distinguished.

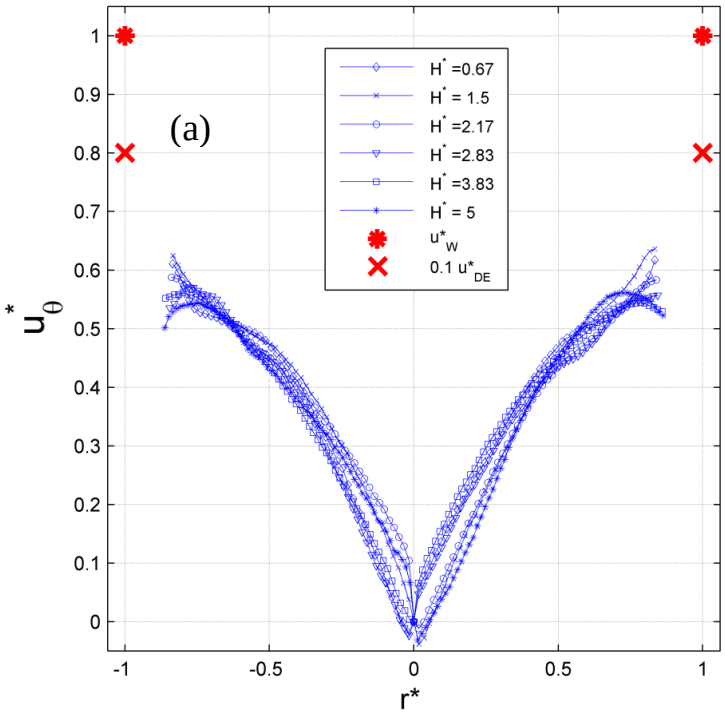
(a)
H* =0.67
H* = 1.5
H* =2.17
H* =2.83
H* =3.83
H* = 5
u*W
0.1 u*DE
u*θ
r*
1
0.9
0.8
0.7
0.6
0.5
0.4
0.3
0.2
0.1
0
-1
-0.5
0
0.5
1

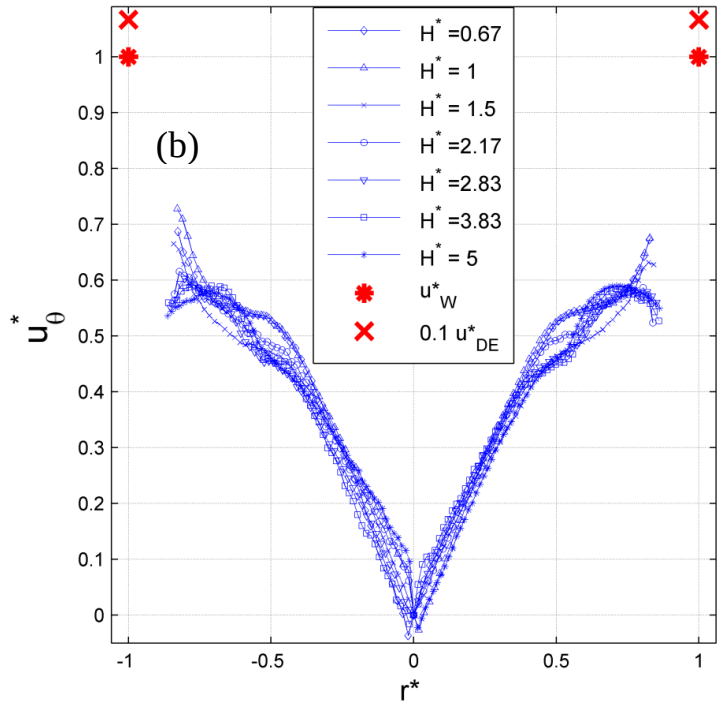
(b)
H* =0.67
H* = 1
H* = 1.5
H* =2.17
H* =2.83
H* =3.83
H* = 5
u*W
0.1 u*DE
u*θ
r*
1
0.9
0.8
0.7
0.6
0.5
0.4
0.3
0.2
0.1
0
-1
-0.5
0
0.5
1

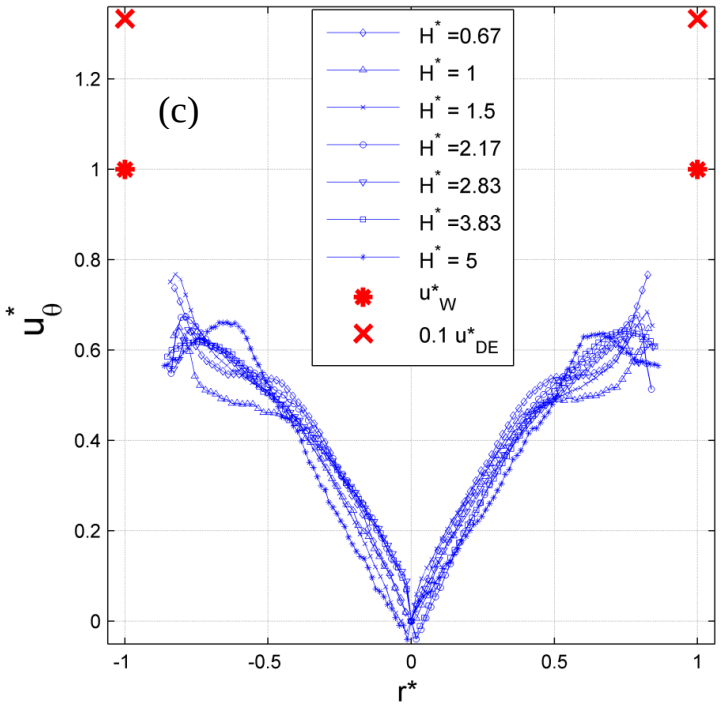

Figure 8.1 Normalized azimuthal velocity profiles averaged over the half-circle-sectors at all the heights for one Co-Rotating Flow case when the wall spinning rate is $\Omega_w^* = 1.5$ and the disk is spinning at rate of (a) $\Omega_d^* = 1$, (b) $\Omega_d^* = 1.6$ and (c) $\Omega_d^* = 2$

Therefore, another method of seeding and imaging is used and both shots in Figure 8.2 were captured by injecting dense smoke from the gap between the bottom disk and the wall. The polygon shapes in the center are due to lack of smoke in this area. Obviously, the light intensity gradient at the edge of these polygons in Figure 8.2 and changing the slope of curves inside and outside of the same region are related. In other words, at $r^* \approx 0.5$ the velocity gradient towards the center increases, and since the particles/smoke are injected at $r^* > 0.5$ this low velocity gradient allows less amount of particle/smokes to enter in the inner region. Number of sides for these polygons varies as the ratio of disk spin rate and the height changes. Therefore, triangles, squares, pentagons and octagons are observed in different conditions. Figure 8.2-a and b, as two examples, respectively demonstrate a triangle and a pentagon for these two conditions:

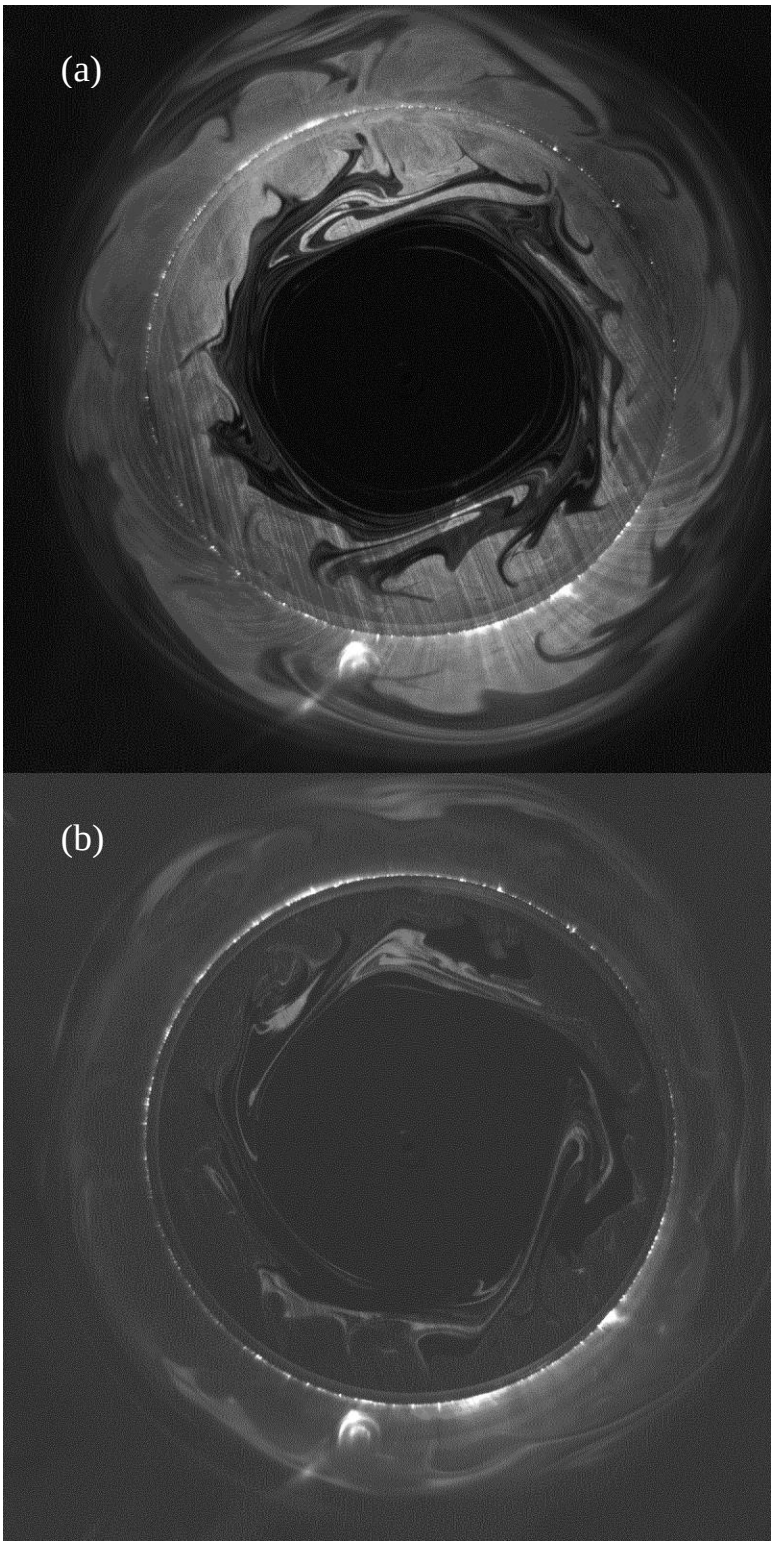

Figure 8.2 Two images from Co-Rotating flow with (a) $\Omega_w^* = 1.5$ and (b) $\Omega_d^* = 1$. The darker polygons in the center surrounded by dense smoke in the outer radii

Similar to the figures of k^*-profiles, in Baseline-Flows and Counter-Rotating flow, Figure 8-3 shows this quantity for one case of Co-Rotating flow where $\Omega_w^* = 1.5$ and $\Omega_d^* = 1.6$. Figures of other disk spin rates are similar and were not brought here. Compared to figures 5.4 and 5.6, curves in this figure seem more random. However, they show two different behaviors under $H^* = 2.17$ and above it. k^* in all curves at $z^* < 2.17$ is much lower in the inner region compared to outer region ($r^* > 0.6$). The slope of this change around $r^* \approx 0.55$ is higher than anywhere else. This is where those polygons are observed. Within this region k^* does not seem to change significantly with respect to r^*. On the other hand, at $z^* = 2.17$ and above curves have a peak at $0.45 < r^* < 0.6$ which separates the inner and outer region clearly. Moreover, in all disk spin rates, as well as the $\Omega_d^* = 1.6$ that is shown in figure 14, the curve associated with the $z^* = 15$ is significantly lower than other ones and the average of k^* is less than other layers. This means that flow becomes remarkably smoother in higher heights. k^* in all three cases of Only-disk, Only-wall and Co-Rotation has the same range. In the next sections it is shown that, compared to Baseline-Flow cases, the range of k^* range is slightly higher in the unheated Counter-Rotating flow cases and much higher (by one order of magnitude) in the heated Counter-Rotating cases.

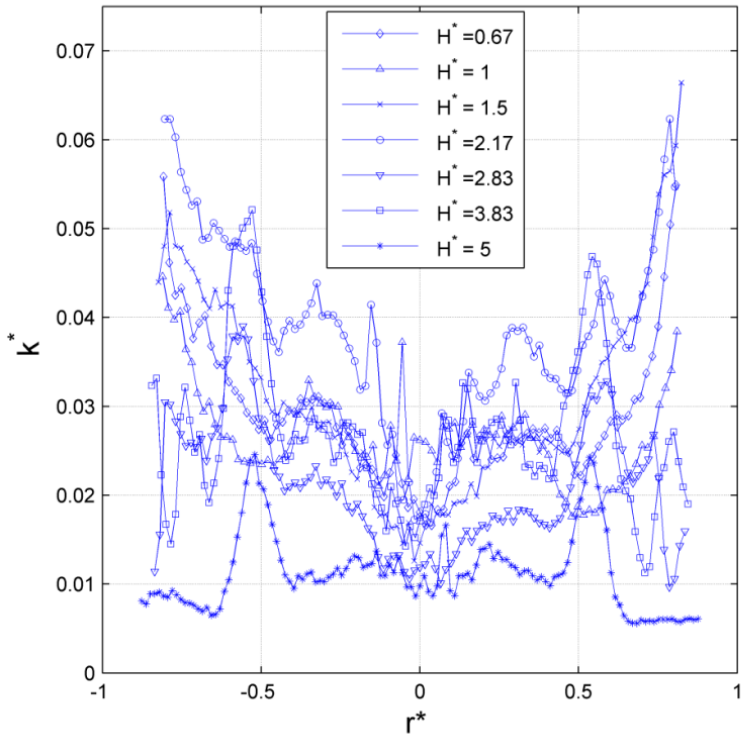

Figure 8.3 The average of k^* along 90 radial sections in all measured heights for one Co-Rotating case when the wall spinning rate is $\Omega_w^* = 1.5$ and the disk is spinning at rate of $\Omega_D^* = 1.6$

In Figure 8-4 the velocity vector fields for all layers, of one disk spin rate, are presented in a similar fashion to figure 5-7 where $\Omega_w^* = 1.5$ and $\Omega_d^* = 1.4$ both rotating counter-clock-wise. Similarly, all other studied 5 disk spin rates could be shown here but since the results are very close to this figure, they are not presented. In all heights, the center of the vortex is approximately located at the centerline of the cylinder, flow structure is smooth and concentric and vector fields in different heights are similar.

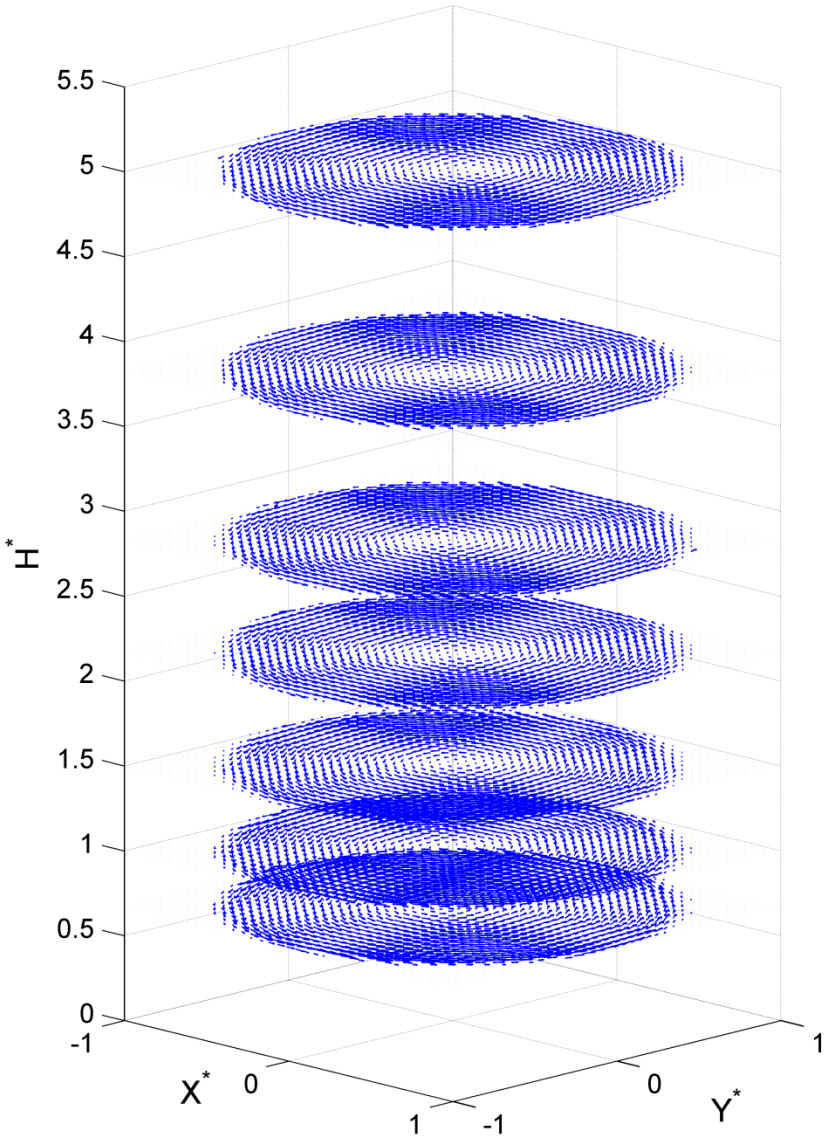

Figure 9.4 Velocity vector field for all studied heights for one Co-Rotating flow case: With the wall spin rate $\Omega_w^* = 1.5$ and the disk spin rate $\Omega_d^* = 1.4$

Since conditions of all studied cases are chosen to be 3 wall spin rates, 6 disk spin rates and 7 different heights, 126 velocity vector/magnitude fields could be presented here. Most of these figures would be very similar and one as an example is presented in Figure 8.4. Again, in this particular case, $\Omega_w^* = 1.5$ and $\Omega_d^* = 1.4$, both rotating counter-clock-wise, and the graph is

extracted from $z^* = 2.17$. A very good agreement between this figure and the corresponding velocity profile curve in Figure 8.1-b can be observed and both indicate the same velocity in the majority of domain ($0 < r^* < 0.85$). As mentioned before, close to the wall results are not reliable and velocity is significantly less than what is expected. Therefore, maximum velocity is approximately located at $r^* = 0.85$ instead of being attached to the side wall (Because it is known that $\lim_{r^* \to 1^+} |u^*| = 1$)

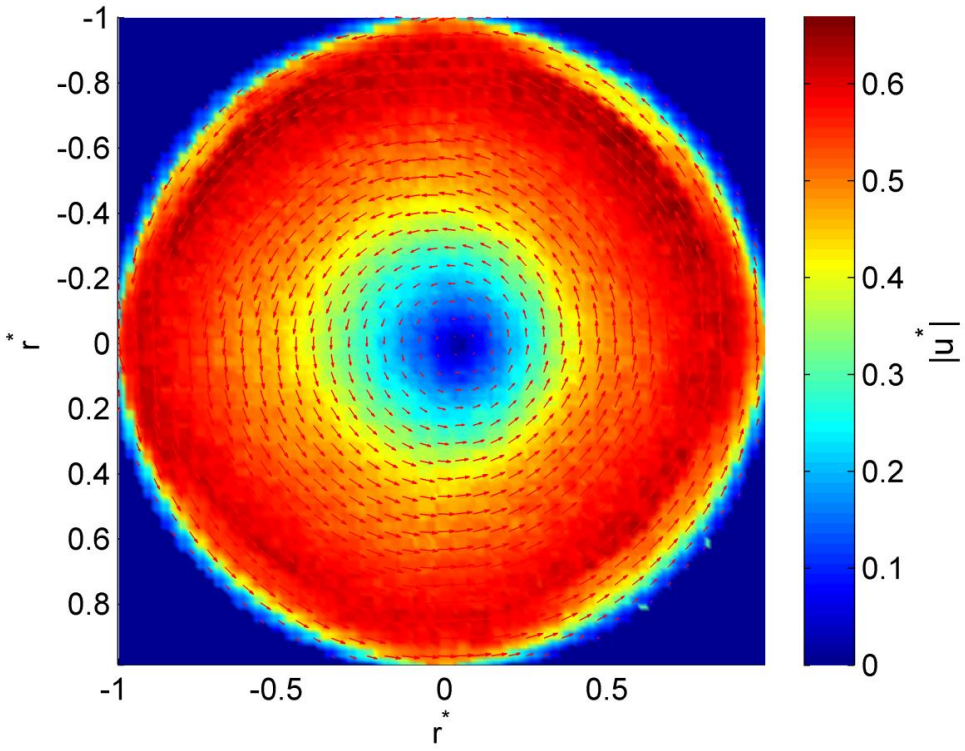

Figure 8.5 The velocity vector and magnitude field for the Co-Rotating Flow when: $\Omega_w^* = 1.5$, $\Omega_d^* = 1.4$ and $z^* = 2.17$

9 Conclusion

In this work, a counter-rotating cylinder-disk system is used to mimic the flow structure of the GRS. The high-speed collar of the GRS is simulated by the high-speed ring flow generated by the inner wall of a rotating circular cylinder. The relatively low-speed inner region and the counter-rotating motion near the center of the GRS are simulated by the flow generated by the interaction between the counter-rotating disk located below and the rotating cylinder. The thermal buoyancy effect is generated by disk heating. The Coriolis force cannot be simulated in this experimental study. The velocity profiles in the cross-sections in the upper domain, as shown in Figure 6.2, are similar to those of the GRS [61, 63, 64, 67]. In particular, the zero-crossing point in the velocity profiles at the center mimics the intriguing counter-rotating motion observed in the GRS. It is speculated that the upward flow induced by the buoyancy effect may play an important role in the formation and maintenance of the GRS [99].

PIV measurements in the vertical plane indeed show the significant upward flow in the vertical direction in the inner region of the flow in the upper domain. The 3D flow structures in the upper domain are represented by an array of the packed torus vortices that induce the upward flow at the center of the tori. The thermal buoyancy effect characterized by the Grashof number intensifies the rotations of the torus vortices and induces the stronger upward flow. From a phenomenological standpoint, these features observed in the present experiments would shed insights into the GRS. The flow structure of the GRS could be considerably 3D such that a torus vortex (or an array of torus vortices) could be a candidate although most studies on the GRS have been based on quasi-2D shallow-water models [99-100]. The upward flow induced by the thermal buoyancy effect in the vertical direction could be significant to maintain and intensify the strength of the GRS.

The flow within a rotating cylinder with a counter-rotating disk located below has been studied based on PIV measurements. In the baseline flow driven by the clockwise rotating cylinder only, the profiles of the normalized azimuthal velocity at all the heights and cylinder spinning rates approximately collapse into a single linear distribution, indicating the axisymmetric and vertically-homogenous nature of the flow. In the baseline flow driven by the clockwise disk only, the normalized azimuthal velocity is high near the disk edge and low in the inner region particularly in the lower heights, and the velocity profile becomes fuller as the vertical location increases due to the viscous diffusion of the momentum.

The flow within the counter-clockwise rotating cylinder with an unheated clockwise rotating disk located below can be generally segmented into the upper, transitional and lower domains. In the upper domain, the overall counter-clockwise velocity vectors indicate that the flows are mainly driven by the counter-clockwise rotating cylinder wall. However, due to the appreciable effect of the counter-rotating disk below, the azimuthal velocity profiles exhibit the extended low-speed inner region where a zero-crossing point may appear near the center indicating the counter-rotating motion there. This resembles the so-called "hollow vortex" structure of the GRS. In contrast, in the lower domain, the velocity vectors are in the clockwise direction, indicating the dominant influence by the clockwise-rotating disk. The intriguing flow phenomenon occurs in the transitional domain between the lower and upper domains, where distinct zero-crossing points appear in the azimuthal velocity profiles, signifying a mixture of the clockwise and counter-clockwise flow motions. The turbulent kinetic energy reaches the maximum there. The circulation in a cross-section increases with the vertical location from the negative value in the lower domain to the positive value in the upper domain. The zero-crossing

point in the circulation occurs in the transitional domain. The location of the transitional domain increases with the disk spinning rate.

For the flow with the heated disk, the thermal buoyancy effect characterized by the Grashof number (Gr) on the flow structures is significant. The buoyancy effect considerably enhances the turbulent kinetic energy, which is particularly evidenced by the elevated peak turbulent kinetic energy in the transitional domain as Gr increases. The increased azimuthal velocity is induced by the buoyancy effect particularly in the inner region, and consequently the circulation in the flow increases with Gr. These phenomena are explained based on the intensified vorticity stretching and the enhanced turbulent mixing induced by thermal buoyancy effect.

The velocity measurements in the cross-sections and the vertical plane reveal the 3D flow structures of the torus vortices. In the lower region, the flow on the torus vortex rotates clockwise around both the z-axis and the axis of the torus, which induces the downward flow at the center of the torus. In contrast, the flow in the upper domain is associated with an array of the packed torus vortices that rotate counter-clockwise around both the z-axis and the axis of the torus, inducing the upward flow at the center of the tori. The transitional domain is located between the lower and upper domains. The rotations of the torus vortices are intensified as Gr increases.

Some of the primary results of this work were presented in the 68th Annual Meeting of the APS Division of Fluid Dynamics [101]. At the time that this draft being written, another manuscript, which covers the most important part of Counter-Rotating flow, is submitted to the journal of Experiments in Fluids for review. Authors plan to complete and publish the results for Co-Rotating flow soon.

References

[1] Kármán, Th V. "Über laminare und turbulente Reibung." ZAMM-Journal of Applied Mathematics and Mechanics/Zeitschrift für Angewandte Mathematik und Mechanik 1.4 (1921): 233-252.

[2] Cochran, W. G. "The flow due to a rotating disc." Mathematical Proceedings of the Cambridge Philosophical Society. Vol. 30. No. 03. Cambridge University Press, 1934.

[3] Zandbergen, P. J., and D. Dijkstra. "Non-unique solutions of the Navier-Stokes equations for the Karman swirling flow." Journal of Engineering Mathematics11.2 (1977): 167-188.

[4] Lentini, Marianela, and Herbert B. Keller. "The von Karman swirling flows."SIAM Journal on Applied Mathematics 38.1 (1980): 52-64.

[5] McLeod, J. B. "The asymptotic form of solutions of von Karman's swirling flow problem." The Quarterly Journal of Mathematics 20.1 (1969): 483-496.

[6] Hannah, D. M. Forced flow against a rotating disc. HM Stationery Office, 1952.

[7] Stuart, J. T. "On the effects of uniform suction on the steady flow due to a rotating disk." The Quarterly Journal of Mechanics and Applied Mathematics 7.4 (1954): 446-457.

[8] Millsaps, Knox. "Heat transfer by laminar flow from a rotating plate." Journal of the Aeronautical Sciences (Institute of the Aeronautical Sciences) 18.5 (2012).

[9] Wagner, Carl. "Heat transfer from a rotating disk to ambient air." Journal of Applied Physics 19.9 (1948): 837-839.

[10] Cobb, E. C., and O. A. Saunders. "Heat transfer from a rotating disk."Proceedings of the Royal Society of London. Series A, Mathematical and Physical Sciences (1956): 343-351.

[11] Riley, N. "The heat transfer from a rotating disk." The Quarterly Journal of Mechanics and Applied Mathematics 17.3 (1964): 331-349.

[12] Dorfman, L. A., and A. Z. Serazetdinov. "Laminar flow and heat transfer near rotating axisymmetric surface." International Journal of Heat and Mass Transfer8.2 (1965): 317-327.

[13] Owen, J. M., C. M. Haynes, and F. J. Bayley. "Heat transfer from an air-cooled rotating disk." Proceedings of the Royal Society of London. A. Mathematical and Physical Sciences 336.1607 (1974): 453-473.

[14] Lentini, Marianela, and Herbert B. Keller. "The von Karman swirling flows."SIAM Journal on Applied Mathematics 38.1 (1980): 52-64.

[15] Kohama Y (1984) Study on boundary layer transition of a rotating disk. Acta Mech 50: 193-199

[16] Wilkinson S P, Malik M R (1985) Stability experiments in the flow over a rotating disk. AIAA journal, 23:588-595.

[17] Lingwood R J (1996) An experimental study of absolute instability of the rotating-disk boundary-layer flow. J Fluid Mech 314: 373-405.

[18] Gauthier G, Gondret P, Moisy F, Rabaud M (2002) Instabilities in the flow between co-and counter-rotating disks. J Fluid Mech 473:1-21.

[19] Corke T C, Matlis E H, Othman H (2007) Transition to turbulence in rotating-disk boundary layers—convective and absolute instabilities. J Eng Math 57: 253-272

[20] Schlichting H (1979) Boundary Layer Theory, McGraw-Hill, New York, pp 165-194

[21] Wedemeyer E H (1964) The unsteady flow within a spinning cylinder. J Fluid Mech 20:383-399

[22] Taylor, G. I. (1923). Stability of a viscous liquid contained between two rotating cylinders. Philos T R Soc Lond 223: 289-343

[23] Gollub J P, Swinney H L (1975) Onset of turbulence in a rotating fluid. Phys Rev Lett 35: 927-930

[24] Chossat P, Iooss G (2012) The Couette-Taylor Problem. Springer Science & Business Media.

[25] Drazin P G, Reid W H (2004) Hydrodynamic stability. Cambridge university press

[26] G.E.Hunt, P. Moore: Jupiter (Rand McNally, Chicago 1981)

[27] Smith, Bradford A., et al. "The Jupiter system through the eyes of Voyager 1."Science 204.4396 (1979): 951-972.

[28] Williams, Gareth P. "Planetary circulations: 1. Barotropic representation of Jovian and terrestrial turbulence." Journal of the Atmospheric Sciences 35.8 (1978): 1399-1426.

[29] Williams, Gareth P. "Jovian and comparative atmospheric modeling."Advances in geophysics 28 (1985): 381-429.

[30] Allison, Michael. "A similarity model for the windy jovian thermocline."Planetary and Space Science 48.7 (2000): 753-774.

[31] Nezlin, M. V., E. N. Snezhkin, and A. S. Trubnikov. "Kelvin-Helmholtz instability and the Jovian Great Red Spot." JETP Lett 36.6 (1982).

[32] Nezlin, M. V., E. N. Snezhkin, and A. S. Trubnikov. "The Common Mechanism of Driving Vortical Structures in Plasma, Planetary Atmospheres and in Galaxies." (1987): 1184-1208.

[33] Nezlin, M. V. "Rossby solitons (Experimental investigations and laboratory model of natural vortices of the Jovian Great Red Spot type)." Physics-Uspekhi29.9 (1986): 807-842.

[34] Rossby, Carl-Gustav. "Relation between variations in the intensity of the zonal circulation of the atmosphere and the displacements of the semi-permanent centers of action." Journal of Marine Research 2.1 (1939): 38-55.

[35] Rossby, Carl-Gustav. "Planetary flow patterns in the atmosphere." Quart. J. Roy. Meteor. Soc 66 (1940): 68-87.

[36] Rossby, C. G. "On displacements and intensity changes of atmospheric vortices." J. mar. Res 7.175 (1948): 71.

[37] Haurwitz, B. "The motion of atmospheric disturbances on the spherical earth."J. mar. Res 3.5 (1940): 254-267.

[38] Lorenz, Edward N. The nature and theory of the general circulation of the atmosphere. Vol. 218. Geneva: World Meteorological Organization, 1967.

[39] Garcıa-Melendo, E., and A. Sánchez-Lavega. "A study of the stability of jovian zonal winds from HST images: 1995–2000." Icarus 152.2 (2001): 316-330.

[40] Antipov, S. V., et al. "Rossby autosoliton and laboratory model of Jupiter's Great Red Spot." Zh. Eksp. Teor. Fiz 89 (1985): 1905-1920.

[41] Nezlin, Mikhail V., and Evgenii N. Snezhkin. "Laboratory Simulation of Galactic Spiral Structures." Rossby Vortices, Spiral Structures, Solitons. Springer Berlin Heidelberg, 1993. 107-127.

[42] Busse, Friedrich H. "Thermal instabilities in rapidly rotating systems." J. Fluid Mech 44.3 (1970): 441-460.

[43] Busse, F. H. "A simple model of convection in the Jovian atmosphere." Icarus29.2 (1976): 255-260.

[44] Proudman, J. "On the motion of solids in a liquid possessing vorticity."Proceedings of the Royal Society of London. Series A 92.642 (1916): 408-424.

[45] Yano, Jun-Ichi, Olivier Talagrand, and Pierre Drossart. "Outer planets: Origins of atmospheric zonal winds." Nature 421.6918 (2003): 36-36.

[46] Busse, F. H. "Convection-driven zonal flows in the major planets." pure and applied geophysics 121.3 (1983): 375-390.

[47] Busse, F. H. "Convection driven zonal flows and vortices in the major planets."Chaos: An Interdisciplinary Journal of Nonlinear Science 4.2 (1994): 123-134.

[48] Christensen, Ulrich R. "Zonal flow driven by deep convection in the major planets." Geophysical research letters 28.13 (2001): 2553-2556.

[49] Aurnou, Jonathan M., and Peter L. Olson. "Strong zonal winds from thermal convection in a rotating spherical shell." Geophysical research letters 28.13 (2001): 2557-2559.

[50] Christensen, U. R. "Zonal flow driven by strongly supercritical convection in rotating spherical shells." Journal of Fluid Mechanics 470 (2002): 115-133.

[51] Sánchez-Lavega, A. G. U. S. T. Í. N., et al. "Observations and models of the general circulation of Jupiter and Saturn." Lecture Notes and Essays in Astrophysics I (2004): 63-85.

[52] Ingersoll, Andrew P., et al. "Dynamics of Jupiter's atmosphere." Jupiter: The Planet, Satellites and Magnetosphere 105 (2004).

[53] Ingersoll, Andrew P. "Atmospheric dynamics of the outer planets." Science 248.4953 (1990): 308-315.

[54] Mitchell, Jim L., et al. "Flow fields within Jupiter's Great Red Spot and white oval BC." Journal of Geophysical Research: Space Physics 86.A10 (1981): 8751-8757.

[55] Dowling, Timothy E., and Andrew P. Ingersoll. "Potential vorticity and layer thickness variations in the flow around Jupiter's Great Red Spot and White Oval BC." Journal of the atmospheric sciences 45.8 (1988): 1380-1396.

[56] Bouchet, Freddy, and Joel Sommeria. "Emergence of intense jets and Jupiter's Great Red Spot as maximum-entropy structures." Journal of Fluid Mechanics 464 (2002): 165-207.

[57] Read, Peter L., Peter J. Gierasch, and Barney J. Conrath. "Mapping potential-vorticity dynamics on Jupiter. II: the Great Red Spot from Voyager 1 and 2 data." Quarterly Journal of the Royal Meteorological Society 132.618 (2006): 1605-1625.

[58] Read, Peter L., et al. "Mapping potential-vorticity dynamics on Jupiter. I: Zonal-mean circulation from Cassini and Voyager 1 data." Quarterly Journal of the Royal Meteorological Society 132.618 (2006): 1577-1603.

[59] Shetty, Sushil, Xylar S. Asay-Davis, and Philip S. Marcus. "On the interaction of Jupiter's Great Red Spot and zonal jet streams." arXiv preprint arXiv:0707.4193 (2007).

[60] Sada, Pedro V., Reta F. Beebe, and Barney J. Conrath. "Comparison of the structure and dynamics of Jupiter's Great Red Spot between the Voyager 1 and 2 encounters." Icarus 119.2 (1996): 311-335.

[61] Vasavada, Ashwin R., et al. "Galileo imaging of Jupiter's atmosphere: The Great Red Spot, equatorial region, and white ovals." Icarus 135.1 (1998): 265-275.

[62] Simon-Miller, Amy A., et al. "New observational results concerning Jupiter's Great Red Spot." Icarus 158.1 (2002): 249-266.

[63] Choi, David S., et al. "Velocity and vorticity measurements of Jupiter's Great Red Spot using automated cloud feature tracking." Icarus 188.1 (2007): 35-46.

[64] Asay-Davis, Xylar S., et al. "Jupiter's shrinking Great Red Spot and steady Oval BA: Velocity measurements with the 'Advection Corrected Correlation Image Velocimetry'automated cloud-tracking method." Icarus 203.1 (2009): 164-188.

[65] Liu, Tianshu, and Lixin Shen. "Fluid flow and optical flow." Journal of Fluid Mechanics 614 (2008): 253-291.

[66] Liu, Tianshu, et al. "Comparison between optical flow and cross-correlation methods for extraction of velocity fields from particle images." Experiments in Fluids 56.8 (2015): 1-23.

[67] Liu, Tianshu, Bo Wang, and David S. Choi. "Flow structures of Jupiter's Great Red Spot extracted by using optical flow method." Physics of Fluids (1994-present) 24.9 (2012): 096601.

[68] Rotunno, Richard. "Numerical simulation of a laboratory vortex." Journal of Atmospheric Sciences 34 (1977): 1942-1956.

[69] Rotunno, Richard. "A study in tornado-like vortex dynamics." Journal of Atmospheric Sciences 36 (1979): 140-155.

[70] Rasmussen, Erik N., et al. "Verification of the origins of rotation in tornadoes experiment: VORTEX." Bulletin of the American Meteorological Society 75.6 (1994): 995-1006.

[71] Nolan, David S., and Brian F. Farrell. "The structure and dynamics of tornado-like vortices." Journal of the Atmospheric Sciences 56.16 (1999): 2908-2936.

[72] Ward, Neil B. "The exploration of certain features of tornado dynamics using a laboratory model." Journal of the Atmospheric Sciences 29.6 (1972): 1194-1204.

[73] Church, C. R., et al. "Characteristics of tornado-like vortices as a function of swirl ratio: A laboratory investigation." Journal of the Atmospheric Sciences36.9 (1979): 1755-1776.

[74] Rotunno, Richard. "A study in tornado-like vortex dynamics." Journal of Atmospheric Sciences 36 (1979): 140-155.

[75] Fiedler, Brian H., and Richard Rotunno. "A theory for the maximum windspeeds in tornado-like vortices." Journal of the atmospheric sciences 43.21 (1986): 2328-2340.

[76] Haan Jr, Fred L., Partha P. Sarkar, and William A. Gallus. "Design, construction and performance of a large tornado simulator for wind engineering applications." Engineering structures 30.4 (2008): 1146-1159.

[77] Yang, Zifeng, Partha Sarkar, and Hui Hu. "An experimental study of a high-rise building model in tornado-like winds." Journal of Fluids and Structures 27.4 (2011): 471-486.

[78] Fujita, T. T. "Mystery of severe storms." The University (1992).

[79] Fiedler, Brian H. "The thermodynamic speed limit and its violation in axisymmetric numerical simulations of tornado-like vortices." Atmosphere-Ocean 32.2 (1994): 335-359.

[80] Rotunno, Richard. "The fluid dynamics of tornadoes." Annual Review of Fluid Mechanics 45.1 (2013): 59.

[81] Frank, William M. "The structure and energetics of the tropical cyclone I. Storm structure." Monthly Weather Review 105.9 (1977): 1119-1135.

[82] Willoughby, H. E. "The vertical structure of hurricane rainbands and their interaction with the mean vortex." Journal of Atmospheric Sciences 35 (1978): 849-858.

[83] Shapiro, Lloyd J. "The asymmetric boundary layer flow under a translating hurricane." Journal of the Atmospheric Sciences 40.8 (1983): 1984-1998.

[84] Bender, Morris A. "The effect of relative flow on the asymmetric structure in the interior of hurricanes." Journal of the atmospheric sciences 54.6 (1997): 703-724.

[85] Kwon, Young C., and William M. Frank. "Dynamic instabilities of simulated hurricane-like vortices and their impacts on the core structure of hurricanes. Part II: Moist experiments." Journal of the Atmospheric Sciences 65.1 (2008): 106-122.

[86] Montgomery, Michael T., Vladimir A. Vladimirov, and Petr V. Denissenko. "An experimental study on hurricane mesovortices." Journal of Fluid Mechanics 471 (2002): 1-32.

[87] Bird, R. Byron, Warren E. Stewart, and Edwin N. Lightfoot. "Transport Phenomena 2 nd edition,(2002).

[88] Bird, R. Byron, R. C. Armstrong, and Ole Hassager. "Dynamics of polymeric liquids. Vol. 1: Fluid mechanics." (1987).

[89] Gebhart, B. "Natural convection flows and stability." Advances in Heat Transfer9 (1973): 273-348.

[90] Hinze, J. O. (1975). Turbulence (2nd ed.). McGraw-Hill. ISBN 0-07-029037-7.

[91] Tennekes, H.; Lumley, J. L. (1972). A First Course in Turbulence. MIT Press. ISBN 0-262-20019-8.

[92] Pope, Stephen B. (2000). Turbulent Flows. Cambridge University Press. ISBN 0-521-59886-9.

[93] http://pivlab.blogspot.com/

[94] Adrian, Ronald J. "Twenty years of particle image velocimetry." Experiments in fluids 39.2 (2005): 159-169.

[95] http://www.engineeringtoolbox.com/air-properties-d_156.html

[96] Schlichting, H. "Boundary Layer Theory, McGraw-Hill, New York, 1979."

[97] Marcus, Philip S. "Jupiter's Great Red Spot and other vortices." Annual review of astronomy and astrophysics 31 (1993): 523-573.

[98] Dowling, Timothy E. "Dynamics of Jovian atmospheres." Annual Review of Fluid Mechanics 27.1 (1995): 293-334.

[99] Cho, James Y-K., et al. "A high-resolution, three-dimensional model of Jupiter's Great Red Spot." Journal of Geophysical Research E 106.E3 (2001): 5099-5105.

[100] Marcus, Philips. "Models of the Great Red Spot." Nature 343 (1990): 517-518.

[101] Makhmalbaf, H., Liu T., Merati P.. "Experimental Simulation of Buoyancy-Driven Vortical Flow in Jupiter Great Red Spot."APS Meeting Abstracts. (2015).

Appendix: Seeding the Flow

Tracing flow structure by any methods, e.g. PIV, PLIF, requires observing the motion of flow elements. Thus, a transparent fluid such as water or air needs some additional material to expose the detail of flow structure during the imaging. This procedure is usually called seeding. It is important to assure the additional material to the flow does not change the fluid property. Otherwise, the study is no more applicable to the original case. Another issue is the concentration of added material. If too much concentration of seeding is applied to the test zone, the space between camera and plane of focus will not be transparent enough and images will become blurry. Too low concentration of seeding however makes the flow structure and its detail untraceable. Approaches of different image processing methods are not necessarily the same. Some (for instance the code that was used in this work: LaVision 7.20) basically search a small box in a pair of images to find the same particle and draw the velocity vector between its position in first and second frame. This type of methods seeks for the peak of intensity in small vicinities and recognizes it as the "particle". Some other (e.g. Optical method which is used in this study) browsing the pair to find the same pattern of intensity gradient in both snapshots. Depends on which method is being used the seeding method should be accordingly chosen. For the former the particle seeding techniques should be used. The whole idea is adding particles like chuck, salt or, in this study, Polyamid Seeding Particles, PSP 5 μm, which can clearly be seen in images. On the contrary, injecting smoke or vapor to test zone requires the intensity-base image processing. In this study, two different types of smoke injection technique, olive oil spray and cigarette smoke have been tried. Results from experiments that were run by PSP 5 μm have been mentioned in previous chapters. In this chapter, the development of techniques using the primary seeding materials, olive oil, is discussed.

A-1: Olive Oil: The first idea is using the olive oil spray to seed the test zone. A tank of oil is connected to a compressed air hose. A uniform smoke made of mixture of air and very fine drops of oil is being discharged by this smoke generator. The flow rate is adjustable with a simple ball valve that controls the compressed air inlet. As examples of results from this method, figures A-1 and A-2 show the raw images, velocity vector/magnitude field and streamline acquired by this method of seeding and processed by Optical Flow for one consecutive and time-averaged of 123 pairs of image. For both of the figures, disk spin rate us set to 1200 RPM counter-clock-wise. Other combinations of boundary condition led to similar quality of results.

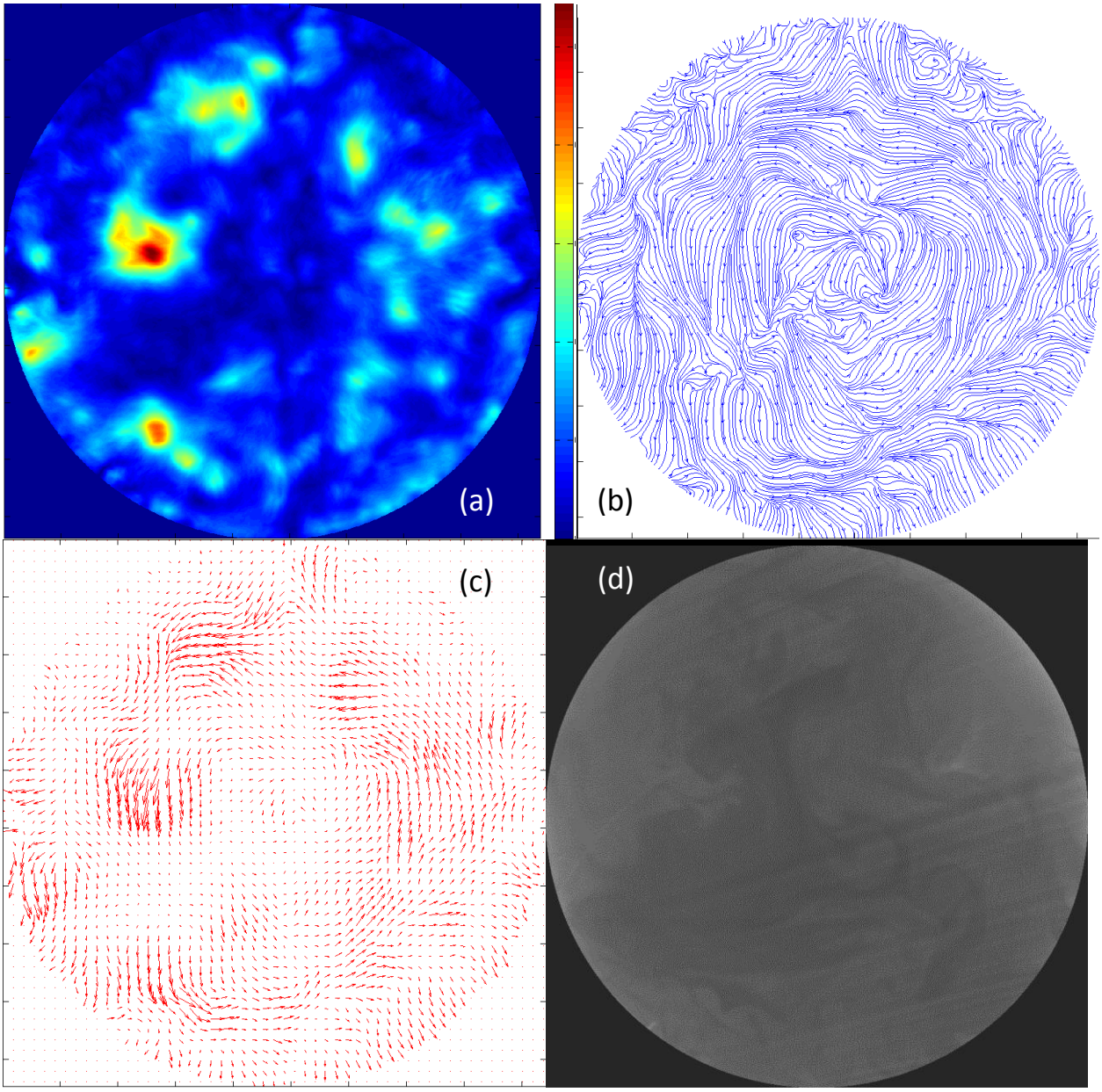

Figure A-1 Normalized velocity magnitude (a), Streamlines (b), Normalized velocity vectors (c) and first raw image of the corresponding pair (d) for $h = 2D$, No heat flux from the disk

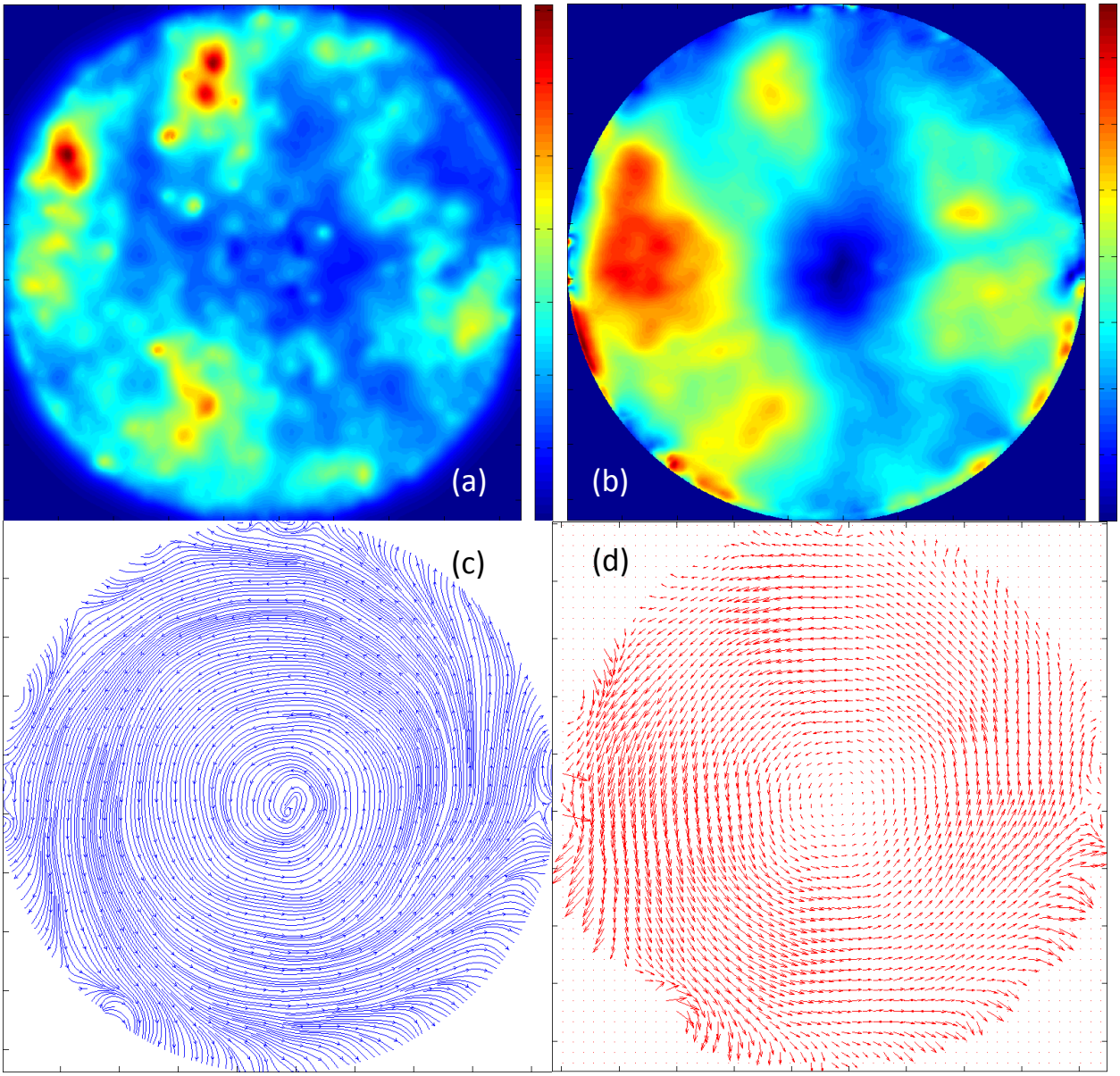

Figure A-2 The root mean square of velocity (a) time-averaged velocity magnitude (b), Streamlines(c) and Normalized velocity vectors (d) for 123 pairs of images in h = 2D , , No heat flux from the disk

Results obtained by spraying olive oil have some deficiencies. For one thing, the images are too dark and they most likely need to be rescaled before the processing. In other word, the difference between darkest and brightest region of images is not as high as the images of the same cases with particle seeding method. Therefore, the magnitude of pixels needs to be multiplied by a ratio number before processing and this amplification can also increase the noise.

For another thing, greasy nature of olive oil smoke makes the inner surface of the wall dirty. The effects of scratches, non-uniform wall thickness and droplets of oil on the inner surfaces change optical behavior of the cylinder. As a result, when the laser sheet comes through the cylinder, the problem with lines in image that was explained before becomes much more disturbing. Moreover, just a few seconds after each injection the density of smoke in the entire chamber becomes uniform. Uniformity makes the imaging complicated because the flow cannot be traced. To enlarge the time period of usable images a continuous injection of smoke is required and this makes the walls even dirtier.

The idea of using capsule to inject the particles/smoke to the test zone was formed during the experiments with this method of seeding when the importance of angularly uniform injection was observed. At first, spraying was being done from one direction. In some snapshots just half or even a quarter of each section (especially in lower heights) becomes smoky. Those snapshots, due to the lack of useful information, needed to be omitted. Not only does this spraying technique (spraying from one point) make the image processing and data analysis difficult, but also, there is no guarantee that everything is angularly symmetric and injection from one direction might flow behavior. Therefore, it has been decided to design and build a capsule that surrounds the cylinder without touching it. The smoke, or any other seeding mixture, can be uniformly injected through the small gap between the cylinder and the disk.

A-2: Cigarette Smoke: Using olive oil had some problems such as the contamination and making the surfaces greasy and difficulties of injection adjustments (low flow rates do not pick up enough microscopic drops of olive oil in the unit volume, whereas, the ball valve of compressed air is not designed for fine adjustments and the flow suddenly becomes much more

than what expected). Therefore, other types of smoke were tried. The cigarette smoke does not have that much of residue and the ash and unwanted solid particles can be filtered and separated from the test zone. As it is demonstrated in figure A-3, a metal chamber that connected to a fist air pump was designed and built to hold and burn a single cigarette as the smoke generator. This chamber can be opened and closed quickly and has a conic seat to holds a burning cigarette's filter. Air from the hand pump with a manually controlled rate of flow is injected through the chamber that the burning cigarette is set at the other end of it. The air flow in order to exit has to pass through the burning tobacco and then the cigarette filter. The flow from outlet is connected to a tube and directed to the capsule (the same capsule that was used for olive oil) that encompasses the intersection of wall cylinder and the bottom disk. During the experiments, as long as the cigarette is burning, a single fist pump every few seconds should suffice. Finally, for the systematic experiment that was performed in previous chapters, this smoke generator was modified and used to inject the polyamide particles to the test zone. In that case cigarette filter was replaced with a fine screen filter to avoid injecting the lumps of particle into the test zone.

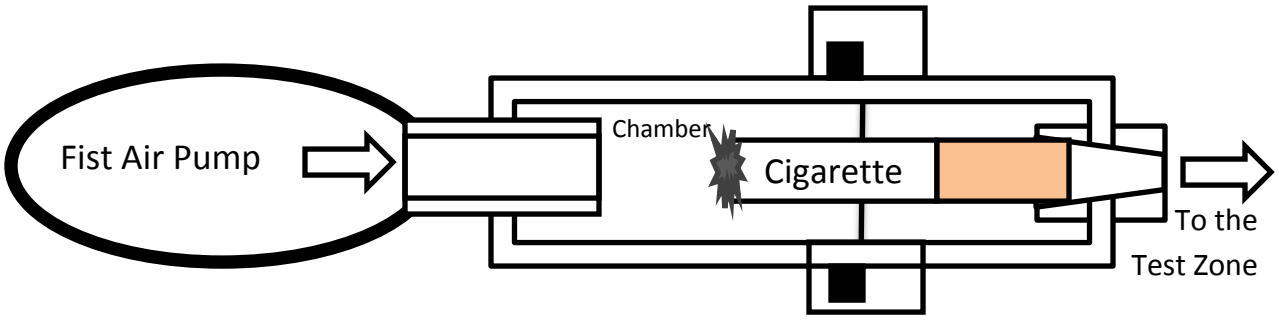

Figure A-3 Schematic diagram of the smoke generator

The same problem that was existed for the olive oil smoke (moving lines in images due to non-uniformity and scratches of wall) was observed in this method of seeding but because the

dirty inner surface problem does not take place in this case, the problem with lines in the images was slightly better. The most important advantage of cigarette smoke technique is it makes the flow structures easy to follow. Once the required boundary conditions and the smoke are applied, tornado-like vortices can clearly be visually observed.